

WATERJET FRACTURE-DIRECTED STEERABLE NEEDLES

By

MAHDIEH BABAIASL

A dissertation submitted in partial fulfillment of  
the requirements for the degree of

DOCTOR OF PHILOSOPHY

WASHINGTON STATE UNIVERSITY  
Department of Mechanical and Materials Engineering

AUGUST 2020

©Copyright by MAHDIEH BABAIASL, 2020  
All Rights Reserved

©Copyright by MAHDIEH BABAIASL, 2020  
All Rights Reserved

To the Faculty of Washington State University:

The members of the Committee appointed to examine the dissertation of MAHDIEH BABAIASL find it satisfactory and recommend that it be accepted.

---

John P. Swensen, Ph.D., Chair

---

Jow-Lian Ding, Ph.D.

---

David Lin, Ph.D.

## ACKNOWLEDGEMENTS

I would like to thank my advisor, Dr. John Swensen, for taking a chance on an unknown Iranian, bringing me to Washington State University, and supporting my research. I feel very fortunate to have learned from such a positive, and hardworking professional. Thanks to my other reading committee members, Dr. Jow-Lian Ding and Dr. David Lin, for their time and interest in my work. Dr. Ding and his graduate student's invaluable help in characterizing the soft tissues was a great addition to my dissertation.

As part of our lab's needle steering project team, I have worked with some outstanding colleagues. Fan Yang paved the way for me, and helped me get started. He was always there to answer my design-related questions and he was always ready to help. I am really grateful to have a great lab mate who also occasionally took me to Emerald Chinese Restaurant. I am also thankful to different undergraduate students who have helped me with the experimental setup. Among those are Alex Rodriguez and Sean Journot. I am also thankful for my other lab mates, Emily with her inspiring hardworking attitude, as well as Lee and Ben for their cheerful banter that could change every dull environment.

This section will not be complete without dedicating a paragraph to my family. I am indebted to my parents Hossein and Leila who instilled the value of science, education and integrity from the early stages of my life. Without them I would both

literally and figuratively not be here today. Thanks to my Brother, Ali who always supports my decisions and my lovely sister, Asal who has been a valuable source of wisdom whenever I needed to (although she is 10 years my junior). I am also thankful for my in-laws who supported my decision of getting a PhD although it is difficult for them not to visit Hamed as often as they used to.

Last but not least, I would like to thank my husband Hamed Mahdioun whose continued support made this dissertation possible. He turned his life upside down as a successful engineer and a businessman to move to WSU with me and literally started over. If I have to choose only one person in my life that I am the most grateful for, that would be Hamed. Throughout this process he, more than anyone else, has supported me, encouraged me, and pushed me to be my best. I am very lucky to have him as the second author on my life story, and I dedicate this dissertation to him.

# WATERJET FRACTURE-DIRECTED STEERABLE NEEDLES

Abstract

by Mahdiah Babaiasl, Ph.D.  
Washington State University  
August 2020

Chair: John P. Swensen

Robotic needle steering is a proposed method in the literature for controlling long flexible needles through curved paths in the soft tissue. Needle steering is proven to be effective in correction of insertion errors, steering around obstacles to reach the targets unreachable through conventional methods, and reaching to multiple targets from a single insertion.

In spite of their many advantages and potential applications, they are limited by a number of factors. First off, they have constant curvatures and the attainable radius of curvature is a function of the needle and soft tissue parameters. Buckling is another issue that happens when the needle goes through structures and tissues that it cannot penetrate. This imposes a large force at the base of the needle and causes it to buckle.

The use of the waterjet in medical applications has been developed more recently

and it is used for different applications such as soft tissue resection, bone cutting, wound debridement, and surgery. Because of the many advantages that the waterjet provides like selective cutting of the tissue layers in which the tissue layers can cut deliberately by controlling the pressure of the waterjet, it is an appealing technique for surgery instead of knife.

From the marriage between conventional steerable needles and the waterjet technology, waterjet steerable needles is born. In this technique, the direction of the fracture is controlled by high velocity waterjet and then the flexible needle follows the fractured path. This process continues until the needle can be steered in the soft tissue. Waterjet steerable needles resemble "drilling" in the sub-millimeter scale which has been proven to have superior advantages to conventional steerable needles.

Our results showed that cutting the tissue with the waterjet can eliminate the cutting force and thus reduces the force at the base of the needle resulting in reduced buckling. Moreover, waterjet steerable needles showed the possibility of smaller radius of curvature with reduced tissue damage. Waterjet steerable needles promise tissue-agnostic steering in which the needle can be chosen to have a low bending stiffness (because the waterjet does the cutting) to obtain super small radii of curvature.

## TABLE OF CONTENTS

	Page
ACKNOWLEDGEMENTS . . . . .	iii
ABSTRACT . . . . .	v
LIST OF FIGURES . . . . .	x
LIST OF TABLES . . . . .	xxi
CHAPTER	
1. ROBOTIC NEEDLE STEERING: STATE-OF-THE-ART AND RESEARCH CHALLENGES . . . . .	1
Motivation . . . . .	3
Clinical Motivation . . . . .	4
Prior Work . . . . .	6
Techniques, and Design Approaches for Needle Steering in Soft Tissue	7
Modeling Approaches for Steerable Needles . . . . .	24
Control Approaches Used in Needle Steering . . . . .	37
Clinical Acceptance of Steerable Needles . . . . .	50
Discussion . . . . .	53
Conclusions . . . . .	62
Contributions . . . . .	70
Dissertation Overview . . . . .	71
2. WATERJET SOFT-TISSUE INTERACTION . . . . .	75

Introduction . . . . .	76
Materials and Methods . . . . .	84
Finite Element Modeling of the Waterjet Soft Tissue Interaction . . . . .	84
Predictive Mechanics-based Model for Depth Of Cut (DOC) . . . . .	88
Experimental Setup and Measurement of Depth-Of-Cut (DOC) . . . . .	107
Soft Tissue Simulant Preparation . . . . .	110
Low Strain Rate Static Compression, High Strain Rate Split-Hopkinson-Pressure-Bar (SHPB) and Fracture Toughness Tests on SEBS Soft Tissue Simulants . . . . .	111
Results . . . . .	121
Mechanical Properties of SEBS Soft Tissue Simulants (constitutive response and fracture toughness) . . . . .	122
Experimental Results: DOC of the waterjet in Soft Tissue is a Function of the waterjet as well as Soft Tissue Properties . . . . .	128
Finite Element Model of the Waterjet Soft Tissue Interaction Result . . . . .	133
Validation of the Predictive Model with Experimental Results and Tissue Properties . . . . .	133
Discussion . . . . .	138
Conclusion and Future Work . . . . .	146
3. FRACTURE-DIRECTED WATERJET NEEDLE STEERING . . . . .	149
Waterjet Needle Insertion Forces . . . . .	150
Introduction . . . . .	151
Materials and Methods . . . . .	155

Results and Discussion . . . . .	162
Conclusions . . . . .	166
Fracture-directed Waterjet Steerable Needles . . . . .	166
Introduction . . . . .	167
Materials and Methods . . . . .	170
Results . . . . .	188
Discussion . . . . .	200
Conclusions . . . . .	207
4. CONCLUSION AND FUTURE WORK . . . . .	209
Waterjet Soft-Tissue Interaction . . . . .	209
Fracture-directed Waterjet Needle Steering . . . . .	210
Extensions . . . . .	212
BIBLIOGRAPHY . . . . .	213

## LIST OF FIGURES

	Page	
1.1	Some common steering methods proposed in the literature. (a) Tip-based steering of a needle with asymmetric tip, (b) Base manipulation of a needle with symmetric tip, and (c) Base manipulation of a needle with asymmetric tip. Note: tip geometry is not shown in the figure.	8
1.2	General Concept of the Robot Insertion Device. Recreated from [267].	8
1.3	Needle tip designs in conventional steerable needles to steer the needle through soft tissue. . . . .	9
1.4	Axial forces reported in [267] with bevel tip steerable needles. It is shown that increasing velocity increases the axial forces. © 2005 IEEE.	12
1.5	Flexure-tip steerable needle proposed by Swaney <i>et al.</i> [235]. (a) CAD model of the flexure-tip needle with the dimensions. (b) Flexure-tip steerable needle prototype. (c) When the flexure-tip needle is inserted into the tissue it bends due to reaction forces from the tissue. It remains straight during the duty cycling control. © 2013 IEEE. . . . .	14
1.6	(Left) Wire and tube steerable needle illustration recreated from the design proposed by Lee <i>et al.</i> [127]. (a) Full extension, and (b) Full retraction. The curvature is controlled by varying the extension length of the wire. (Right) "Airfoil" bevel needle with varying stylet offset illustration recreated from [34]. (a) Needle's design, and (b) Needle under applied forces from surrounding soft tissue. The curvature can be controlled by changing the control offset. . . . .	15
1.7	Principle of fracture-directed stylet-and-tube steering. First the inner stylet is advanced, followed by the outer tube. The shape of the tissue fracture closely matches the geometry of the inner stylet. After the outer tube follows the inner stylet, the resulting tip position depends on the static equilibrium of the wire, tube, and tissue. . . . .	17

1.8	(Right) Steerable needle designed by Scali <i>et al.</i> [216] © 2019 Scali <i>et al.</i> (A, B) with its actuation unit (C). (Left) The tendon-driven needle proposed by Van de Berg <i>et al.</i> [247] © 2015 ELSEVIER. FBG sensors are used to sense and recreate the shape of the needle and measure the tip position during insertions. $\phi$ can be up to $20^\circ$ . . . . .	20
1.9	Magnetic Needle steering system proposed by Ilami <i>et al.</i> [97] © The Authors 2020. . . . .	22
1.10	Flexture-based active needle design proposed by Dalta <i>et al.</i> [48] with SMA actuators. © 2015 by ASME. . . . .	23
1.11	Unicycle and Bicycle kinematic models for asymmetric-tip needles (bevel-tip and pre-curved needles) proposed by Webster <i>et al.</i> [270]. Translation and rotation of the wheels are shown with straight, and curved arrows, respectively. For the Bicycle model, the rotation occurs naturally, but for the unicycle model the rotation should be added artificially. . . . .	26
1.12	position and orientation of the needle tip . . . . .	29
1.13	Bending stiffness of a flexible needle. Under the same loading conditions (for instance forces from the surrounding tissue), the needle with less bending stiffness deflects more. . . . .	34
1.14	Mechanics-based models for needle-tissue interaction using virtual springs (Down), and a continuous load (Up). . . . .	35
1.15	(Up) Example of closed loop control of image-guided needle steering. Steering controller provides needle rotation and curvature needed to reach to the target. Robot controller included motor controllers and command motor control hardware to move the needle tip along the desired path to the target. Imaging system provides visual feedback for measurement of the tip pose. (Down) Example of an estimation scheme for closed loop control of image-guided needle steering. Output of the estimation scheme is given to the steering controller which identifies the needle rotation and curvature necessary to reach a target point. Estimation scheme is necessary when the outputs of the imaging feedback are noisy. Kalman-filter is a common estimator used in the literature [8]. . . . .	46

1.16	Clinically viable steerable needle system. Clinical trials with real patients has been one of the main components missing in the needle steering research to date. . . . .	52
1.17	Principle of steering in conventional steerable needles. Tip steerable needles rely on interaction forces from the soft tissue to be able to steer.	55
1.18	Tip-based needle steering concept. Steerable Needles can steer around obstacles and reach multiple targets from one insertion that are unreachable by straight needles. Anatomical obstacles can be veins, bones, nerves, and other structures that a needle cannot penetrate or can cause unwanted consequences. Steering direction can be chanced by rotating the needle at the base. . . . .	55
1.19	The effect of torsional windup and torsional friction when rotating a long flexible needle. Torsional friction and rotational inertial effects cause the tip angle to be out of sync with the base angle due to the rotational dynamics along the length of the needle. . . . .	57
1.20	Visual organization of the current thesis. This thesis is organized into four chapters. . . . .	74
2.1	Definition of DOC of the waterjet in soft tissue. The waterjet cuts a small path in front of the nozzle and the length of this path is dependent on the tissue properties (constitutive response and fracture toughness) as well as the waterjet properties (diameter and velocity). . . . .	82
2.2	Definition of depth of cut shown experimentally for a water-jet needle [23]. © 2019 IEEE. . . . .	82
2.3	Finite element solution algorithm for laminar and turbulent flow regimes.	86
2.4	Model of tissue and the needle in ANSYS. The tissue is modeled as a cube with 40 mm sides and the needle is modeled to the shape and diameter of each Nitinol tube. © 2019 IEEE. . . . .	86
2.5	Meshes used for needle penetration into the soft tissue simulant. The soft tissue and the needle are meshed with the Patch Conforming Tetra mesh and the Hex Dominant mesh, respectively. © 2019 IEEE. . . .	88

2.6	Schematic of crack formed by the waterjet in soft tissue. (left) Waterjet initiates a crack and then the crack opens to accommodate the waterjet with diameter $D$ followed by the waterjet displacing the tissue and (right) Crack left with diameter $d$ after the waterjet removal. . . . .	90
2.7	Schematic of crack expansion from radius $s_1$ to $s_2$ in penetration of the waterjet with radius $r_2$ into a crack with steady state radius of $r_1$ . . .	93
2.8	Schematic of the simple model for depth of cut of the waterjet in soft tissue. $v$ , $h$ and $D$ are velocity of the waterjet ( $\frac{m}{s}$ ), cut-depth ( $m$ ) and waterjet diameter ( $m$ ). . . . .	97
2.9	Simplified view of the flow field inside the region of cut: injected water impacts the surface of cut in the stagnation point and backflows from the sides. . . . .	100
2.10	Approximation of the surface of cut via ellipsoid. Left: superposition with experiment. Right: growth in time with constant aspect ratio. .	103
2.11	Effective area where the bulk of viscous dissipation happens. . . . .	104
2.12	Experimental setup to measure the depth of cut of the waterjet in soft tissue. A linear actuator is used to drive the needle into the soft tissue. Once the needle is in the tissue, the pump is run with a given volumetric flow rate and after about 30 (s) the camera will take a photo to be processed with a MATLAB program to measure the DOC. . . .	108
2.13	Custom-designed water-jet needle with a copper tubing ( $ID = 0.94$ mm and $OD = 1.59$ mm) soldered to a superelastic material Nitinol (first needle: $ID = 0.32$ mm and $OD = 0.58$ mm and second needle: $ID = 0.24$ mm and $OD = 0.33$ mm). The copper tubing is attached to a ferruled reducer and then standard PEEK tubing. . . . .	109

2.14	Custom designed molds and resultant tissues used for cut-depth experiments, static compression tests, SHPB tests and fracture toughness tests. (A and B) SEBS tissue simulant used for DOC experiments and Acrylic mold of $100 \times 100 \times 30$ mm dimensions. (C) Resultant tissue used for fracture toughness tests. (D) Acrylic-3D printed mold of thickness 2 mm to make tissues for SHPB tests. 10 mm punch is used to cut cylindrical samples for SHPB tests. (E and F) SEBS tissue simulant and custom-designed 3D printed mold of diameter 25 mm and height of 10 mm used for static compression tests. (images not to scale)	112
2.15	Instron 600DX machine used to perform quasi-static tests on soft tissue simulants. . . . .	114
2.16	Split Hopkinson Pressure Bar (SHPB) Experimental setup. . . . .	116
2.17	Schematic of the SHPB test setup. The SHPB consist of a striker and incident bar, a transmitted bar and a buffer. The bars are adjusted for soft tissue experiments and the material used for the bars is PEEK. . .	116
2.18	Schematic of the experimental setup to measure the fracture toughness of the SEBS soft tissue simulants. Trouser tear test is used to measure the fracture toughness of the SEBS soft tissue simulants to mode I crack propagation. . . . .	117
2.19	Example static compression test results (stress vs. stretch ratio) on 20% SEBS G1650 soft tissue simulants with the corresponding Ogden fit. Tissue properties are measured at three strain rates of $0.001s^{-1}$ , $0.01s^{-1}$ and $0.1s^{-1}$ . The same J-shaped stress vs. stretch ratio with the same trend is also observed for other tissue simulants. For each strain rate, two tests are conducted and the averages of these tests are shown in this figure. . . . .	123
2.20	Example SHPB compression test results on 15% SEBS G1650 soft tissue simulants. Tissue properties are measured at three strain rates of $3000s^{-1}$ , $4500s^{-1}$ and $6000s^{-1}$ . The same J-shaped stress vs. stretch ratio with the same trend is also observed for other tissue simulants. For each strain rate, three tests are conducted and the averages of three tests are shown in these figures. . . . .	124

2.21	Shear modulus vs. strain rate and linear fit to data to extrapolate to higher strain rates. (up) G1650 SEBS soft tissue simulants and (down) G1652 SEBS soft tissue simulants. Due to the linear pattern in high strain rates, the shear modulus can be extrapolated to the desired strain rate depending on the application. . . . .	127
2.22	Experimental DOC of the waterjet in SEBS soft tissue simulants vs. volumetric flow rate. (up) DOC vs. Flow Rate for the Needle with 0.32 mm inner diameter (ID) in SEBS Tissue Simulants and (down) DOC vs. Flow Rate for the Needle with 0.24 mm ID in SEBS Tissue Simulants. The data show the average of 5 tests for each volumetric flow rate and error bars show the standard deviation of the data. . . .	129
2.23	DOC of the waterjet as a Function of Needle Diameter for two needle inner diameters tested in this study ( $D = 0.32mm$ and $D = 0.24mm$ ). The volumetric flow rate and tissue stiffness are held constants. The result is shown as an example for 15% G1650 SEBS soft tissue simulants. The data are the average of 5 experiments and the error bars are standard deviation of the data. . . . .	130
2.24	DOC as a Function of percentage of G1650 SEBS soft tissue simulants. The volumetric flow rate and inner diameter of the needle ( $D = 0.32$ mm) are held constants. The data shown are the average of 5 experiments and the error bars are the standard deviation of the data.	131
2.25	Example output of the finite element modeling for depth of cut of water-jet. In this example, maximum depth of cut is interpreted from the outlet of the needle. . . . .	134
2.26	DOC vs. time for 15% and 20% G1652 tissues; Experimental results (symbols) vs fluid model (lines) with best-fitting $\eta$ . Needle diameter $D = 0.32mm$ and waterjet velocities (for G1652 15% $v = 10.36\frac{m}{s}$ and for G1652 20% $v = 14.51\frac{m}{s}$ ) are remained constant. . . . .	135
2.27	Up: values of $\eta$ that match the DOC at 30 seconds (symbols) and parabolic fit (dashed lines). Down: DOC prediction from the fitted $\eta$ (solid lines) and experimental values (symbols). . . . .	137

2.28	New class of needle steering techniques namely fracture-directed water-jet needle steering. In this method, the direction of the tissue fracture is controlled by the controllable waterjet nozzle and then the flexible needle made of Nitinol follows the cut path by the waterjet. This process continues until the needle reaches to the desired location in the soft tissue to perform the designated task either surgical or drug delivery. The direction of the needle can be controlled by rotating the nozzle inside the tissue and cutting a new path in another direction by the waterjet. . . . .	145
3.1	Schematic of the forces acting on the needle passing through the tissue for: (a) the no water-jet case with a traditional needle and (b) using water-jet cutting. $F_{elastic}$ is the elastic force that fractures the tissue and forms a crack (this force only exists before puncture and from the surface of the undeformed tissue to the maximally deformed one), $F_{cutting}$ is the cutting force and $F_{friction}$ is the friction force acting along the shaft of the needle (these two forces act on the needle from puncture to maximally inserting the needle and before exiting the tissue). (c) In the case of the waterjet (blue schematic), the tip forces are eliminated and only friction along the shaft of the needle exists (it is even expected to be lower than friction due to lubrication provided by water). For traditional needles (red schematic), insertion force can be defined as $F_{insertion} = F_{elastic} + F_{cutting} + F_{friction}$ and in the case of the needle with water-jet, relationship $F_{insertion} = F_{friction}$ holds. Experimental results also verified these relationships (Our results do not show $F_{elastic}$ because we started after puncture.) . . . . .	154
3.2	Experimental setup of the water-jet system to measure the forces at the base of the needle. A linear actuator drives the needle into tissue with a given velocity of insertion adjusted in the customized software. A high-pressure pump with changeable flow rate is used to create high-pressure water for experiments with water-jet. A load cell at the base of the needle measures insertion forces and the data are gathered in the control software. . . . .	158
3.3	Custom-designed needle for insertions. The needle consists of a copper tubing soldered to a superelastic material named Nitinol as its "needle". The copper tubing is attached to a ferruled reducer and then standard tubing. . . . .	160

3.4	Force <i>vs.</i> displacement measurement for ten trials each in: (A - C) 10% SEBS tissue simulant with 3 different velocities of insertion (D - F) 15% SEBS tissue simulant with 3 different velocities of insertion and (G - I) 20% SEBS tissue simulant with 3 different velocities of insertion. The black plot (the one with circles) shows the total insertion force in the case of the traditional needle insertion after puncture. This force is equal to $F_{cutting} + F_{friction}$ . The red plot (the one with asterisks) depicts only friction force ( $F_{friction}$ ) (acquired with inserting the needle into the previously cut channel). The last plot (blue one with squares) represents the total insertion force with water-jet needle. As is evident from all figures, total insertion force using water-jet is even lower than the friction force since water-jet eliminates tip forces and lubricates the channel while insertion. . . . .	163
3.5	Underlying Principle of the Waterjet Steerable Needles. First, the direction of the tissue fracture is controlled by angled sub-millimeter waterjet and then the flexible Nitinol tube follows the cut path. This process continuous till the needle avoids the obstacles and reaches to a target location. Direction of the curvature can be changed by rotating the base of the needle. Note that this figure shows the general principle of the waterjet needle steering and the experiments in this chapter are conducted using a fixed-angle nozzle shown in Fig. 3.7. . . . .	171
3.6	CAD model of the Waterjet Needle that consist of a Nitinol tube with sub-millimeter diameter soldered to a copper tubing which is connected to the waterjet nozzle and then PEEK tubing. Two custom-designed gears along with the motor provide the rotation at base of the needle to change the direction of the steering. . . . .	174
3.7	Waterjet fixed-angle tip used in the experiments in this section. (Left) Schematic of the fixed-angle nozzle principle and (Right) Waterjet needle tip with $38^\circ$ angle. . . . .	175

3.8	Setup for waterjet needle steering tests. For curvature control by varying cut-depth tests: First, high-pressure pump is set to the desired flow rate based on the desired depth-of-cut and then waterjet cuts a channel in tissue at $30^\circ$ , the pump is turned off and the needle follows the channel with the velocity of insertion of $1 \frac{mm}{s}$ . This process continues until the needle is steered in the tissue. For curvature control using waterjet duty cycling tests: First, high-pressure pump is set to the desired flow rate based on the stiffness of the tissue (for 10% SEBS, 15% SEBS and Knox Gelatin, the flow rates are set to 40, 70 and $10 \frac{mL}{min}$ ) and then waterjet cuts a channel in tissue at $38^\circ$ angle. The pump is turned off and then the needle follows the channel with the velocity of insertion of $1 \frac{mm}{s}$ . For insertions without waterjet, the pump is turned off and the needle is inserted with velocity of insertion of $0.5 \frac{mm}{s}$ . Telescopic sheath made of two copper tubes is used to prevent buckling of the needle during insertions without waterjet. The needle has inner diameter (ID) of 0.24 mm and outer diameter (OD) of 0.33 mm and the tip has ID = 0.24 mm. . . . .	176
3.9	Schematic of the duty cycling of the waterjet in order to control the radius of curvature of the needle. For 0% duty cycling, the waterjet is off through the length of insertion and needle is inserted without waterjet and 100% duty cycling means that waterjet is ON for the entire length of insertion. . . . .	178
3.10	The kinematic model of the waterjet needle steering. The z-axis is assumed to be tangent to the needle at the tip and the y-axis is towards the center of the curvature. The needle follows a path in y-z plane with radius r and arc length $\ell$ . The frame advances as the needle tip progresses during waterjet needle steering. $\delta\theta$ , $\delta\ell$ and r are the incremental needle rotation angle, incremental insertion distance and radius of curvature, respectively. Note that, $\delta\ell$ equals h (depth-of-cut).	182
3.11	Definition of $\beta$ in (3.9). $\beta$ is defined as the deflection of the needle around x-axis. . . . .	183
3.12	The flow chart of the algorithm used for path planning. . . . .	187

3.13	An example of the waterjet needle steering in the z-y plane in SEBS G1650 10% tissue simulant. (up) Experimental results of the needle steering using two different waterjet velocities (two figures are overlaid on top of each other). (bottom) Experimental results (derived with image processing on successive photos of the needle path to determine the tip position) along with the kinematic model. Average radii of curvature for three experiments are: For $20 \frac{ml}{min}$ : $r_{ave} = 97.25mm$ (total insertion length $\ell = 65$ mm) and for $40 \frac{ml}{min}$ : $r_{ave} = 81.79mm$ (total insertion length $\ell = 57$ mm). . . . .	190
3.14	An example of the waterjet needle steering on z-y plane in SEBS G1650 15% tissue simulant. (up) Experimental results of the needle steering using two different waterjet velocities (the figures are overlaid on top of each other). (bottom) Experimental results along with the kinematic model. Average radii of curvature for three experiments are: For $30 \frac{ml}{min}$ : $r_{ave} = 66.49mm$ (total insertion length $\ell = 56$ mm) and for $50 \frac{ml}{min}$ : $r_{ave} = 58.42mm$ (total insertion length $\ell = 52$ mm). . . . .	191
3.15	An example of the waterjet needle steering with a base rotation during the insertion. In this example, $\delta\ell = 2.2$ 2.2 mm with 10 steps for the first bend, $\delta\theta = 0$ 180° to flip the nozzle direction and 20 steps for the second bend. $Q = 50 \frac{ml}{min}$ for both bends. The figure shows an overlap of the experimental result with the kinematic model. . . . .	192
3.16	2D path planning of the waterjet steerable needle with no base rotation. The Figure shows an overlap of the simulated path and experimental results. . . . .	194
3.17	2D path planning of the waterjet steerable needle with one 180° base rotation. The Figure shows an overlap of the simulated path and experimental result. . . . .	195
3.18	2D path planning of the waterjet steerable needle with different base rotations. As can be seen from this figure, the curvature of the waterjet steerable needle can be controlled by changing the depths-of-cut of the waterjet that can be controlled by changing the velocity of the waterjet. It can also be seen from this figure that the waterjet steerable needle can reach different targets from one insertion in the soft tissue. . . . .	197

3.19	Waterjet duty cycling to control the radius of curvature of the waterjet steerable needle. (Left) 10% SEBS in mineral oil soft tissue simulants (Tissue A) and (Middle) 15% SEBS in mineral oil soft tissue simulants (Tissue B). The figures are obtained by overlaying 6 different experiments. The total insertion length is 70 mm. Flow rates of $40 \frac{ml}{min}$ and $70 \frac{ml}{min}$ are used to get the same cut-depths in the same amount of time for Tissue A and Tissue B, respectively. The best ROC for Tissue A and Tissue B are 75 and 49 mm. (Right) obtaining straight insertion using waterjet needle with no tip. The needle follows the cut path by the waterjet. . . . .	198
3.20	UP(Left) Controlling the curvature of the needle in 10% by weight Knox Gelatin soft tissue phantoms (Tissue C) by duty cycling of the waterjet. The total insertion length is 60 mm. Flow rate of $10 \frac{ml}{min}$ is used to get the depth of cut of 3mm in each insertion step. UP(Right) Bicycle model of the needle motion and (Bottom) Overlay of the needle path with model. . . . .	199
3.21	Curvature of the waterjet steerable needle vs. duty cycling of the waterjet for two different tissue stiffnesses. The values reported for Curvature are the average of the 3 trials. The error bars are one standard deviation above and one standard deviation below the data points. For Tissue A, the goodness of the fit is $R^2 = 0.9839$ and for Tissue B, $R^2 = 0.98$ . . . . .	202
3.22	Curvature of the waterjet steerable needle vs. duty cycling of the waterjet in Tissue C. The values reported for Curvature are the average of the 3 trials. The error bars are one standard deviation above and one standard deviation below the data points. The goodness of the fit is $R^2 = 0.9973$ . . . . .	203

## LIST OF TABLES

	Page
1.1 Soft tissue mimicking materials used in the literature and their preparation methods. . . . .	63
1.2 Soft tissue simulants and soft tissues that they simulate in terms of mechanical properties. . . . .	64
1.3 Optical, and acoustical properties of soft tissue mimicking materials and their real soft tissue counterpart that share the similar properties. These properties are useful for image-guided medical interventions. . .	65
1.4 fake . . . . .	65
2.1 Strain rates ( $\dot{\epsilon}$ ) and crack growth rates ( $\dot{r}$ ) associated with the waterjet diameters ( $D$ ) and velocities ( $v$ ) used in this chapter. The values of this table are calculated using (2.49) and (2.51). In order to accurately validate the depth of cut model, the tissue properties should be measured at the strain rates and crack growth rates related to the waterjet penetration into soft tissue. Note: the waterjet diameters are taken to be the inner diameters of the Nitinol tubes. . . . .	121
2.2 Mechanical properties of G1650 SEBS tissue simulants obtained from Ogden fit to data. $\mu$ (kPa), $\alpha$ and $R^2$ are shear modulus, strain hardening factor and goodness of the Ogden fit, respectively. . . . .	125
2.3 Mechanical properties of G1652 SEBS tissue simulants obtained from Ogden fit to data. $\mu$ (kPa), $\alpha$ and $R^2$ are shear modulus, strain hardening factor and goodness of the Ogden fit, respectively. . . . .	125
2.4 Linear fit to shear modulus vs. strain rate data. Shear modulus can be extrapolated to higher strain rates based on these fits according to the intended application. $\mu$ (MPa), $\dot{\epsilon}(s^{-1})$ and $R^2$ are shear modulus, strain rate and goodness of the linear fit, respectively. . . . .	126
2.5 Fracture toughness ( $J_{IC}$ ) of G1650 SEBS soft tissue simulants at three test rates of 0.1, 0.5 and $1 \frac{mm}{s}$ . Crack growth rate ( $\dot{r}$ ) is assumed to be half of the rate at which the test is performed. . . . .	128

2.6	Fracture toughness ( $J_{IC}$ ) of G1652 SEBS soft tissue simulants at three test rates of 0.1, 0.5 and 1 $\frac{mm}{s}$ . Crack growth rate ( $\dot{r}$ ) is assumed to be half of the rate at which the test is performed. . . . .	128
2.7	Calculated values of $P_w$ from (3.4) at different waterjet velocities for 15% and 20% G1652 SEBS soft tissue simulants for the needle with $D = 0.32mm$ . . . . .	134
2.8	Coefficients from parabolic least-squares fitting of $\eta$ as a function of $P_w$ (equation 2.52), for different tissues and needles; N1: $D = 0.32$ mm, N2: $D = 0.24$ mm. . . . .	138
3.1	Soft tissue phantoms, their properties and corresponding waterjet velocities and Depths-of-cut. These data are derived from tests described in Chapter 2. . . . .	189
3.2	Comparison of the Smallest Radius of Curvature (ROC) of the waterjet Steerable Needle with Conventional Steerable Needles in the Same Medium. . . . .	201

## Dedication

*This dissertation is dedicated to my husband Hamed Mahdioun who has been a constant source of support and encouragement during the challenges of graduate school and life.*

**CHAPTER ONE**

**ROBOTIC NEEDLE STEERING: STATE-OF-THE-ART AND**

**RESEARCH CHALLENGES**

Medical robotics is an interdisciplinary field that came to existence to improve the medical procedures utilizing robotics technology. Medical robotics range from minimally-invasive surgeries using robotics to robots that support patients in rehabilitation (exoskeleton, and end-effector-based) to image-guided systems for different medical interventions. Different advantages of robots made them appealing to be used for medical interventions. Among these advantages are being precise, untiring, dexterous, and the ability to work in environments that are not safe to human clinicians. Limitations of robots include being expensive, hard to install, and occasional failure due to damage or wear that can be deadly in clinical environments.

This dissertation relates to the waterjet application in medical robotics including waterjet-soft tissue interaction, and waterjet steerable needles that can be used in interventional radiology and other medical procedures for percutaneous applications.

In order to address several challenges and gaps in the literature, a new needle steering system is proposed in this dissertation that we call Fracture-directed Waterjet Steerable Needles in which the direction of the tissue fracture is controlled by the waterjet and angled tip after which the flexible needle follows. The major contributions of the research in this dissertation can be summarized as follows:

- Waterjet Soft tissue interaction is characterized and validated with experiments in terms of developing finite element model, and mechanics-based model based on fracture mechanics to predict the penetration pressure as well as depth of cut of the waterjet into soft tissue as a function of the waterjet properties (diameter, velocity), and soft tissue properties (constitutive response, and fracture toughness).
- Proposed and developed a curvature-controllable waterjet steerable needle system that is improved over conventional steerable needles in terms of being curvature variable without the need for rotational duty cycling, smaller radius of curvature even in softest soft tissues, no buckling issue while inserting with the waterjet, no rotational duty cycling for controlling curvature and thus no torsional friction, as well as reduced insertion forces compared with the conventional needles.
- Proposed, and validated a discrete kinematic model for the waterjet steerable needles that consist of two parts: (1) the mechanics-based model that predicts the cut-depth of the waterjet in soft tissue based on soft tissue properties, waterjet diameter, and water exit velocity, and (2) a discrete-step adaptation of kinematic bicycle model of the steerable needle travel.

In this Chapter, the motivations for needle steering as a whole are first demonstrated and then the state-of-the-art of the different needle steering techniques in the

literature are analyzed. This includes their modeling, path planning, control, and clinical applications. Finally, a discussion of the advantages and limitations of these existing techniques is presented, and concluding remarks as well as contributions and overview of the current dissertation are provided.

## 1.1 Motivation

Needles are least invasive surgical tools that are used to administer or draw liquids to or from the body. The wound made by a needle is self-healing for most insertion using needles up to 5 mm in diameter [128, 133]. Inflexible needles often cannot reach to targets in difficult anatomical places without deformation of the needle or of the anatomical structure between the insertion point and the destination point. Thus, the need arises for flexible needles that can be steered around the anatomical obstacles, thus improving the placement accuracy of the tip of the needle and improving outcomes for targeted drug delivery and biopsy.

Robotic needle steering allows for insertion of long flexible needles along curved, and controlled paths through soft tissue [59, 270]. Robotic needle steering can improve the medical interventions in different ways. First off, it allows the clinicians to correct for errors during insertion and reach a target location with increased accuracy in comparison to the straight insertion. Second, obstacles can be steered around to avoid anatomical constraints to reach targets that were unreachable with the traditional methods. Third, multiple targets can be reached from a single insertion site, and this

will decrease complications such as bleeding, and infection.

### 1.1.1 Clinical Motivation

There are some clinical procedures that can greatly benefit from robotic needle steering. Examples of these procedures are as follows:

#### *Liver Cancer:*

Liver cancer is the second leading cause of cancer deaths among men with about 500k deaths each year [244]. Radiofrequency ablation (RFA) is the most common procedure for treatment of liver tumors [130]. In this method, the tumor or other target tissue is thermally destroyed by heat generated by high frequency alternating current at the end effector of a small electrode that can be limited by the maneuverability of the needle. Accurate placement of the electrode under image guidance can avoid further dramatic consequences such as hepatic bleeding and destruction of healthy tissues. Approximately three quarters of the patients are ineligible for surgery, and thus minimally invasive ablations are preferred. Adebar *et al.* [6] stated the need for needles with tighter curvatures to target more points per entry wound that reduces the risk of hemorrhage. They also stated that minimum radius of curvature of 50 mm or less is required for ablation of liver tumors.

### *Biopsy for Cancer Diagnosis:*

According to the global cancer statistics [244], there were an estimated 8.2 million deaths from cancer in 2015. Prostate cancer, and breast cancer are two of the most prevalent cancers among men, and women, respectively, and the lung cancer is the leading cause of death in both men and women. Early diagnosis of the cancer is important for the success of treatment and decrease mortality rates. Biopsy is the common diagnostic method to identify the malignancy of the target tissues. In this method, a needle is used to get small samples of the target tissues for further lab analysis. Accurate placement of the needle is very important for correct diagnosis since the needle should be placed such that it can sample the malignant tissue instead of healthy tissue. Manual insertions can have different results and they are highly dependent on the skill and expertise of the physician performing the operation. As a result, robotic needle guidance under visual feedback has a great potential to enhance biopsy performance [238]. Ultrasound (US) feedback, and Computerized Tomography (CT) are examples of visual feedback used for performing biopsies [106, 287].

### *Brachytherapy:*

Brachtherapy is the most effective known treatment for prostate cancer [84] in which the radioactive seeds are placed in the tumors to destroy them. Success of the treatment is dependent on the accurate placement of about 100 small radioactive

seeds. In the case of inaccurate placement, sensitive surrounding tissues like bladder, rectum, seminal vesicles, or urethra can be destroyed too. Robotic needle guidance can be helpful here too since it can be used to perform accurate and repetitive insertions under transrectal ultrasound guidance [223, 106]. Magnetic Resonance Imaging (MRI) can also be used with robotic needle guidance device [222].

## 1.2 Prior Work

This section provides a review of relevant state-of-the-art. First, techniques, and design approaches for needle steering in soft tissue is demonstrated. Then, modeling approaches for steerable needles are classified into kinematic models, finite element models, and mechanics-based models. After that, control approaches used in the needle steering are discussed.

It should first be noted that there are steerable catheters such as the ones discussed in [161, 268, 220, 269, 271, 63, 62, 236, 254, 237, 105, 262, 213] that operate in open spaces through body canals. They are categorized into Continuum robots [210, 140, 111], Concentric tubes that are made of several telescoping pre-curved superelastic tubes [86, 180], and active cannulae [212]. Steering the catheter through an open space is fundamentally different from steering the needle through soft tissue, and thus these state-of-the-art is out of the scope of this literature review.

### 1.2.1 Techniques, and Design Approaches for Needle Steering in Soft Tissue

From the needle design and its mode of manipulation point of view [250], steerable needles can be classified into *passive* and *active* categories. Passive methods include base manipulation in which lateral translation and rotation motions of the base of the needle are utilized during insertion [80], rotating beveled needle [9, 5], pre-curved needle tip [272], pre-bent needle tip [232, 149] in which a needle with an asymmetric tip design is used to create curvature, Stylet-and-Tube Steerable Needles [284], and notched shaft [110]. Active methods include telescoping cannula [78], programmable bevel [221, 36, 266, 151], tissue manipulation in which deformations of the surrounding tissue is used to alter the position of the target and obstacles [243], and controlled articulating tip [247, 6]. Active needles can take into account for any misalignment using their actuation forces. However, they can increase the manufacturing cost and the thickness of the needle. Fig. 1.1 provides an illustration of the some of the common steering methods in literature.

For all techniques of inserting the needles into the soft tissue, an insertion device is used that can insert and rotate the needle, and actuate other degrees of freedom where applicable. Fig. 1.2 shows the general concept of the robot insertion device which is recreated from [267].

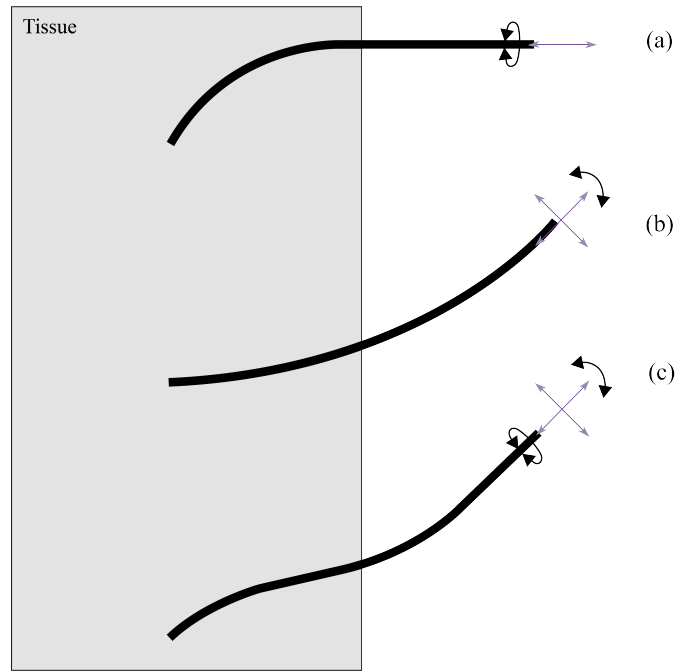


**Figure 1.1:** Some common steering methods proposed in the literature. (a) Tip-based steering of a needle with asymmetric tip, (b) Base manipulation of a needle with symmetric tip, and (c) Base manipulation of a needle with asymmetric tip. Note: tip geometry is not shown in the figure.

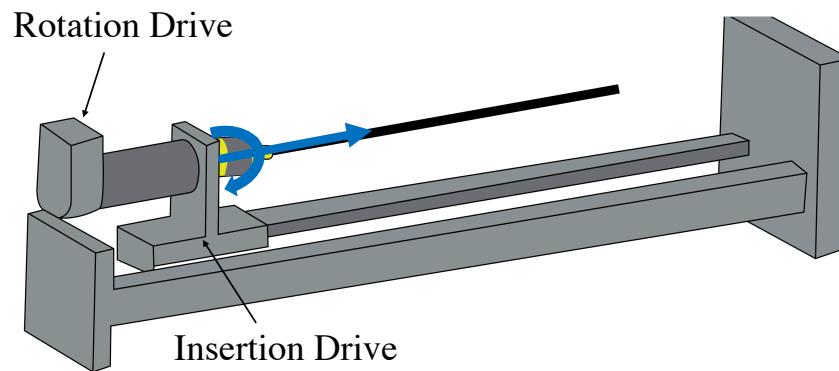


**Figure 1.2:** General Concept of the Robot Insertion Device. Recreated from [267].



**Figure 1.3:** Needle tip designs in conventional steerable needles to steer the needle through soft tissue.

*Tip-based Needle Steering:*

Once considered a disadvantage by physicians who would rotate the needle at the base to avoid its deflection, tip-based needle steering use this as an advantage for steering. Tip-based steering methods use the asymmetry of the needle tip to create forces at the tip needed to steer the needle (see Fig. 1.3). These needles are usually made of Nitinol which is a superelastic alloy of nickel and titanium. This allows the needle to be more flexible than straight needles, relative to the surrounding tissue, which allow for deflection of the needle as it cuts into tissue. This resultant needle deflection has been described using kinematic models. Some of these first kinematic models proposed by Webster *et al.* [270] apply to tip-based steerable needles. Control of the needle is accomplished through 2 degrees of freedom (DOF): insertion and rotation of the needle at its base along the central axis. Duty cycling control strategy [67, 155] uses the cycles of pure insertion of the needle (maximum curvature), and insertion with continuous rotation (straight path) to control the curvature of the tip-based steerable needles. The resulting needle tip path can be approximated by an arc of a circle with an effective curvature  $\kappa_{eff}$  that can be tuned between 0, and the

maximum curvature  $\kappa_{max}$ . The relationship between  $\kappa_{eff}$ , and the duty cycle ratio DC can be approximated by the following linear function [155]:

$$DC = \frac{\ell_{rot}}{\ell_{rot} + \ell_{ins}} \quad (1.1)$$

$$\kappa_{eff} = (1 - DC)\kappa_{max}$$

Where  $\ell_{ins}$ , and  $\ell_{rot}$  are the insertion lengths of the pure insertion, and insertion with continuous rotation, respectively. If the insertion velocity is constant, then the duty-cycle DC can be found from the duration of each phase instead of their insertion length [277, 251, 31, 188, 41, 153]. The limitations of the duty cycle control are as follows. First, the maximum curvature  $\kappa_{max}$  should be known beforehand to compute DC. This parameter is difficult to find in practice and online estimation scheme is required [166]. The other limitation is that continuously rotating the needle along its axis is not always possible especially when there are sensors, or trackers embedded in the needle.

The effect of the bevel angle on needle path has been studied in artificial tissue simulants [267], ex-vivo tissues [149], and in-vivo soft tissues [146]. For bevel-tip steerable needles, the smaller the bevel angle, the smaller the radius of curvature [215]. The curvature of the bevel tip steerable needles in very soft and biological tissues is very low and this limits the use of duty cycle control in clinical practice. In order to increase the curvature of the needle, pre-bent tips [6], and pre-curved tips [249]

are introduced. However, these needle tips are not suitable for duty cycling control due to increase in tissue damage during rotation of the needle. Needle curvature is dependent on the needle, and tissue material properties, tip bevel angle, and friction between the shaft of the needle and surrounding tissue.

Webster *et al.* [267] developed a robotic needle steering device that include force/torque sensor, horizontal needle insertion, and stereo image data acquisition, and showed that during experiments in tissue phantoms, needle path is not dependent on insertion velocity, but depends on bevel tip angle. They also measured the forces acting on the needle during insertion, and showed that these forces does depend on the insertion velocity. The rubber-like Simulated Muscle Ballistic Test Media from Corbin, Inc. is used as the soft tissue simulant. The tissue simulant is fairly stiff with stiffness of  $4.9 \frac{N}{mm}$  by a blunt indentation test, and applies less friction to the shaft of the needle in comparison to the similar phantoms like silicone with similar stiffness. The stiffness of the soft tissue used is more than most human soft tissues. The needle used is a 0.83 mm diameter Nitinol (alloy of 55% Nickel and 45% Titanium, and when heat-treated becomes a superelastic material) with a hand-machined bevel tip with  $40^\circ$  angle. Bevel angle has little effect on the axial force. Steering is found to improve (smaller radius of curvature) with decreasing bevel angle down to  $5^\circ$ . Fig. 1.4 depicts the axial forces with bevel-tip steerable needles. Increasing velocity increases the axial forces.

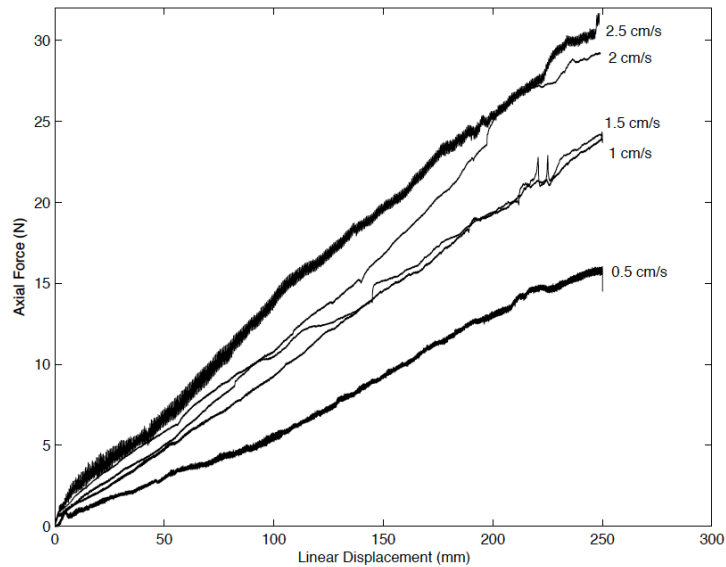


**Figure 1.4:** Axial forces reported in [267] with bevel tip steerable needles. It is shown that increasing velocity increases the axial forces. © 2005 IEEE.

Misra *et al.* [158] obtained the minimum radius of curvature of 179.4 mm (which is quite high) with 0.4 mm pre-curved needle in Plastisol soft tissue phantoms with a plastic to softener ratio of 4:1. Park *et al.* [183] used a beveled tip needle of 0.57 mm diameter in Plastisol soft tissue phantoms with a plastic to softener ratio of 4:1 and achieved a radius of curvature of 161.3 mm. Reed *et al.* [199] used a 15° pre-bent needle with a bevel tip of 45° with 0.61 mm diameter in Plastisol soft tissue phantoms with a plastic to softener ratio of 4:1 and achieved a radius of curvature of 61 mm. Majewicz *et al.* [149] used a pre-bent needle tip with 0.58 mm diameter and achieved a minimum ROC of 34 mm in goat liver. They found that bevel-tip needle with the diameter of 0.58 mm obtains 667 mm minimum radius of curvature. Wedlick and

Okamura [272] used pre-curved needles with 0.48 mm diameter made of Nitinol and obtained a minimum ROC of 15.5 mm in Plastisol rubber with a 4 to 1 ratio of regular stiffness plastic to plastic softener as a phantom tissue. However, they stated that the methods of needle fabrication are not perfectly repeatable. The curvature can only be controlled by duty cycling which causes considerable tissue damage.

Okazawa *et al.* [178] proposed a hand-held steerable needle of 0.902 mm diameter consisting of a pre-bent stylet inside a straight cannula. They concluded that the the curvature of the needle path increases as the phantom stiffness, and needle extension increase. Stiffer tissues generate a more immediate lateral reaction against the curved portion of the stylet, and thus resulting in a greater curvature. Tissue mimicking phantoms are made of polyvinyl chloride compound. The insertion velocity is  $5 \frac{mm}{s}$ . They showed that changing the insertion speed within the range of the velocities used in clinical practice ( $1-10 \frac{mm}{s}$ ) did not change the tip path curvature. Their steering method is based on the fact that the cannula must be stiffer than the stylet, and the tissue must be stiffer than the cannula. This limits the achievable smaller radius of curvature. They obtained the maximum lateral deflection of 35 mm in tissue with elastic modulus of 157 kPa, and with 12 mm extension of the inner stylet.

Swaney *et al.* [235] designed a flexure-based needle tip that provided the high curvature of the pre-bent needles during insertion and low tissue damage of the bevel-tip needles during rotations. Duty cycling is used to control the curvature of the

needle. The outer diameter (OD), and the inner diameter (ID) of the needle are 0.91 mm, and 0.6 mm, respectively with  $10^\circ$  bevel angle. The tip flexes to the maximum angle of about  $22^\circ$ . The tissue phantoms used for the experiments are made of 10% by weight Knox Gelatin (Kraft Foods Global Inc., IL), and *ex vivo* pork loin. They found that curvature decreases linearly by increasing duty cycle rate with the curvature of 0 for 100% duty cycling (constant axial rotation) and maximum curvature for 0% duty cycling (no axial rotation). The velocity of insertion into soft tissues is  $0.5 \frac{cm}{s}$ . They got minimum radius of curvature (0% duty cycle) of 12.1 cm in gelatin phantoms and 17.6 cm in *ex vivo* pork loin. Fig. 1.5 shows the proposed steerable needle.

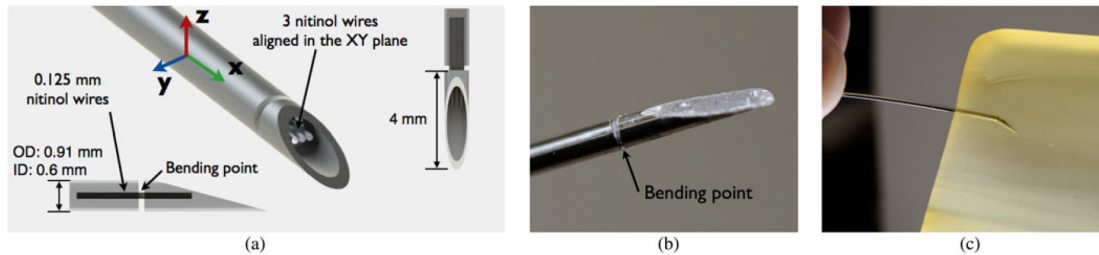


**Figure 1.5:** Flexure-tip steerable needle proposed by Swaney *et al.* [235]. (a) CAD model of the flexure-tip needle with the dimensions. (b) Flexure-tip steerable needle prototype. (c) When the flexure-tip needle is inserted into the tissue it bends due to reaction forces from the tissue. It remains straight during the duty cycling control. © 2013 IEEE.

Lee *et al.* [127] proposed a tube-wire type flexible steerable needles with variable curvature. The design consists of the inner pre-bent wire and an outer tube. The needle is controlled from the base inputs (insertion and rotation commands). The performance of the needle is tested in ballistic gelatin and animal tissue samples.

The wire has 0.8 mm diameter, and the outer tube is of 1 mm inner diameter (ID), and 1.2 mm outer diameter (OD). The extension length of the wire can control the curvature. They obtained a minimum radius of curvature of 20 mm in ballistic gelatin. They obtained the minimum radius of curvature of 104.5 mm in cow liver, and 18.6 mm in beef. Fig. 1.6-Left gives an illustration of the proposed design by Lee *et al.* [127].

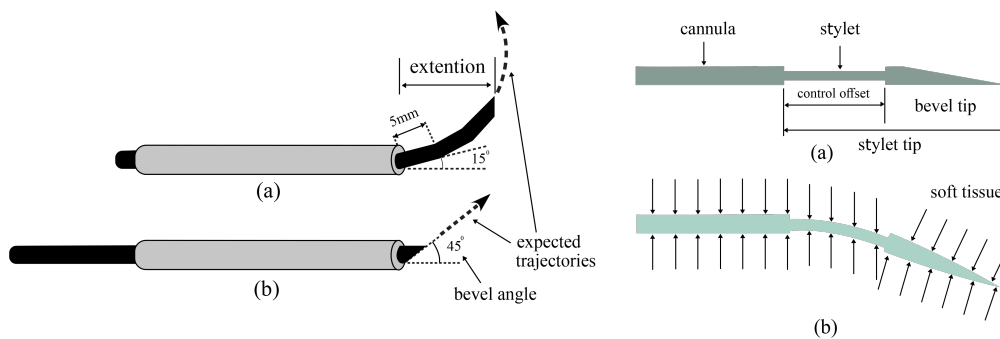


**Figure 1.6:** (Left) Wire and tube steerable needle illustration recreated from the design proposed by Lee *et al.* [127]. (a) Full extension, and (b) Full retraction. The curvature is controlled by varying the extension length of the wire. (Right) "Airfoil" bevel needle with varying stylet offset illustration recreated from [34]. (a) Needle's design, and (b) Needle under applied forces from surrounding soft tissue. The curvature can be controlled by changing the control offset.

Bui *et al.* [34] proposed a variation of the bevel-tip steerable needles with "airfoil" tip. This steerable needle does not need duty cycling to control its curvature. The proposed needle consist of a stylet with a bevel-tip and a cannula and the curvature of the needle path can be controlled by varying the control offset (the amount of the stylet retraction). The needle has an OD of 0.46 mm and is tested *in vitro* gelatin

soft tissue phantoms and *ex vivo* cow liver tissue. The minimum radii of curvature are 125 mm, 72 mm, and 263 mm in 6% by weight gelatin phantom, 10% by weight gelatin phantom, and cow liver, respectively. They experimentally showed that the curvature is a linear function of the control offset. Fig. 1.6-Right shows the proposed steerable needle.

Khadem *et al.* [108] proposed a way to decrease the bending stiffness of the tip steerable needles and thus increasing the maximum achievable curvature by adding one or more notches on the needle shaft. The notched needle design achieved a minimum radius of curvature of 198 mm in Plastisol soft tissue phantoms (80% liquid plastic and 20% plastic softener resulting in elastic modulus of 35 kPa) which is 67% better than standard needles. In another study, Khadem *et al.* [110] used a notched needle tip and achieved a minimum Radius of Curvature (ROC) of 171 mm by increasing number of notches in Plastisol soft tissue phantoms.

#### *Fracture-directed Stylet-and-Tube Needle Steering:*

Yang *et al.* [284] developed a new method of needle steering called "fracture-directed needle steering", in which the objective is to first control the direction of tissue fracture and then have the needle follow the fractured path. The principle of fracture-directed steering promised the potential of significantly improved radius of curvature and steerability that is currently attainable with tip-steerable needles. Figure 1.7 describes the principle of the stylet-and-tube form of fracture-directed

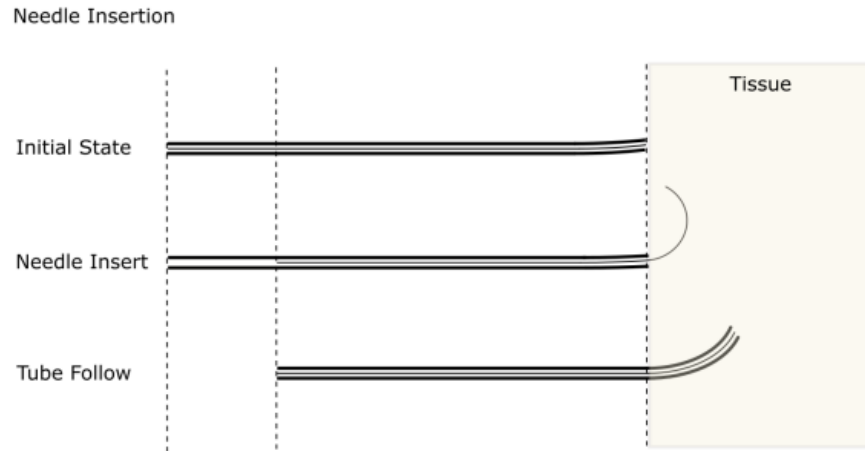


**Figure 1.7:** Principle of fracture-directed stylet-and-tube steering. First the inner stylet is advanced, followed by the outer tube. The shape of the tissue fracture closely matches the geometry of the inner stylet. After the outer tube follows the inner stylet, the resulting tip position depends on the static equilibrium of the wire, tube, and tissue.

steerable needles, where an inner stylet with a predefined geometry is first extended from the tube to fracture the tissue, after which the tube follows the stylet along the fracture direction. The proposed method of fracture-directed needle steering consists of a straight outer elastic tube and an inner elastic wire stylet. Silicon rubber, 15%, and 20% SEBS soft tissue simulants are used as tissue mimicking materials for needle steering experiments. The lowest insertion radius attained in experiments with silicone compound tissue phantom ( $E = 687$  kPa) using Nitinol tube (Tube ID = 0.6, OD = 0.8, and needle diameter = 0.47 mm), and SEBS tissue phantom ( $E = 128$  kPa) using SemiFlex tube (tube OD = 1.45, ID = 0.7, and needle diameter = 0.47 mm) are 29.58 mm, and 6.88 mm, respectively.

### *Needle Steering Using Base Manipulation:*

Base manipulation is controlling the needle tip trajectory using control of the 6 DOFs of the needle base. This is shown in Fig. 1.1-b, and -c. This is the natural way physicians use to steer a needle when holding it by its base. Dimaio *et al.* [59] first introduced the method of controlling the needle from its base. They performed the steering in open-loop. Glozman and Shoham [79] performed closed loop needle base manipulation under fluoroscopic feedback, and Neubah and Shoham [170] did it under ultrasound guidance. Bending the needle and pushing on the tissues to control the lateral motion of the tip which is used in base manipulation method can potentially induce more tissue damage than only inserting the needle. This limits the use of base manipulation in the real world scenarios.

### *Active Steerable Needles:*

Ayvali *et al.* [19] proposed an active segmented cannula with pre-curved SMA wires. They evaluated the proposed needle in Knox Gelatin. The cannula has 1.4 mm inner diameter (ID), and 3 mm outer diameter (OD). Black *et al.* [33] developed active needles with two degrees of freedom (DOF) with a single SMA wire. Evaluated the needle in a tissue phantom simulating the mechanical properties of a human prostate. No curvature data is given in the paper.

Konh and Podder [120] developed an active needle actuated by a single SMA wire,

and showed the efficacy of the needle through 2D experiments [119]. The needle is evaluated in air and in tissue mimicking gel. The tissue mimicking gel is made of Plastisol with a 3 : 1 ratio of plastic (polyvinylchloride suspension) to softener. The velocity of insertion into the tissue is  $2.54 \frac{mm}{s}$ , and the maximum needle deflection is about 32 mm in gels. Overall diameter of the needle is 2.6 mm. Konh *et al.* [121] 3D manipulated an active steerable needle via actuation of three SMA wires. The experiments are conducted in free space and not in the soft tissue. Curvature can be controlled by changing the applied current to the actuator wire.

There are also steerable needles that can be steered by cable actuation. These needles are capable of on-demand steering at the tip in one plane [6, 77], or on-demand steering in two perpendicular planes [247, 142], and changing of the needle trajectory "on the spot" [216]. Cable-actuated steerable needles allow for a high level of maneuverability, but they are more complex and diameters need to be larger than 1 mm since smaller diameters lead to smaller moment arms and higher actuation force will be needed.

Scali *et al.* [216] developed a needle with 0.5 mm probe that can steer in 3D without the need for axial rotations. The needle consists of 3 Nitinol wires each with a diameter of 0.125 mm with a pre-curved tip inside a stainless steel tube. They tested the efficacy of the needle in 10% by weight Gelatin soft tissue phantoms (they obtained a Young's Modulus of 17 kPa). Their design is a combination of the cable-

actuated needles with the pre-bent needles. The insertion speed of the experiments is  $2 \frac{mm}{s}$ . Tip angles can only be  $10^\circ$ ,  $20^\circ$ , and  $50^\circ$ . Fig. 1.8-Right shows the proposed design.

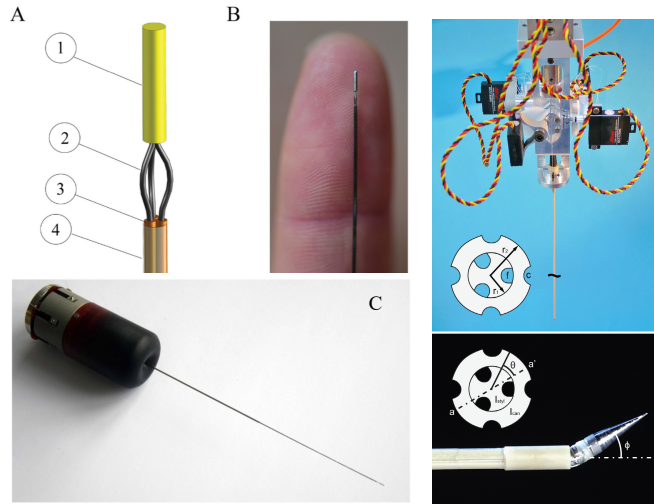


**Figure 1.8:** (Right) Steerable needle designed by Scali *et al.* [216] © 2019 Scali *et al.* (A, B) with its actuation unit (C). (Left) The tendon-driven needle proposed by Van de Berg *et al.* [247] © 2015 ELSEVIER. FBG sensors are used to sense and recreate the shape of the needle and measure the tip position during insertions.  $\phi$  can be up to  $20^\circ$ .

Van de Berg *et al.* [247] used four actuation cables running alongside the shaft and connecting to the tip to change the tip's angle (refer to Fig. 1.8-Left). They obtained a minimum ROC of 181 mm. Fiber Bragg Gratings (FBGs) are used to sense and measure the needle shape and tip position during operation. PI-controller is used to steering to predefined targets. They achieved a targeting accuracy of  $6.2 \pm 1.4$  mm (mean  $\pm$  std), and steering precision of  $2.6 \pm 1.1$  mm in 15% gelatin soft tissue phantoms with Young's moduli of 10 kPa which is in the order of the stiffness of the

liver (it should be noted that the tissue stiffnesses are variable among the literature due to variability in techniques and test conditions.). The needle consists of a 0.5 mm radius ( $r_1$ ) stainless steel stylet, and 0.9 mm radius ( $r_2$ ) PEEK plastic cannula. The outer needle radius is approximately 1 mm. 4 actuation cables are fixed at the tip and each connects to one servo motor. The velocity of insertion during experiments is  $5 \frac{mm}{s}$ .

Burrows *et al.* [36] developed a complex needle with 4 actuated shafts to change the tip geometry and obtained a minimum ROC of 58 mm. Adebar *et al.* [7] developed an actuated hinge near the needle tip and achieved a minimum ROC of 55.8 mm in *ex vivo* liver with 16 mm tip length. They showed that increasing the tip length, and tip angle decreases the achieved minimum radius of curvature. They obtained the minimum radius of curvature of 46.7 mm with tip angle of  $60^\circ$ .

Ilami *et al.* proposed a magnetic needle steering method [97]. Unlike the traditional needle techniques that depend on the radial forces and rotation at the base of an asymmetric tip needle for steering, and other magnetic steering of catheters, and continuum robots that rely on mechanical or manual shaft advancement methods, this method uses magnetic forces and torques to both steer and advance a sharp magnetic tip. In this method, the needle is magnetically pulled rather than mechanically pushed which avoids buckling and obtains minimal Radius of Curvature (ROC). Needle tip has a diameter of 1.59 mm. They obtained minimum ROC of 10.2 mm.

Their system has the ability of variable Radii of Curvature without duty cycling, therefore it does not need rotation for steering. Possible disadvantage is prolonged human exposure to powerful magnetic fields. Because of the limitations on magnetic field strength, they have chosen soft tissue stiffnesses that are lower than human soft tissues. They have examined two soft tissue phantoms with 1.96 (1.2 g of agar gelling powder and 0.08 g of pure agarose powder per 100 mL of distilled water), and 2.70 (1.6 g of agar gelling powder and 35  $\mu$ g of pure charcoal per 100 mL of distilled water) kPa stiffnesses, respectively.

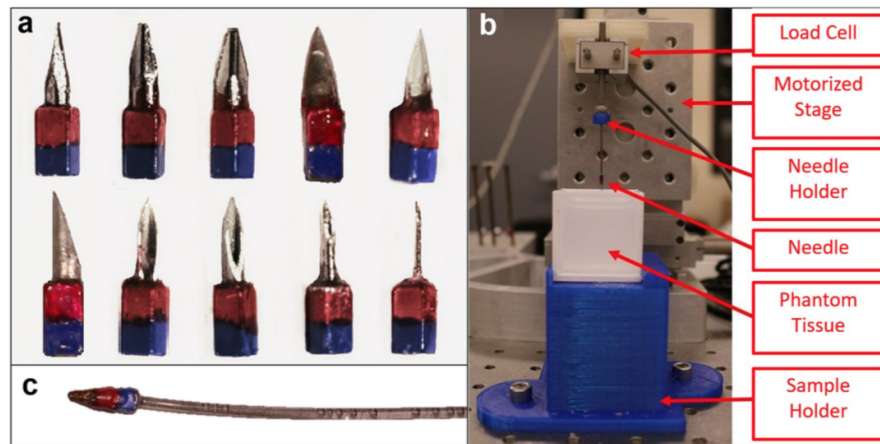


**Figure 1.9:** Magnetic Needle steering system proposed by Ilami *et al.* [97] © The Authors 2020.

Dalta *et al.* [48] proposed a flexure-based active needle for needle steering in soft tissue. Needle curvature is controlled by shape memory alloy (SMA) wires applying actuator forces to bend the needle. They evaluated the needle in air, tissue-mimicking gel (polyvinylchloride (PVC) gel with 3:1 ratio of plastic (PVC suspension) to softener

with elastic modulus of 25.6 kPa comparable to elastic modulus of normal prostate tissue (22.74 kPa)), and *ex vivo* pig liver. The needle consists of two hollow tubes, an actuator wire, a flexible connector, and a needle tip. The hollow tubes are made of superelastic Nitinol of 2.2 mm OD, and 1.7 mm ID. The velocity of insertion is  $2.54 \frac{mm}{s}$ . The bend angle of the SMA wire can be controlled by applied current. The maximum deflection of the needle in pig liver, and in gels are 41.9 mm, and 29.5 mm, respectively.

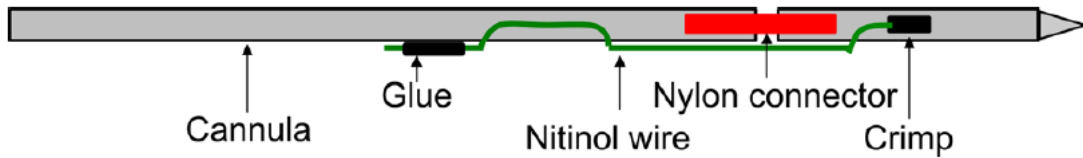


**Figure 1.10:** Flexture-based active needle design proposed by Dalta *et al.* [48] with SMA actuators. © 2015 by ASME.

Roesthuis *et al.* [206] proposed a flexible steerable needle with a tendon-driven actuated tip. Fiber Bragg Grating (FBG) sensors are used to measure the needle tip pose. The performance of the needle is evaluated in porcine gelatin soft tissue phantoms (14.9% by weight with Young’s modulus of 35 kPa which is in the order of the stiffness of human breast tissue). The needle tip has conical shape with length of 5 mm. The tip is on a ball joint and four steering tendons are used to actuate the tip. The needle is made of a Nitinol stylet of diameter 1 mm, and a PEEK plastic cannula of 2 mm diameter. The velocity of insertion in experiments is  $5 \frac{mm}{s}$ .

Maximum curvature is obtained with an angle of  $15^\circ$  resulting in minimum radius of curvature of 200 mm.

#### *Needle Steering Using Tissue Manipulation:*

Needle steering using tissue manipulation is done by deforming the internal parts of the tissues by moving one [243] or multiple points [150, 189] of the surface of the tissues. Accurate finite element modeling (FEM) of the tissues is required for this type of control which is difficult to obtain in practice. On the other hand, the computational burden of the FEM also hinders its real-time use that limits the pre-planning. Tissue manipulation is only used to move superficial targets and not deep anatomical structures.

#### *1.2.2 Modeling Approaches for Steerable Needles*

Needle-tissue interaction models provide an understanding of the flexible needle interacting with soft tissue. This understanding is useful in the sense that the needle path can be predicted before real needle insertion. This can be helpful for predicting the behavior of the steerable needle in reaching to the targets. Needle modeling approaches can be classified into kinematic models which consider the trajectory of the needle tip, finite element models that can model the behavior of the needle and the tissue, and mechanics-based models. Developing accurate models are also important to construct efficient controllers and estimators.

*Kinematic Models:*

Webster *et al.* [270] proposed and validated a nonholonomic model for bevel-tip needle steering. The model is a generalization of the 3 DOF nonholonomic unicycle and bicycle models to 6 DOF using Lie group theory. The models are validated using experiments with needle insertion device into soft tissue phantoms. They used a 0.7 mm diameter needle with bevel angle of  $45^\circ$ . Soft tissue phantoms used are Simulated Muscle Ballistic Test Media (SimTest) from Corbin, Inc. The stiffness of this soft tissue simulant is similar to muscle (4.9 N/mm). They found that the root mean squared error between the model prediction and the observed data points is 1.3 mm for the bicycle model, and 2.6 mm for the unicycle model, thus concluding that the two-parameter bicycle model describes the needle behavior better than a single-parameter unicycle model. Fig. 1.11 shows the definition of the bicycle and unicycle model proposed by Webster *et al.* [270].

These models are summarized as follows:

$$\begin{aligned} \dot{g}_{ab}^{-1}(t)g_{ab}(t) &= u_1\hat{V}_1 + u_2\hat{V}_2 \\ V_1 &= \begin{bmatrix} e_3 \\ \kappa e_1 \end{bmatrix}, V_2 = \begin{bmatrix} 0 \\ e_3 \end{bmatrix} \end{aligned} \tag{1.2}$$

$$n(t) = R_{ab}(t)\ell_2 e_3 + p_{ab}(t), \text{ for bicycle model}$$

$$n(t) = p_{ab}(t), \text{ for unicycle model } (\ell_2 = 0)$$

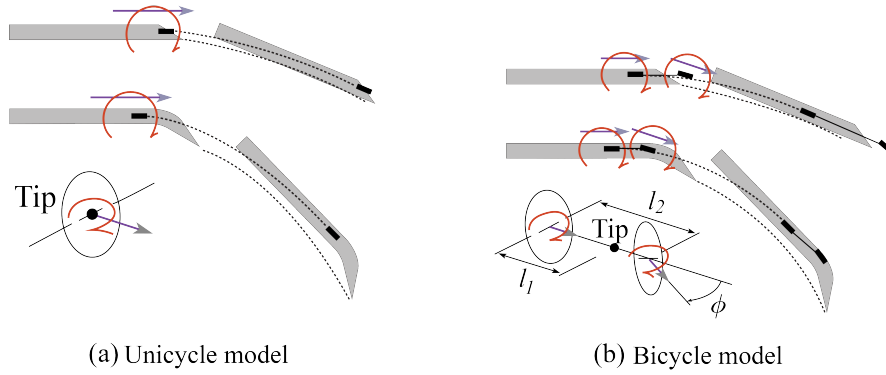


**Figure 1.11:** Unicycle and Bicycle kinematic models for asymmetric-tip needles (bevel-tip and pre-curved needles) proposed by Webster *et al.* [270]. Translation and rotation of the wheels are shown with straight, and curved arrows, respectively. For the Bicycle model, the rotation occurs naturally, but for the unicycle model the rotation should be added artificially.

Where  $\kappa$ ,  $u_1$ ,  $u_2$ ,  $g_{ab}$ ,  $R_{ab}$ ,  $p_{ab}$ ,  $e_1$ ,  $e_2$ , and  $e_3$  are curvature, insertion, and rotational velocities, transformation matrix, rotational matrix, position matrix, the relationship between  $R^3$  and the Lie algebra of  $SE(3)$ , and unit vectors, respectively.  $n \in R^3$  is the needle tip position.

It can be demonstrated that the needle tip pose can be calculated using the following equation [270]:

$$\begin{bmatrix} \dot{x} \\ \dot{y} \\ \dot{z} \\ \dot{\alpha} \\ \dot{\beta} \\ \dot{\theta} \end{bmatrix} = \begin{bmatrix} \sin(\beta) & 0 \\ -\cos(\beta)\sin(\alpha) & 0 \\ \cos(\alpha)\cos(\beta) & 0 \\ \kappa \cos(\theta)\sec(\beta) & 0 \\ \kappa \sin(\theta) & 0 \\ -\kappa \cos(\theta)\tan(\beta) & 1 \end{bmatrix} \begin{bmatrix} u_1 \\ u_2 \end{bmatrix} \quad (1.3)$$

In which  $q = [x \ y \ z \ \alpha \ \beta \ \theta]^T$  is the generalized coordinates for the needle tip position and orientation, and  $\kappa$  is the radius of curvature of the needle path. This equation is especially suitable for control purposes.

Minhas *et al.* [155] proposed a kinematic model to describe the trajectory of passive steerable needles with duty-cycled spinning. Duty-cycled spinning is the approach to control the curvature of the passive steerable needles from the natural curvature of the needle in the soft tissue to zero curvature. They validated the model in Knox Gelatin (1.3 cc of Gelatin in 20 cc of water) tissue simulants which has similar insertion force profile to that of the brain tissue *in vitro*. The minimum radius of curvature obtained in Knox Gelatin is 5 cm and it is found that the curvature decreases linearly with duty cycle. The needle used in the experiments is a custom-made needle with a 1.27 mm diameter stainless steel hypodermic needle tip attached to a 0.28 mm diameter Nitinol wire. The bevel angle is  $10^\circ$  and is bent an additional  $15^\circ$  at a distance

of 6.3 mm from the end of the tip. The proposed kinematic model is as follows:

$$g(t) = \begin{cases} g(0)e^{(u_1\hat{V}_1+u_2\hat{V}_2)t}, & jT \leq t < T(j+D), j = 0, 1, 2, \dots \\ g(0)e^{u_1\hat{V}_1t}, & \text{else} \end{cases} \quad (1.4)$$

$$n(t) = R(t)l_2e_3 + p(t)$$

Where  $T$ ,  $l_2$ ,  $u_1$ ,  $u_2$ ,  $g(0)$ ,  $R(t)$ ,  $p(t)$ , and  $V_1$ ,  $V_2 \in R^6$  are duty cycle period, back wheel to needle tip distance in bicycle model, insertion speed, rotational speed, initial configuration of the needle, rotational component of the needle configuration, translational component of the needle configuration, and twist coordinates of the twists  $\hat{V}_1, \hat{V}_2 \in \text{se}(3)$ .  $V_1 = [0 \ 0 \ 1 \ \kappa \ 0 \ 0]^T$ , and  $V_2 = [0 \ 0 \ 0 \ 0 \ 0 \ 1]^T$ .  $e_3$  is the z-coordinate unit vector.

Yang *et al.*[284] presented a discrete analogue of the bicycle model for the proposed method of stylet-and-tube fracture-directed needles. In this model, the independent variable is the step length of the stylet before following with the tube. Consider a pre-curved stylet that is driven by step length from the end of the tube. As the stylet exits the tube and enters the tissue, the stylet will nominally follow the pre-defined shape of the stylet. The step length is modeled as the input to the system. A mathematical model is developed for position of needle tip with respect to the base frame as a function of the step lengths and it is fit to the experimental data. Fig.1.12 shows the three distinct stages of needle insertion into the tissue. First, the

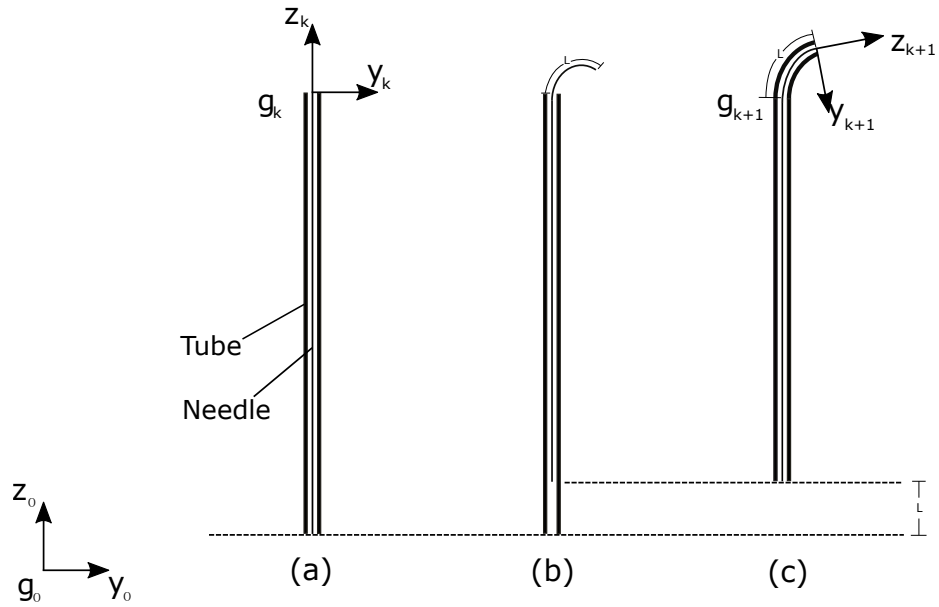


**Figure 1.12:** position and orientation of the needle tip

stylet is extended out of the tube, after which the tube follows the stylet. The z-axis of the body fixed frame is the direction of insertion. The arc length of each step is parameterized by  $l$ , in millimeters.

The twist coordinates of the system are defined as follows:

$$\xi(l) = \begin{bmatrix} \omega \\ v \end{bmatrix} = \begin{bmatrix} \kappa(l) \\ 0 \\ 0 \\ 0 \\ 0 \\ 1 \end{bmatrix} \quad (1.5)$$

The twist describes the discrete-step needle motion and is a function of  $l$ , which is the length of the needle that is inserted before the tube follows. By inspection of the vector field defined by the twist, the needle system has rotation around the body-fixed x-axis and linear translation along the z-axis. The pose of the needle after a step is calculated as the product of matrix exponential of the twist and the previous pose using the matrix exponential of the twist describing the motion in each discrete step of the stylet and tube:

$$g_{k+1} = e^{\hat{\xi}_k l} g_k. \quad (1.6)$$

The discrete-step position/ orientation change is only a function of the length of the needle that is inserted before the tube follows. The matrix  $g_k \in SE(3)$  is the tube tip position/orientation before the needle is inserted and  $g_{k+1} \in SE(3)$  is the tube tip position/orientation after the needle has been inserted and the tube has followed.

Kinematic modeling is easy to implement and is not computationally expensive. The main disadvantage of kinematic modeling is that the model parameters should be measured through performing preliminary experiments in the tissues. This is not feasible in practice for real surgical operations, and therefore online estimation of the needle trajectory using methods based on Kalman filter are necessary [166]. Kinematic models also do not consider the interaction between the shaft of the needle, and the surrounding tissue. It is assumed that the shaft of the needle follows the tip trajectory. This assumption is valid when the needle is very flexible and the tissues are stiff so that the bending forces of the needle are small enough to cause little tissue motions. These assumptions are difficult to provide in real clinical operations where there are patient motions, and variable inhomogeneous tissues.

#### *Finite Element Models:*

Finite element modeling (FEM) is used to model the interactions of the needle with the surrounding tissue [243, 189]. FEM needs geometry, and some physical parameters of the tissues and the needle. A 1D beam model is often used for modeling the needle. A rigid beam [57], a flexible beam [58], and a succession of rigid beams linked by angular springs [82, 87] are used to model the needle in the literature. 3D models of the needle are also proposed in the literature [157, 282] to efficiently represent the needle's deformations and the effect of the tip geometry. Tissues are modeled with 2D rectangular mesh with elastostatic behavior [58], 3D mesh with real

organ shape [43], and dynamic nonlinear behavior [242]. The needle-tissue interaction can be modeled through adding interaction forces due to the lateral displacements of the needle, and tangential forces as friction and stiction along the needle shaft [64]. Konh *et al.* [121] proposed a Finite Element Model to predict the 2D, and 3D paths of an active needle with multiple Shape Memory Alloy (SMA) actuators.

The computational complexity of FEM is high in comparison to the other modeling approaches. The time needed for computation is in direct relationship with the detailed levels of the model (number of the elements), and the number and complexity of the factors taken into account. Finding exact boundary conditions, and properties of the real biological tissues are also challenging. Because of these limitations, using FEM in real time is difficult to use [10, 88].

#### *Mechanics-based Models:*

In order to model the entire shaft of the needle and its interactions with surrounding soft tissue, mechanical-based models are used. The needle is usually modeled as a 1D beam with mechanical properties of the real needle. The tissues are not modeled entirely (as is done in FEM), but rather the local interaction with the needle is taken into consideration.

The first method to model the needle-tissue interaction is using Bernoulli beam equations in which a set of discrete virtual springs are used along the shaft of the needle which is cut into multiple flexible beams. This is done in 2D by Glozman

*et al.* [80]. This is depicted in Fig. 1.14-Down. Bernoulli beam equations for small deflections is used to compute the shape of the needle considering that the pose of the needle base, and the position of the springs are known. The Euler-Bernoulli equation that relate the needle' deflection ( $\delta$ ) to the applied load ( $f_i$ ) can be expressed as follows:

$$\frac{d^2}{dx^2}(EI \frac{d^2\delta}{dx^2}) = f_i \quad (1.7)$$

Where  $x$ , and  $EI$  are position, and flextural rigidity of the needle, respectively. This principle is used by Glozman *et al.* [80]. Under the same loading conditions on the needle, the needle with less flextural rigidity will deflect more. This is shown in Fig.1.13. Flextural stiffness for a needle with Young's modulus of  $E_n$ , and radius of  $r_n$  is defined as follows:

$$(EI)_{needle} = \frac{E_n \pi r_n^4}{4} \quad (1.8)$$

According to this equation, a needle with lower elastic modulus, and lower diameter has smaller bending stiffness and thus more flexible.

Distributed load applied along the needle shaft can be used to model the needle-tissue interaction instead of discrete springs to have a smoother behavior [107].

Bernoulli equations are also applicable here. This is illustrated in Fig. 1.14-Up.

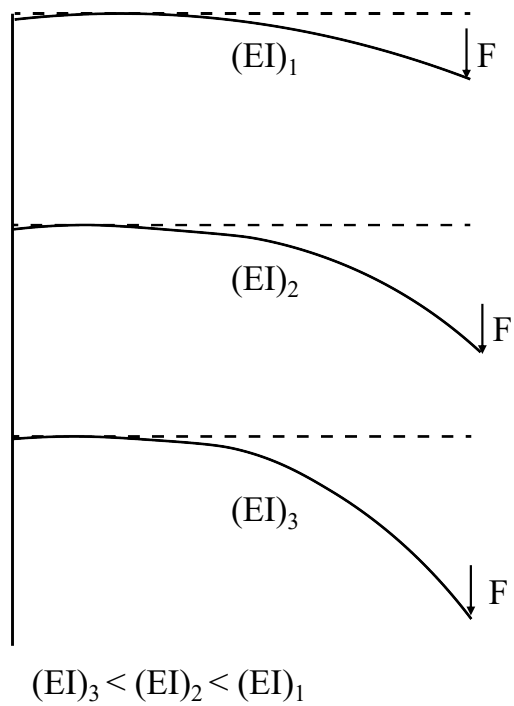


**Figure 1.13:** Bending stiffness of a flexible needle. Under the same loading conditions (for instance forces from the surrounding tissue), the needle with less bending stiffness deflects more.

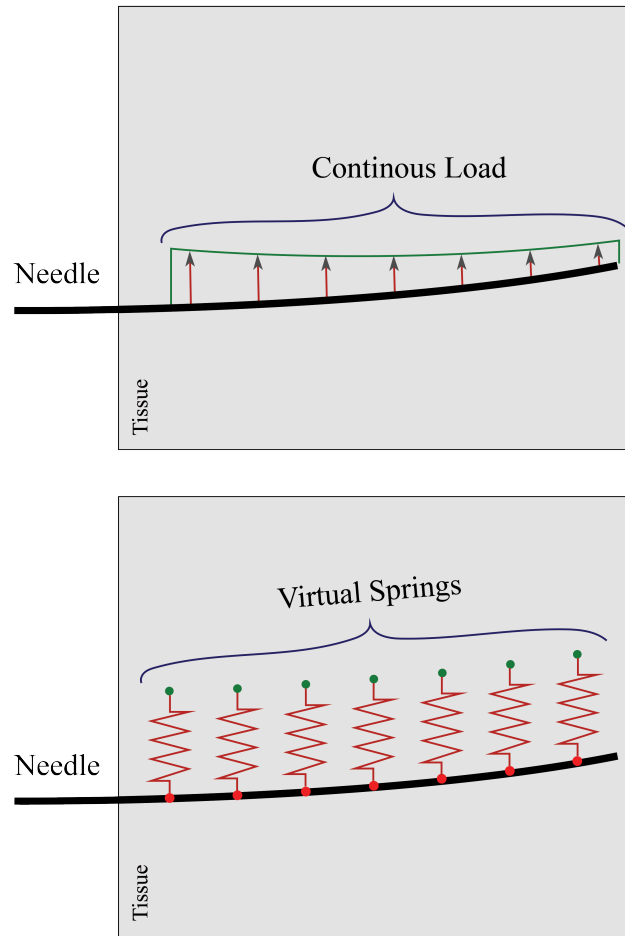


**Figure 1.14:** Mechanics-based models for needle-tissue interaction using virtual springs (Down), and a continuous load (Up).

The second method of the mechanics-based modeling approaches is energy-based method (also known as Rayleigh-Ritz method) that can be used instead of directly using the Bernoulli equations to compute the needle shape. Misra *et al.* [159] used this method to compute the shape of the needle minimizing the total energy stored in the system. This energy is the sum of the bending energy stored in the needle, the deformation energy stored in the tissues, and the works that are due to tissue cutting at the tip and the insertion force at the base. Roesthuis *et al.* [205] used a combination of virtual springs along the needle shaft, and continuous load at the end of the needle to model the needle-tissue interactions. There are different approaches proposed in the literature to find these continuous loads such as online estimation proposed in [261]. Goksel *et al.* [82] modeled the needle as a succession of rigid rods linked by angular springs to model the compliance of the needle.

The third method of the mechanics-based modeling is modeling the dynamic behavior. The previous modeling approaches allow for modeling the quasi-static behavior of the needle insertion into soft tissue. The dynamic behavior of the needle insertion into soft tissue can be considered through adding a mass to the needle beams, adding viscoelastic properties of the soft tissues, and adding a model of the friction along the needle shaft [283, 109]. A model for torsional friction, and needle torsion is also needed for needle rotation around its axis [240].

### 1.2.3 Control Approaches Used in Needle Steering

The trajectory planning approaches for passive steerable needles cannot directly be applied to active steerable needles because of the difference in their structure. Motion planning for steerable needles is defined as a method to find a set of controls (such as insertions and base rotations for tip-steerable needles) so that the needle tip reaches to the specified target while avoiding obstacles, and not violating the workspace constraints.

#### *Control of Passive Steerable Needles:*

Passive steerable needles are nonholonomic systems that are difficult to control at joint space because they are under-actuated and have unintuitive kinematic constraints. Trajectory, and motion planning algorithms consist of the minimization of a suitable cost function. Additional constraints such as obstacle avoidance and minimum path can also be imposed on trajectory planning.

Trajectory planning is challenging with passive steerable needles because the curvature of the needle is dependent on the complex needle-tissue interactions [121, 118]. The other reason that trajectory planning is difficult for passive needles with bevel tips or pre-bent tips is that the needle can only steer in 2D with a constant curvature and in order to vary the radius of curvature, base rotation is needed which result in the asynchronous angle between the base, and the tip rotation due to torsional

friction. Thus, complicated trajectory planning algorithms are needed for passive steerable needles.

Different image-guided control methods are proposed in the literature to autonomously steer the needles [79, 200]. Image-guided control of passive steerable needles guides the needle to the target based on a known target location in 3D [147, 104]. These control schemes can provide greater needle dexterity, and improved accuracy. However, they usually cannot make necessary compensations when the path errors arise [33]. Reed *et al.* [200] developed a needle steering system with several path planners and controllers to drive the needle to a desired location. They initially used plastisol artificial tissue simulants made of plastic and softener in the ratio of 4:1 which simulate the Young's modulus of the prostate (approximately 60 kPa). Two needles with the inner diameters of 0.37 mm, and 0.58 mm, and bevel angles of  $45^\circ$ , and  $40^\circ$  with  $12^\circ$ , and  $37^\circ$  bend angles with 4 mm, and 12 mm tip lengths are used for the experiments. They obtained radii of curvature of 6 cm, and 5.5 cm with the small and large needles, respectively. The velocity of insertion is  $0.25 \frac{cm}{s}$ . They also simulated a brachytherapy procedure in *ex vivo* tissue using this needle.

Duindam *et al.* [61] discretized the control space of the flexible needles, and proposed an optimization problem that utilizes a cost function that minimizes the control effort and path length. They planned their needle trajectory while considering a stop-and-turn strategy by alternating between rotation-only steps, and insertion-only

steps. Hauser *et al.* [90] used the helical shape of the paths that are generated while constant insertion, and rotation velocities are applied to the needle. Best velocities are chosen based on the helical path that lets the final tip position to be the closest to the target. A model predictive control approach is used in which the best chosen velocities are applied for a short time and the procedure is repeated until reaching to the target.

Park *et al.* [182] proposed a numeric diffusion-based method for trajectory planning of flexible bevel-tip needles in a 3D environment without obstacles. The path is computed numerically based on this algorithm, and the algorithm does not handle uncertainty of the response of the needle to insertion or direction change inputs. The tissue is modeled as isotropic. Inverse kinematics that use the probability density information are utilized to create needle tip paths to reach desired targets. This is solely a theoretical work and the theories are not validated with experiments. The planning problem is formulated as a nonholonomic kinematics problem based on a 3D extension of a unicycle model.

Alterowitz *et al.* [12] used a stochastic motion roadmap to model the probability of obtaining a given 2D pose of the needle tip starting from another tip position, and orientation. Based on the map, an optimal set of control inputs is computed to minimize the probability of hitting an obstacles and maximizing of reaching the target. Lee *et al.* [126] used fuzzy logic as a way to deal with uncertainty in control

inputs. Glzman and Shoham [81] passed a spline trajectory through three points of the location of the obstacle, needle tip, and the target that are obtained from fluoroscopic images of the tissue before needle insertion. PID controller was used to direct the needle to the target location and for a 40 mm insertion the error was 0.5 mm.

Rapidly exploring random trees (RRT) are used by Xu *et al.* [279] to find the feasible paths in a configuration space. RRT is a probabilistic algorithm that randomly choose multiple possible control inputs and generates the corresponding output trajectories. Then, a best trajectory is chosen and is applied to the real system. Xu *et al.* [279] used the kinematic model of the needle with constant curvature to predict the motion of the needle tip knowing the insertion and rotation velocities. Because of the constant curvature limitation, the control inputs were constrained to a stop-and-turn strategy. In their method, a lot of trajectories should be generated before reaching to a suitable one, and due to being slow, it can only be used for pre-operative planning of the insertion. The concept of duty cycling control that helped to eliminate the requirement of constant curvature for path planning is used in 2D by Bernardes *et al.* [31], and 3D by [187, 29]. RRT is also used in 2D with FEM instead of kinematic models to provide a more accurate pre-planning that also considers the tissue deformations due to needle insertion [189].

Alterovitz *et al.* [9] developed a finite-element modeling for planning paths around

obstacles in deformable tissue. The planning algorithm is developed for bevel-tip steerable needles and the obstacles are considered to be in a 2D plane. The planner compensates for tissue deformations, and avoids obstacles. Finite element model computes the soft tissue deformations that takes into account the effects of the needle tip and frictional forces using a 2D mesh. The planning problem is a constrained nonlinear optimization problem that is minimized locally with a penalty method. The planner is not verified experimentally. This method assumed that the bevel direction can only be set once before the insertion. The method uses a local optimization that will fail to find a globally optimal solution while encountering obstacles.

Alterovitz *et al.* [11] proposed a motion planning algorithm for bevel-tip steerable needles based on dynamic programming where the path of the needle is not certain because of the uncertainties in tissue properties, needle mechanics, and interaction forces. The algorithm involves a cost function to minimize in order for the needle to reach to a target location while avoiding obstacles. The motion planning problem is formulated as a Markov Decision Process (MDP), and infinite horizon dynamic programming is used to compute an optimal control sequence (insertions and direction changes). Without uncertainty, the needle response to controls (insertion, and rotation) is a certain and known constant curvature path. In the uncertain case, the probability distribution of responses to control inputs is considered to be known. In the case of discretization error, the planner may not find a feasible solution. Tissue

inhomogeneity that causes uncertainty and noise into the needle tip orientation is considered. No experimental validation is provided.

DiMaio, and Salcudean [57, 59] developed a model-based trajectory planning approach for passive steerable needles. They formulated a Needle Manipulation Jacobian that used numerical needle insertion models with needle deflection and soft tissue deformation. The Jacobian is the relationship between the needle tip and base velocities. Potential field-based path planning technique is used for target reaching and obstacle avoidance. The insertion experiments are done in an open loop fashion. Needle and tissue are modeled using Finite Element Analysis (FEA) approach. This method is complicated and does not allow for online correction of the targeting error. The inverse kinematics of the needle is solved by iterative numerical computing of the needle’s Jacobian. Their work did not take the tip asymmetry into consideration. Due to the computational complexity of FEM, only pre-planning of the needle trajectory was done, and the actual insertion was done in open-loop. If  $\begin{bmatrix} x_t & y_t & \theta_t \end{bmatrix}^T$ , and  $\begin{bmatrix} x_b & y_b & \theta_b \end{bmatrix}^T$  are tip, and base pose of the needle, then:

$$\begin{bmatrix} \dot{x}_t \\ \dot{y}_t \\ \dot{\theta}_t \end{bmatrix} = J(q) \begin{bmatrix} \dot{x}_b \\ \dot{y}_b \\ \dot{\theta}_b \end{bmatrix} \quad (1.9)$$

The Jacobian defined as the relationship between the needle base and the tip

velocities can be found using the following equation:

$$J = \left[ \begin{bmatrix} \frac{\partial x_t}{\partial x_b} & \frac{\partial x_t}{\partial y_b} & \frac{\partial x_t}{\partial \theta_b} \end{bmatrix} \quad \begin{bmatrix} \frac{\partial y_t}{\partial x_b} & \frac{\partial y_t}{\partial y_b} & \frac{\partial y_t}{\partial \theta_b} \end{bmatrix} \quad \begin{bmatrix} \frac{\partial \theta_t}{\partial x_b} & \frac{\partial \theta_t}{\partial y_b} & \frac{\partial \theta_t}{\partial \theta_b} \end{bmatrix} \right]^T \quad (1.10)$$

Glozann, and Shoham [80] proposed an optimal trajectory planning (defined as the computation of the needle base pose for a given tip trajectory) for passive flexible needle steering. Needle insertion into the soft tissue is modeled using a linear beam supported by virtual springs, and the forward, and inverse kinematics of the needle are solved analytically. Simulation and path planning are done in real-time. The experimental tests are demonstrated in 2D space. Fig. 1.14-Down depicts the proposed virtual springs model for flexible needle insertion into the soft tissue. The reaction of the tissue on the needle are modeled using virtual springs distributed over the length of the needle, and friction force tangent to the needle shaft. The stiffness coefficients of the virtual springs are found experimentally. They did not model the bevel tip.

Despite the attainable accuracy with autonomous needle steering systems, having the physician in the control loop is desirable from clinical acceptance point of view of steerable needles. Other than that, passive steerable needles exhibit unpredictable behavior in nonlinear and anisotropic biological tissues.

Romano *et al.* [208] proposed a teleoperation control scheme in joint space. This control scheme puts the burden of the prediction of the needle's nonholonomic behavior on the user. Majewicz, and Okamura [147] proposed Cartesian and joint space

teleoperation for nonholonomic steerable needles. The Cartesian space control allows the user to select the desired position of the robot in Cartesian space, and provides force feedback to represent kinematic constraints and the position error of the robot. They showed the efficacy of the proposed control through simulations and not real experiments.

Sun and Altrerovitz [234] considered the sensor placement directly during the design of the planning and LQG controller to minimize the uncertainty on the tip location along the planned trajectory. In that way, the obstacles are avoided without the need to pass far away from them to avoid collision. Online re-planning of the trajectory which is regularly computing a new trajectory based on the current state of insertion can also be utilized instead of taken the uncertainties in the model into account. This method is used by Bernardes *et al.* [32], and Patil *et al.* [188]. Online replanning is only possible if simplified kinematic models are used and they are not possible with FEM.

Sliding mode control can be used to control the bevel tip steerable needles. The advantage of such a control method is that it does not depend on the parameters of an interaction model with the tissue. Rucker *et al.* [211] used this method and showed that by selecting a suitable ratio between insertion and rotation velocities, accuracy can be reached. Different feedback modalities are used successfully with sliding mode control such as electromagnetic (EM) tracker [211], fiber Bragg grating (FBG) sensors

[1, 227], ultrasound (US) imaging [3, 70], and computerized tomography (CT)-scan with EM tracking [226].

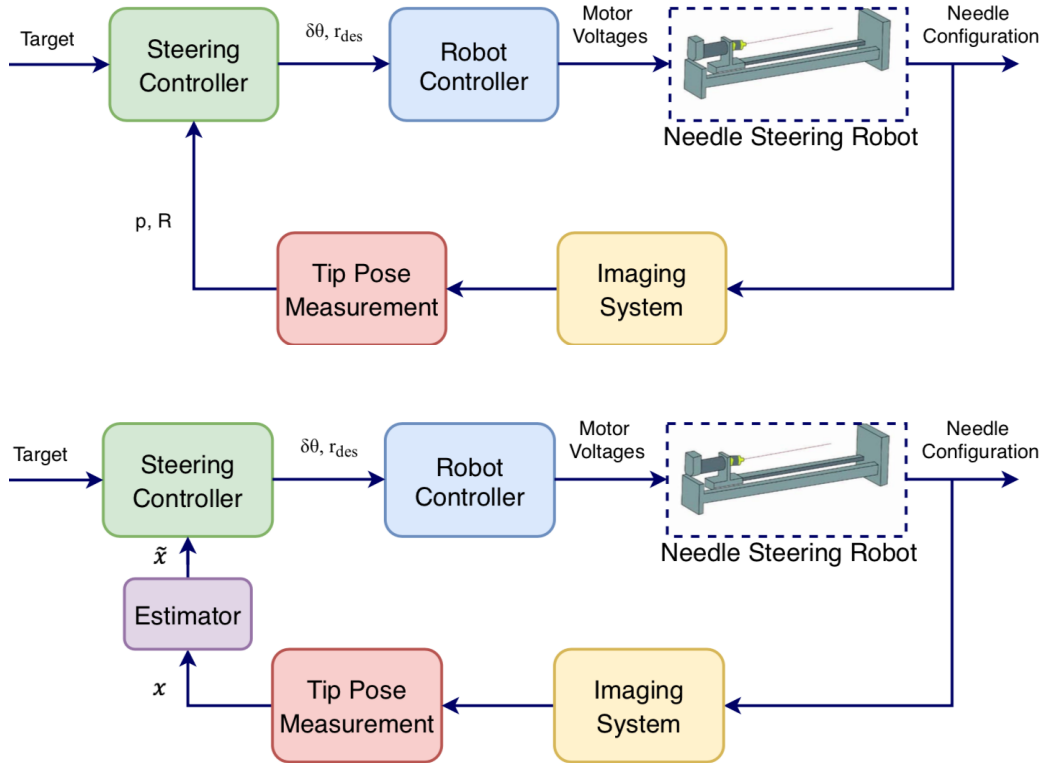
Visual servoing is a control approach based on visual feedback. Krupa [124], and Chatelain *et al.* [41] used visual servoing with 3D US imaging and the duty cycling method to control the needle trajectory. This method can compensate for modeling errors because of the fact that the control is directly defined in the image.

Fig. 1.15 shows an example schematic of the image guided robotic needle steering control and estimation-based control.

#### *Control of Active Steerable Needles:*

Active steerable needles are controlled with direct dynamic control of needle deflection without the need for complex robotic path planning [33]. Active steerable needles provide controllable actuation from the proximal end and this gives the physicians real-time manipulation of the needle tip for quick re-orientation utilizing image feedback. Common imaging systems include Ultrasound (US), Computed Tomography (CT), and Magnetic Resonance Imaging (MRI).

Lyons *et al.* [143] used a cost function that depends on the tubular environment geometry to plan trajectories for the active cannula used in lung biopsy procedures. Black *et al.* [33] proposed an active needle with Shape Memory Alloy (SMA) that is compatible with MRI guidance. Ayvali *et al.* [19] used a kinematic approach for trajectory planning for the active cannula. They proposed an approach to find



**Figure 1.15:** (Up) Example of closed loop control of image-guided needle steering. Steering controller provides needle rotation and curvature needed to reach to the target. Robot controller included motor controllers and command motor control hardware to move the needle tip along the desired path to the target. Imaging system provides visual feedback for measurement of the tip pose. (Down) Example of an estimation scheme for closed loop control of image-guided needle steering. Output of the estimation scheme is given to the steering controller which identifies the needle rotation and curvature necessary to reach a target point. Estimation scheme is necessary when the outputs of the imaging feedback are noisy. Kalman-filter is a common estimator used in the literature [8].

a minimum path between the desired and final configurations in an obstacle-free environment. They used 6 markers along the shaft of the needle to find the pose of the cannula, and stereo system for stereo imaging. The 3D locations of the markers are found by triangulating the 2D location of the markers on left and right images. Two PWM-based controllers for SMA actuators are proposed. One is a PWM-based vision feedback controller and the other is a temperature-based feedback controller. Overall, a position control with stereo vision feedback is used to control the cannula, and the ultimate control goal is to combine the temperature feedback controller with the image-guided position control so that the controller can shift to the temperature feedback controller when the image feedback is not optimal. In the vision-based feedback controller, a proportional controller is used to correct the error between the desired angle and the current angle by adjusting the heating time of the SMA wire:

$$t_i = k(\alpha_{desired}^i - \alpha_{current}^i), \quad (1.11)$$

where  $\alpha_{desired}^i$  and  $\alpha_{current}^i$  are the desired bending angle for the i-th joint, and current joint angle for i-th joint, respectively. The position error is calculated using the stereo image couples.

Van de Berg *et al.* [248] studied the ability of the human operator to manually correct for errors in the needle insertion path. They used an active, tip-articulated steerable needle with OD of 1.32 mm with flexure joint near the tip with retractable

stylet. Bending stiffness is in the order of a 20-gauge hypodermic needle. They achieved a targeting error of  $0.5 \text{ mm} \pm 1.1$  during manual steering of the needle under image guidance to 5 different targets. 4 wt.%, 8 wt.% Gelatin tissue simulants are used to do the steering experiments. Moreover, Van den Burg *et al.* [251] proposed a linear-quadratic Gaussian (LQG) controller in order for the needle to robustly follow the pre-planned trajectory using RRT. The controller can compensate for the current state uncertainty to minimize the probability of hitting an obstacle.

#### *Sensing Modalities in Robotic Needle Steering:*

Needle steering robotic systems should be able to monitor the state of the insertion in order to accurately guide the needle. Different feedback modalities are used in the literature to provide different information about the needle and the tissue. Different feedback modalities include Shape feedback, Real-time imaging techniques, and force feedback.

Fiber Bragg Grating (FBG) sensors are used to reconstruct the shape of the needle in the literature [184]. They consist of several optic fibers that are integrated into the needle, and depending on the curvature of the fiber at certain location, the light propagation vary allowing to measure the curvature of the needle and retrieve the needle's shape [184]. Integrating theses fibers into the needle makes the design of the needle more complicated since the fibers should follow the exact same deformations of the needle.

Electromagnetic (EM) trackers are usually used to track the pose (position, and orientation) of the tip of the needle. Currently, there are miniaturized trackers that can be embedded in standard needles.

The above-mentioned sensors provide the information about the needle position, and in order to know the target location, different imaging modalities should be used. Imaging techniques can provide feedback both on the position of the needle tip, and the target region. Ultrasound (US) is the most common imaging modality since it has fast acquisition rate of 2D, and 3D images, good resolution, and safety. Limitation of the ultrasound imaging is the low quality of the images. Computerized Tomography (CT)-scan, and Magnetic Resonance Imaging (MRI) are other commonly used imaging techniques. Unlike US, they provide high quality images, and large field of view. However, their limitation for real-time image-guided robotic needle insertion is long acquisition time, and they cannot be used in real-time. Another option for real-time imaging is CT-fluoroscopy. The limitation is that it can expose the physician to a high dose of harmful radiations. Using them in tele-operated robotic needle insertion systems also expose the patient to the radiations which is unnecessary for real-time procedures. Patel *et al.* [186] used a fast MRI acquisition system for image-guided needle insertion. They have acquired a 2D image every 750 ms by reducing the image size, and quality.

Force sensors are used in the literature to measure the forces applied to the needle

and the tissue. Force sensing is useful to evaluate the needle performance while puncturing through different tissue layers [177]. Force sensing is also used with tele-operated robotic systems to provide to the physician or compensate for tissue motion [193, 102].

#### 1.2.4 *Clinical Acceptance of Steerable Needles*

There are several limitations of needle steering that have hindered the widespread clinical use of steerable needles to date. These limitations are buckling and compression of the shaft, excessive tissue damage because of needle base rotation, difficulty of control due to torsional effects on the shaft and needle deflection at tissue boundaries (needle deflects from its desired path while puncturing a tissue interface), and limited workspace because of restricted radius of curvature [267, 235, 202, 201, 240, 239]. There are also several limitations associated with the magnetically steered catheters and continuum manipulators such as limited curvature and buckling.

Compression effects such as buckling of the needle shaft and torsional effects in the shaft cause unnecessary damage in the tissue, inaccuracies in control, and increased model complexity. Buckling can occur when the needle tip faces a tissue that it cannot penetrate or due to collision and inhomogeneity in the tissue [169]. This can be solved if the elastic shaft is not load bearing. The fact that the shaft should be strong enough to withstand the compression stress contradicts with the fact that it should be flexible enough to allow steering. Eliminating this conflict can show the

potential to reduce restrictions on achievable ROC caused by load bearing shafts. Torsion in the needle shaft can be caused by the friction between the needle shaft and the tissue. Torsional effects can cause the base and the tip to rotate out of sync. Differences between the base and tip rotations as high as 45 degrees for needle insertions of only 10 cm are reported in the literature [203, 201]. It can also cause difficulty in modeling and control [239, 240]. Another necessity for clinical acceptance is the ability of the steerable needle follow complex trajectories and maneuver in all three dimensions (3D).

Almost no steerable needle was used on a patient as one of the main components of the needle steering system (see Fig. 1.16). However, there are some research in the literature that demonstrate the use of steerable needles in the clinical environment. Majewicz *et al.* [148] showed that an enlarged prostate cannot be reached with a straight needle insertion due to pubic bone, and suggested pubic arch interference (PAI). Webster *et al.* [270] proposed that robotic needle steering can be used for the treatment of hepatocellular cancer using thermal ablation. Systems are proposed in the literature [54, 10, 98, 144] for brachytherapy of prostate cancer. Needle steering is useful for compensation of needle deflection, tissue deformation, and target dislocation during needle insertion. Needle steering scenarios are also designed to emulate environments for neurosurgery [74, 66] in which deep tumors can be difficult to reach by straight needle insertions. Fig. 1.16 shows a schematic of clinically viable steerable

needle.

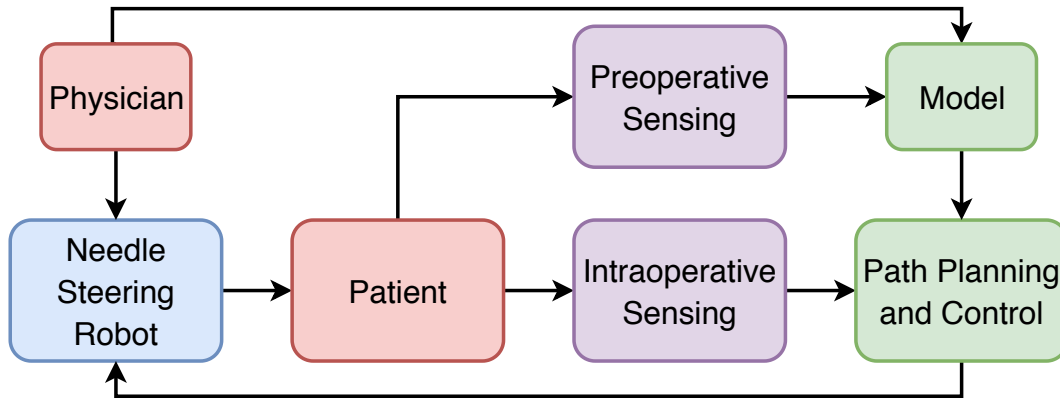


**Figure 1.16:** Clinically viable steerable needle system. Clinical trials with real patients has been one of the main components missing in the needle steering research to date.

Majewicz *et al.* [146] evaluated the performance of tip steerable needles in inhomogeneous soft tissues in terms of radius of curvature and insertion forces. They concluded that steerable needles curved more in kidney than in liver and prostate because of the tissue properties differences. Higher insertion forces in liver was observed with pre-bent needles and they exhibited more curvature *in vivo* than *ex vivo*. Minimum radius of curvature of 5.23 cm is achieved with prebent needles in *ex vivo* tissue, and 10.4 cm in *in vivo* tissue. Bevel tip needles achieved negligible curvature for *in vivo* tissue, and minimum radius of curvature of 16.4 cm in *ex vivo* tissue. They only showed the feasibility of clinical application for needle steering through targeting and ablating cadaveric canine liver. Needle diameter for insertions into the liver, and the prostate is 0.74 mm, and for kidney it is 0.58 mm. Bevel tip needles had a bevel

angle of  $30^\circ$ , and pre-bent tip steerable needles had a  $15^\circ$  pre-bent tip angle with  $30^\circ$  bevel angle. Needles are made of Nitinol wires. Insertion speed for needle insertions is  $0.5 \frac{cm}{s}$ . Mean insertion force was measured to be  $1 < F_{insertion} < 2$  for bevel, and bent-tips in *ex vivo* prostate, kidney and liver, and  $0 < F < 1$  for insertions into *in vivo* prostate, kidney and liver using bevel and prebent.

Constant curvature steerable cannula is used by Burgner *et al.* [35] to debulk the simulated clot in the brain phantom to show an application of steerable needles in neurosurgery. The tip of the cannula is controlled by insertion, retraction, and axial rotation of the cannula under image guidance. *In vitro* experiments showed the feasibility of evacuating 83-92% of hemorrhage volume.

### 1.3 Discussion

Needle steering systems came into existence with the aim of improving percutaneous interventions. Using a superelastic needle that can follow curved trajectories, the needle can be steered around anatomical obstructions to a target area (lesion or tumor). This can reduce trauma to the patient to a great deal. This potential has drawn a significant research interest in this direction.

In most needle steering methods proposed in the literature, curvature is created using an asymmetric force at the tip of the needle that changes the direction of tissue fracture. Traditionally, this has been accomplished through beveled tips or pre-curved sections near the end of the needle. These asymmetric forces between the needle tip

and the tissue cause the deflection of the needle (see Fig. 1.17). Because of the radial component of the force acting on the tip, the needle moves sideways. Orientation of the tip is controlled by rotation at the base (see Fig. 1.18). Radius of curvature can be controlled for a given tissue/needle combination using complex methods such as manipulating the tissue via external forces and duty cycling (continual spinning of the needle at the base). Note that with duty cycling, the needle curvature can only be decreased and the maximum curvature can only be achieved through 0% duty cycling. The mechanism at the tip that results in this asymmetric force can take on a variety of design paradigms: beveled, complex, active, inactive, programmable, composite, and articulated. Conventional steerable needles have large radii of curvature especially in very soft tissues because the stiffness of the tissue is too low to apply forces large enough to curve the traditional needles, and the needle tend to move in straight paths. The steerability of a steerable needle is defined as the minimum achievable radius of curvature which is the reciprocal of the curvature of the needle circular path. Large radii of curvatures restrict the reachable workspace, and this shows the importance of achieving smaller radii of curvature by proposing new and effective methods.

Bevel tipped needles made of superelastic materials (mostly Nitinol) dominate the needle steering literature. The similarity in design to conventional clinical needles, and ease of manufacture made them an attractive alternative to these needles. Several researchers tried to tweak the bevel tipped needles to overcome their limitations. From

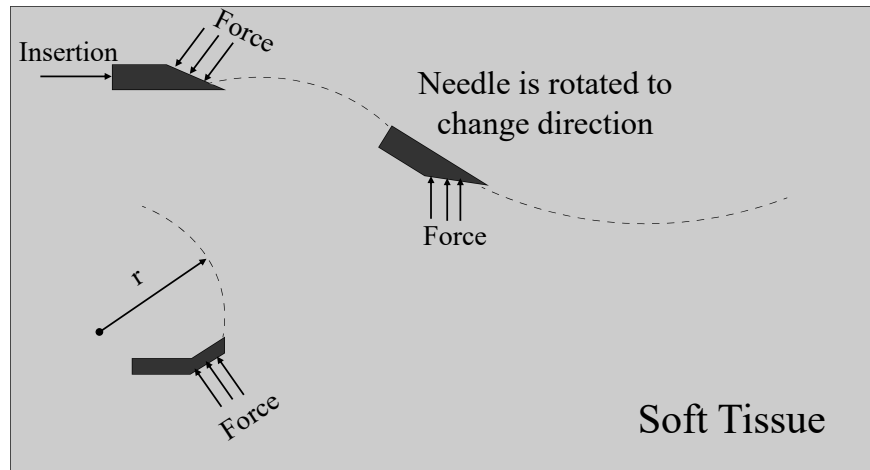


**Figure 1.17:** Principle of steering in conventional steerable needles. Tip steerable needles rely on interaction forces from the soft tissue to be able to steer.

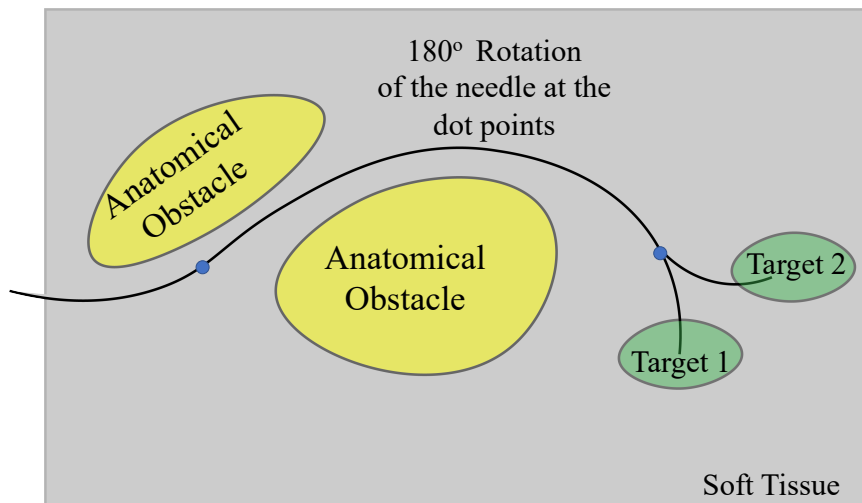


**Figure 1.18:** Tip-based needle steering concept. Steerable Needles can steer around obstacles and reach multiple targets from one insertion that are unreachable by straight needles. Anatomical obstacles can be veins, bones, nerves, and other structures that a needle cannot penetrate or can cause unwanted consequences. Steering direction can be changed by rotating the needle at the base.

there, pre-curved, pre-bent [199], "airfoil" tip [67], articulated tip [6], and flexure tip [235] steerable needles came into existence.

Bevel-tip needles rely on the asymmetric force interaction between the surface area of the bevel-tip and the tissue to steer. Steering in 3D requires the reorientation of the bevel tip through spinning around its axis, and straight insertion needs continuous rotation while being pushed forward. Furthermore, rotating a flexible long needle inside the soft tissue generates torsional friction on the needle body that leads to difference in orientation of the needle tip and the needle body that causes loss of control over the needle path [202, 200, 216, 240, 239] (see Fig. 1.19). Continuous rotation can also cause spiral track in the soft tissue that increases tissue damage [152, 30]. Especially for pre-bent, and pre-curved designs, duty cycling causes significant tissue damage [235]. Pre-bent needles also do not have direct control over the needle curvature, and the only way to correct is to retract the stylet, rotate it, and re-insert it. This increases the time of procedure, and damage to the tissue [202]. Therefore, the remaining challenges of conventional steerable needles to be solved are: needle steering with less damage to surrounding tissues, decreasing the minimum radius of curvature for better steerability and controllability, especially in very soft tissues such as brain and liver, and varying the curvature in a more efficient way than duty cycling.

It is also proven that the needles with diameters less than 1 mm reduce the risk

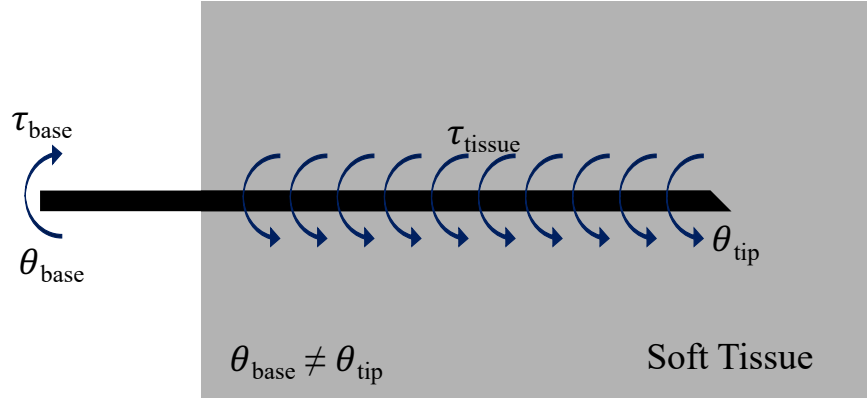


**Figure 1.19:** The effect of torsional windup and torsional friction when rotating a long flexible needle. Torsional friction and rotational inertial effects cause the tip angle to be out of sync with the base angle due to the rotational dynamics along the length of the needle.

of complication, and patient’s discomfort [216]. Decreasing needle diameter decreases the second moment of inertia which in turn lowers the bending stiffness of the needle, and thus increases flexibility, and steerability [215]. Thus, it seems that proposing steerable needles with sub-millimeter diameters to decrease patient trauma and increase needle curvature is necessary.

Without local actuation, the minimum radius of curvature obtained with the steerable needles is limited which in turn limits the steerability. In the case of tissue inhomogeneity, and also crossing tissue boundaries or going through one tissue to the other, the needle deflects from its preplanned trajectory. Developing needles that can exert localized forces to correct for errors in trajectory instead of dependency

on the needle and soft tissue interaction forces for steering is a possible solution for this. Active-type steerable needles came into existence in recent years to solve this issue. These designs lack the proper modeling, and control developed for them. Programmable bevel [113, 266], tendon-actuated steerable needles [247] (embedding tendons in the steerable needle design increases the thickness of the needle), and Shape memory alloy (SMA) steerable needles [121, 120] are some of the proposed designs in the literature. The programmable bevel steerable needle proposed by Ko *et al.* [113] is inspired by the ovipositor of the wood wasp and can achieve variable curvatures. The proposed needle is too thick (12 mm) because of its special design. Moreover, using SMA for Needle steering is promising, however there are currently size limitations for it and are not suitable for thin needle manipulation, and navigation.

Recent research trends show a considerable effort on the control strategies for steerable needles [247, 154, 165]. Control strategies and motion planners are developed for solving the control problem for dynamic environments with uncertainties. Adaptive controllers [211, 166] in which parameters can be estimated and updated on-line offer a potential advantage to steerable needles since the system does not need to go through pre-operation calibration through prior insertions, and are best for regions that tissue mechanical properties change. On-line adaptive path planning became more and more frequent in recent years. Pre-operative planners are computationally expensive since they should find an optimal path based on the surgeon's

input. Moreover, they need the behaviour of the soft tissue beforehand to find the best possible trajectory. Online planners can solve these limitations by adapting to changing environment or uncertainties. They seem to be essential in case the target location changes during the course of operation.

Robotic needle steering has now been a research discipline for over a decade, yet the progress towards clinical testing and implementation has been slow. It is believed that much of the slow adoption of steerable needles for real clinical applications has been caused by the poor curvature performance of many of the needle strategies in biologically relevant tissue stiffnesses. Only one case of *in vivo* studies is reported by Majewicz *et al.* [146] that did some open-loop curvature measurements and did not simulate a real clinical scenario. Most of the needle steering techniques are validated in artificial tissues rather than actual biological tissues, and most of them have very little curvature in soft tissues. Soft tissue phantoms made of Gelatin are very common. According to literature, Gelatin 5 wt.% phantoms have stiffnesses of 4.6 kPa which correspond to the stiffness of brain tissue (0.5 - 6 kPa) [71]. Gelatin 10%, and 20% soft tissue phantoms have the Young's moduli of 25 kPa, and 90 kPa, respectively and can simulate normal fat tissue ( $E = 22$  kPa), and a cancerous prostate ( $E \approx 96$  kPa) [165]. 6% by weight gelatin soft tissue phantoms is reported to simulate the resistance of the *in vitro* canine brain at 38° C [115, 204]. From compression tests conducted in [51], it is found that the elastic moduli of the 5%, and 7% by weight

gelatin phantoms are 21 kPa, and 80 kPa, respectively (note that the elastic moduli reported by different literature differ significantly).

Despite the vast research in needle steering area, this research is still immature to be used for clinical setting. However, almost all of needle steering experiments are conducted in soft tissue phantoms such as gelatin, and agar [159] or *ex vivo* tissue samples [149]. One *in vivo* study is reported in the literature that is carried out on canine prostate, liver, and kidneys [146]. This is the only *in vivo* study reported in the literature. This suggests that there are still fundamental issues to be solved before clinical adoption of this technology. One limitation is the complex closed-loop control of the steerable needles that makes their application in clinical settings challenging. As an example, it is a big challenge to change the control parameters in real time as the local tissue mechanical properties change. Other unsolved challenge is registration of the needle and the local tissue environment in order to avoid large placement errors.

Most of the needle steering systems are designed to be controlled autonomously with the human operator to setup the system and monitor it during operation. However, for clinical acceptance, human-in-the-loop control is needed. Adopting a clinically acceptable placement error for needle steering procedures is challenging, and successful procedure depend on how effective the therapy was (in brachytherapy for instance this translates into accurate placement of the radioactive seeds). Typical

misplacement errors are reported to be approximately 4 mm in the literature for brachytherapy [141, 257], however this can be reduced to 1.8 mm with proper insertion method.

The vast majority of robotic steerable needles are validated in soft tissue mimicking phantoms. Phantoms are interesting because they can partially mimic the properties of real tissues and thus steer clear of the need for testing these devices on patients. Although no soft tissue mimicking phantom can simulate all the properties of a real soft tissue, they can provide many advantages that make them appealing to characterize and test different needle insertion modalities. This is also important from training point of view since most residents and trainees do not have the required licences to do medical operations on patients and thus using soft tissue phantoms can improve their expertise during training. A soft tissue has several properties that are important image-guided needle interventions including microstructure characteristics, mechanical properties, optical properties, and acoustical properties. Based on the application, the soft tissue phantom should mimic one or more of these characteristics. Table 1.1 summarizes the soft tissue phantoms in the literature along with their preparation methods. Table 1.2 summarizes different compositions of the soft tissue mimicking materials, and the soft tissue that they simulate in terms of mechanical properties. Note a variation in the data among different literature. Table 1.3 provides information on the optical and acoustical properties of soft tissue mim-

icking materials and their soft tissue counterparts. These information are useful for image-guided medical interventions.

An overview of the robotic needle steering systems along with their design, modeling, planning, and clinical applications that are discussed so far is summarized in Table 1.4. As can be seen from this table the majority of the literature is prevalent with tip steerable needles in which the interaction of the needle tip with surrounding tissue causes the needle to steer. The curvature is constant and can only be controlled by duty cycling to worsen the radius of curvature. There exists only one radius of curvature for a combination of a tissue and the needle. Active steerable needles have some form of control on the tip of the needle and can steer in 3D without the need for base rotation. However, because of the design complexity, they have larger diameters.

## 1.4 Conclusions

In this Chapter, the state-of-the-art in robotic needle steering is presented, and the advantages and disadvantages of the proposed approaches are discussed. This review has also identified many of the limitations of previously existing steerable needle designs, and some of the potential reasons why robotic needle steering has not gained much clinical acceptance.

Robotic needle steering came into existence with the promise of improving medical interventions. However, the clinical acceptance of steerable needles is hindered by limitations of the traditional steerable needles. The most salient limitations in previ-

**Table 1.1:** Soft tissue mimicking materials used in the literature and their preparation methods.

Soft Tissue Simulant	Preparation Method
Polyvinyl Alcohol (PVA) gels	PVA powder plus deionized water and heated up to 93° C while magnetically stirring. Allow to cool down to room temp.
Polyvinyl Chloride (PVC) Plastisol	PVC resin in liquid plasticizer then heating to (170 – 190° C) while stirring. Allow to cool down.
Gelatin gels	Gelatin powder with deionized water. Heat to dissolve. For cooling refrigerate at 4 – 8° C.
Agar/Agarose gels	Agar in the gel form: heated until becoming liquid and then cooled and refrigerated overnight. Agarose is a solution of 4% agarose powder in distilled or deionized water while magnetically stirring. Then cooling.
Silicone gels	A mixture of polyorganosiloxanes (65-85 wt%), amorphous silica (20-25%), platinum-siloxane complex (0.1 wt%), and some other ingredients (10 wt%). Vaseline oil is added to improve acoustic properties. Mineral oil is used to adjust the mechanical properties.

PVA is non-toxic, hydrophilic, and biocompatible. Properties can be controlled by varying the ratio of the additive materials or changing the cross-linking method. PVA, PVC, gelatin, and Agar phantoms are water-based.

**Table 1.2:** Soft tissue simulants and soft tissues that they simulate in terms of mechanical properties.

Soft Tissue Simulant Composition	Needle insertion Peak force (N)	Elastic Modulus (kPa)	Soft Tissue	Reference
PVA hydrogel 1	-	-	human vitreous	[134]
PVA hydrogel 2	5.3	11.4	porcine liver	[100]
PVA hydrogel 3	8.05	-	prostate	[132]
PVA hydrogel 4	-	1-2	brain	[263, 73]
PVA hydrogel 5	0.23 $\pm$ 0.04	116	kidney	[101]
PVA hydrogel 6	-	9.44	brain white matter	[156]
PVA hydrogel 7	0.11 - 0.16	-	liver	[52]
Gelatin gel 1	-	0.997-50.71	layers of skin	[42]
PVC gel 1	5.2	3-200	prostate	[96]
PVC gel 2	0.04 - 0.36	6-45	liver	[136, 135]
Silicone with 20, 30, and 40 wt% mineral oil	0.4 - 1	10.3-13	liver and muscle	[265]
Gelatin 3.4 wt%	-	3-4.5	brain	[129]
Gelatin 15 wt%	-	10	liver	[247]
Gelatin 14.9 wt%	-	35	breast	[206]
1.3 cc of Gelatin in 20 cc of water	comparable insertion force	-	brain	[155]
Gelatin 5 wt%	-	4.6	brain	[71]
Gelatin 10 wt%	-	25	normal fat tissue	[165]
Gelatin 20 wt%	-	90	cancerous prostate	[165]

PVA hydrogel 1: PVA hydrogel with Sodium trimetaphosphate (STMP) additive in the ratio of 8:1. PVA hydrogel 2: PVA hydrogel with Dimethyl-sulfoxide (DMSO) additive (3 wt% PVA + DMSO + deionized water). PVA hydrogel 3: PVA hydrogel with 3 g PVA + 17 g deionized water + 90 g DMSO + 4 g NaCl + 1.5 g NaOH + 3 g ECH. PVA hydrogel 4: 6% PVA and phytigel (PHY) 0.85% separate solutions in 1:1 weight ratio. PVA hydrogel 5: PVA concentration of 8 g/dl with 4wt% NaCl concentration with mix water/DMSO solvent prepared under 7 freeze/thaw cycles. PVA hydrogel 6: (PVA + Polyvinyl pyrrolidone(PVP)) polymers are mixed with deionized water at a concentration of 10 wt% heated to 85° C for 3 hrs. PVA hydrogel 7: 4 m% PVA with 2 freeze/ thaw cycles. Gelatin gel 1: gelatin powder + agar powder dissolved in distilled water (different concentrations for different layers) + (synthetic melanin powder + Intralipid-20% + molecular absorbing dyes + India ink) for optical properties + (bovine serum albumin (BSA) + 40 m diameter monodisperse silica microspheres) for acoustic properties. PVC gel 1: PVC polymer solution and the softener diethyl hexyl adipate (different concentrations). PVC gel 2: PVC polymer solution and the softener diethyl hexyl adipate (soft PVC).

**Table 1.3:** Optical, and acoustical properties of soft tissue mimicking materials and their real soft tissue counterpart that share the similar properties. These properties are useful for image-guided medical interventions.

Soft Tissue Simulant	Absorption Coefficient ( $cm^{-1}$ )	Reduced Scattering Coefficient ( $cm^{-1}$ )	Speed of sound (m/s)	Attenuation Coefficient (dB/cm)	Soft Tissue	Reference
PVC 1	0.1-0.6	5.9-16.2	1499	6.2-22.7	breast	[255]
PVC 2	-	-	1360-1400	-	prostate	[96]
PVC 3	0.4-2.8	0.1-2.8	1403-1409	0.5-0.69	liver, fat	[72]
PVC 4	-	-	1379.3-1397.9	0.29-0.94	breast, and lesions	[50]
soft PVC plastisol	-	-	1395	0.441	fat, muscle, liver	[39]
PVC 5	-	-	1393-1407	0.38-0.61	in, fat, muscle, prostate	[135]
Agar 1	-	-	1050	0.08	skin, breast	[286]
Oil + Gelatin + Agar	-	-	1490-1570	0.1-0.9	breast tissue: glandular tissue, adipose tissue, skin, and Cooper's ligaments	[37]
PVA + water + DMSO	-	-	1570	0.58	skin, breast	[286]
Silicone 1	-	-	1030	2.8	skin, breast	[286]
Silicone 2	-	-	964.7-1250	0.546	fat, muscle, liver	[39]

PVC 1: PVC plastisol with glass microsphere. PVC 2: PVC polymer solution and the softener diethyl hexyl adipate (different concentrations). PVC 3: PVC plastisol (PVC + softener). PVC 4: PVC plastisol mixed with graphite (different concentrations). PVC 5: polymer solution + softener phthalate ester with mineral oil and spherical glass beads ( $50 \mu m$  average diameter). Agar 1: 2% solution agar powder in distilled water heated to  $160^\circ C$  while stirring and then cooling down. Silicone 1: A two-compound silicone (9:1 mass ratio of platinum catalyst:hardener). Silicone 2: Silicone mixed with silicone oil with different ratios.

Table 1.4: Overview of the state-of-art in robotic needle steering, their design, specifications, Modeling, planning, and clinical applications.

Ref.	Needle Design	Needle Material	Needle Diameter (mm)	Insertion Velocity (mm/s)	Soft Tissue	ROC (mm)	Needle Localization	Planning	Model	Clinical Application
[8]	Passive Articulated tip (45°, 16 mm)	Nitinol	0.8 (body) 2 (hinge) 1 (tip)	1.6	<i>ex vivo</i> Porcine liver	55.8	3D US	-	Kinematic	Liver Biopsy
[36]	Passive "Airfoil" Bevel-tip (12°)	Nitinol	0.46 (cannula) 0.24 (stylet)	3	Gelatin 6% Gelatin 10% <i>ex-vivo</i> Cow Liver	125 72 263	Camera	-	-	-
[110]	Passive 4 sets of Notches	Stainless Steel (SS)	1.02	5	80% liquid plastic + 20% plastic softener E = 35 kPa		US Guidance	-	Finite Elements	-
[120]	Passive Bevel-tip (30°)	Steel	0.38	2.5	Plastisol (3:1 plastic to softener)	-	-	-	Finite Elements	-
[148]	Passive Bevel-tip (30°)	Nitinol	0.58	5	<i>ex vivo</i> Canine Kidney	164.5	X-ray + Camera	-	-	Brachytherapy Biopsy
[148]	Passive Prebent (15°) Bevel tip (30°)	Nitinol	0.58	5	<i>ex vivo</i> Canine Kidney <i>in vivo</i> Canine Kidney	52.3 104	X-ray + Camera	-	-	Brachytherapy Biopsy
[151]	Passive Prebent (45°)	Nitinol	0.58	15	<i>ex vivo</i> Goat Liver	34	X-ray + Camera	-	-	Biopsy
[157]	Passive Prebent (15°) Bevel tip (10°)	Nitinol (body) SS (bevel-tip)	1.27 (tip) 0.28 (body)	-	Gelatin 6.5 wt% (Brain Phantom)	52	-	-	Kinematic	-
[160]	Passive Bevel-tip (38°)	Nitinol	0.4	2.5	Plastisol (4:1 Plastic to softener)	179.4	Camera	-	Mechanics-based	-
[180]	Passive Cannula & Pre-bent stylet	Nitinol	0.902	5	PVA gel (E = 157 kPa)	-	-	-	Mechanics-based	Biopsy
[213]	Passive Bevel-tip (35°)	Nitinol	0.86	-	Simulated Muscle <i>ex vivo</i> Bovine Liver	128 400	EM Tracker	Adaptive	Kinematic	-
[238]	Passive Bevel-tip (10°) Flexure max. angle (22°)	SS (body) Nitinol (flexure)	OD = 0.91 ID = 0.6	5	Gelatin 10 wt% <i>ex vivo</i> pork loin	121 176	-	-	-	Bronchoscopy
[190]	Passive Pre-bent Bevel-tip	Nitinol	0.88	-	Simulate Muscle <i>ex vivo</i> Porcine loin	67 137	2.5D US	Simulated Annealing	Vibrating Beam	-

Table 1.4 continued from previous page

Ref.	Needle Design	Needle Material	Needle Diameter (mm)	Insertion Velocity (mm/s)	Soft Tissue	Best ROC (mm)	Needle Localization	Planning	Model	Clinical Application
[276]	Passive Flexure needle tip Bevel (10°) Notched wall	Nitinol	0.91	-	Knox Gelatin 10 wt% <i>ex vivo</i> Bovine liver	91.4 224.11	-	-	-	-
[281]	Passive Bevel tip (7°)	Nitinol	0.52	-	Kidney Phantom	333	-	-	-	-
[59]	Passive Base Manipulation	-	-	-	PVC Phantom E = 20 kPa	-	Camera	Inverse Kinematics	Finite Elements	-
[34]	Passive Bevel tip (20°)	Nitinol	0.508	-	Agar + 10% Glycerin	60	Camera	Rapid-RRT	Kinematic	-
[7]	Passive Pre-bent (4.5 mm) Bevel-tip (45°)	Nitinol	0.48	-	<i>ex vivo</i> Bovine liver	51.4	2.5D US Doppler	-	Kinematic	Liver Biospy
[2]	Passive Bevel tip (30°)	Nitinol	1	4	<i>ex vivo</i> Chicken breast embedded in Gelatin	270	2.5D US	Rapid-RRT	Kinematic	-
[184]	-	-	-	-	-	-	MRI	Inverse Kinematics	Kinematic	-
[156]	Passive Prebent (3 mm) Bevel tip (30°)	Nitinol	0.5	-	Paraffin phantom <i>ex vivo</i> Pork tenderloin	500 600	3D US	Rapid-RRT	Kinematic	-
[273]	Passive Bevel tip (45°)	Nitinol	0.7	5 to 25	Simulated Muscle	-	Camera	-	Kinematic	-
[201]	Passive Prebent (15°) Bevel tip (45°)	Nitinol	0.61	-	Plastisol (4:1 Plastic to Softener)	61	Camera	Stochastic Motion Roadmap (SMR)	Kinematic	-
[69]	Passive "Airfoil" Prebent (16°, 6.3 mm) Bevel tip (20°)	Nitinol	0.15	-	Knox Gelatin (20 cc boiling water + 1.3 cc Gelatin)	100	Magnetic Displacement Sensor	-	-	-
[185]	Passive Bevel tip (45°)	Nitinol	0.57	2.5	Plastisol (4:1 Plastic to Softener)	161.3	Camera	-	Kinematic	-
[275]	Passive Pre-curved	Nitinol	0.48	1.5	Plastisol (4:1 Plastic to Softener)	15.5	Camera	-	-	-
[129]	Passive Tube-Prebent Wire type	Nitinol	Wire (0.8 mm) Tube (ID = 1, OD = 1.2)	-	Ballistic Gelatin Cow liver Beef	20 104.5 18.6	Camera	-	-	-

Table 1.4 continued from previous page

Ref.	Needle Design	Needle Material	Needle Diameter (mm)	Insertion Velocity (mm/s)	Soft Tissue	Best ROC (mm)	Needle Localization	Planning	Model	Clinical Application
[81]	Passive Base Manipulation	SS 22-Gauge Bevel tip	OD = 0.711 ID = 0.394	-	Turkey breast muscle Beef liver	-	Fluoroscopic feedback	Inverse Kinematics	Virtual Springs	-
[172]	Passive Base manipulation	SS 20-Gauge Bevel tip	0.908	-	Two-layer Dermasol Phantom prepared with TiO2	-	US Guidance	Inverse Kinematics	Virtual Springs	-
[35]	Active Single SMA wire	Flexinol	Variable	-	Prostate Phantom	-	Optical FBG Temperature Sensors	-	-	Percutaneous Surgery Biopsy
[122]	Active Single SMA wire	Nitinol/ Flexinol	2.6	2.5	Plastisol (3:1 Plastic to Softener E = 25.6 kPa)	-	-	-	-	-
[123]	Active Three SMA wires	Solid base/ Flexinol	OD = 2.6 ID = 1.8	-	air	-	-	-	ID Constitutive Material Model of SMAs	-
[219]	Active Cable actuated Prebent (10, 20, and 30°)	Nitinol wires SS Tube	0.5	2	Gelatin 10 wt% (E = 17 kPa)	-	Camera	-	-	-
[250]	Active Cable Actuated (4 cables)	SS Stylet PEEK Plastic Cannula	Stylet (0.5) Cannula (0.9) OD = 1	5	Gelatin 15 wt% (E = 10 kPa)	181	FBG	PI-controller	-	-
[99]	Active Magnetic	Different Gauge Medical Needles	1.59	0.5	Tissue 1 (E = 1.96 kPa) Tissue 2 (E = 2.7 kPa)	10.2	Magnetic Sensor	PID	-	-
[50]	Active Flexure based SMA wires	Nitinol (body) SS (tip)	OD = 2.2 ID = 1.7	2.54	Plastisol (3:1 Plastic to Softener) <i>ex vivo</i> Pig liver	387 267	-	-	-	-
[208]	Active Tendon-driven actuated tip (conical shape, l = 5 mm)	Nitinol (needle) PEEK (cannula)	Needle (1) Cannula (2)	5	Gelatin 14.9 wt% (E = 35 kPa)	200	FBG Sensors	Online Estimation	Kinematic	-
[216]	Active SMA-actuated with Symmetric tip	Nitinol/ PTFE	1.67	0.5	Plastisol (4:1 Plastic to Softener E = 40 kPa)	-	Optical Fiber Sensing	-	-	Prostate Biopsy
[38]	Active 4 Actuated Shafts	Special Flexible and Rigid materials	8	1	Gelatin 6 wt%	100	EM Sensor	-	-	Neurosurgery
[116]	Active 2-Segment Programmable bevel	VeroWhite	4	0.5	Gelatin 6 wt% (E = 7 kPa)	70	EM sensor + Camera	Gradient-based Optimization	Kinematic	Neurosurgery

Table 1.4 continued from previous page

Ref.	Needle Design	Needle Material	Needle Diameter (mm)	Insertion Velocity (mm/s)	Soft Tissue	Best ROC (mm)	Needle Localization	Planning	Model	Clinical Application
[21]	Active Segmented cannula Pre-curved SMA wires	Flexinol	ID = 1.4 OD = 3	-	Knox Gelatin	-	OCT imaging	Optical flow Algorithm	Kinematic	-
[115]	Active 4-Segment Programmable bevel	Rubber-like	12	1	Gelatin 6 wt% (E = 7 kPa)	178.6	2D US	Inverse Kinematics	Virtual Springs	-

Tissue 1: 1.2 g agar powder + 0.08 g agarose powder + 100 mL distilled water; Tissue 2: 1.6 g agar powder + 35  $\mu$ g pure charcoal + 100 mL of distilled water; US: Ultrasound, EM: Electromagnetic, FBG: Fiber Bragg Grating, OCT: Optical Coherence Tomography, ROC: Radius of Curvature. Note that some of the values for Radius of Curvature are extracted from the data in the paper.

ously existing designs have been buckling, torsional windup, and a limited workspace. This limited workspace is most affected by the poor degree of achievable radius of curvature in conventional steerable needles. Other ancillary limitations for some past steerable needle strategies include unwanted tissue damage and increased torsional friction that cause the rotation at the base to be out of sync with the rotation angle of the tip. Developing new techniques that can compensate for some of the listed issues and move the steerable needles towards their clinical acceptance seems to be of utmost importance.

## 1.5 Contributions

In order to address several challenges and gaps in the literature, a new needle steering system is proposed in this dissertation that we call Fracture-directed Waterjet Steerable Needles in which the direction of the tissue fracture is controlled by the waterjet and angled tip after which the flexible needle follows. The major contributions of the research in this dissertation can be summarized as follows:

- Waterjet Soft tissue interaction is characterized and validated with experiments in terms of developing finite element model, and mechanics-based model based on fracture mechanics to predict the penetration pressure as well as depth of cut of the waterjet into soft tissue as a function of the waterjet properties (diameter, velocity), and soft tissue properties (constitutive response, and fracture

toughness).

- Proposed and developed a curvature-controllable waterjet steerable needle system that is improved over conventional steerable needles in terms of being curvature variable without the need for rotational duty cycling, smaller radius of curvature even in softest soft tissues, no buckling issue while inserting with the waterjet, no rotational duty cycling for controlling curvature and thus no torsional friction, as well as reduced insertion forces compared with the conventional needles.
- Proposed, and validated a discrete kinematic model for the waterjet steerable needles that consist of two parts: (1) the mechanics-based model that predicts the cut-depth of the waterjet in soft tissue based on soft tissue properties, waterjet diameter, and water exit velocity, and (2) a discrete-step adaptation of kinematic bicycle model of the steerable needle travel.

## 1.6 Dissertation Overview

Chapter 1 provides the state-of-the-art in needle steering techniques in the literature. The advantages, disadvantages, modeling, path planning, and control methods are discussed. In Chapter 2, waterjet - soft tissue interaction problem is studied. It provides a Finite Element Analysis of the waterjet interacting with soft tissue. This model can accurately predict the depth of cut of the waterjet in soft tissue and

provided an insight in penetration pressure of the waterjet but it is computationally time-consuming. Thus, a mechanics-based model is provided to solve the physics of the waterjet - soft tissue interaction. This model provides a prediction for penetration pressure and depth of cut of the waterjet in soft tissue based on the mechanical properties of the soft tissue (constitutive response, and fracture toughness) as well as the waterjet needle properties (diameter, and waterjet velocity).

In Chapter 3, we have shown that the waterjet can get rid of cutting force and thus decreases the forces applied to the base of the needle. This can drastically decrease buckling of the needle while inserting into the soft tissue since the needle will not do the cutting and it is the waterjet that does the actual cutting. Then, design, modeling, and path planning for fracture directed waterjet steerable needles are discussed. A kinematic model that is a discrete adaptation of the famous "Bicycle" model is proposed for the waterjet in which the length of the steps is predicted with the mathematical description of depth of cut of the waterjet. The feasibility of the waterjet steerable needle to reach different targets is shown, and the effect of step length (= depth of cut) on radius of curvature is studied. Then, it is shown that the curvature of the waterjet steerable needle can also be controlled by duty cycling of the waterjet (alternate ON and OFF of the waterjet) and that the curvature is a linear function of the duty cycling rate. It is shown that the radii of curvature for tissues with Young's moduli of 112, and 25 kPa are 49mm, and 78 mm, respectively.

Chapter 4 provides the conclusions and suggestions for future research direction.

Fig. 1.20 depicts a visual organization of the current thesis.

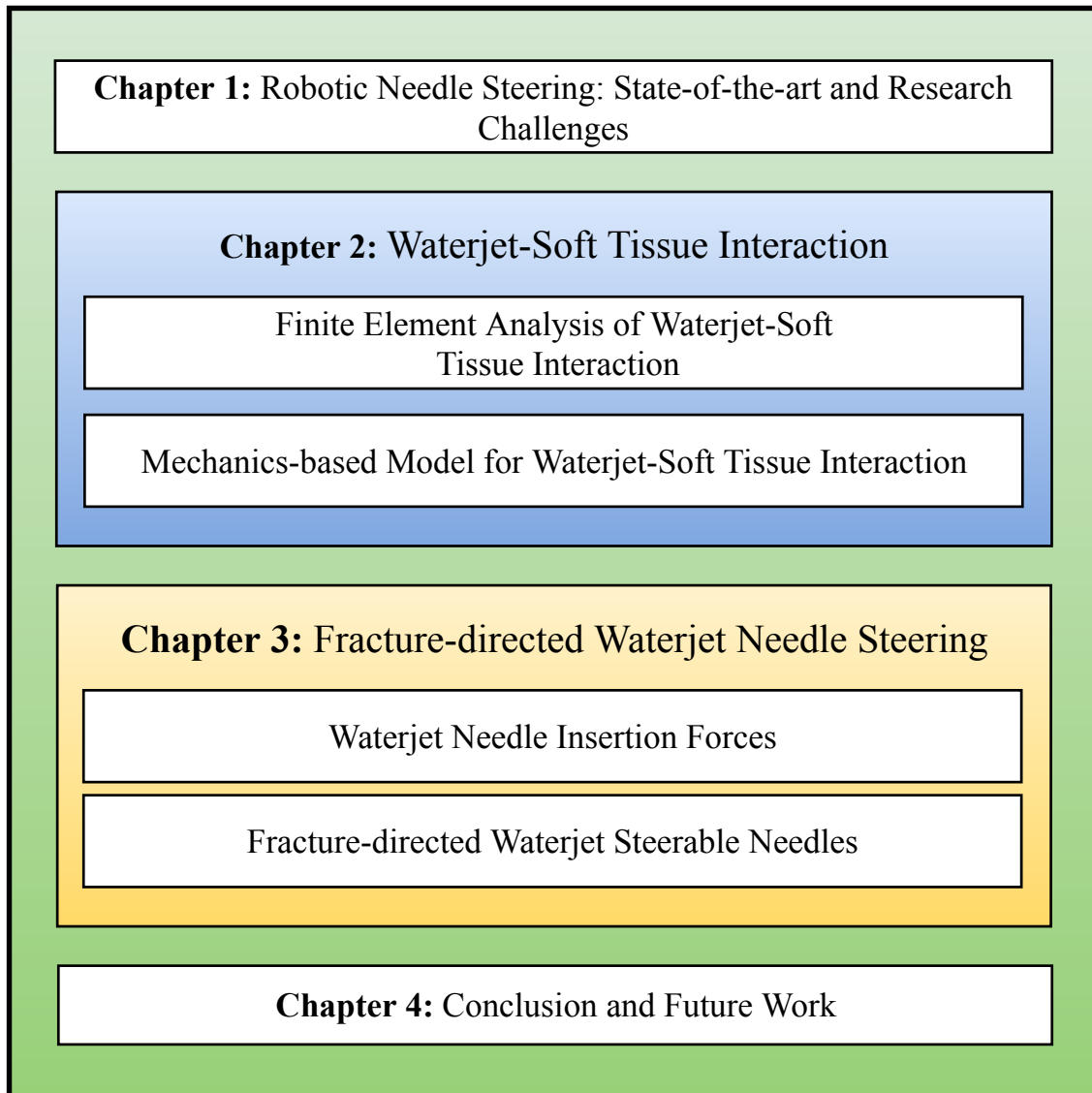


**Figure 1.20:** Visual organization of the current thesis. This thesis is organized into four chapters.

## CHAPTER TWO

### WATERJET SOFT-TISSUE INTERACTION

The use of the waterjet technology is now prevalent in medical applications including surgery, soft tissue resection, bone cutting, waterjet steerable needles and wound debridement. The depth of cut (DOC) of the waterjet in soft tissue is an important parameter that should be predicted in these applications to help improve the desired medical outcome. For instance, for the waterjet-assisted surgery, selective cutting of the tissue layers is a must to avoid damage to deeper tissue layers. For our proposed fracture-directed waterjet steerable needles, predicting the cut-depth of the waterjet in soft tissue is important to develop an accurate motion model, as well as control algorithms for this class of the steerable needles. To date, most of the proposed cutting models are heuristically determined and only valid in the conditions of the experiments and if the soft tissue or the system properties change, the models will become invalid.

The mechanics-based model proposed in this chapter is formulated to allow for variation in parameters related to both the waterjet geometry and the tissue. In this chapter, finite element model of the waterjet soft tissue interaction is presented and argued that although FEM can be accurate, it is very time consuming and is not suitable for real-time control and other applications. Therefore, a model based on the properties of the tissue and the waterjet is proposed to predict the DOC of the

waterjet in soft tissue. The cut-depths of the waterjet in soft tissue simulants are measured experimentally and the effect of the tissue stiffness, waterjet velocity and nozzle diameter are studied on DOC. In order to verify the model, soft tissue properties (constitutive response and fracture toughness) are measured using low strain rate compression tests, Split-Hopkinson-Pressure-Bar (SHPB) tests and fracture toughness tests. The results show that the proposed model can predict the DOC of the waterjet in soft tissue with acceptable accuracy if the tissue and waterjet properties are known.

## 2.1 Introduction

The use of the waterjets in strong solids has been used for decades in manufacturing and machining. Models have already been developed for depth of cut of the waterjet in strong solids [137], [259], [276], [260], [65], [176] and [258]. Wang *et al.* [259] developed a predictive model for depth of cut of the abrasive waterjet in alumina ceramics using a dimensional analysis technique. Other researchers used solid particle erosive theories [276], an energy conservation approach [260], fracture mechanics [65] and dimensional analysis [258] to predict the DOC of the waterjet in hard solids. In all of these models, the constants are found by the cutting tests, so they are mostly dependent on the experiments. On the other hand, the models developed for strong solids are not applicable to soft solids since the penetration mechanism into the strong solid is different from that of the soft tissue [228].

Recently, waterjets have been used as a surgical tool in the waterjet-assisted surgery [26, 162, 281, 198, 172, 171, 225, 103, 280, 16, 256, 214, 245, 197, 173]. Shi *et al.*[231] has described many advantages that the waterjet cutting has over similar approaches to tissue cutting. Waterjets have also been used to drill holes in bones [56, 55, 117]. The mechanism of cutting in these applications is through delivering the kinetic energy of the high-velocity waterjet coming out of a sub-millimeter nozzle to the target tissue. In these applications, predicting the DOC of the waterjet in soft tissue is a necessity for selective tissue cutting in order to avoid damage to deeper layers.

Oertel *et al.* [172] used a waterjet device called Helix Hydro-Jet (Erbe, Tübingen, Germany) to dissect the brain parenchyma. They showed that the waterjet allows for accurate, precise and reliable dissection of the porcine cadaver brain while preserving the vessels by controlling the waterjet pressure. They experimentally showed that there is a linear relationship between the waterjet pressure and depth of dissection. Therefore, their device provides manual control of the depth of cut by manually adjusting the waterjet pressure.

Yamada *et al.* [281] used a pulsed waterjet to dissect swine livers. They have evaluated the depth of dissection using the light microscopy and histology. They experimentally concluded that the depth of dissection has a direct relationship with the velocity of the waterjet and an inverse relationship with the breaking strength

of the liver parenchyma. In their study, no predictive model for DOC is proposed. Furthermore, the mechanical properties of the soft tissue were measured at a penetration rate of  $1 \frac{mm}{s}$  that is not comparable to the penetration rate of the high-velocity waterjet. Morad *et al.* [162] tried to control the cut depth of the waterjet surgical device by controlling the pressure of the waterjet; however they stated that while using the waterjet surgical device there is a risk of cutting unwanted tissue layers. They proposed to experimentally tune DOC based on the applied pressure; however they left this to a future study.

The Erbejet device [231, 245] is a waterjet device that allows for tissue-selective cutting based on a pre-selected pressure. The pressure range with a  $120 \mu m$  nozzle for this device is  $1 - 8$  MPa with a volumetric flow rate of  $1 - 55 \frac{ml}{min}$ . For this device, also, the depth of cut is controlled by controlling the pressure and no closed-loop control system is available to control the cut-depth.

Predicting the DOC of the liquid in soft tissue is also important from needle-free drug injections point of view [160, 164]. In these devices, the desired drug is ejected from a nozzle of diameter in the range of  $30$  to  $560 \mu m$  at a velocity of  $\approx 100 \frac{m}{s}$  [209]. It is important to know how deep the drug has penetrated into the soft tissue using a jet injector to ensure the efficacy of the treatment. In the literature, some researchers studied the penetration characteristics of these devices [28, 217, 218]. These studies experimentally showed that the jet penetration is a function of injected volume of the

drug, jet velocity, nozzle diameter and stiffness of the penetrated soft solid.

Microjet injection devices inject small amounts of drug in a repetitive way [15, 209]. Romhens *et al.* [209] studied the effect of velocity of the microjet on its penetration capacity using a repetitive microjet injection device. They experimentally concluded that microjets with over  $90 \frac{m}{s}$  velocity can penetrate epidermal skin sample and their study does not lead to a predictive model for depth of penetration of microjet into the skin. The diameter of the microjets are  $50 \mu m$  each.

Morad *et al.* [163] developed a waterjet cutting probe for flexible surgical robot to excise cancerous tissue from the spine. They experimentally studied the effect of tissue and waterjet properties on cut depth. They concluded that the depth of cut has a direct relationship with the waterjet pressure and the duration of the application of the waterjet but has an inverse relationship with modulus of elasticity of the soft tissue. They also mentioned that although waterjet cutting provides many advantages compared to traditional methods, however there is a risk of jet cutting through the soft tissue and going to underlying tissues and damaging them. Thus, this necessitates an approach to predict the depth of cut based on the waterjet and soft tissue properties.

Schramm-Baxter *et al.* [218] developed a simple model based on fluid dynamics to predict the penetration depth as a function of centerline velocity. In another study, Schramm-Baxter *et al.* [217] proposed a lumped parameter called exit jet power  $P_{jet}$  that collects all the jet parameters including diameter and velocity into one parameter

to study the jet mechanics. They showed that the jet penetration depth increases with increasing the jet power up to some point. Their proposed models are oversimplified and are far from the real penetration situation. For instance, in their models, the surrounding soft tissue is considered to be fluid and its effects are described by a lumped parameter of critical stress.

Different empirical models are proposed in the literature for the penetration depth of the liquid jet in soft solid. Baxter *et al.* [28] developed an empirical model based on a critical stress and centerline velocity for turbulent jet flows. Tagawa *et al.* [241] proposed a viscous stress model based on the stress at the wall of the hole formed by the liquid jet. Thus resulting in a simple model for the depth of penetration as a function of velocity and time. This model provides a reasonable prediction when the duration of the penetration is small enough. For longer penetration times, the interaction between the soft tissue and the liquid jet is significant. At the beginning, the penetrating jet must be powerful enough to puncture the surface and then provide enough inertial pressure to overcome both the elastic stress of the surrounding soft tissue and the hydrodynamic stress to penetrate soft tissue. Thus for longer duration penetration, the properties of the soft tissue should also be considered to accurately describe the dynamics of liquid jet penetration into soft tissue.

From this overview of the literature, there is an explicit need for the development of a mechanics, non-heuristic model that can predict the depth of cut as a function of

the needle and tissue parameters. This work presented in this dissertation provides the development and validation of such a model. We demonstrate the use of this model for our lab's research, waterjet-assisted steerable needles [23] in which the direction of the tissue fracture is controlled by the waterjet and then the flexible needle follows. Having a closed-form mathematical relation for depth of cut of the waterjet in soft tissue is a necessity to accurately control the trajectory of these devices.

Initially, a finite element model of the waterjet soft-tissue interaction is developed. However, finite element analysis require high computation time and is not suitable from feedback control point of view. This raises the need to have a closed-form mathematical solution to be embedded in the control software of the waterjet steerable needles. Fig. 2.1 shows the definition of the DOC of the waterjet in soft tissue and Fig. 2.2 depict the depth of cut experimentally for the waterjet needle. The depth of cut of the waterjet in soft tissue is dependent on the tissue properties such as shear modulus, strain hardening factor and fracture toughness as well as the waterjet properties such as diameter and velocity.

In this chapter, initially, the Finite Element Modeling of the waterjet soft tissue interaction is presented and then a physics-based model to predict the DOC of the waterjet in soft-tissue is proposed for the waterjet-assisted medical applications. This model is based on fracture mechanics and is a function of tissue properties such as fracture toughness and shear modulus, as well as the waterjet properties such as

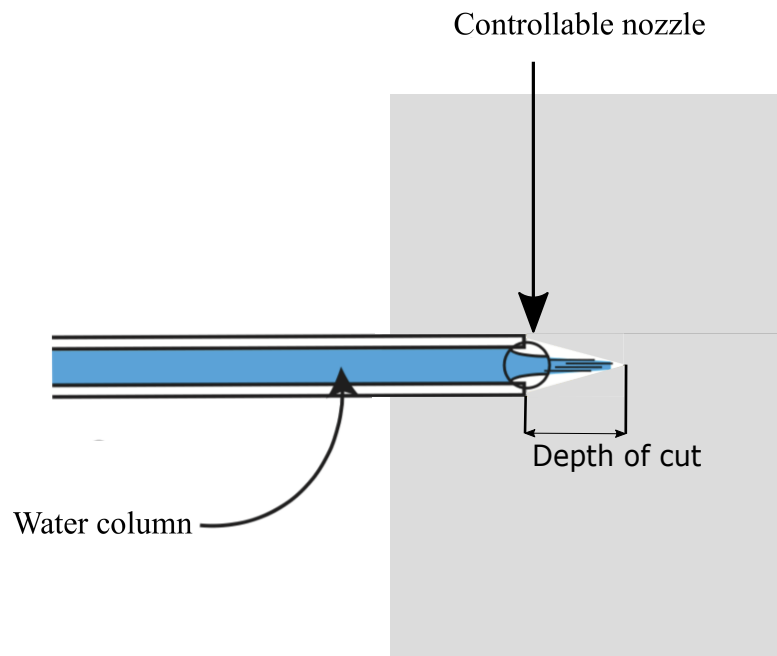


**Figure 2.1:** Definition of DOC of the waterjet in soft tissue. The waterjet cuts a small path in front of the nozzle and the length of this path is dependent on the tissue properties (constitutive response and fracture toughness) as well as the waterjet properties (diameter and velocity).

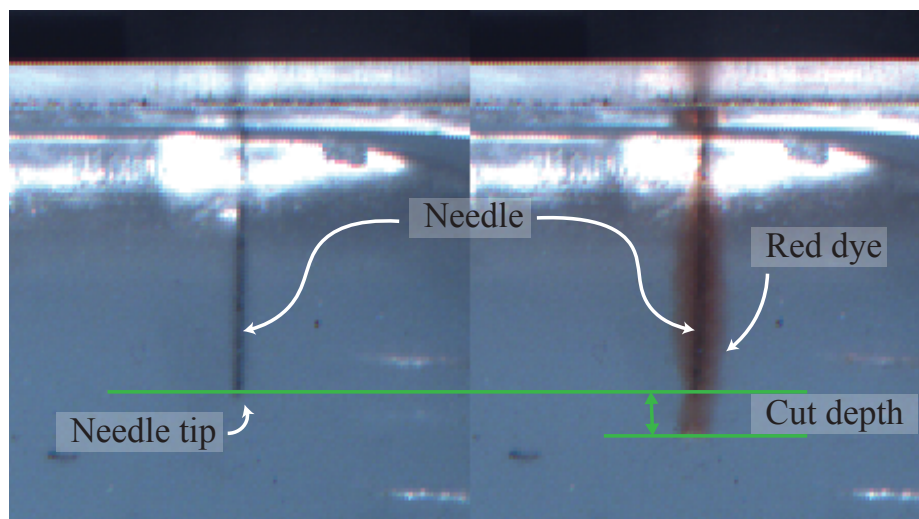


**Figure 2.2:** Definition of depth of cut shown experimentally for a water-jet needle [23]. © 2019 IEEE.

diameter and velocity. The model is validated using the mechanical properties of SEBS soft tissue simulants. Tissue properties are measured at the corresponding strain rates associated with the waterjet cutting of the soft tissue. SEBS is chosen as the main material for soft tissue simulants whose viscoelastic nature makes it a good candidate as a substitute for real biological tissues [168]. On the other hand, these soft tissue simulants are optically clear, have better durability due to non-aqueous solvents and their mechanical properties are easily changed to study the wide range of potential tissue properties. Characterization of the SEBS soft tissue simulants are done using static compression tests, SHPB tests and fracture toughness tests. These tests are modified from their traditional forms to fit the challenging tests on soft materials.

The experimental data of this chapter along with codes to run the data are uploaded to Mendeley Data in order for other researchers to use them for their own research purposes. The experimental data for depth of cut are available at (<http://dx.doi.org/10.17632/zvdrpzmkcb.2>), the data for Static compression tests are available at (<http://dx.doi.org/10.17632/gswfx544cs.3>) and the data for SHPB tests are available at (<http://dx.doi.org/10.17632/msvjxfh7nh.1>).

The results of this chapter are published in the Proceedings of 2019 International Symposium on Medical Robotics (ISMR) and Medical & Biological Engineering & Computing (MBEC) Journal [22, 21].

## 2.2 Materials and Methods

In this section, the material and methodology used for soft tissue preparation, tests to characterize tissue properties, experimental setup used for experiments, Finite Element Modeling and mathematical description of the predictive mechanics-based model for depth-of-cut (DOC) are described.

### 2.2.1 Finite Element Modeling of the Waterjet Soft Tissue Interaction

In order to have an understanding of the waterjet soft tissue interaction, a finite element model was developed. Since a soft solid is interacting with the liquid water, the case can be assumed to be a fluid-soft solid interaction. Therefore, a system to analyze the fluid flow in the needle and a system to analyze the structural deformation of the soft solid should be deployed. Since the data from both systems are inter-dependent, both systems are coupled together to form an FSI (fluid-solid interaction) solver.

The flow regimes of water inside the needle can be either laminar or turbulent. The critical flow rate, which is the highest flow rate ( $\frac{mL}{min}$ ) to achieve laminar flow in the specific section of the tube can be calculated by the Equation 2.1.

$$Q_{critical} = \frac{Re_{critical}\pi d_{tube}u}{4\rho \times 1000 \times 1000 \times 60} \quad (2.1)$$

In which,  $Re_{critical}$  is the critical Reynolds number where flow transitions from

laminar to turbulent and is considered to be  $Re_{critical} = 2300$ ,  $\rho$ ,  $u$  and  $d_{tube}$  are the density  $\frac{kg}{m^3}$  (for the water:  $\rho = 997$ ), dynamic viscosity  $\frac{kg}{ms}$  ( $\mu = 0.891 \times 10^{-3}$ ) and diameter of the tube in meters, respectively. The above equation gives the critical flow rate in  $\frac{mL}{min}$ . The critical flow rates for 0.32 mm and 0.24 mm needles are 30.99 and 23.24  $\frac{mL}{min}$ , respectively. Therefore, two different models for laminar and turbulent cases have been applied to determine the pressure parameters in finite element modeling.

In order to determine the depth of cut of water-jet in the finite element modeling, the solution algorithm depicted in Fig. 2.3 is used for laminar and turbulent flow regimes. Since the pump provides volumetric flow rate,  $Q_{pump}$  ( $\frac{m^3}{s}$ ) and the inlet and outlet of the software are mass flow rate, the following equation is used to calculate the mass flow rate,  $\dot{m}$  ( $\frac{kg}{s}$ ):

$$\dot{m} = \rho Q_{pump} \quad (2.2)$$

In this equation,  $\rho$  ( $\frac{kg}{m^3}$ ) is the density of the liquid (in this case, water).

CFX solver and Transient Structural Solver in ANSYS will cater for the fluid flow section and Structural domain of the above algorithm, respectively. Both solvers will share the geometry and the solution data from CFX to the Transient Structural. The tissue is modeled as a cube with the sides of length 40 mm. Fig. 2.4 depicts the model of tissue and the needle.

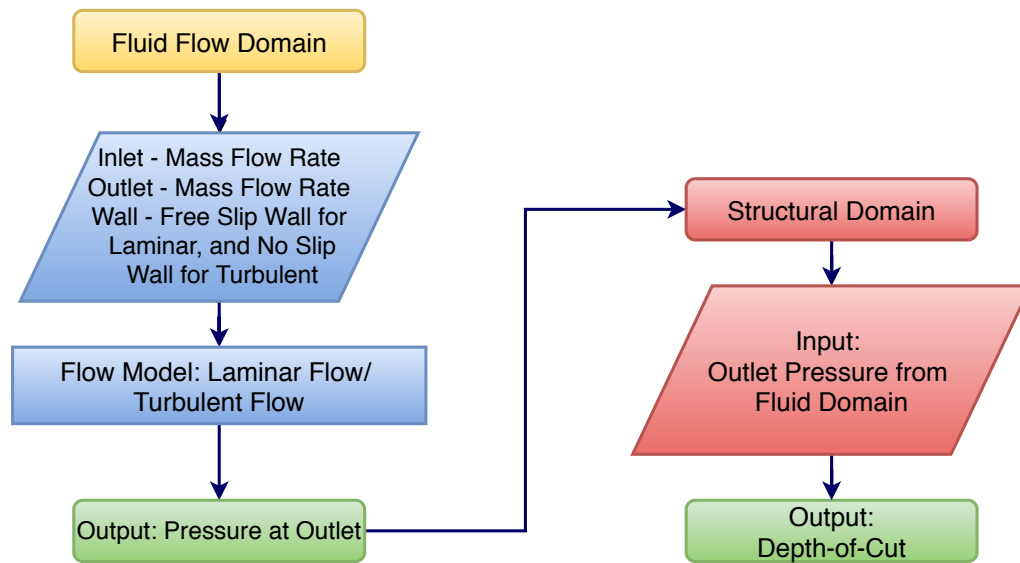


**Figure 2.3:** Finite element solution algorithm for laminar and turbulent flow regimes.

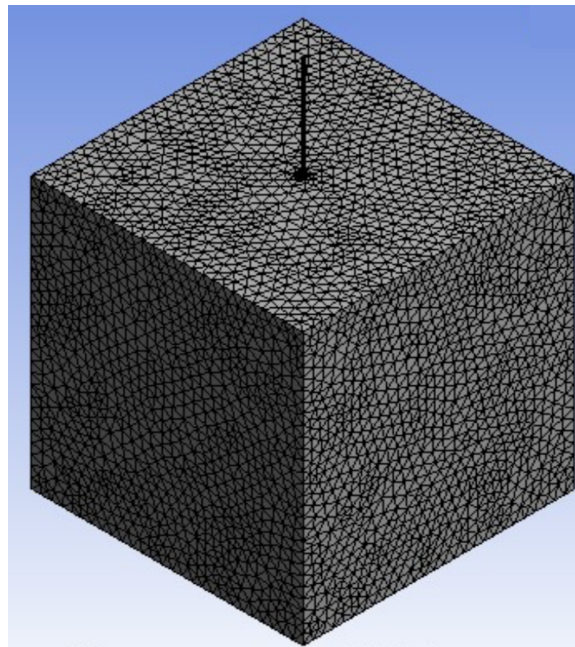


**Figure 2.4:** Model of tissue and the needle in ANSYS. The tissue is modeled as a cube with 40 mm sides and the needle is modeled to the shape and diameter of each Nitinol tube. © 2019 IEEE.

In the CFX solver, the first layer thickness is  $\frac{r}{38}$  for the mesh used in the laminar case. The first layer thickness is added as inflation and the inner layers are meshed using the Patch Conforming Tetra Mesh. For the boundary conditions, the water is set as the working material. The wall is considered as the wall of the needle and is assigned a free slip wall. The inlet and outlet are assumed to be mass flow rates since the input and output flow rates are the same (the pump provides a constant flow rate). The Turbulent flow simulation is the same as laminar flow except Shear Stress Transport model is used and for the boundary condition, the wall is considered as the wall of the needle and is assigned a no slip wall.

For the transient structural analysis, the pressure from the fluid flow analysis is imported into the structural solver. The needle penetrating into the soft tissue is meshed using a hex dominant mesh and the soft tissue is meshed using the patch forming method. The quality obtained for hex dominant mesh is 0.85. In this mesh, 8792 nodes and 5947 elements are used. The mesh used for the tissue simulant has a concentrated face mesh of size  $1 \times 10^{-3}$  near the pressure loaded area to capture the deformation of the soft tissue. An average element quality of 0.82 was achieved which is well within the permissible limits (0.8 – 1) for the solution convergence. 62660 nodes and 19451 elements are used. Fig. 2.5 shows the soft tissue simulant with the Patch Conforming Tetra mesh and the needle with the Hex Dominant mesh.

The soft tissue simulant is assumed to be an isotropic material with the properties

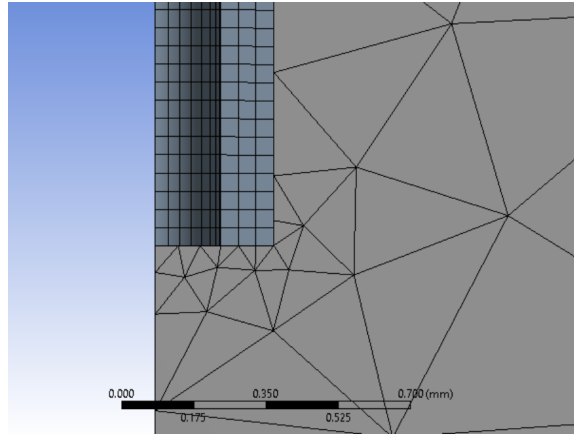


**Figure 2.5:** Meshes used for needle penetration into the soft tissue simulant. The soft tissue and the needle are meshed with the Patch Conforming Tetra mesh and the Hex Dominant mesh, respectively. © 2019 IEEE.

obtained in this chapter. The strain is considered to be small. The specimen is given the boundary conditions of a fixed support on all 4 sides and bottom and the pressure is automatically updated in the outlet region.

### 2.2.2 Predictive Mechanics-based Model for Depth Of Cut (DOC)

In this part, the predictive mechanics-based model of depth of cut of the waterjet in soft tissue is presented. This model is based on fracture mechanics and is dependent on the waterjet and tissue properties such as velocity, diameter, fracture toughness and shear modulus.

The model developed for the penetration pressure is based on the fracture-mechanics-based force model presented in Barnett *et al.* [27] and the principles presented in [13]. The advantage of using the methods based on fracture mechanics is that models based

on this method have a better prediction especially when failure happens [27] and [13]. In waterjet cutting of the soft tissue, when the velocity of the waterjet is higher or equal with respect to the minimum velocity that can cause failure in soft tissue, the tissue will be cut and an initial crack will be formed. The crack is then widened to accommodate the waterjet column.

Fig. 2.6 depicts a simplified schematic of the waterjet cutting the soft tissue. First, a crack is initiated by the waterjet and then the crack opens to let the waterjet with diameter of  $D$  through. The waterjet displaces the tissue during the penetration as demonstrated. Upon waterjet removal, the crack closes and reaches to the steady state diameter of  $d$ . Although several studies showed that the waterjet cuts soft material with mode I crack propagation (similar to sharp needles) by wedging open the soft tissue [44], [228] and [229], others [224] showed that in needle-free injections, the waterjet penetrates the cheek of human cadavers by formation of a cylinder-shaped holes. In Schramm-Baxter *et al.* [217], they divide the jet penetration into polyacryamide gels into three phases namely erosion, stagnation and dispersion. They showed that during the erosion phase, the jet removed the gel and led to the formation of a cylindrical hole. Tagawa *et al.* [241] also observed a cylindrical hole in the penetration of microjets into the gelatin and artificial skin. To avoid complexity of the model and steer clear of finite element methods associated with sharp needle penetration models, the displacement of soft tissue with the waterjet is considered to

be cylindrical like [224].

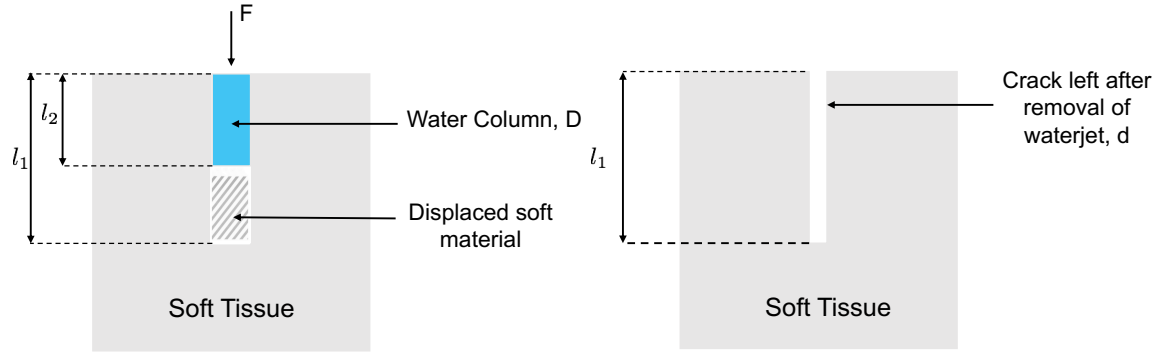


**Figure 2.6:** Schematic of crack formed by the waterjet in soft tissue. (left) Waterjet initiates a crack and then the crack opens to accommodate the waterjet with diameter  $D$  followed by the waterjet displacing the tissue and (right) Crack left with diameter  $d$  after the waterjet removal.

The fracture-based mechanics model that will be described in the following paragraphs is focused on predicting the penetration pressure of the waterjet  $P_w$  and thus predicting the depth of cut (DOC) defined by the following equations:

$$P_w = f(D, d, J_{IC}, \alpha, \mu) \quad (2.3)$$

and,

$$DOC = f(\rho, v, T, D, d, J_{IC}, \alpha, \mu) \quad (2.4)$$

In these equations,  $D$ ,  $d$ ,  $J_{IC}$ ,  $\alpha$ ,  $\mu$ ,  $\rho$ ,  $v$  and  $T$  are the waterjet diameter, steady-state diameter after the waterjet removal, mode I fracture toughness, strain hardening factor, shear modulus, water density, waterjet velocity and time, respectively.

As waterjet advances in the soft tissue, it does work on the soft tissue that equals to  $F\delta l_2$ , where  $F$  is the force exerted on soft tissue and  $\delta l_2$  is a differential insertion length. Then, the waterjet forms a crack in the soft tissue and displaces the tissue to accommodate the diameter of the waterjet. The work done in advancing the waterjet is equal to the sum of crack work  $\delta W_C$  and strain energy stored in soft tissue while being displaced  $\delta E_S$ :

$$F\delta l_2 = \delta W_C + \delta E_S \quad (2.5)$$

The work associated with crack formation in the soft tissue  $\delta W_C$  can be expressed by the following equation:

$$\delta W_C = J_{IC}\delta A_C \quad (2.6)$$

In which  $A_C = 2\pi(\frac{d}{2})l_1$  is the steady state area of the crack after the waterjet removal. Thus,  $\delta A_C = \pi d\delta l_1$  is the increment in crack area. Therefore equation (2.6) can be re-written as:

$$\delta W_C = J_{IC}\pi d\delta l_1 \quad (2.7)$$

In which  $J_{IC}$  is mode I fracture toughness ( $\frac{J}{m^2}$ ) which is dependent on crack growth rate already developed in (2.51).

The strain energy stored in the soft solid can be defined by:

$$E_S = E_d + E_e \quad (2.8)$$

In which,  $E_d$  and  $E_e$  are strain energy due to displacement of the soft tissue and strain energy due to widening of the hole in the soft tissue while accommodating the waterjet.

If we define  $\delta E_d = \frac{\partial E_d}{\partial l_1} \delta l_1$  and  $\delta E_e = \frac{\partial E_e}{\partial l_1} \delta l_1$ , then  $\delta E_S = \frac{\partial E_d}{\partial l_1} \delta l_1 + \frac{\partial E_e}{\partial l_1} \delta l_1 = (\frac{\partial E_d}{\partial l_1} + \frac{\partial E_e}{\partial l_1}) \delta l_1$  and thus (2.5) can be re-written as:

$$F \delta l_2 = \left( J_{IC} \pi d + \frac{\partial E_d}{\partial l_1} + \frac{\partial E_e}{\partial l_1} \right) \delta l_1 \quad (2.9)$$

This equation relates the work done in advancing the waterjet to the fracture work and strain energy stored in the soft solid due to displacement and expansion.

According to the conservation of volume, the volume of the displaced soft tissue to accommodate to the waterjet of diameter  $D$  is the same as the volume of the crack after the waterjet removal:

$$\pi \left( \frac{D}{2} \right)^2 (l_1 - l_2) = \pi \left( \frac{d}{2} \right)^2 l_1 \quad (2.10)$$

Thus,  $l_1 = \frac{D^2}{D^2 - d^2} l_2 \rightarrow \frac{\delta l_1}{\delta l_2} = \frac{D^2}{D^2 - d^2}$ .

By dividing the sides of (2.9) by  $A_w \delta l_2$ , in which  $A_w = \frac{\pi D^2}{4}$  is the cross sectional

area of the waterjet, we can write:

$$P_w = \frac{F}{A_w} = \frac{4}{\pi D(1 - (\frac{d}{D})^2)} \left[ J_{IC} \pi \frac{d}{D} + \frac{1}{D} \left( \frac{\partial E_d}{\partial l_1} + \frac{\partial E_e}{\partial l_1} \right) \right] \quad (2.11)$$

This equation provides a prediction of the penetration pressure of the waterjet into soft tissue. In order to have a closed form equation for it, one should find equations for  $\frac{\partial E_d}{\partial l_1}$  and  $\frac{\partial E_e}{\partial l_1}$ .

In order to find the  $\frac{\partial E_e}{\partial l_1}$ , suppose that  $d = 2r_1$  and  $D = 2r_2$  in which  $r_1$  and  $r_2$  are radius of the crack in steady state and radius of the waterjet column, respectively. When the waterjet penetrates into soft tissue, the ring of the crack expands from initial radius  $s_1$  to final radius  $s_2$ . Suppose that these rings have thicknesses of  $ds_1$  and  $ds_2$  with unit heights. The concept of the expansion of the crack is depicted in Fig. 2.7.

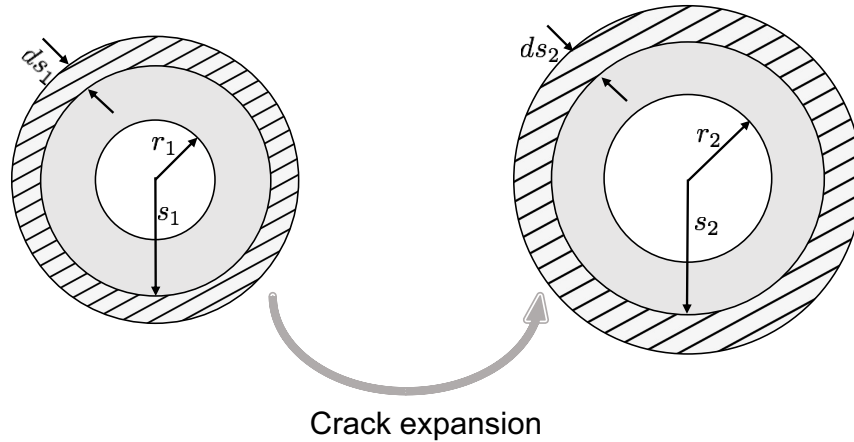


**Figure 2.7:** Schematic of crack expansion from radius  $s_1$  to  $s_2$  in penetration of the waterjet with radius  $r_2$  into a crack with steady state radius of  $r_1$ .

Due to conservation of volume, the volume of the column is equal before and after the expansion:

$$\pi(s_1^2 - r_1^2)(1) = \pi(s_2^2 - r_2^2)(1) \quad (2.12)$$

Another result that is deduced from volume conservation is that the multiplication of the stretch ratios are one. Considering the cylindrical coordinates  $(r, \theta, z)$ , one can write:  $\lambda_r \lambda_\theta \lambda_z = 1$ , in which  $\lambda_r$ ,  $\lambda_\theta$  and  $\lambda_z$  are principal stretch ratios. With the assumption of plain strain expansion of the crack (i.e. expansion happens in plane), one can conclude that  $\lambda_z = 1$ . Since  $\lambda_r = \frac{s_1}{s_2}$ , it is easy to see that  $\lambda_\theta = \frac{1}{\lambda_r} = \frac{s_2}{s_1}$ .

In order to model the constitutive response of the soft tissue, Ogden model [175] and [174] is used in this chapter. This model is proved to be a good fit for materials that go through strain hardening such as soft tissues [27]. The one-term Ogden model for an isotropic, incompressible and hyperelastic material can be described as:

$$\phi = \frac{2\mu}{\alpha^2}(\lambda_1^\alpha + \lambda_2^\alpha + \lambda_3^\alpha - 3) \quad (2.13)$$

Where  $\phi$ ,  $\mu$ ,  $\alpha$  and  $\lambda_i$  are strain energy density function ( $\frac{J}{m^3}$ ), shear modulus, strain hardening and the principal stretch ratios, respectively. Considering  $\lambda_1 = \frac{s_1}{s_2}$ ,  $\lambda_2 = 1/\lambda_1$  and  $\lambda_3 = 1$ , one can re-write the equation (2.13) as:

$$\phi = \frac{2\mu}{\alpha^2} \left[ \left( \frac{s_1}{s_2} \right)^\alpha + \left( \frac{s_2}{s_1} \right)^\alpha - 2 \right] \quad (2.14)$$

With above definition of strain energy density function, one can write:

$$\frac{\partial E_e}{\partial l_1} = \int_{r_1}^{\infty} \phi dV_1 = \int_{r_2}^{\infty} \phi dV_2 \quad (2.15)$$

In which,  $dV_1 = 2\pi s_1 ds_1$  and  $dV_2 = 2\pi s_2 ds_2$ , are the volume change elements in crack expansion. Thus (2.15) can be written in the final form as:

$$\frac{\partial E_e}{\partial l_1} = \frac{\pi\mu D^2}{2\alpha^2} \int_1^{\infty} f\left(\frac{d}{D}, \gamma\right) d\gamma \quad (2.16)$$

In which,  $f\left(\frac{d}{D}, \gamma\right)$  can be expressed in the closed form as:

$$f\left(\frac{d}{D}, \gamma\right) = \left( \frac{\gamma + \left(\frac{d}{D}\right)^2 - 1}{\gamma} \right)^{\frac{\alpha}{2}} + \left( \frac{\gamma}{\gamma + \left(\frac{d}{D}\right)^2 - 1} \right)^{-\frac{\alpha}{2}} - 2 \quad (2.17)$$

Considering  $\alpha = 2$ , this integral has an analytic solution but other than that it needs to be solved numerically. Appendix A provides a procedure for derivation of these equations.

Now that a closed form solution is found for  $\frac{\partial E_e}{\partial l_1}$ , it is time to find a similar formula for  $\frac{\partial E_d}{\partial l_1}$ . From volume conservation, we already know that  $\lambda_r \lambda_\theta \lambda_z = 1$ . If we take  $\lambda_r = \lambda_\theta$ , then we can write:

$$\lambda_r = \lambda_\theta = \frac{1}{\sqrt{\lambda_z}} = \frac{D}{d} \quad (2.18)$$

Then, the strain energy density function can be re-written as:

$$\phi = \frac{2\mu}{\alpha^2}(2\lambda_r^\alpha + \lambda_r^{-2\alpha} - 3) \quad (2.19)$$

Therefore:

$$\begin{aligned} \frac{\partial E_d}{\partial l_1} &= \pi \left(\frac{d}{2}\right)^2 (1)\phi = \\ &= \frac{\pi d^2}{d} \frac{2\mu}{\alpha^2} (2\lambda_r^\alpha + \lambda_r^{-2\alpha} - 3) = \\ &= \frac{\pi D^2}{4} \frac{2\mu}{\alpha^2} \left[ 2 \left(\frac{d}{D}\right)^{2-\alpha} + \left(\frac{d}{D}\right)^{2\alpha+2} - 3 \left(\frac{d}{D}\right)^2 \right] \end{aligned} \quad (2.20)$$

Substituting (2.16) and (2.20) into (2.11), we can write the closed form mathematical solution for penetration pressure of the waterjet in soft tissue as:

$$P_w = \frac{4}{D(1 - (\frac{d}{D})^2)} \left\{ J_{IC} \left(\frac{d}{D}\right) + \frac{D}{4} \frac{2\mu}{\alpha^2} \left[ \int_1^\infty f\left(\frac{d}{D}, \gamma\right) d\gamma + 2 \left(\frac{d}{D}\right)^{2-\alpha} + \left(\frac{d}{D}\right)^{2\alpha+2} - 3 \left(\frac{d}{D}\right)^2 \right] \right\} \quad (2.21)$$

Where,  $f(\frac{d}{D}, \gamma)$  is already given in (3.5). This equation provides a closed form

solution for penetration pressure of the waterjet in soft tissue in terms of diameter of the waterjet and crack as well as tissue mechanical properties. Crack dimensions should be such that the penetration pressure is minimized. It is assumed that the penetration occurs in this minimum penetration pressure.

Now that the penetration pressure can be predicted, we should develop a predictive model for depth of cut of the waterjet in soft tissue. For this, the simple model shown in Fig. 2.8 is proposed, where  $v$ ,  $D$  and  $h$  are the waterjet velocity ( $\frac{m}{s}$ ), waterjet diameter ( $m$ ) and cut-depth in soft tissue ( $m$ ), respectively.

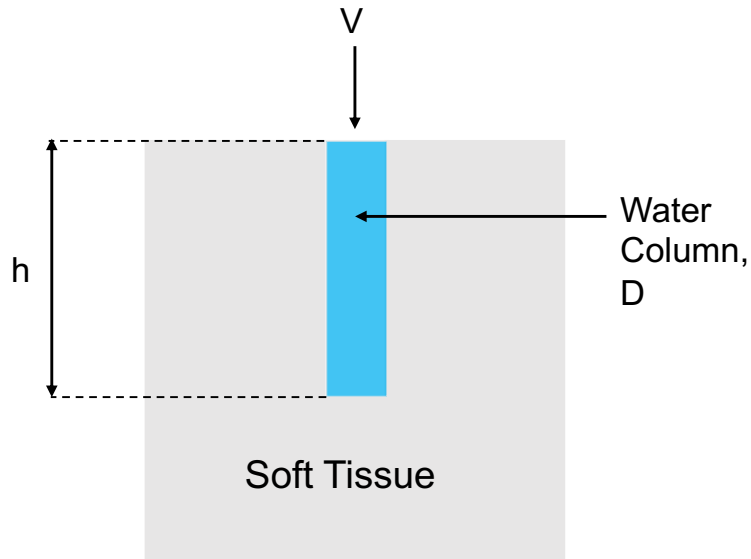


**Figure 2.8:** Schematic of the simple model for depth of cut of the waterjet in soft tissue.  $v$ ,  $h$  and  $D$  are velocity of the waterjet ( $\frac{m}{s}$ ), cut-depth ( $m$ ) and waterjet diameter ( $m$ ).

In order to find the depth of cut, the kinetic energy of the waterjet should be equated to the energy expended during the waterjet penetration:

$$KE_w = E_C \quad (2.22)$$

Where  $KE_w$  is the kinetic energy of the waterjet and  $E_C$  is the consumed energy during the waterjet penetration.  $KE_w$  can be calculated as follows:

$$KE_w = \int_0^T P dt = \int_0^T \frac{1}{2} \dot{m} v^2 dt \quad (2.23)$$

In which P is the power of the waterjet and mass flow rate of water jet  $\dot{m}$  can be defined as:

$$\dot{m} = \rho A_w v = \rho \frac{\pi D^2}{4} v \quad (2.24)$$

Thus, 2.23 can be re-written as:

$$KE_w = \int_0^T \frac{1}{2} \rho \frac{\pi D^2}{4} v^3 dt \quad (2.25)$$

For the consumed energy during the waterjet penetration, we can write:

$$E_C = P_w \frac{\pi D^2}{4} h \quad (2.26)$$

Now, equating (2.25) and (2.26), one can write:

$$h = \frac{\frac{1}{2}\rho \int_0^T v^3 dt}{P_w} \quad (2.27)$$

Where,  $P_w$  can be calculated using (3.4). This equation gives a closed form physics-based mathematical solution for depth of cut of the waterjet in soft tissue as a function of the waterjet properties (diameter and velocity) as well as soft tissue mechanical characteristics (constitutive response and fracture toughness).

Equation (2.27) will overpredict the depth of cut of the waterjet in soft tissue since it does not consider the fact that a large proportion of the jet's kinetic energy is dissipated during the penetration into soft solid. In order to have a more accurate description for DOC, we also need to take the effects of these parameters into consideration. Next section is going to deal with this and provide a more accurate model to predict the depth of cut of the waterjet in soft tissue.

The volume of water coming out of the nozzle can be calculated by the following equation:

$$V = A_w \int_0^T v dt = \pi \frac{D^2}{4} v T \quad (2.28)$$

In which,  $A_w$ ,  $T$ ,  $v$  and  $D$  are cross sectional area of the waterjet ( $m^2$ ), time (s), waterjet velocity ( $\frac{m}{s}$ ) and waterjet diameter (m), respectively.

### *Lumped Parameters Fluid Model*

The detailed shape of the surface of cut deeply influences the efficiency of the cutting process. In particular, the geometry of the excavated channel determines the amount of injected energy that actually reaches the soft tissue walls and the fraction that is lost in the backflow. While the full process could be accurately simulated via finite-element methods or through smooth particle hydrodynamics codes, we develop a simple lumped parameters model, able to retrieve a realistic value for the depth of cut in different tissues, with minimal computational cost. The model has a free parameter, that can be fitted to retrieve best results for a given combination of tissue and needle size.

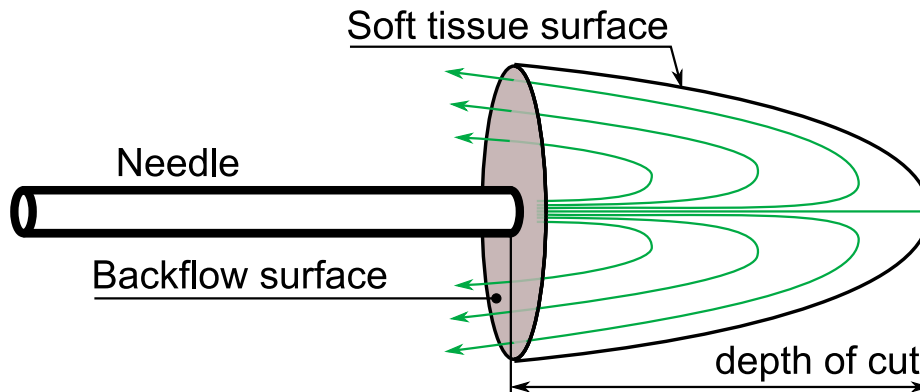


**Figure 2.9:** Simplified view of the flow field inside the region of cut: injected water impacts the surface of cut in the stagnation point and backflows from the sides.

We assume that the fluid behavior can be well approximated by the scheme in figure 2.9. Part of the injected energy flux  $\Phi_E^{inj}$  acts on the soft tissue walls of area

$A_{\text{surf}}$ , partly backflows from the surface with area  $A_{\text{out}}$  and partly may be dissipated by the viscous forces. Of the three, only the first one produces useful cutting work, such that (2.27) should be detailed further.

As the energy is spread from the injection area  $A_{\text{inj}} = \pi(D/2)^2$  equal to the needle internal cross section, towards the side and backflow surfaces, the energy flux is to be scaled by a factor  $A_{\text{inj}}/(A_{\text{surf}} + A_{\text{out}})$ . Of this energy, only the fraction  $A_{\text{surf}}/(A_{\text{surf}} + A_{\text{out}})$  reaches the walls, the rest being lost in the backflow. Equation 2.27 becomes:

$$h = \frac{1}{P_w} \int_0^T \left( \frac{\Phi_E^{\text{inj}} - P_{\text{visc}}}{A_{\text{inj}}} \right) \left( \frac{A_{\text{inj}}}{A_{\text{surf}} + A_{\text{out}}} \right) \left( \frac{A_{\text{surf}}}{A_{\text{surf}} + A_{\text{out}}} \right) dt \quad (2.29)$$

where  $P_{\text{visc}}$  accounts for the energy dissipated by the viscous forces. These terms injected energy, the soft tissue cutting surface and backflow areas assuming a given shape for the surface of cut and the power of viscous forces will be detailed in the next paragraphs.

**Injected energy** The amount of energy injected per unit time by the needle, previously expressed as  $\frac{1}{2}\rho v^3 A_{\text{inj}}$ , can be improved from an analysis of the flow inside the needle. The velocity in the needle channel can be assumed to follow a Poiseuille profile [125], changing from a maximum value at the channel centerline to zero velocity

at the needle walls:

$$v(r) = \frac{2Q}{\pi} \frac{R^2 - r_p^2}{R^4} \quad (2.30)$$

with  $Q$  the volumetric flow rate in [m<sup>3</sup>/s],  $R = D/2$  the needle inlet radius and  $r_p$  the considered radial position. The injected energy flux thus reads:

$$\Phi_E^{\text{inj}} = \int_{A_{\text{inj}}} \frac{\rho v^2}{2} \vec{v} \cdot d\vec{S} \equiv \int_{A_{\text{inj}}} \frac{\rho v^3}{2} dS = \frac{\rho Q^3}{\pi^2 R^4} \left[ \frac{\text{J}}{\text{s}} \right] \quad (2.31)$$

The term  $\frac{1}{2}\rho v^3$  appearing in Eq. (2.27) thus transforms into (except for the viscous dissipation term, treated later on):

$$\frac{\rho v^3}{2} \rightarrow \frac{\Phi_E^{\text{inj}}}{A_{\text{inj}}} \left[ \frac{\text{J}}{\text{m}^2 \text{s}} \right] \quad (2.32)$$

**Surface of cut model** As an approximation, we assume the shape of the surface of cut can be well described by an ellipsoid (see Fig. 2.10), with one axis equal to the depth of cut  $h$  and the other two axis equal to  $b = \eta h$  with eccentricity  $\eta$ . As the depth of cut grows in time during the water-cut process, the ellipsoid is supposed to expand keeping the same value for the eccentricity. This area growth progressively reduces the energy deposited per unit surface and thus reduces the effect of the waterjet, explaining experimental data.

As two semi-axes of the ellipsoid are the same, the surface area is that of half of

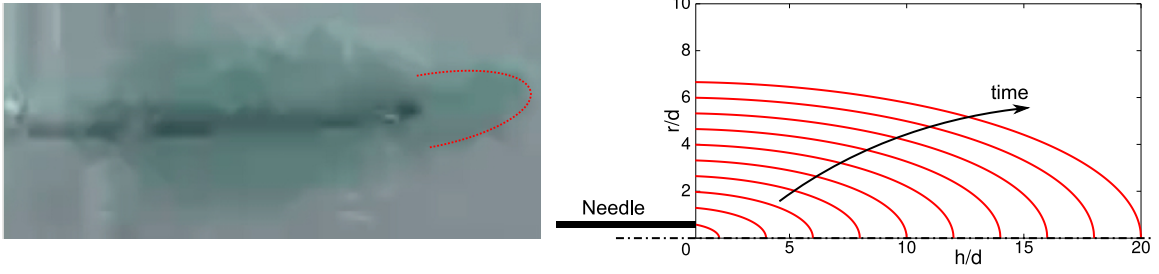


**Figure 2.10:** Approximation of the surface of cut via ellipsoid. Left: superposition with experiment. Right: growth in time with constant aspect ratio.

either an oblate ( $\eta > 1$ ) or prolate ( $\eta < 1$ ) spheroid, reading:

$$A_{\text{surf}} = \begin{cases} \pi b^2 \left[ 1 + \frac{h^2}{eb^2} \tanh^{-1}(e) \right], & e^2 = 1 - \frac{h^2}{b^2} & \text{if } \eta > 1 \\ \pi b^2 \left[ 1 + \frac{h}{eb} \sin^{-1}(e) \right], & e^2 = 1 - \frac{b^2}{h^2} & \text{if } \eta < 1 \\ 2\pi h^2 & & \text{if } \eta = 1 \end{cases} \quad (2.33)$$

And from the semi-axis  $b$  and the outer needle diameter  $d_{\text{out}}$ , the backflow area is found as:

$$A_{\text{out}} = \pi \left[ b^2 - (d_{\text{out}}/2)^2 \right] \quad (2.34)$$

In general, the shape of the cutting surface can depend on the tissue stiffness properties. Despite the crude simplicity of the fluid model developed here, taking  $\eta$  as a free parameter fitted on experimental data, will allow to reproduce closely the measured DOC. The procedure will be detailed in Section 2.3.4 and  $\eta$  will be treated as a free parameter for the time being.

**Viscous dissipation of energy** Viscous forces can dissipate part of the injected energy into heat. However, preliminary analysis suggests that their effect is rather small, amounting to roughly the 2.5% of the injected energy, depending on the operating conditions. For this reason, we model viscous losses using a simple lumped-parameters model.

We assume most of the energy is dissipated on a cylindrical surface, where water backflows. This is equivalent to considering the power lost by the friction for a water column moving inside a fixed medium. The scheme is shown in Fig. 2.11.

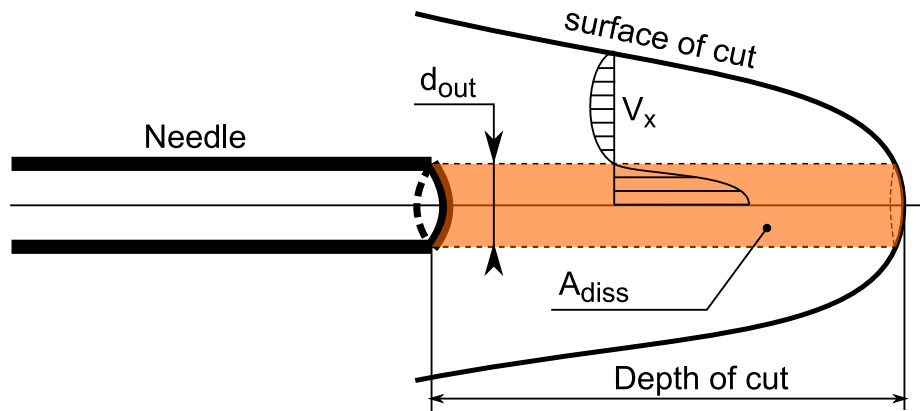


**Figure 2.11:** Effective area where the bulk of viscous dissipation happens.

The power dissipated by the viscous forces  $P_d$  can be written as:

$$P_d = \tau A_d \langle U \rangle \quad (2.35)$$

where  $\tau$  is the viscous stress tensor;  $A_d$  the area along which the velocity reverses and most of the dissipation is thus supposed to take place;  $\langle U \rangle$  the average flow velocity

across the considered section. We take the value of  $\langle U \rangle$  equal to half of the average inlet fluid velocity  $U$ , accounting for the fact that most dissipation likely happens close to the nozzle exit and decreases moving towards the stagnation point. The dissipation area is assumed to be defined by the outer needle diameter and a length equal to the depth of cut:  $A_d = \pi d_{out} h$ . The viscous stress term  $\tau$  is evaluated by estimating the radial derivative using the  $\langle U \rangle$  velocity:

$$\tau = \mu \frac{d\langle U \rangle}{dr} = \mu \frac{U/2}{d_{out}/2} = \mu \frac{U}{d_{out}} \quad (2.36)$$

with  $\mu$  the dynamic viscosity of water, which in standard conditions reads:  $\mu \approx 8.9 \times 10^{-4} [\text{Pa s}]$ . Therefore, the dissipated power reads:

$$P_d = \tau A_d \langle U \rangle = \left( \mu \frac{U}{d_{out}} \right) (\pi d_{out} h) \frac{U}{2} = \frac{\pi}{2} \mu U^2 h \quad (2.37)$$

The small value assumed by this term justifies *a posteriori* its simplified treatment. For the same reason, while this term should appear in (2.29), it will be directly neglected.

**Numerical integration** The value of the depth of cut appearing in (2.29) can be readily integrated numerically. By introducing the value for  $\Phi_E^{\text{inj}}$  derived in (2.31) and

differentiating both sides with respect to time, we obtain:

$$\frac{dh}{dt} = \frac{1}{P_w} \frac{\rho Q^3}{\pi^3 R^6} \frac{A_{\text{inj}} A_{\text{surf}}}{(A_{\text{surf}} + A_{\text{out}})^2} \quad (2.38)$$

where the viscous power dissipation was neglected as discussed in previous paragraph. This is an ordinary differential equation, where  $A_{\text{surf}}$  and  $A_{\text{out}}$  are function of  $h$  and can be readily integrated using standard methods such as Runge-Kutta integrators.

We shall finally note that the model described here can be used for a dual purpose:

- It can allow to reproduce efficiently and accurately the evolution of depth of cut in time, once a proper calibration of  $\eta$  is assigned for a certain tissue and needle size, or
- It can be employed by assigning a given value of  $\eta$  (for example  $\eta = 1/3$  or following optical measurements of the surface of cut at different times) and used to estimate the mechanical properties of the material, which better reconstruct the measured depth of cut.

In any case, once  $\eta$  is known or assigned, the simplicity of the model allows for real-time prediction of the depth of cut with minimal computational efforts.

### 2.2.3 Experimental Setup and Measurement of Depth-Of-Cut (DOC)

The experimental setup used for all experiments is depicted in Fig. 3.8. A linear actuator is used to drive the needle with the velocity of insertion of  $1 \frac{mm}{s}$  approximately  $1cm$  into the soft tissue simulant. A high pressure pump (PR-class Dual Piston, PR100PFT3D, Scientific Systems Inc., State College, PA, USA) provides a constant volumetric flow rate (up to  $100 \frac{mL}{min}$ ) and when run, water-jet needle will cut a channel in front of it in the tissue. After about 30 seconds, the camera takes a photo and the photo will be processed in image processing software to measure the depth of cut of water-jet. The software is developed in Matlab to measure the DOC. The software first loads the image and zooms in the area of interest. Then it asks to select a real world measurement and enter the real value of it for calibration (this is done using the rulers on the lightbox). Then the user will select the area of interest to measure and the software associates the pixel distance to a real-world measurement. Suction canister and a vacuum pump are used to collect the water sprayed back during experiments.

For the water-jet needle, first a piece of Nitinol tube is cut to a length of 52.8 mm. Next, the Nitinol tube is soldered inside the copper tube of 45 mm length with inner diameter of  $ID = 0.94$  mm and outer diameter  $OD = 1.59$  mm. Finally, the copper tubing is attached to the ferruled reducer and then to the water pump via PEEK tubing ( $ID = 1.58$  mm and  $OD = 3.2$  mm). Two needles were manufactured

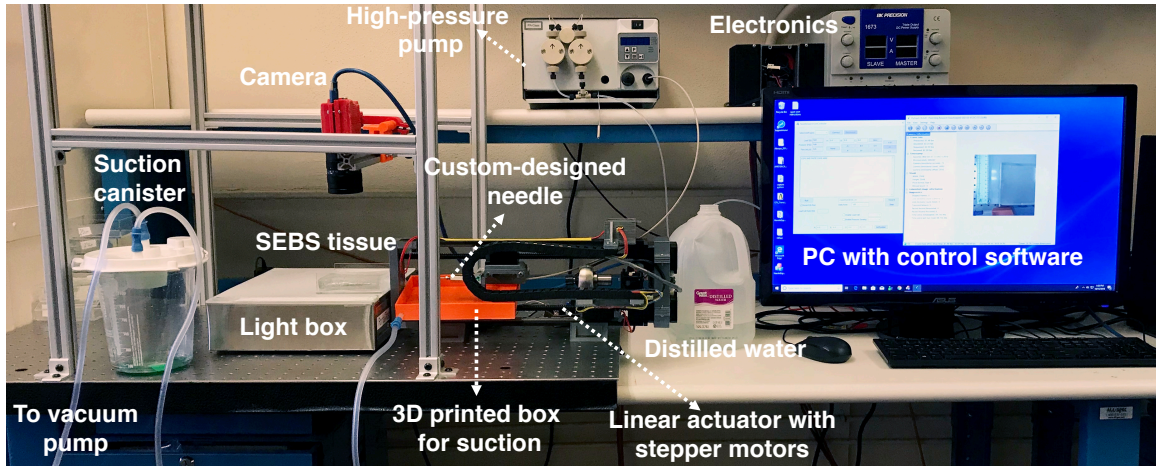


**Figure 2.12:** Experimental setup to measure the depth of cut of the waterjet in soft tissue. A linear actuator is used to drive the needle into the soft tissue. Once the needle is in the tissue, the pump is run with a given volumetric flow rate and after about 30 (s) the camera will take a photo to be processed with a MATLAB program to measure the DOC.

with two different diameters to study the effect of diameter on depth of cut. The first needle has Nitinol tube with  $ID = 0.32$  mm and  $OD = 0.58$  mm and the Nitinol tube of the second needle has  $ID = 0.24$  mm and  $OD = 0.33$  mm. Fig. 2.13 shows the first designed needle (the second needle is the same only with a different diameter Nitinol tube).

To measure the depth of cut of water-jet in SEBS tissue, the pump is turned on with the specific flow rate and the water-jet needle is inserted into soft tissue about 1 cm using the linear actuator and with velocity of insertion of  $1 \frac{mm}{s}$ . This will ensure that the excess water will be sprayed back and will not be trapped in the channel to cause ballooning in the tissue. When the needle is inserted 1 cm into the tissue, the

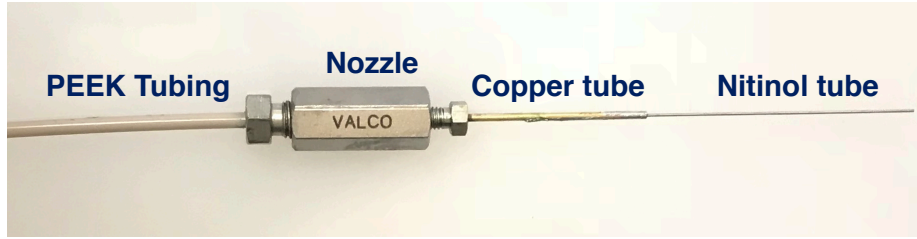


**Figure 2.13:** Custom-designed water-jet needle with a copper tubing ( $ID = 0.94$  mm and  $OD = 1.59$  mm) soldered to a superelastic material Nitinol (first needle:  $ID = 0.32$  mm and  $OD = 0.58$  mm and second needle:  $ID = 0.24$  mm and  $OD = 0.33$  mm). The copper tubing is attached to a ferruled reducer and then standard PEEK tubing.

pump will be turned off and turned on again to ensure maximum depth of cut. After 30 seconds and using the overhead high-resolution camera and the control software, a photo is taken and saved for further processing. For better visibility, edible food dye was added to the water. To study the effects of tissue stiffness, needle diameter and flow rate on cut depth, 6 different tissue stiffnesses (10 %, 15 % and 20 % G1650 and G1652 SEBS), 2 different needle diameters (first needle:  $ID = 0.32$  mm,  $OD = 0.58$  mm and second needle:  $ID = 0.24$  mm,  $OD = 0.33$  mm) and different flow rates up to  $100 \frac{mL}{min}$  are tested. To make sure that the data are statistically significant, 5 experiments are done for each flow rate and the average of them is taken as the cut-depth. The photos are processed using a customized Matlab program that measures the depth of cut in front of the needle from the pixels of the photo based on the calibrated measurement provided by the ruler on the light-box.

#### 2.2.4 *Soft Tissue Simulant Preparation*

Because of the challenges related to using, storing and imaging of real biological tissues, different substitute materials as soft tissue simulants are used by the researchers around the world for experiments [168], [17], [159], [206] and [157]. These tissue-mimicking phantoms give an average approximation of the soft tissue. Common materials used in tissue mimicking simulants are Gelatin, rubber, leather, silicone elastomers, PVA and lard. The mechanical properties of water-based tissue mimicking simulants such as Gelatin and PVA are variable with respect to time, temperature and humidity.

Because of the mentioned difficulties in common tissue mimicking simulants, we have used Poly (styrene-b-ethylene-co-butylene-b-styrene) triblock copolymer (SEBS), Kraton Polymers LLC (G1650 and G1652, Houston, TX, USA) as the main material for our tissue-mimicking simulants [168], [68] and [69]. The solvent used for SEBS is light mineral oil, which makes it a more environmentally stable substitute for the water-based hydrogels. This increases its operational temperature ranges and storage life. Soft tissue simulants that are made of SEBS are optically clear. This feature is desirable from imaging point of view. So, optical cameras can be used instead of pricey imaging devices to see what is going on inside the soft tissue during experiments. A wide range of tissue stiffnesses can be studied by the simply changing the ratio of polymer content to mineral oil. In comparison to silicone rubbers, SEBS has

also low friction due to its oil solvent.

To make the tissue simulants, SEBS material and mineral oil are weighed out to produce mixtures with 10, 15 and 20 vol% SEBS. To calculate the necessary weight, the densities of SEBS and mineral oil are considered to be  $\rho_{SEBS} = 0.91 \frac{g}{cm^3}$  and  $\rho_{oil} = 0.85 \frac{g}{cm^3}$ , respectively. Then the mass of the required material can be calculated using  $m = \rho V$ , in which  $m$ ,  $\rho$  and  $V$  are required mass of the material (either SEBS or mineral oil), density (SEBS or mineral oil) and volume of the material (SEBS or mineral oil). The mixture is then put in the oven at  $150^\circ C$  for about 2 to 8 hours based on the percentage of SEBS and it was mixed from time to time to get a homogeneous solution without any undissolved powder. After this time, the solution is degassed using a vacuum pump with a chamber to put SEBS to eliminate any air bubbles trapped in the solution. The solution is then poured into molds of desired dimensions based on the experiment to be conducted and then let cool down to room temperature and solidify before releasing from the molds.

### *2.2.5 Low Strain Rate Static Compression, High Strain Rate Split-Hopkinson-Pressure-Bar (SHPB) and Fracture Toughness Tests on SEBS Soft Tissue Simulants*

According to our compression tests at low rates of strain as well as tensile, compression and rheological tests conducted in [168] at lower rates of strain, the material properties of SEBS is not dependent on low and medium rates of strain. Thus, in order to find the shear modulus at higher rates of strain, the data from SHPB tests

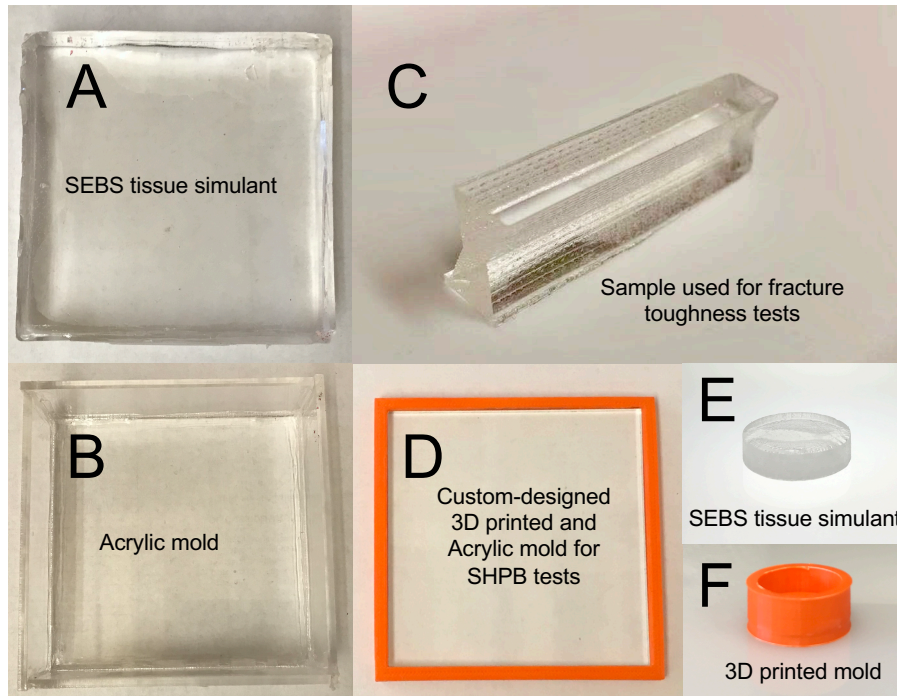


**Figure 2.14:** Custom designed molds and resultant tissues used for cut-depth experiments, static compression tests, SHPB tests and fracture toughness tests. (A and B) SEBS tissue simulant used for DOC experiments and Acrylic mold of  $100 \times 100 \times 30$  mm dimensions. (C) Resultant tissue used for fracture toughness tests. (D) Acrylic-3D printed mold of thickness 2 mm to make tissues for SHPB tests. 10 mm punch is used to cut cylindrical samples for SHPB tests. (E and F) SEBS tissue simulant and custom-designed 3D printed mold of diameter 25 mm and height of 10 mm used for static compression tests. (images not to scale)

are extrapolated to higher rates of strain.

The quasi-static tests are performed with an Instron 600DX machine controlled by the Bluehill 3 software (see Fig.2.15). The samples are compressed between metal plates with constant strain rates of 0.001, 0.01 and 0.1  $s^{-1}$ . The change of gauge length is measured with the build-in function of the Instron machine and the force is measured by a 25lb load cell. The engineering strain can be calculated by:

$$\varepsilon = \frac{\Delta L}{L_0} \quad (2.39)$$

where  $\Delta L$  is the thickness and  $L_0$  is the initial length of the specimen. The engineering stress can be calculated by:

$$\sigma = \frac{F}{A_0} \quad (2.40)$$

where  $F$  is the force applied and  $A_0 = \frac{\pi D_0^2}{4}$ , with  $D_0$  being the initial diameter, is the initial cross sectional area of the sample.

The high strain rate tests were conducted with Split-Hopkinson-Pressure-Bar (SHPB) adapted for soft materials (See Fig. 2.16 for the experimental setup). Fig. 2.17 is a schematic of the SHPB setup, which consists of a striker, an incident bar, a transmitted bar and a buffer. The specimen is sandwiched between the incident bar and transmitted bar. When the striker impacts the free end of incident bar, a

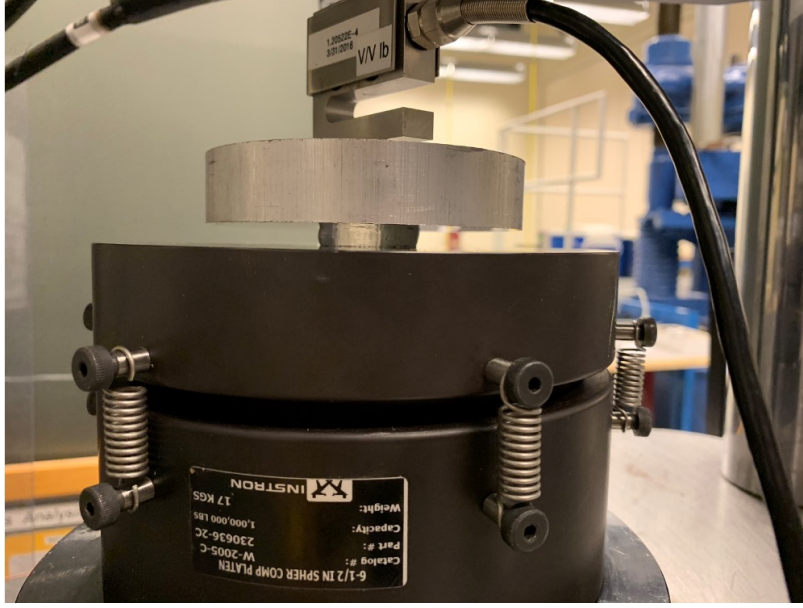


**Figure 2.15:** Instron 600DX machine used to perform quasi-static tests on soft tissue simulants.

compressive stress pulse is generated at the impact surface and propagate along the incident bar. When the incident wave reaches the specimen, part of the wave transmits through the specimen and propagates into the transmitted bar and the other part is reflected to the incident bar. The strains generated by the passing waves are recorded by the strain gauges attached to the bars as  $\varepsilon_I$ ,  $\varepsilon_T$  and  $\varepsilon_R$  for incident, transmitted and reflected waves, respectively. The strain rate of the specimen can be calculated by:

$$\dot{\varepsilon}_s(t) = -\frac{2c_b}{L_0}\varepsilon_R(t) \quad (2.41)$$

where  $c_b = \sqrt{E_b/\rho_b}$  is the longitudinal sound speed of the bar material, with  $E_b$

and  $\rho_b$  being the elastic modulus and density of the bar material, respectively. The engineering strain of the specimen can be calculated by:

$$\varepsilon_s(t) = \int_0^t \dot{\varepsilon}_s(t) dt \quad (2.42)$$

and the engineering stress is calculated by:

$$\sigma_s(t) = \frac{E_b A_b}{A_0} \varepsilon_T(t) \quad (2.43)$$

where  $A_b$  is the cross-sectional area of the bar and  $A_0$  is the original area of the specimen [94], [40].

In the tests, the striker velocity is adjusted to achieve strain rates in the specimen of 3000, 4500 and 6000  $s^{-1}$ .

Fracture toughness is measured with trouser tear test. An initial notch is cut on the centerline of the specimen, then the two arms are fixed with two 3D printed holders that connect to the Instron machine as shown in Fig. 2.18. During the tests, the specimen is pulled vertically at constant speeds of 0.1, 0.5 and 1  $\frac{mm}{s}$ . The load is measured with a 1 kg load cell. The fracture toughness can be calculated by:

$$J = \frac{F_{ave}}{2w} \quad (2.44)$$

Where  $F_{ave}$  is the average force during the crack growth and  $w$  is the width of the



**Figure 2.16:** Split Hopkinson Pressure Bar (SHPB) Experimental setup.

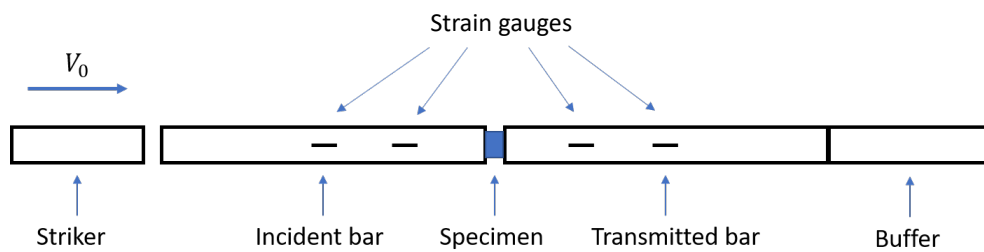


**Figure 2.17:** Schematic of the SHPB test setup. The SHPB consist of a striker and incident bar, a transmitted bar and a buffer. The bars are adjusted for soft tissue experiments and the material used for the bars is PEEK.

specimen [285].



**Figure 2.18:** Schematic of the experimental setup to measure the fracture toughness of the SEBS soft tissue simulants. Trouser tear test is used to measure the fracture toughness of the SEBS soft tissue simulants to mode I crack propagation.

In order to predict the constitutive response of the tissue in static compression and SHPB tests, Ogden model [175] presented in 2.13 is used. This strain energy per undeformed unit volume function describes the constitutive response of an incompressible, isotropic and hyperelastic solid. Research showed that strain hardening factor  $\alpha$  is constant with strain rate and only the shear modulus changes with strain rate [230]. Therefore we adopted  $\alpha$  from fitting stress strain data at strain rate of  $\dot{\epsilon} = 0.01/s$  with Ogden model. When  $\alpha$  is found at this strain rate, it is held constant

for other strain rates so that only shear modulus  $\mu$  varies with strain rate. In order to fit the data with Ogden model and evaluate constants  $\mu$  (shear modulus) and  $\alpha$  (strain hardening factor), the following procedure is adopted.

In short, the nominal stress in the direction of the applied load is predicted using Ogden model and then it is compared to the measured nominal stress during tests. By definition, one can write:

$$\sigma_i = \frac{d\phi}{d\lambda_i} \quad (2.45)$$

Where,  $\sigma_i$  are principal stresses associated with principal stretch ratios  $\lambda_i$  ( $i = 1, 2, 3$ ). With the assumption that the tissue sample is at the state of plane stress during the compression tests,  $\sigma_x = \sigma_y = 0$  holds (suppose a Cartesian coordinate system where the z-axis is aligned with the direction of load applied during the test). In this chapter, soft solid is considered to be incompressible. Therefore, from conservation of volume, one can conclude  $\lambda_x \lambda_y \lambda_z = 1$  for the principal stretch ratios. Therefore  $\lambda_x = \lambda_y = \frac{1}{\sqrt{\lambda_z}}$ . From (2.13), (2.45) and the relationship between principal stretch ratios, it is easy to deduct a relationship for  $\sigma_z$  as follows:

$$\sigma_z = \frac{d\phi}{d\lambda_z} = \frac{2\mu}{\alpha} [\lambda_z^{\alpha-1} - \lambda_z^{-1-\frac{\alpha}{2}}] \quad (2.46)$$

Therefore the optimization problem is finding values for  $\mu$  and  $\alpha$  such that the

error between the measured (from compression tests) and calculated stress (or nominal stress) is minimized. In order to solve this problem, *lsqcurvefit* function from the Optimization Toolbox of MATLAB is used which solves nonlinear data-fitting problems in least-squares sense. Trust-region-reflective method is used as the option for the descent algorithm.

As mentioned before,  $\alpha$  is not strain rate dependent, however, shear modulus  $\mu$  varies with strain rate. In waterjet cutting of soft tissue, the velocity of the waterjet determines the strain rate. To find the strain rate  $\dot{\epsilon}$  relevant to the waterjet penetration into soft tissue, it is assumed that the tissue is strained perpendicular to the penetration direction. Thus the value of strain can be calculated by the following equation:

$$|\epsilon| = \left| \frac{\pi D - 2d}{2d} \right| = \left| \frac{\pi}{2} \left( \frac{d}{D} \right)^{-1} - 1 \right| \quad (2.47)$$

Where,  $D$  and  $d$  are the waterjet diameter and steady state diameter of the crack (that opens to accommodate a waterjet of diameter  $D$ ). Therefore strain rate can be defined as:

$$|\dot{\epsilon}| = \frac{|\epsilon|}{t} = \frac{|\epsilon|}{\frac{D}{v}} = \left| \frac{v}{D} \left[ \frac{\pi}{2} \left( \frac{d}{D} \right)^{-1} - 1 \right] \right| \quad (2.48)$$

In this equation,  $v$  is the velocity of the waterjet. For simplicity we assume that

$d \approx D$ . Therefore strain rate equation can be re-written as:

$$|\dot{\varepsilon}| \approx 0.57 \frac{v}{D} \quad (2.49)$$

Since the pump provides volumetric flow rate  $Q$  ( $\frac{m^3}{s}$ ), it is more convenient to re-write the velocity of the waterjet in terms of  $Q$ . Velocity of the waterjet at the nozzle depends on volumetric flow rate of water, as well as diameter of the nozzle and it can be calculated with the following equation:

$$v = \frac{Q}{A} = \frac{4Q}{\pi D^2} \quad (2.50)$$

In which  $A$  is the area of jet coming out of a nozzle of inner diameter  $D$ .

The crack growth rate related to the waterjet penetration into soft solid (formation and advancement of the crack) can be predicted as follows:

$$\dot{r} = \frac{d}{D} \left( \frac{v}{2} \right) \quad (2.51)$$

In which  $2r = d$ . For simplicity as experiments in literature [229] have already shown, one can take  $d \approx D$ , so that (2.51) can be written as  $\dot{r} \approx 0.5v$ . In which,  $v$  is the average velocity of the waterjet coming out of a nozzle of diameter  $D$  and  $d$  is the steady state crack length after the waterjet is turned off. Thus the crack growth rate is approximated to be half of the waterjet velocity.

**Table 2.1:** Strain rates ( $\dot{\epsilon}$ ) and crack growth rates ( $\dot{r}$ ) associated with the waterjet diameters ( $D$ ) and velocities ( $v$ ) used in this chapter. The values of this table are calculated using (2.49) and (2.51). In order to accurately validate the depth of cut model, the tissue properties should be measured at the strain rates and crack growth rates related to the waterjet penetration into soft tissue. Note: the waterjet diameters are taken to be the inner diameters of the Nitinol tubes.

$D = 0.32mm$				$D = 0.24mm$			
$Q \left(\frac{mL}{min}\right)$	$v\left(\frac{m}{s}\right)$	$\dot{\epsilon}(s^{-1})$	$\dot{r}\left(\frac{m}{s}\right)$	$Q \left(\frac{mL}{min}\right)$	$v\left(\frac{m}{s}\right)$	$\dot{\epsilon}(s^{-1})$	$\dot{r}\left(\frac{m}{s}\right)$
20	4.15	$7.40 \times 10^3$	2.07	20	7.37	$1.75 \times 10^4$	3.69
30	6.22	$1.11 \times 10^4$	3.11	30	11.06	$2.63 \times 10^4$	5.53
40	8.30	$1.48 \times 10^4$	4.15	40	14.74	$3.51 \times 10^4$	7.37
50	10.37	$1.85 \times 10^4$	5.18	50	18.43	$4.38 \times 10^4$	9.21
60	12.44	$2.22 \times 10^4$	6.22	60	22.12	$5.26 \times 10^4$	11.06
70	14.51	$2.59 \times 10^4$	7.26	70	25.80	$6.14 \times 10^4$	12.90
80	16.59	$2.96 \times 10^4$	8.29	80	29.49	$7.01 \times 10^4$	14.74
90	18.66	$3.33 \times 10^4$	9.33	90	33.17	$7.89 \times 10^4$	16.59
100	20.73	$3.7 \times 10^4$	10.37	100	36.86	$8.77 \times 10^4$	18.43

For the two nozzle diameters and different volumetric flow rates used in this chapter, the corresponding strain rates and crack growth rates associated with the waterjet penetration into soft tissue is reported in Table 2.1.

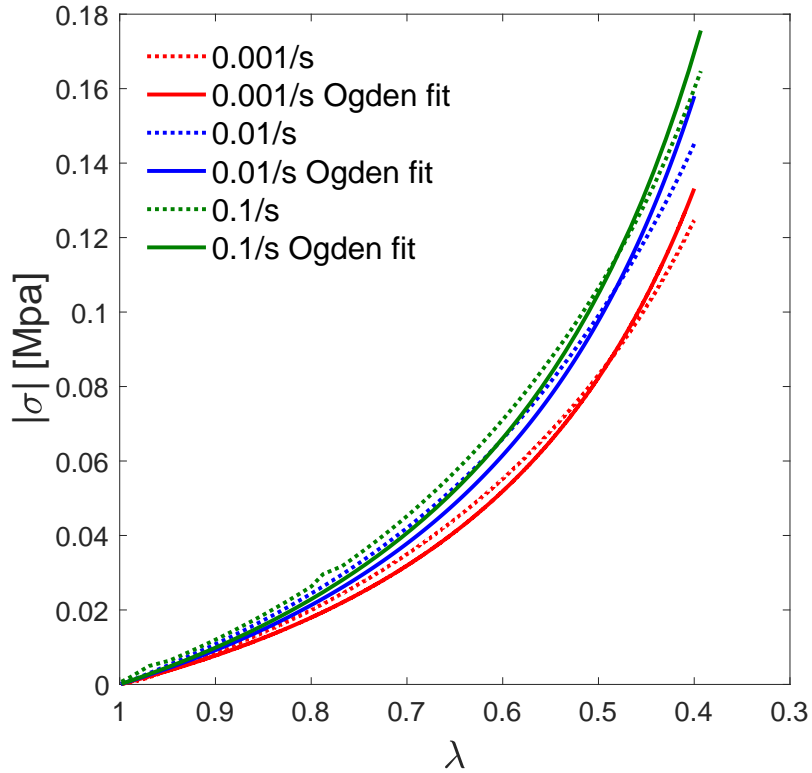
### 2.3 Results

In this section, the proposed model is validated with experimental data. In order to do so, the results of characterization of the SEBS soft tissue simulants using static compression tests, SHPB tests and fracture toughness tests are presented.

### 2.3.1 Mechanical Properties of SEBS Soft Tissue Simulants (constitutive response and fracture toughness)

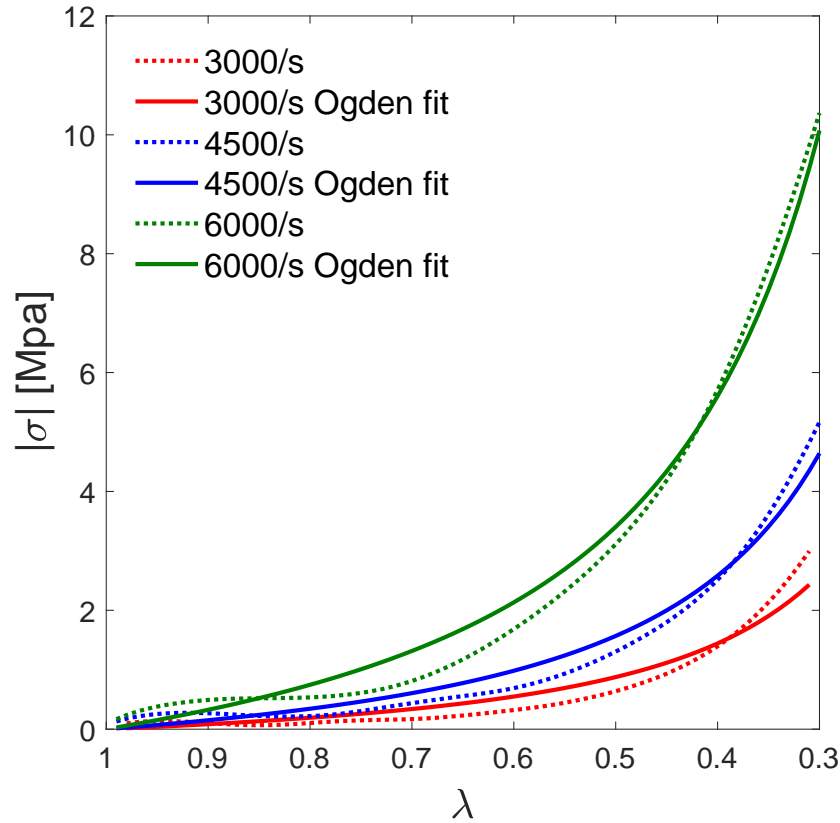
Fig. 2.19 shows an example of the results of the static compressive stress vs. stretch ratio response of SEBS soft tissue simulants at uniaxial nominal strain rates of 0.001, 0.01 and 0.1  $s^{-1}$ . Ogden strain energy density function is calibrated to represent the constitutive response of each soft tissue simulant at the specified strain rate. The results of the static compressive strain vs. stretch ratio of the SEBS soft tissue simulants showed that the constitutive response is not sensitive to low rates of strain and that Ogden model can describe the behavior of these soft tissue simulants with a reasonable agreement.

Fig. 2.20 shows example results of the high strain rate compressive stress vs. stretch ratio response of SEBS soft tissue simulants. From this figure, one can see that the SEBS soft tissue simulants go through strain hardening at high strains and that the response is strain rate dependent. In order to capture the shape of the strain hardening response, uniaxial compressive strains in excess of 0.3 are required (note that the figures show compressive stress vs. stretch ratio responses; however for compressive tests relation  $\lambda = 1 - \varepsilon$  holds between strain ( $\varepsilon$ ) and stretch ratio ( $\lambda$ )). Comparing these results to results of low strain rate (0.001 to 0.1  $s^{-1}$ ) static compression tests on SEBS reveal that the response of these soft tissue simulants is sensitive to increasing rates of strain as shown for real biological tissues [230]. The



**Figure 2.19:** Example static compression test results (stress vs. stretch ratio) on 20% SEBS G1650 soft tissue simulants with the corresponding Ogden fit. Tissue properties are measured at three strain rates of  $0.001s^{-1}$ ,  $0.01s^{-1}$  and  $0.1s^{-1}$ . The same J-shaped stress vs. stretch ratio with the same trend is also observed for other tissue simulants. For each strain rate, two tests are conducted and the averages of these tests are shown in this figure.

strain rate sensitivity of the soft tissue simulants is described by increasing shear modulus with strain rate. This shows that strain rate sensitivity is related to the viscous properties of the soft tissue simulants.



**Figure 2.20:** Example SHPB compression test results on 15% SEBS G1650 soft tissue simulants. Tissue properties are measured at three strain rates of  $3000s^{-1}$ ,  $4500s^{-1}$  and  $6000s^{-1}$ . The same J-shaped stress vs. stretch ratio with the same trend is also observed for other tissue simulants. For each strain rate, three tests are conducted and the averages of three tests are shown in these figures.

Table 2.2 and 2.3 represents the Constants of one-term Ogden strain energy density function, that are shear modulus and strain hardening factor of the soft solid that characterize the constitutive response of the G1650 and G1652 SEBS soft tissue

**Table 2.2:** Mechanical properties of G1650 SEBS tissue simulants obtained from Ogden fit to data.  $\mu$  (kPa),  $\alpha$  and  $R^2$  are shear modulus, strain hardening factor and goodness of the Ogden fit, respectively.

G1650 10%				G1650 15%				G1650 20%			
$\dot{\epsilon}(s^{-1})$	$\mu(kPa)$	$\alpha$	$R^2$	$\dot{\epsilon}(s^{-1})$	$\mu(kPa)$	$\alpha$	$R^2$	$\dot{\epsilon}(s^{-1})$	$\mu(kPa)$	$\alpha$	$R^2$
0.001	7.01	1.25	0.99	0.001	16.65	1.7	1	0.001	22.68	1.08	0.99
0.01	7.28	1.25	0.99	0.01	16.75	1.7	0.99	0.01	26.89	1.08	0.99
0.1	8.82	1.25	0.99	0.1	19.54	1.7	0.99	0.1	28.88	1.08	0.99
3000	193.85	1.25	0.92	3000	249.25	1.7	0.93	3000	278.03	1.08	0.93
4500	511.40	1.25	0.96	4500	554.58	1.7	0.97	4500	605.60	1.08	0.97
6000	761.50	1.25	0.97	6000	967.93	1.7	0.98	6000	993.87	1.08	0.98

**Table 2.3:** Mechanical properties of G1652 SEBS tissue simulants obtained from Ogden fit to data.  $\mu$  (kPa),  $\alpha$  and  $R^2$  are shear modulus, strain hardening factor and goodness of the Ogden fit, respectively.

G1652 10%				G1652 15%				G1652 20%			
$\dot{\epsilon}(s^{-1})$	$\mu(kPa)$	$\alpha$	$R^2$	$\dot{\epsilon}(s^{-1})$	$\mu(kPa)$	$\alpha$	$R^2$	$\dot{\epsilon}(s^{-1})$	$\mu(kPa)$	$\alpha$	$R^2$
0.001	2.77	1.26	0.99	0.001	7.34	1.41	1	0.001	11.60	1.16	0.99
0.01	2.92	1.26	0.99	0.01	8.12	1.41	0.99	0.01	15.96	1.16	0.99
0.1	4.18	1.26	1	0.1	13.76	1.41	0.99	0.1	22.76	1.16	0.99
3000	229.93	1.26	0.94	3000	307.83	1.41	0.93	3000	334.69	1.16	0.95
4500	429.22	1.26	0.96	4500	537.95	1.41	0.97	4500	559.89	1.16	0.97
6000	808.46	1.26	0.98	6000	952.07	1.41	0.98	6000	961.11	1.16	0.98

simulants. The strain rate sensitivity of the constitutive response is described by an increase in shear modulus with increasing strain rate, while strain hardening factor is kept constant.  $\alpha$  is calculated by fitting the Ogden model to experimental data at  $0.001 s^{-1}$  and this  $\alpha$  is used as the strain hardening factor for the rest of strain rates. Thus the optimization problem only had one constant to calculate, which is the shear modulus.

Fig. 2.21 depicts the shear modulus vs. strain rate data with a linear fit. As it is evident from this figure, the shear modulus is a linear function of the strain rate at

**Table 2.4:** Linear fit to shear modulus vs. strain rate data. Shear modulus can be extrapolated to higher strain rates based on these fits according to the intended application.  $\mu$  (MPa),  $\dot{\epsilon}(s^{-1})$  and  $R^2$  are shear modulus, strain rate and goodness of the linear fit, respectively.

tissue type	linear fit	$R^2$
G1650 10%	$\mu = 1.89 \times 10^{-4}\dot{\epsilon} - 0.36$	0.99
G1650 15%	$\mu = 2.4 \times 10^{-4}\dot{\epsilon} - 0.49$	0.99
G1650 20%	$\mu = 2.39 \times 10^{-4}\dot{\epsilon} - 0.45$	1
G1652 10%	$\mu = 1.93 \times 10^{-4}\dot{\epsilon} - 0.38$	0.97
G1652 15%	$\mu = 2.15 \times 10^{-4}\dot{\epsilon} - 0.37$	0.97
G1652 20%	$\mu = 2.09 \times 10^{-4}\dot{\epsilon} - 0.32$	0.97

high rates of strain. Thus it is proposed that shear modulus can be extrapolated to higher rates of strain based on the intended application (please see Table 2.4). For example, for the waterjet fracture-directed steerable needles [22], the shear modulus of the soft tissue at strain rates in the order of  $10^4$  is required. Thus, extrapolating data to higher strain rates will give us the strain rate required for these applications.

Comparison of the results of static compressive tests and SHPB tests reveal that the constitutive response of SEBS soft tissue simulants are sensitive to high rates of strain and does not change much at low strain rates.

Table 2.5 and 2.6 represent the results of fracture toughness tests on SEBS soft tissue simulants. At least two tests are done for each test rate and the average of the results are provided here.

Measuring the fracture toughness data in crack growth rates associated with the waterjet penetration is found to be the out of scope of this research. Therefore in order to have an approximation of the fracture toughness data at higher crack growth

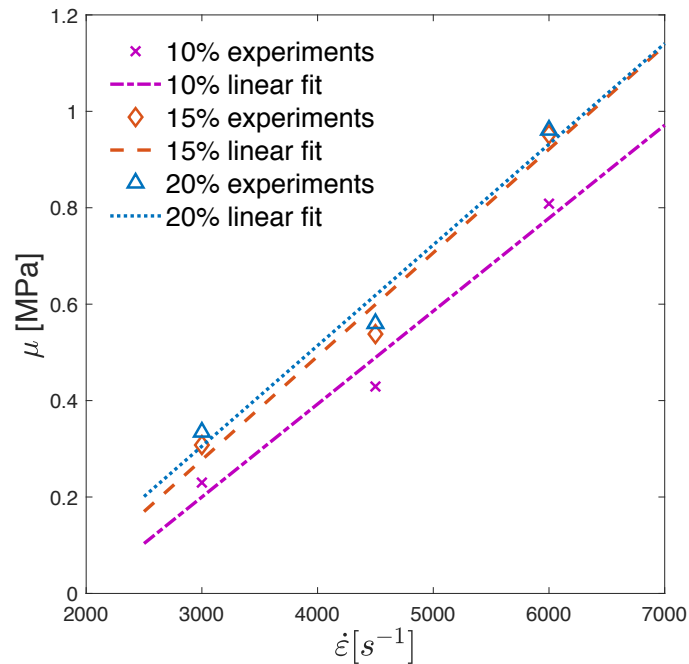
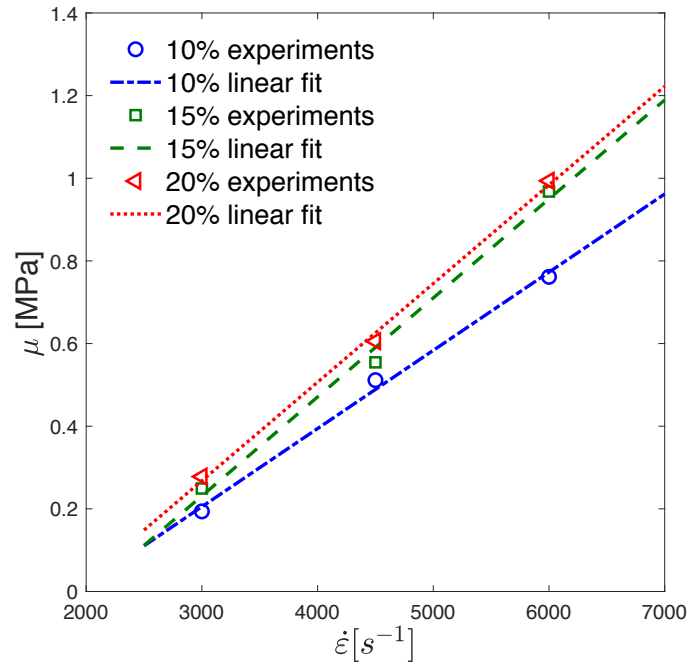


**Figure 2.21:** Shear modulus vs. strain rate and linear fit to data to extrapolate to higher strain rates. (up) G1650 SEBS soft tissue simulants and (down) G1652 SEBS soft tissue simulants. Due to the linear pattern in high strain rates, the shear modulus can be extrapolated to the desired strain rate depending on the application.

**Table 2.5:** Fracture toughness ( $J_{IC}$ ) of G1650 SEBS soft tissue simulants at three test rates of 0.1, 0.5 and 1  $\frac{mm}{s}$ . Crack growth rate ( $\dot{r}$ ) is assumed to be half of the rate at which the test is performed.

G1650 15%			G1650 20%		
Test Velocity ( $\frac{mm}{s}$ )	$\dot{r}$ ( $\frac{mm}{s}$ )	$J_{IC}$ ( $\frac{J}{m^2}$ )	Test Velocity ( $\frac{mm}{s}$ )	$\dot{r}$ ( $\frac{mm}{s}$ )	$J_{IC}$ ( $\frac{J}{m^2}$ )
0.1	0.05	7.44	0.1	0.05	26.14
0.5	0.25	10.81	0.5	0.25	26.55
1	0.5	14.43	1	0.5	49.51

**Table 2.6:** Fracture toughness ( $J_{IC}$ ) of G1652 SEBS soft tissue simulants at three test rates of 0.1, 0.5 and 1  $\frac{mm}{s}$ . Crack growth rate ( $\dot{r}$ ) is assumed to be half of the rate at which the test is performed.

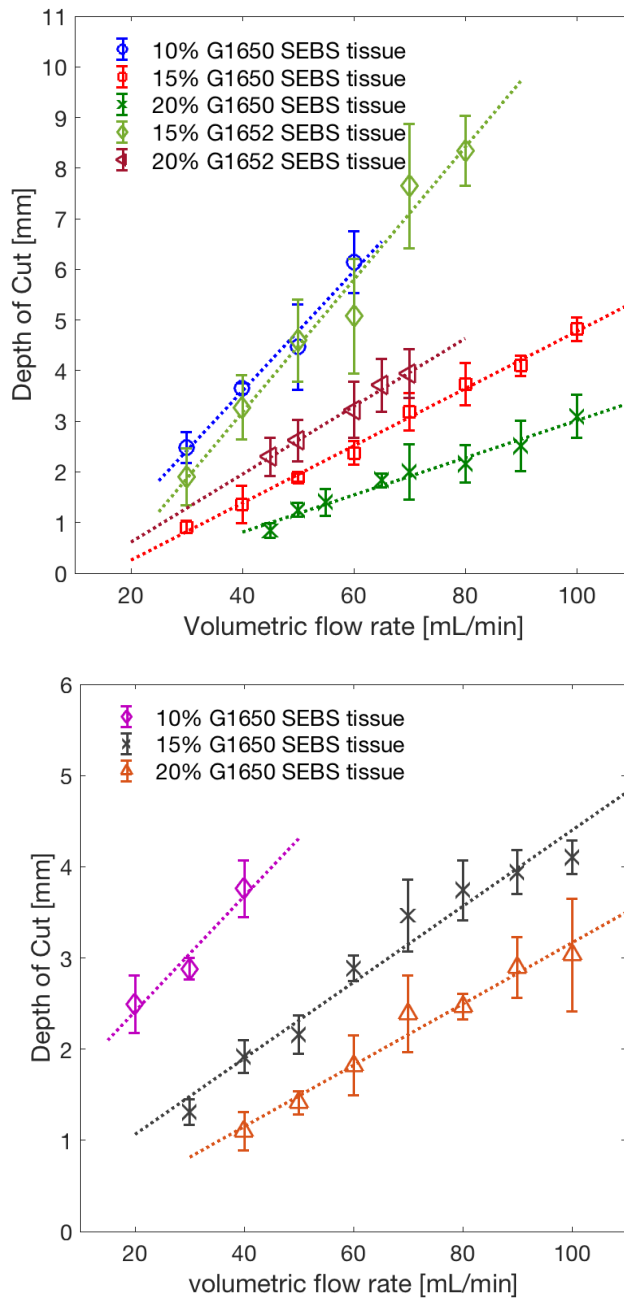
G1652 15%			G1652 20%		
Test Velocity ( $\frac{mm}{s}$ )	$\dot{r}$ ( $\frac{mm}{s}$ )	$J_{IC}$ ( $\frac{J}{m^2}$ )	Test Velocity ( $\frac{mm}{s}$ )	$\dot{r}$ ( $\frac{mm}{s}$ )	$J_{IC}$ ( $\frac{J}{m^2}$ )
0.1	0.05	4.43	0.1	0.05	8.62
0.5	0.25	7.61	0.5	0.25	11.85
1	0.5	9.24	1	0.5	18.01

rates, data at low rates are extrapolated to higher crack growth rates to approximate the fracture toughness of the SEBS soft tissue simulants at high crack growth rates.

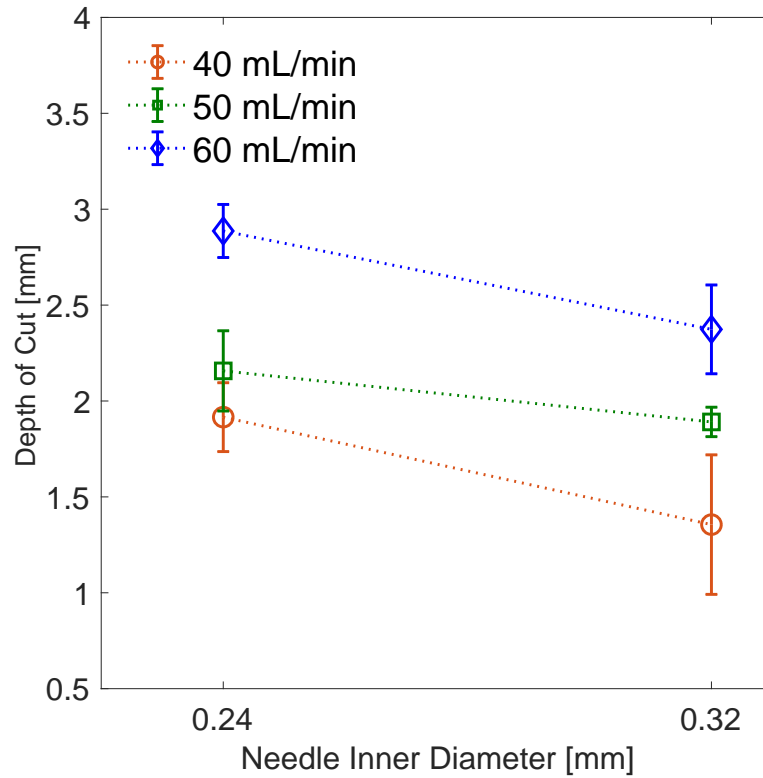
### 2.3.2 Experimental Results: DOC of the waterjet in Soft Tissue is a Function of the waterjet as well as Soft Tissue Properties

Fig. 2.22 shows the average measurements of depth of cut as a function of fluid velocity with different percentages of SEBS tissues and needles with inner diameters of 0.24 mm and 0.32 mm. Fig. 2.23 and Fig. 2.24 show the depth of cut of water-jet as a function of needle diameter and tissue stiffness, respectively.

From these experimental data, one can derive the following conclusions:



**Figure 2.22:** Experimental DOC of the waterjet in SEBS soft tissue simulants vs. volumetric flow rate. (up) DOC vs. Flow Rate for the Needle with 0.32 mm inner diameter (ID) in SEBS Tissue Simulants and (down) DOC vs. Flow Rate for the Needle with 0.24 mm ID in SEBS Tissue Simulants. The data show the average of 5 tests for each volumetric flow rate and error bars show the standard deviation of the data.



**Figure 2.23:** DOC of the waterjet as a Function of Needle Diameter for two needle inner diameters tested in this study ( $D = 0.32mm$  and  $D = 0.24mm$ ). The volumetric flow rate and tissue stiffness are held constants. The result is shown as an example for 15% G1650 SEBS soft tissue simulants. The data are the average of 5 experiments and the error bars are standard deviation of the data.

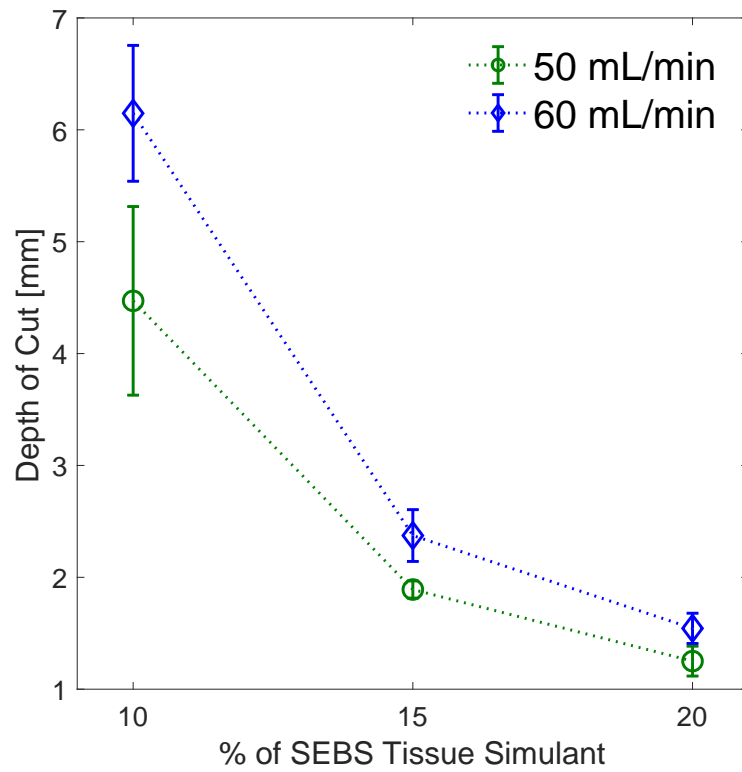


**Figure 2.24:** DOC as a Function of percentage of G1650 SEBS soft tissue simulants. The volumetric flow rate and inner diameter of the needle ( $D = 0.32$  mm) are held constants. The data shown are the average of 5 experiments and the error bars are the standard deviation of the data.

- Depth of cut is almost a linear function of flow rate ( $Q$ ) when the width of the water-jet nozzle is sufficiently small.
- The depth of cut is a function of the waterjet velocity  $v$  (and thus volumetric flow rate  $Q$ ), stiffness of the tissue and diameter of the needle ( $D$ ). It has a direct relationship with flow rate and inverse relationship with tissue stiffness and needle diameter.
- There is a minimum flow rate that the fracture in the tissue actually begins and this flow rate is dependent on the stiffness of the tissue. As the tissue becomes stiffer, larger flow rate is required to cause fracture in the tissue.
- For smaller diameter needle, the minimum flow rate needed to cut is lower. This is likely due to the higher contact stress which leads to the earlier fracture of the tissue. The higher residual jet velocity associated with smaller needle diameter after the initial penetration also leads to larger DOC.
- For higher flow rates, water cuts more of the surrounding tissue, which is undesirable. For fracture-directed steerable needles [23], larger depth of cut is not necessary and it is important that a small amount is cut and then the needle follows the path.
- Observation that the depth of cut of a smaller diameter needle is larger explains the reason of tissue fracture by the water-jet. According to the equation 2.50,

as the diameter of the needle decreases the velocity of water-jet increases and thus the kinetic energy of water-jet increases. The increased kinetic energy is the reason that the depth of cut of water-jet needle with smaller diameter is larger than that of with bigger diameter.

### 2.3.3 Finite Element Model of the Waterjet Soft Tissue Interaction Result

The solution is solved for a time-step size of 30s with a minimum step size of 0.5s. The obtained deformation is visualized using the total deformation tool to evaluate the depth of cut as required. Fig. 2.25 is an example of the output that shows that the deformation is interpreted as 3.5mm from the outlet of the needle.

### 2.3.4 Validation of the Predictive Model with Experimental Results and Tissue Properties

In order to validate the proposed model for DOC of the waterjet in soft tissue, experimental DOC and tissue properties are obtained in the previous sections. It is assumed that the penetration occurs at the minimum of the  $P_w$  vs.  $\frac{d}{D}$  given in (3.4). *fmincon* function in MATLAB is used to solve this optimization problem and find a  $\frac{d}{D}$  that minimizes  $P_w$  given in (3.4) based on the given tissue properties. The calculated values for  $P_w$  for G1652 SEBS soft tissues at different waterjet velocities used in the validation of the model are given in Table 2.7. The values for other tissues can be calculated in a similar fashion and are not included for brevity.

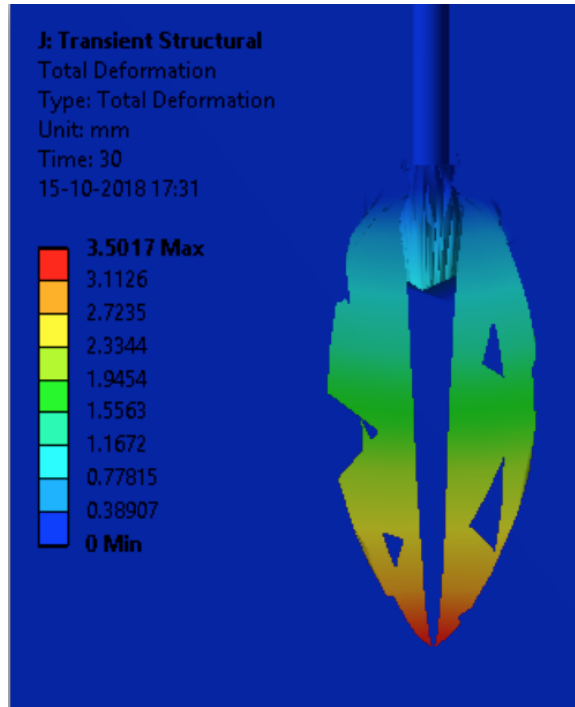


**Figure 2.25:** Example output of the finite element modeling for depth of cut of water-jet. In this example, maximum depth of cut is interpreted from the outlet of the needle.

**Table 2.7:** Calculated values of  $P_w$  from (3.4) at different waterjet velocities for 15% and 20% G1652 SEBS soft tissue simulants for the needle with  $D = 0.32mm$ .

G1652 15%, $D = 0.32mm$		G1652 20%, $D = 0.32mm$	
$v(\frac{m}{s})$	$P_w(MPa)$	$v(\frac{m}{s})$	$P_w(MPa)$
6.22	5.41	9.33	6.89
8.29	7.55	10.37	7.73
10.36	9.68	12.44	9.42
12.44	11.81	13.47	10.27
14.51	13.94	14.51	11.11
16.59	16.08		

In Figure 2.26 we compare the outcome of the model to the experimental values of the depth of cut vs time for the tissue obtained from the G1652-15% and 20%, with the 0.32 mm inner diameter needle and with flow velocities of 10.37 and 14.51  $\frac{m}{s}$ , respectively. The value of  $\eta$  has been chosen *ad hoc* to match the experimental results, equal to the value of 0.75 for the first and 1.8 for the latter. A more detailed discussion on the choice of the ellipsoid aspect ratio  $\eta$  is provided in Section 2.3.4.

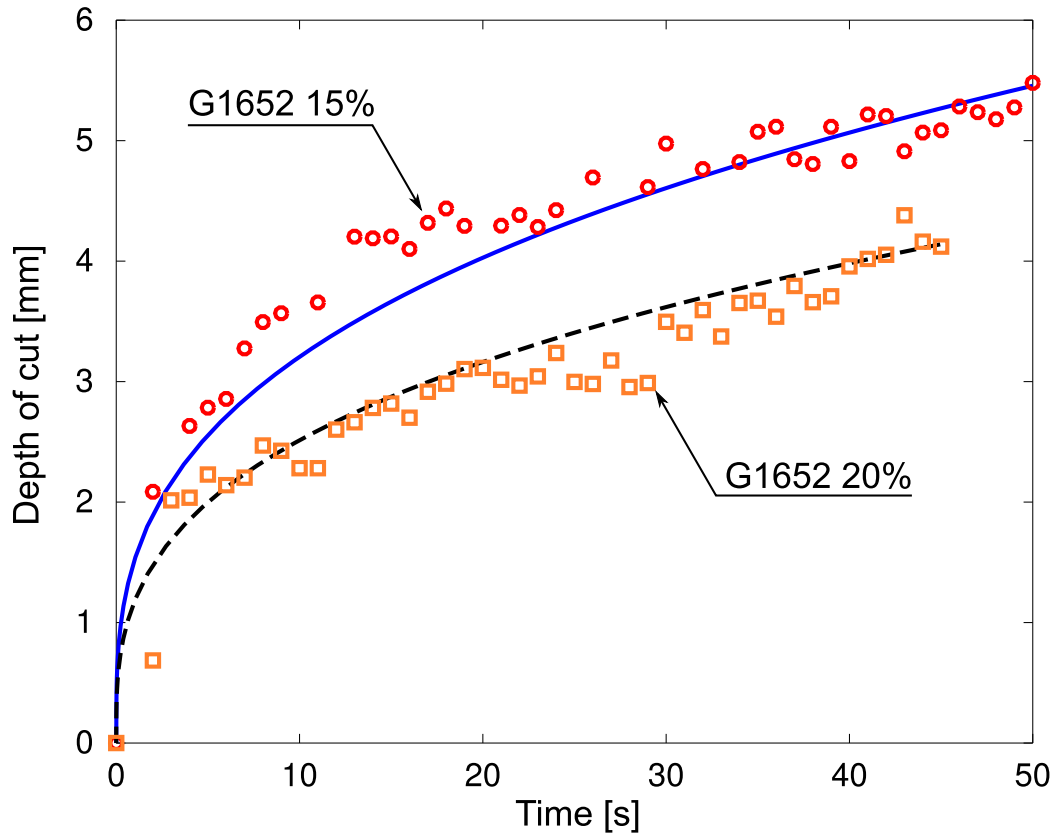


**Figure 2.26:** DOC vs. time for 15% and 20% G1652 tissues; Experimental results (symbols) vs fluid model (lines) with best-fitting  $\eta$ . Needle diameter  $D = 0.32mm$  and waterjet velocities (for G1652 15%  $v = 10.36\frac{m}{s}$  and for G1652 20%  $v = 14.51\frac{m}{s}$ ) are remained constant.

The Integration is performed with a starting condition of  $h = 0$ . To help the first

integration steps, we assume that for values of  $h < d_{out}/2$ , at the very beginning of the cutting process, the surface of cut is not an ellipsoid, but a simple cone with  $d_{out}$  as base. This has no visible impact on the solution, but avoids the initial singularity in the ellipsoid for  $h = 0$ , which may crash the integration.

### *Ellipsoid aspect ratio*

We are interested here to prove the flexibility of the fluid model and check how accurately we are able to reproduce experimental values for the DOC by fitting the value of the free parameter  $\eta$ . As mentioned previously, writing the aspect ratio  $\eta$  of the ellipsoid as a function of the penetration pressure gives us the freedom necessary to fit closely to the experimental data.

Considering the results reported in Table 2.7, we run the fluid model for every velocity- $P_w$  condition, finding the value of  $\eta$  which reproduces best DOC value at 30 seconds. This value is shown in Figure 2.27-Up, for different tissues and needles. A parabolic least-squares fit shows to reproduce fairly well the relation  $\eta - P_w$ . The values of the coefficients are reported in Table 2.8, following the relation (with  $P_w$  in Pascal):

$$\eta = aP_w^2 + bP_w + c \tag{2.52}$$

The fitted expression for  $\eta(P_w)$  was then inserted into the model, to reproduce the value of the DOC at 30 seconds. A good agreement is shown in Figure 2.27. While a

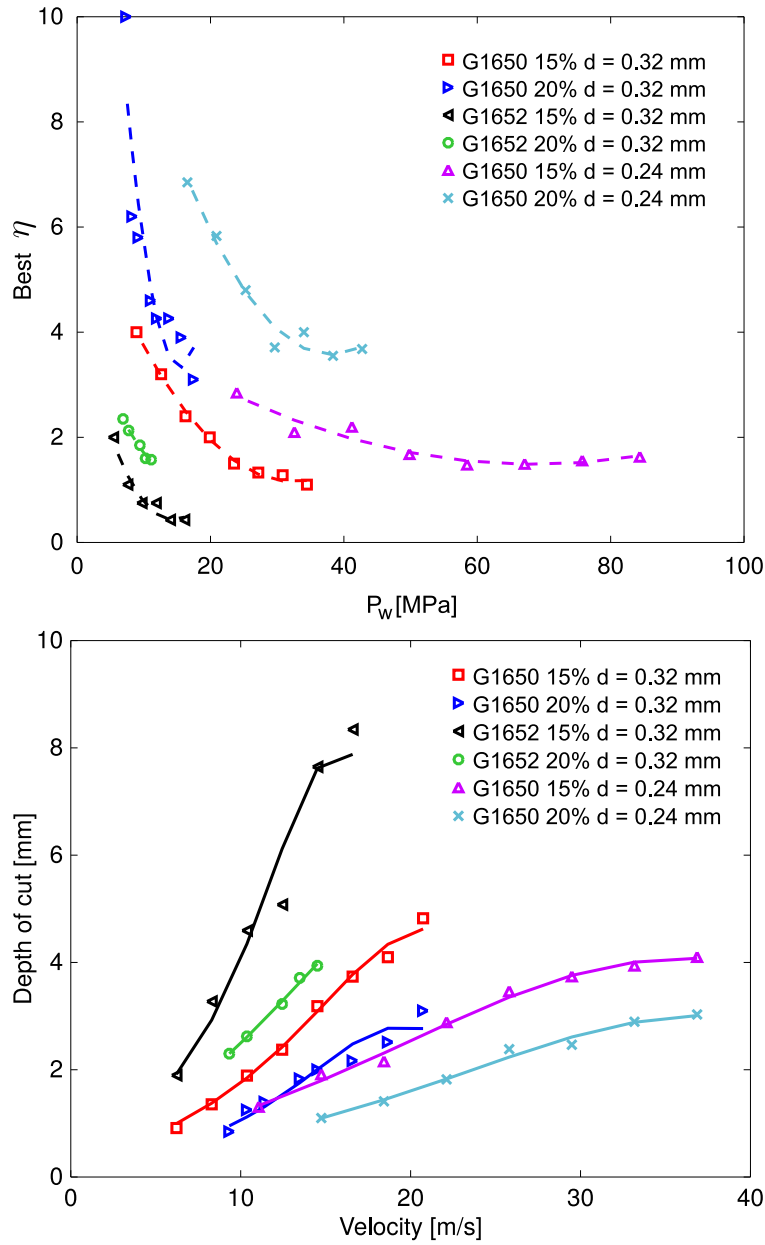


**Figure 2.27:** Up: values of  $\eta$  that match the DOC at 30 seconds (symbols) and parabolic fit (dashed lines). Down: DOC prediction from the fitted  $\eta$  (solid lines) and experimental values (symbols).

**Table 2.8:** Coefficients from parabolic least-squares fitting of  $\eta$  as a function of  $P_w$  (equation 2.52), for different tissues and needles; N1:  $D = 0.32$  mm, N2:  $D = 0.24$  mm.

	G1650 15% N1	G1650 20% N1	G1652 15% N1	G1652 20% N1	G1650 15% N2	G1650 20% N2
a	5.11e-15	8.22e-14	1.81e-14	1.65e-14	6.49e-16	7.12e-15
b	-3.31e-07	-2.52e-06	-5.21e-07	-4.86e-07	-8.90e-08	-5.44e-07
c	6.53e+00	2.27e+01	4.18e+00	4.91e+00	4.54e+00	1.39e+01

physically sound procedure would be desirable for future modeling, the present results fully confirm the flexibility of the present model, which is able to retrieve the DOC to a good approximation, once  $\eta$  is tuned on the proper tissue-needle configuration.

## 2.4 Discussion

In this chapter, first a finite element model is proposed to understand the Waterjet soft tissue interaction. It is a preliminary study and finite element modeling is computationally expensive and each run takes a long time and is not suitable for real-time applications. Based on the complexity of the finite element modeling and the fact that it is highly time-consuming, developing a predictive mechanics-based model for depth of cut as a function of tissue and needle properties seems to be necessary.

Therefore, a mechanics-based model is proposed for DOC of the waterjet in soft tissue that only needs the properties of the tissue and the waterjet to predict the DOC. Unlike other models discussed in the introduction section that their parameters are tuned based on the experiments, the proposed model is independent of the experiments and is only dependent on the mechanical properties of the tissue being

cut and the operating properties of the waterjet.

The model developed for penetration pressure in this chapter is based on the fracture mechanics-based force model developed in [27] and [145]. The process of crack formation in the soft solid show that both fracture toughness and constitutive response are important parameters in determining the penetration pressure. The solid goes through deformation before cracking starts. The advantage of using methods based on fracture mechanics is that models based on this method can predict better especially when failure happens [27] and [13]. This is specifically important for the waterjet cutting of the soft tissue since the tissue goes through failure when fracture happens. Traditionally, researchers utilized fracture mechanics-based models for cutting of industrial materials [18], [138] and [179]. This method has recently been used to model the needle penetration into soft materials [20] and [145]. By equating the work done in advancing the waterjet to the sum of the energy for tissue fracture and stored strain energy in soft tissue, the penetration pressure of the waterjet is modeled in this chapter. The developed penetration pressure model is a function of tissue mechanical characteristics such as fracture toughness and shear modulus as well as the waterjet properties such as diameter. Since soft tissue is viscoelastic, its properties such as shear modulus and fracture toughness are strain rate dependent. Therefore, in order to have a better validation of the model, these properties should be measured in strain rates corresponding to the waterjet cutting of soft tissue.

The work done in this chapter characterized the response of the soft material while going through failure with the waterjet and provided a mechanics-based model to predict the DOC of the waterjet in soft material. This work will be the foundation for research in the waterjet-assisted surgery and waterjet steerable needles. The penetration mechanism of the waterjet in soft tissue can be determined by the failure mechanics of the soft tissue being penetrated. Criteria that can be used for soft tissue failure include: comparison of the local stress induced by the waterjet impact to a critical stress and comparison of the energy density input to the tissue to a critical energy density or work of fracture. The latter is the used method in this chapter.

There are many advantages that are reported in literature for use of the waterjet in medical applications. For instance it is proved that when using high-pressure waterjet for surgical wound debridement for abrasion of necrotic tissue, the treatment is performed in one session [26], [38] lowered the risk of infection [83] and less cost in comparison to the usual surgical debridement [139]. Other advantages are less intraoperative hemorrhage [26] and no thermal damage [26] in comparison to the common approaches. Because of the mentioned advantages and promising results with the waterjet, it was worth that the efficacy of the operations performed by the waterjet was increased by providing closed-form mathematical equations to predict the DOC of the waterjet as we did in this chapter.

From, the DOC vs. time response of the waterjet cutting soft tissue presented

in Fig. 2.26, one can see that the depth of cut of the waterjet increases with higher slope at the beginning of cutting and this slope decreases by increasing time that imply the dependence of the energy of the waterjet on depth of penetration. This result is consistent with other studies such as [26] where the authors mentioned that the highest impact of the waterjet can be achieved at the very beginning when the waterjet hits soft tissue and after that the water starts to flow radially that results in decrease of the impact of the jet. This result is also consistent with the result of the DOC vs. time presented by Morad *et al.* [163] in which the slope of the DOC vs. time decreased after about 30 (s) and also with the results of depth of cut vs. time presented in [164], [225] and [241]. In other words, the effective velocity of the waterjet in soft medium is less than the velocity of the waterjet coming out of the nozzle. This result is consistent with the result presented in [168] that the effective velocity of the projectile in the viscoelastic medium is lower than the velocity measured before the impact happens.

Several studies also confirm our results that the depth of the waterjet penetration depends on the material properties of the penetrated soft tissue and characteristics of the waterjet [224], [162], [163], [26] and [28]. Seok *et al.* [224] argued that the depth of jet penetration into cadaveric cheeks increases as the velocity and pressure of the jet increases. Baxter *et al.* [28] showed that skin parameters such as Young's modulus play an important role in the skin penetration depth. They concluded that depth of

penetration increases as the Young's modulus of skin decreases considering that the jet velocity and nozzle diameter are kept constant. Our finding that DOC is almost linear with increasing the waterjet velocity is in line with the results of Bahls *et al.* [26] that confirm that there is a linear relationship between the waterjet pressure and DOC. This result is also consistent with the results of the depth of penetration of the high velocity projectile into soft tissue presented in [168] and the DOC of microject into gelatin vs. velocity of the microject presented in [241]. The effect of the modulus of elasticity on depth of penetration of the projectile is consistent with our results that as the modulus of elasticity increases, the depth of penetration decreases. Bahls *et al.* [26] also conducted some experiments with different combinations of gelatin and water and found that the higher the ratio of the gelatin to water, the smaller the DOC. This is consistent with our finding that the DOC has an inverse relationship with the stiffness of the SEBS soft tissue simulants.

Equation (3.4) shows that the penetration pressure of the waterjet increases as the diameter of the waterjet decreases, therefore there is an inverse relationship between penetration pressure and diameter of the waterjet. It also shows that penetration pressure has a direct relationship with fracture toughness, shear modulus and strain hardening factor of the soft solid. (2.27) shows that depth of cut of the waterjet in soft solid has a direct relationship with the waterjet velocity and an inverse relationship with penetration pressure. These are in agreement with the experimental results

depicted in [162] stating that DOC has a direct relationship with volumetric flow rate of the waterjet (thus the velocity of the waterjet) and an inverse relationship with diameter of the waterjet and stiffness of the soft solid. Although decreasing diameter increases the penetration pressure, however, according to (2.50) as diameter of the waterjet decreases the velocity of the waterjet increases and this increase is more than the increase in penetration pressure. Thus, the overall impact of decreasing diameter is the increase of DOC.

The shape of the stress-strain curve presented in Fig. 2.19 and 2.20 is consistent with the findings of the Shergold *et al.* [230] who measured the uniaxial stress vs. strain response of pig skin and silicone rubber at low and high strain rates (in the range of 0.004 to 4000  $s^{-1}$ ). It is also demonstrated that the common Mooney-Rivlin model is not suitable to describe the constitutive behavior of rubber-like solids and Ogden strain energy density function is a better option to describe the constitutive response of the soft solids with strong strain hardening capacity. According to their results, the constitutive response of pig skin is sensitive over the range of 0.004 to 4000  $s^{-1}$ , but the silicone rubber stiffens and strengthens at strain rates over 40  $s^{-1}$ . A similar trend is observed between the results of Shergold *et al.* [230] and our results. The stress level is increased by increasing the strain rate, but the shape of the constitutive response is unchanged. Similarly to this research, our results also consider that the strain hardening factor  $\alpha$  does not change with strain rate, however

increasing strain rates increase the shear modulus  $\mu$  of the soft solid. The stiffening of the soft tissue while applying the waterjet is also observed in the researches like [280]. In this research, authors observed that the colon wall was thickened by more than three times after application of the waterjet device.

The strain rate dependency of human tissues are explored in different studies. For instance Comley *et al.* [45] argued that adipose tissue has a Young's modulus of approximately  $E = 1\text{kPa}$  at low rates of strain on the order of  $0.001\text{ s}^{-1}$  and goes through a considerable stiffening with Young's modulus of  $E = 3\text{ MPa}$  at high rates of strain on the order of  $1000\text{ s}^{-1}$ . This is in line with our results presented in Fig. 2.20.

According to several studies [27] and [230], the stress-strain curve of the soft tissue response is J-shaped and that it is also strain rate dependent. The Ogden fit [175] is proved to be a good model to describe the constitutive response of materials that go through strain hardening like soft tissues. The Ogden model is good for incompressible, isotropic and hyperelastic materials. The selected model for soft tissue assumed nonlinear elastic behavior whereas viscoelastic effects can also be present. The fact that the mechanical properties of the SEBS soft tissue simulants are strain rate sensitive implies the presence of viscoelastic effects over high rates of strain. SEBS is chosen as the main material for soft tissue simulants for model verification because of its viscoelastic nature that could mimic the response of real

biological tissues while going through failure [168].

This research is done in line with developing motion models for a new class of steerable needles called Fracture-directed waterjet steerable needles [22], [284] and [23], in which the direction of tissue fracture is controlled by the waterjet and then the flexible needle follows the path. Fig. 2.28 depicts the idea of the fracture-directed waterjet steerable needles. Predicting the DOC of the waterjet in soft tissue is the first step towards developing control-friendly motion models for this class of steerable needles.

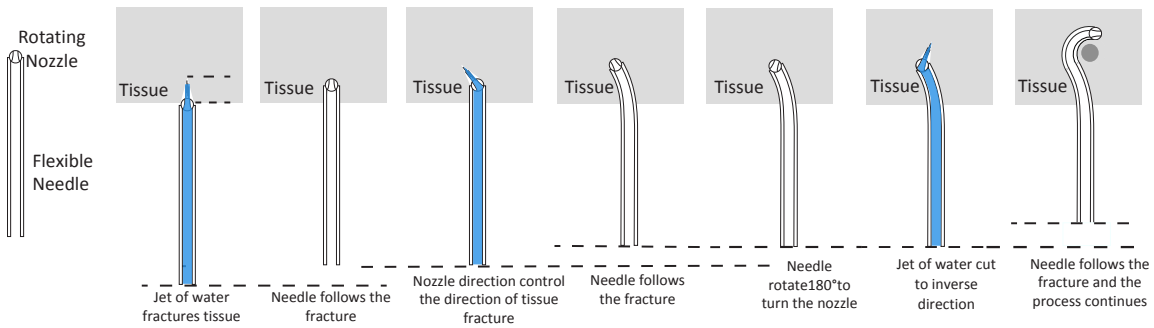


**Figure 2.28:** New class of needle steering techniques namely fracture-directed waterjet needle steering. In this method, the direction of the tissue fracture is controlled by the controllable waterjet nozzle and then the flexible needle made of Nitinol follows the cut path by the waterjet. This process continues until the needle reaches to the desired location in the soft tissue to perform the designated task either surgical or drug delivery. The direction of the needle can be controlled by rotating the nozzle inside the tissue and cutting a new path in another direction by the waterjet.

## 2.5 Conclusion and Future Work

In this chapter, a mechanics-based model is proposed to predict the depth of cut of the waterjet in soft tissue. The model can predict the DOC of the waterjet in soft tissue based on the tissue properties (constitutive response and fracture toughness) and waterjet properties (velocity and diameter). The model is verified with experiments in SEBS soft tissue simulants. This research sets foundation to predict the depth-of-cut of the waterjet in soft tissue for the waterjet-assisted medical applications including waterjet surgery and waterjet steerable needles. Future work include verifying the model with experiments in real biological tissues.

### Appendix A: Procedure for Derivation of (2.16) and (3.5)

In this appendix, the procedure for derivation of the (2.16) and (3.5) is explained.

Equation (2.15) can be re-written using the volume change elements as:

$$\frac{\partial E_e}{\partial l_1} = \int_{r_1}^{\infty} \phi 2\pi s_1 ds_1 = \int_{r_2}^{\infty} \phi 2\pi s_2 ds_2 \quad (2.53)$$

Starting with  $\int_{r_2}^{\infty} \phi 2\pi s_2 ds_2$  and incorporating equation (2.14) one can write:

$$\int_{r_2}^{\infty} \phi 2\pi s_2 ds_2 = \int_{r_2}^{\infty} 2\pi s_2 \frac{2\mu}{\alpha^2} \left[ \left( \frac{s_1}{s_2} \right)^\alpha + \left( \frac{s_2}{s_1} \right)^\alpha - 2 \right] ds_2 \quad (2.54)$$

In order to make this integral neater, we can define:  $\gamma = \left( \frac{s_2}{r_2} \right)^2$  and thus  $d\gamma =$

$\frac{1}{r_2^2}(2s_2 ds_2)$ . Therefore:

$$\begin{aligned} \frac{\partial E_e}{\partial l_1} &= \int_{r_2}^{\infty} \pi r_2^2 \frac{2\mu}{\alpha^2} \left[ \left( \frac{s_1}{s_2} \right)^\alpha + \left( \frac{s_2}{s_1} \right)^\alpha - 2 \right] \frac{2s_2}{r_2^2} ds_2 = \\ &= \int_1^{\infty} \pi r_2^2 \frac{2\mu}{\alpha^2} \left[ \left( \frac{s_1}{s_2} \right)^\alpha + \left( \frac{s_2}{s_1} \right)^\alpha - 2 \right] d\gamma = \\ &= \frac{2\pi\mu r_2^2}{\alpha^2} \int_1^{\infty} \left[ \left( \frac{s_1}{s_2} \right)^\alpha + \left( \frac{s_2}{s_1} \right)^\alpha - 2 \right] d\gamma \end{aligned} \quad (2.55)$$

$\left(\frac{s_1}{s_2}\right)^\alpha$  and  $\left(\frac{s_2}{s_1}\right)^\alpha$  can be re-written as:

$$\left( \frac{s_1}{s_2} \right)^\alpha = \frac{s_1^\alpha}{(s_2^2)^{\frac{\alpha}{2}}} = \frac{s_1^\alpha}{(\gamma r_2^2)^{\frac{\alpha}{2}}} = \frac{s_1^\alpha}{\gamma^{\frac{\alpha}{2}} r_2^\alpha} \quad (2.56)$$

Using the same procedure,  $\left(\frac{s_2}{s_1}\right)^\alpha = \frac{\gamma^{\frac{\alpha}{2}} r_2^\alpha}{s_1^\alpha}$ .

From volume conservation we already know that  $s_1^2 - r_1^2 = s_2^2 - r_2^2$ . Dividing the sides of this equation by  $r_2^2$ , we can write:

$$\frac{s_1^2 - r_1^2 + r_2^2}{r_2^2} = \left( \frac{s_2}{r_2} \right)^2 = \gamma \quad (2.57)$$

And thus:

$$\left( \frac{s_1}{r_2} \right)^2 = \left( \frac{r_1}{r_2} \right)^2 + \gamma - 1 = \left( \frac{d}{D} \right)^2 + \gamma - 1 \quad (2.58)$$

From here, the following equation can be deduced:

$$\begin{aligned}
& \left(\frac{s_1}{s_2}\right)^\alpha + \left(\frac{s_2}{s_1}\right)^\alpha - 2 = \\
& \left(\frac{\gamma + \left(\frac{d}{D}\right)^2 - 1}{\gamma}\right)^{\frac{\alpha}{2}} + \left(\frac{\gamma}{\gamma + \left(\frac{d}{D}\right)^2 - 1}\right)^{\frac{\alpha}{2}} - 2 \qquad (2.59) \\
& \qquad \qquad \qquad := f\left(\frac{d}{D}, \gamma\right)
\end{aligned}$$

And thus (2.16) and (3.5) can be derived.

## CHAPTER THREE

### FRACTURE-DIRECTED WATERJET NEEDLE STEERING

In this chapter, a new class of the steerable needles that we name Fracture-directed Waterjet Steerable Needles is presented. In this type of the steerable needles, the direction of the tissue fracture is controlled by the high velocity waterjet coming out of a sub-millimeter angled nozzle and then flexible needle follows. This process continues until the needle is steered to the target point (Refer to Fig. 2.28).

First off, the insertion forces of the waterjet needle are measured and compared to that of the needle with no waterjet. It is shown that waterjet reduces the tip forces reflected back to the base of the needle (the cutting is done by the waterjet thus cutting forces are eliminated). Then, the effect of the varying cut-depth is presented to control the curvature of the waterjet steerable needles. A kinematic model is proposed for the waterjet steerable needles and a path planning scheme based on Genetic Algorithm is explored. Finally, the effect of the duty cycling of the waterjet on curvature of the needle is explored and shown that duty cycling of the waterjet can control the curvature from zero (no Waterjet ON) to maximum curvature (Waterjet ON for all steps).

### 3.1 Waterjet Needle Insertion Forces

Water-jet technology has been used extensively for decades industrially for many applications including mining, plastic, metal, stone, wood and produce cutting. The use of the water-jet in medical applications has been developed more recently and it is used for different applications such as soft tissue resection, bone cutting, wound debridement and surgery. We have proposed a new application of the water-jet technology in the medical field is proposed, namely water-jet steerable needles.

In order to show the efficacy of the proposed waterjet steerable needles in comparison to traditional steerable needles, we have measured the insertion forces of the waterjet needle and compared it to the traditional needle. To accomplish this, we have designed and built a needle insertion system which has a custom-designed water-jet nozzle attached to a Nitinol needle as its "needle" (refer to Fig. 2.13). Insertions with and without water-jet into 10%, 15% and 20% Poly (styrene-b-ethylene-co-butylene-b-styrene) triblock copolymer (SEBS) tissue-mimicking simulants are performed and the associated force data is measured using a force sensor at the base of the needle. The results of the force *vs.* displacement show that the water-jet reduces the insertion force associated with traditional needles by eliminating cutting forces.

### 3.1.1 Introduction

The use of the high-pressure water in industry dates back over a century. In the mid-1880s, water-jets were first used in hydraulic mining to flush out coal from the working surface of a mine [233]. The development of high-pressure pumps makes the cutting of the harder materials a possibility. To date, water-jet cutting has been used for cutting plastic, high-strength alloys, metals, stone, wood and food products.

Cutting occurs when energy is introduced into the material to overcome its chemical bindings in the structure of the material. For instance, thermal cutting methods use the energy of chemical reactions, electricity, or light to create high temperatures to melt or ablate the material at the point of the cutting. Mechanical methods use the kinetic energy of the moving tool or create ductile materials by using pressure [233]. Water-jet cutting can be considered as a mechanical method in which energy of the high speed jet is applied to the work-piece. The water acts as a cooling agent also and leads to a very high quality cut—low kerf with low surface roughness.

Water-jet cutting has more recently been applied in medical applications. In surgery, Waterjet is used to dissect organs. Water-jet techniques have also been used to resect liver [181], where a saline jet of 965.27 kPa was created using a standard agricultural electrically-driven spray system. Waterjets have also been used for dissections of the liver [192, 246, 24, 25]. The efficiency of the water jet for hepatic resections are examined in [256]. They came into conclusion that water jet dissection

reduces large blood volume loss. The water jet system called the Helix Hydro-jet was introduced for dissection of the Glioma and normal brain tissue. It has a hand-piece with nozzle of  $100\ \mu\text{m}$  in diameter [194]. In [171], the authors performed water-jet dissection of 50 porcine brains. They used different nozzle types ( $80 - 150\ \mu\text{m}$ ) and different levels of the water-jet pressure ( $96.57 - 3,999\ \text{kPa}$ ). They concluded that water-jet can dissect the brain parenchyma precisely with vessel preservation and that there is a linear relationship between water-jet pressure and depth of dissection. Water-jet is also used in renal surgery [95, 191]. They successfully removed the tumor of the lower pole of the left kidney and cleaned the renal parenchyma. Other medical applications of the water-jet technology include wound debridement [85], orthopedic surgery [219] and bone cutting [92].

Water-jet cutting has several advantages compared to conventional cutting methods. One advantage of the water-jet cutting is that because the water acts as a coolant, there are not temperature-related damages to the surrounding tissues, as seen with thermal ablation, grinding, or sawing. Second, water-jet cutting is precise, fast and removes minimal material, where the water washes out the debris and leaves low-roughness surfaces. Using water-jet during surgery also decreases bleeding [256]. These advantages made water-jet to be appealing for medical applications.

Percutaneous therapies constitute a large fraction of the medical procedures, including blood and tissue sampling, injecting drugs and anesthetics, implanting ra-

radioactive seeds, *etc.* In brachytherapy cancer treatment and tissue biopsy, needles are used to reach precise locations in the body. High insertion forces can complicate reaching the intended target with high accuracy. Research shows that lower insertion force can reduce needle bending and tissue deflection [253]. Therefore, researchers have actively researched ways to reduce the insertion forces. Methods proposed in the literature to reduce the insertion forces include changing needle geometry [195, 264], using smaller needles [49] and inserting the needle with different insertion speeds and/or vibration [91].

Figure 3.1 depicts forces acting on the needle in traditional needle insertion and in the proposed water-jet method.  $F_{elastic}$  is the elastic force that fractures the tissue and forms a crack. This force exists before puncturing the tissue and acts on the needle from point at which the needle comes in contact with the undeformed surface of the tissue to when tissue is maximally deformed, just prior to puncture. Our experimental results do not show this force because we started to collect data after puncture.  $F_{cutting}$  is the cutting force and  $F_{friction}$  is the friction force acting along the shaft of the needle. The red line depicts the forces acting on the needle in the case of the traditional needles and the blue diagram is the force acting on the needle in the case of the water-jet needle, which is only friction. Our experimental results showed that the frictional force with the waterjet is even lower than a traditional needle, likely due to lubrication provided by the water during insertion.

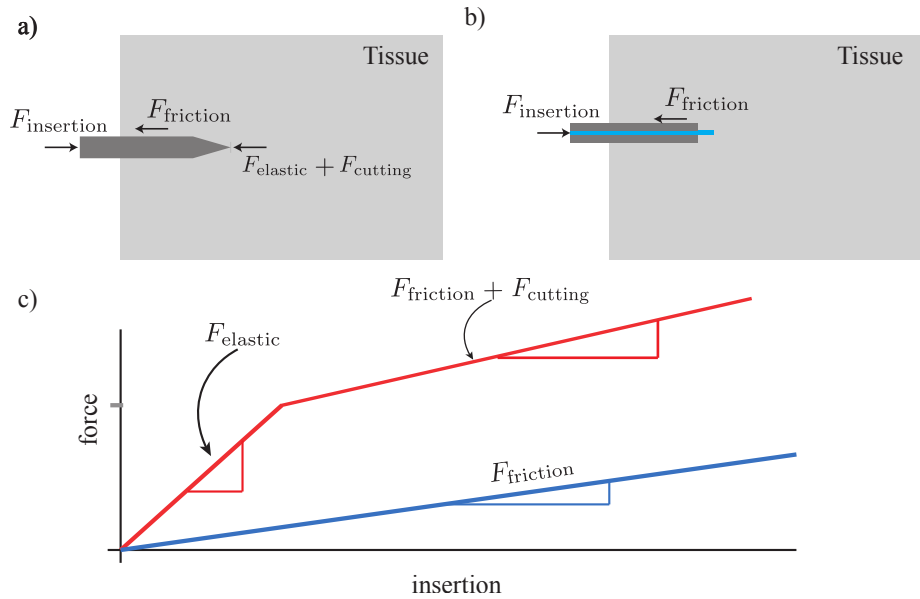


**Figure 3.1:** Schematic of the forces acting on the needle passing through the tissue for: (a) the no water-jet case with a traditional needle and (b) using water-jet cutting.  $F_{elastic}$  is the elastic force that fractures the tissue and forms a crack (this force only exists before puncture and from the surface of the undeformed tissue to the maximally deformed one),  $F_{cutting}$  is the cutting force and  $F_{friction}$  is the friction force acting along the shaft of the needle (these two forces act on the needle from puncture to maximally inserting the needle and before exiting the tissue). (c) In the case of the waterjet (blue schematic), the tip forces are eliminated and only friction along the shaft of the needle exists (it is even expected to be lower than friction due to lubrication provided by water). For traditional needles (red schematic), insertion force can be defined as  $F_{insertion} = F_{elastic} + F_{cutting} + F_{friction}$  and in the case of the needle with water-jet, relationship  $F_{insertion} = F_{friction}$  holds. Experimental results also verified these relationships (Our results do not show  $F_{elastic}$  because we started after puncture.)

In this section, it is shown that using water-jet, the tip forces are eliminated and only the friction force remains. To explain it more precisely, the insertion force experienced by a physician (or robot) at the base of the needle has been reduced. This force experienced at the base of the needle is the combination of the elastic,

friction and cutting force at the tip. The proposed method reduces the forces that build up at the tip and are transmitted along the shaft of the needle back to the user at the base of the needle. Much of the force that is experienced by the user at the base of the needle is due to the elastic buildup at the tip that is necessary to cause sufficient pressure at the very tip of the needle to start fracture. With the water jet, this elastic buildup is not necessary because the  $300\mu\text{m}$  waterjet is only putting pressure on the tiny amount of the tissue it is trying to fracture. The second reason is looking forward to needles that are curving in tissue that experience buckling and using waterjet, this effect will be eliminated.

The experimental force data along with codes to run the data are uploaded to Mendeley Data in order for other researchers to use them for their own research purposes is available at <http://dx.doi.org/10.17632/dzhg3d69mb.1>.

### *3.1.2 Materials and Methods*

#### *Tissue Preparation*

Common materials for tissue-mimicking simulants are gelatin, rubbers, leather, silicon elastomers, soap, lard and clay [14]. These materials can provide an average representation of the soft tissue. In the case of the gelatin, the ratio of the solid content to water can be changed to alter the mechanical properties. Most common combinations of the gelatin are 10% and 20% solid with the remaining water. The

amount of the solid determines the softness of the gel. Water-based nature of the gelatin causes time, temperature and humidity-dependent issues. Properties can be changed due to excessive heating during production or storage. The advantage of using SEBS as the tissue simulant material is containing non-aqueous solvents, which makes it more environmentally stable substitute for water-based hydrogels (such as gelatin) in terms of increased operational temperature ranges and lifetime. Additionally, SEBS tissues are optically clear, their Young's modulus can easily be altered by changing the polymer content, they have low Young's modulus but high fracture toughness, which is similar to bio-tissues and lower friction than many other materials with low Young's modulus like silicone rubbers.

Poly (styrene-*b*-ethylene-*co*-butylene-*b*-styrene) triblock copolymer (SEBS), Kraton Polymers LLC (G1652, Houston, TX, USA) is used as the main ingredient of the tissue-mimicking phantoms. Light mineral oil is used as the solvent. SEBS material and mineral oil are weighed out to produce mixtures containing 10, 15 and 20 vol% SEBS. The mixture was then put into the oven at 120° C for 6 hours (for mixtures containing a lower amount of the SEBS this time is lower) and was mixed occasionally to produce a homogeneous solution without any visible undissolved powder. It was degassed afterwards using a vacuum chamber to eliminate any air bubble trapped in the solution. The solution is then poured into rectangular molds of dimensions 100 × 100 × 50 mm, then let to cool down in room temperature before removing

from the molds. The Young's modulus of these tissue simulants can be found from (3.1), which we derived from the log-log plot of the Young's modulus versus polymer fraction figure presented in [168].

$$\text{Young's modulus} = c(\text{Polymer fraction})^m \quad (3.1)$$

Where  $c = 4.6018 \times 10^6$  and  $m = 2.2234$ . Therefore, the Young's modulus of 10%, 15% and 20% SEBS are 27, 68 and 128 kPa, respectively, which are relevant to stiffnesses of the real biological tissues [274]. In particular, Young's moduli of 10%, 15% and 20% are similar to uterus and cervix tissues, the Young's moduli of which are in the range of 30 – 90 kPa [112], prostate in the range of 62 – 69 kPa [123], thrombus in the range of 8 – 38 kPa [278], breast with modulus of 29 kPa [89] and muscle in the range of 7 – 57 kPa [185, 131].

### *Experimental Setup*

The experimental setup used for all experiments is shown in Fig. 3.2. A linear actuator is used to drive the needle into the tissue simulant with the velocity of insertions 1, 5 and 10  $\frac{mm}{s}$ . These insertion velocities are known to be relevant to insertions in real medical applications [4]. These velocities can be adjusted in the designed graphical user interface (GUI) by setting the depth of insertion and time. This multi-threaded application developed using Microsoft Visual C++ is not only

capable of communicating with and controlling the needle experiment but also reading the force sensor and control the pump system through serial communications. This user interface records data to a .CSV file and is capable of the feedback control.

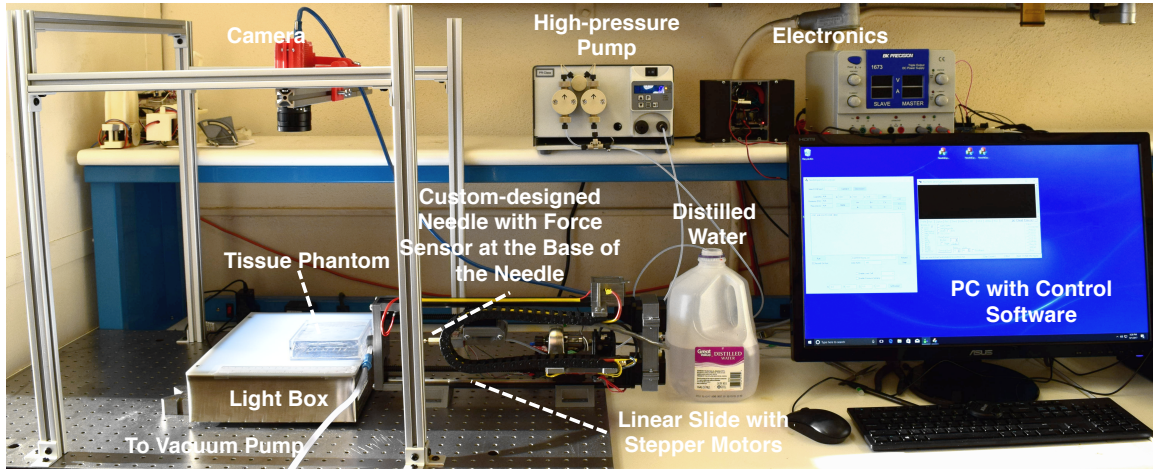


**Figure 3.2:** Experimental setup of the water-jet system to measure the forces at the base of the needle. A linear actuator drives the needle into tissue with a given velocity of insertion adjusted in the customized software. A high-pressure pump with changeable flow rate is used to create high-pressure water for experiments with water-jet. A load cell at the base of the needle measures insertion forces and the data are gathered in the control software.

To allow high-fidelity control of the volumetric flow rate and the ability to measure pressure at the pump, an off-the-shelf pump traditionally used for high-performance liquid chromatography (HPLC) named PR-class Dual Piston is used (PR100PFT3D, Scientific Systems Inc., State College, PA, USA). This system can provide pressures up to 27.58 MPa and flow rates up to  $100 \frac{mL}{min}$  at the maximum pressure. Pure distilled water is used in this Pure Waterjet cutting system and a suction system attached near

the base of the needle avoids the water from splashing while inserting and cutting. The suction tube is attached to a suction canister and a vacuum pump.

One major concern here may be the volume of the water that needs to be cleared from the cutting area. It seems that if the water is not cleared fast enough, the remaining pressure near the needle tip causes potential problems with the surrounding tissue and diminish the effectiveness of the water cutting. However, the reality is that in waterjet insertions while the water hits and cuts the tissue the majority of it splashes back and is suctioned through the suction tube and gathered in suction canister that is attached to a vacuum pump and this does not let water to be trapped in the cutting path.

For the water-jet needle, first, a piece of 1.59 mm copper tubing is cut to about 45 mm of length. Then, a piece of the Nitinol is cut and sanded to remove the oxide layer, so that the solder would adhere. Next, the Nitinol wire was soldered inside the 1.59 mm copper tubing. Finally, the copper tubing is attached to the ferruled reducer and then to the water pump via standard tubing. The Nitinol tube acts as a needle with inner diameter of 0.32 mm and outer diameter of 0.58 mm. Superelastic properties of the Nitinol makes it a good candidate to be used as a material for steerable needles [60]. Fig. 3.3 represents the custom-designed needle used in needle insertions with and without water-jet.

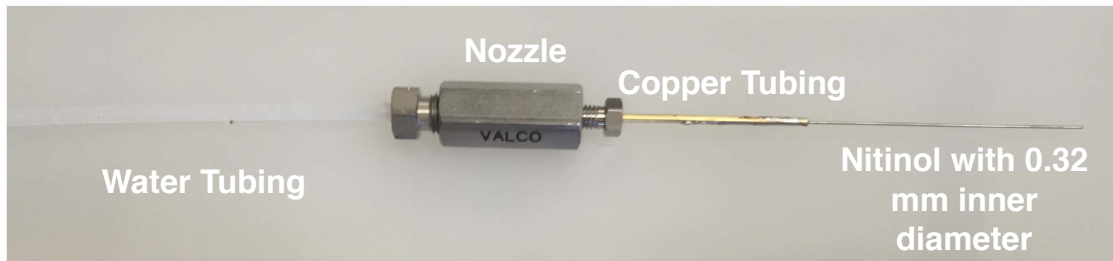


**Figure 3.3:** Custom-designed needle for insertions. The needle consists of a copper tubing soldered to a superelastic material named Nitinol as its "needle". The copper tubing is attached to a ferruled reducer and then standard tubing.

*Force measurement using insertions with and without water-jet*

Three distinct experiments are conducted to compare the insertion forces of the traditional needles and waterjet needles. These include: (a) insertion of a needle without the waterjet to give a baseline for a traditional needle's insertion forces, (b) reinserting a needle without waterjet in the existing channel from (a) to determine the frictional component of (a) and (c) a new insertion with the waterjet enabled (in a fresh channel) to compare the insertion forces against both the traditional needle insertion and the friction-only component of a traditional insertion.

These three different tests are done on 10%, 15% and 20% SEBS tissues, with each test sample of size  $100 \times 100 \times 50$  mm. First, the needle is inserted into the tissue with velocities of insertion of 1, 5 and  $10 \frac{mm}{s}$  using the linear slide and without running the water-jet. These insertion velocities are relevant to insertion velocities

during clinical percutaneous needle insertion procedures [4]. The needle is inserted 50 mm through the tissue and force data is recorded at the rate of 5 data per second using the customized GUI. The data is recorded until the needle reaches the maximum insertion depth. The needle is then retracted and reinserted into the same channel using the same velocity of insertion and without water running and the force data for the second insertion in the same channel is also recorded. This second insertion in the same channel is intended to disambiguate the frictional forces from the cutting forces at the tip for the non-waterjet scenario. To insure that the needle will follow the same path, the setup was remained unchanged between the two sets of the experiments. Then, another insertion is conducted when the pump is turned on with volumetric flow rates of 10, 20 and 30  $\frac{mL}{min}$  for 10%, 15% and 20% SEBS tissues, respectively. In these trials, the needle is inserted with the same velocities of insertion along with the jet of water that cuts a small distance in front of the needle to let the needle pass the tissue. 10 experiments are done for each stage, with total of 90 experiments for each tissue so  $3$  (tissues)  $\times$   $3$  (velocities of insertion)  $\times$   $3$  (number of different tests)  $\times$   $10$  (number of the experiments in each stage) = 270 experiments are done and the average of 10 experiments and the standard deviation of the data are calculated for each stage, so that the results are statistically meaningful.

### 3.1.3 Results and Discussion

In this part, results of the tests with insertions with and without water-jet are provided. Results of the force measurements with and without water-jet are presented and demonstrate how using the water-jet for cutting can decrease the insertion force by eliminating tip forces.

#### *Waterjet Needles Result in a Reduction in Insertion Force of Over 50 %*

The average force from 3 different experiments on each tissue is plotted against the needle displacement. Fig. 3.4 shows the force *vs.* displacement for insertions with no water, no water reinsertion through the same channel and with water-jet for 10%, 15% and 20% SEBS tissues with 3 different velocities of insertion. The bars on the figure represent one standard deviation above and one standard deviation below the data. The following results can be observed from these figures:

- Comparing the forces in the case of the insertions with no waterjet and insertions with water-jet, it is apparent that water-jet reduces the insertion force by eliminating the tip forces and only friction force exists. The total insertion force by water jet is even lower and the authors propose that this is due to the lubrication effect of the water in the channel.
- The needle passing through the tissue (in traditional needle insertion methods) experiences different phases of cutting. In phase 1, the tissue deflects and the

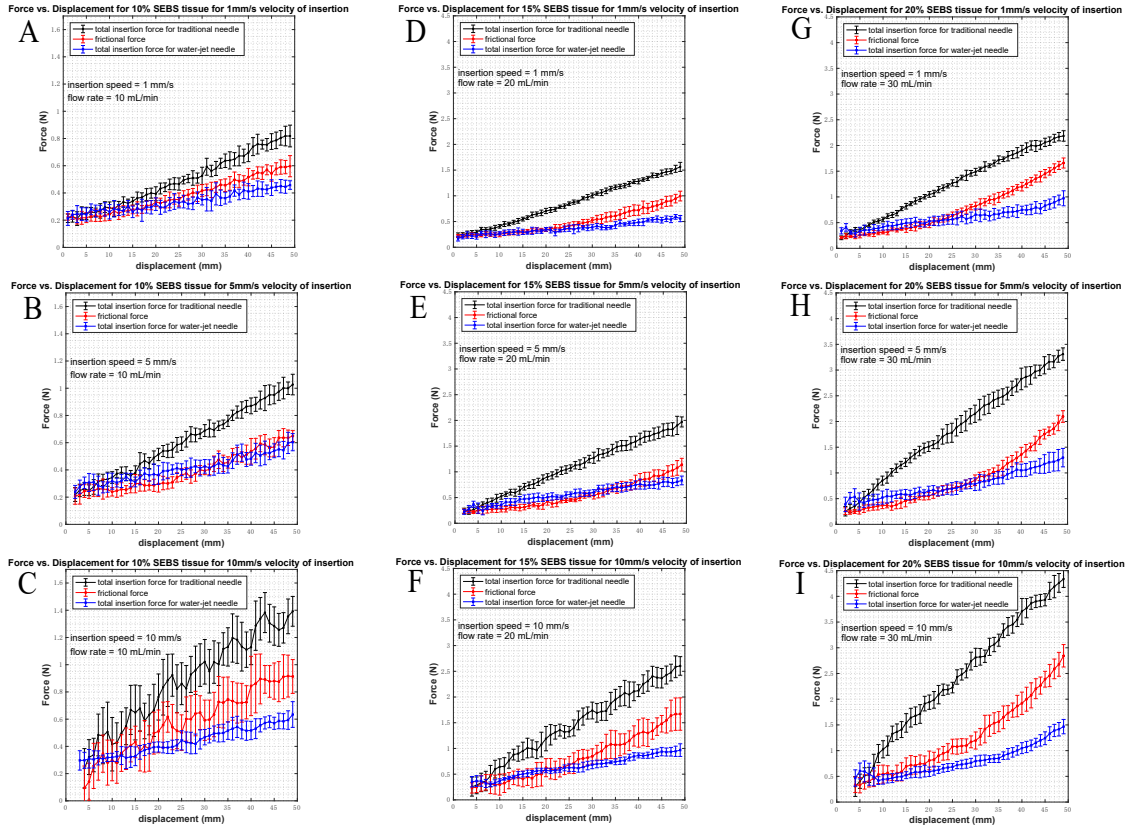


**Figure 3.4:** Force *vs.* displacement measurement for ten trials each in: (A - C) 10% SEBS tissue simulant with 3 different velocities of insertion (D - F) 15% SEBS tissue simulant with 3 different velocities of insertion and (G - I) 20% SEBS tissue simulant with 3 different velocities of insertion. The black plot (the one with circles) shows the total insertion force in the case of the traditional needle insertion after puncture. This force is equal to  $F_{cutting} + F_{friction}$ . The red plot (the one with asterisks) depicts only friction force ( $F_{friction}$ ) (acquired with inserting the needle into the previously cut channel). The last plot (blue one with squares) represents the total insertion force with water-jet needle. As is evident from all figures, total insertion force using water-jet is even lower than the friction force since water-jet eliminates tip forces and lubricates the channel while insertion.

force gradually rises due to elastic forces. This occurs from the surface of the undeformed tissue to when the tissue is maximally deformed (before puncture).

This is represented in Fig. 3.1 as  $F_{elastic}$ . The results shown in Fig. 3.4 do not include this stage since we started to gather the data after puncture. In phase 2, the tissue is cut and initial crack is formed (puncture). Needle geometry widens the crack and the needle passes through with friction acting between the needle and the tissue. This is from when puncture occurs till the needle is inserted maximally into the tissue. This is expressed as  $F_{cutting} + F_{friction}$  in the top panel of the Fig. 3.1 - c. This stage is obvious in our results with traditional needle insertion. There is also phase 3 that the needle exits the tissue and only the frictional force is present. This stage is not relevant to our data since we went 50 mm into the tissue and did not pass all the way through it. These 3 stages are consistent with previous research on traditional needle insertions [99].

- The 20% SEBS tissue has a higher frictional force. This is in agreement with standard sliding friction models where the friction is a function of a coefficient and the normal force (or normal pressure across the surface area). In the case of the 20%, even though the needle is the same size and displacing the same amount of the tissue, because it has a higher elastic modulus then the normal force/pressure will be higher for the same volume of the tissue displaced by the needle.
- The insertion forces in both the traditional needle insertions and in water-jet

needle insertions show a rate-dependent behavior. The forces are higher for higher velocities of insertions. This observation is consistent with previous research in needle insertions [47]. Webster et al. [267] also observed that the force data are variable at different velocities and some of the plots are smoother than others. Mechanical resonance of the linear stage-stepper motor combination is the reason for this. At velocities near to its resonances, it will vibrate more that this causes the vibrations in the force readings.

- The frictional force is dependent on the depth of insertion and increases as the insertion depth increases. It also depends on the stiffness of the tissue. These observations are in line with previous research on traditional needle insertions [207]. This will lead to overall increased insertion force in stiffer tissues.
- The purpose of using needles in the first place is to reduce the tear in the tissue while accessing a target. It may seem that waterjet increases tear surrounding the needle, but considering that the diameter of the water jet is smaller than the needle and the time that the water jet is in contact with the tissue is so small, only a small cutting in front of the needle will be achieved and there is not enough time for the water-jet to tear the surrounding tissue. This can be achieved by calculating an optimum velocity of insertion that ensures small cutting and avoids the tear and damage to the tissue.

### 3.1.4 *Conclusions*

In this section, a linear actuator was utilized to drive the needle into tissue with known insertion velocity. Force data were collected in the experiments with and without water-jet. The results with the force data showed that this method can be used as a promising method to decrease the insertion force, which is very important in medical applications.

## 3.2 **Fracture-directed Waterjet Steerable Needles**

Steerable needles are a type of medical devices that can steer around obstacles to reach to a target location and thus can improve the accuracy of the medical procedures. Radius-of-Curvature (ROC) is of paramount importance while designing steerable needles and achieving smaller radius and being able to control it is very important in evaluating the efficacy of the steerable needles.

In this section, we present a new class of the steerable needles, which we call waterjet-directed steerable needles, where the underlying principle is to first control the direction of the tissue fracture with waterjet, after which the needle will follow during subsequent insertion. Here, the direction of the tissue fracture is controlled by an angled waterjet nozzle and control of the water velocity and then the flexible Nitinol needle follows.

It is shown that changing the velocity of the waterjet and thus depth of cut,

radius of curvature can be controlled. It is found out that fixed waterjet tip angle and varying water exit velocity to control the depth of cut is one way of controlling the curvature of the waterjet needle. The other way to control the radius of curvature is by duty cycling of the waterjet and it is shown that it can be controlled from about 0 (when waterjet is OFF at all steps) to maximum curvature (when waterjet is ON for all steps). It is also found that the curvature is a linear function of the duty cycling and that the smallest ROC of the waterjet steerable needle (when waterjet is ON at all steps) is improved in comparison to the smallest ROC of the traditional steerable needles in the same tissue medium.

A discrete-step kinematic model is used to model the motion of the waterjet steerable needle. This model consist of two parts: (1) the mechanics-based model that predicts the cut-depth of the waterjet in soft tissue based on soft tissue properties, waterjet diameter and water exit velocity which explained in detail in Chapter 2 and (2) a discrete-step kinematic bicycle model of the steerable needle travel. Path planning is accomplished through a genetic algorithm and the efficacy of the waterjet steerable needle is tested for different paths.

### *3.2.1 Introduction*

Steerable needles technology is relatively a new endeavor by several research groups around the world that is developed with the promise of improving the efficacy of the medical procedures and biopsies [93, 167, 238, 2, 284]. Steerable needles

came into existence to correct unwanted needle bending and tissue motion in addition to steering around obstacles to avoid anatomical constraints and reach to targets in the anatomy with greater accuracy [53, 46].

There are several steering techniques developed in the literature that an extensive review is provided in [250] and in Chapter 1 of this dissertation. These techniques include base manipulation [57], bevel tip with and without curve [267, 9], precurved stylet [178] and active cannula [220, 268] among others. Among these methods, Flexure-Based Steerable Needles achieved the best radius-of-curvature to date [235]. These methods mostly rely on creating an asymmetric force at the tip of the needle to change the direction of the tissue fracture as the needle is inserted [6, 235]. Furthermore, these methods rely on the complex elastic interaction between the tip of the needle and the surrounding tissue to achieve an angled fracture direction. A complete discussion on the current limitations of the steerable needles is provided in Chapter 1. Therefore, introducing new methods for needle steering that promise smaller ROC is necessary.

In traditional steerable needles, rotational duty cycling (periods of continual spinning) is used to adjust the curvature [235, 75, 155, 148]. However, rotational duty-cycle methods must account for the inherent torsional windup associated with twisting a long, super-elastic needle about the insertion axis[203, 239]. Therefore, introducing new and more efficient ways to adjust the radius of curvature in steerable needles

seems to be lacking too.

In this section, a new class of the steerable needles namely fracture-directed waterjet steerable needles is used to achieve a significantly greater control over the direction of the tissue fracture. In waterjet needle steering, first the direction of the tissue is controlled by the waterjet with sub-millimeter diameter and then the flexible tube made of Nitinol follows the fractured path. The depth of the tissue fracture is controlled by adjusting the volumetric flow rate of the pump since our previous research [22] showed that considering all other variables constant, the depth-of-cut of the waterjet in soft tissue is a linear function of the waterjet velocity exiting the needle.

Furthermore, the angle of the tissue fracture is achieved using a fixed-angle nozzle that shoots the waterjet in an angle relative to the needle tip. Although this is one possible way of implementing fracture-directed steerable needles, this promises the potential of the radius of curvature and steerability that are unattainable with current tip steerable needles.

First off, the effect of the waterjet velocity and thus length of the cut channel is explored on achievable radius of curvature of the needle in two tissue stiffnesses. However, a better approach to control the curvature would be by duty cycling of the waterjet. Thus, as a better approach, duty cycling of the waterjet is used to control the curvature of the waterjet needle. By duty cycling of the waterjet, the

curvature can be controlled from approximately 0 (insertion without waterjet) to maximum curvature (insertion with waterjet ON for all steps) and it is shown that the curvature of the needle is a linear function of the duty cycling. The minimum radius of curvature achieved with this method in 10% by Weight Knox Gelatin soft tissue simulants is compared to the best ROCs obtained in the steerable needles literature in the same medium. It is shown that waterjet steerable needles can reach a smaller ROC in comparison to the conventional steerable needles in the same soft tissue simulants. A kinematic model relating the depth of cut and the base rotation to the motion of the needle is also presented.

Fig. 3.5 shows the underlying principle of the waterjet steerable needles, in which the direction of the tissue fracture is controlled by angled waterjet and then the flexible Nitinol tube follows. This process continues until the waterjet needle reaches to a target location avoiding obstacles. This photo shows the general form of the waterjet steerable needles in which the the nozzle angle can be controlled, however in the experiments in this section, a fixed angle nozzle shown in Fig. 3.7 is used.

### *3.2.2 Materials and Methods*

In this section, the materials and methodology used for soft tissue preparation, the experimental setup used for experiments, the curvature measurements of the waterjet steerable needle, the modeling of the needle motions and the path planning algorithm are described.

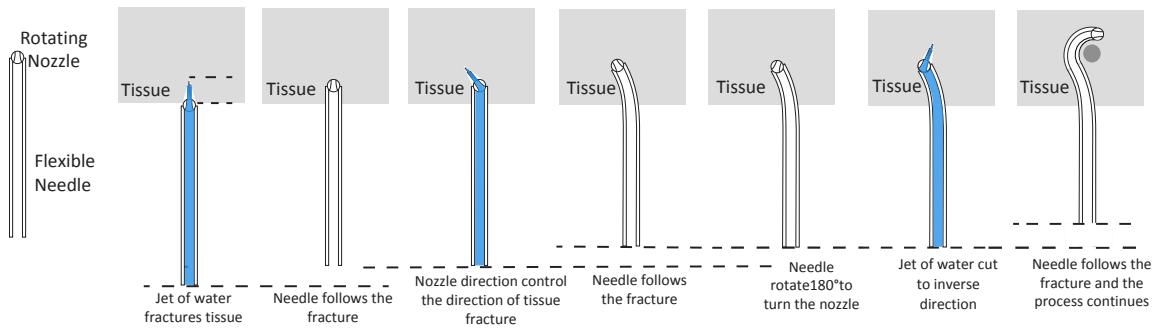


**Figure 3.5:** Underlying Principle of the Waterjet Steerable Needles. First, the direction of the tissue fracture is controlled by angled sub-millimeter waterjet and then the flexible Nitinol tube follows the cut path. This process continuous till the needle avoids the obstacles and reaches to a target location. Direction of the curvature can be changed by rotating the base of the needle. Note that this figure shows the general principle of the waterjet needle steering and the experiments in this chapter are conducted using a fixed-angle nozzle shown in Fig. 3.7.

### *Tissue Simulants Preparation*

Because of the difficulties associated with using real biological tissues (some of these are mentioned in previous section), we have used Poly (styrene-b-ethylene-co-butylene-b-styrene) triblock copolymer (SEBS) by Kraton Polymers LLC (G1650, Houston, TX, USA) as the main material for our tissue-mimicking simulants. The solvent used for SEBS is light mineral oil, which makes it a more environmentally stable substitute for water-based hydrogels [22, 284]. To make the tissue simulants, SEBS material and mineral oil are weighed out to produce mixtures with 10 and 15 vol% SEBS. The mixture is then put in the oven at  $150^{\circ}C$  for about 2 to 6 hours based on the percentage of the SEBS and it was mixed from time to time to get a homogeneous solution without any undissolved powder. After this time, the

solution is degassed in a vacuum chamber to eliminate any air bubbles trapped in the solution. The solution is then poured into molds of  $100 \times 100 \times 30$  mm and then let cool down to room temperature and solidify before releasing from the molds. One of the most attractive features of the SEBS is the ability to accurately control the elastic properties of the materials through control of the volume fractions of the SEBS powder and mineral oil solvent [168].

10% by Weight Knox Gelatin (Kraft Foods Global Inc., IL) soft tissue simulants are also used as the main tissue substitutes in experiments to compare the waterjet needle with traditional steerable needles since 10% by weight Knox Gelatin is the common tissue used in the literature for experiments with traditional steerable needles. Knox Gelatin is mixed with hot water until completely dissolved. Then the mixture is put in the vacuum chamber so that all the air bubbles trapped in the solution are disappeared. The solution is then poured into molds of  $100 \times 100 \times 30$  mm and then put in the refrigerator at  $4^{\circ}$  C for 8 hours before removing from the molds. Because of the water-based nature of the samples and to avoid the samples from drying, all the experiments are done in the same day.

As described fully in Chapter 2, low strain rate static compression, high strain rate split-Hopkinson-pressure-bar (SHPB) and fracture toughness tests were conducted on SEBS soft tissue simulants to characterize the tissue phantoms. The high strain rate tests are conducted to have the tissue properties at strain rates associated with

waterjet velocities. An Ogden model was used to find the shear modulus and strain hardening factor of the soft tissues at different waterjet velocities by fitting the stress-strain curve of the tissues. These results are used to predict the cut depth of the waterjet in soft tissue based on tissue and waterjet properties (refer to Chapter 2 for detailed explanations).

### *Waterjet Steerable Needle Design and Experimental Setup*

The insertion unit consists of two components, a 85mm long nickel-titanium tube (GoodFellow Corporation, Coraopolis, PA) and a 6.85 mm long 3D-printed polycaprolactone (PCL) nozzle. The nickel-titanium tube has 0.33 mm outer diameter with 0.24 mm inner diameter and the PCL nozzle has 1.6mm outer diameter with 0.33mm inner diameter at the base and 0.24mm diameter at the tip. The PCL nozzle was 3D-printed by FDM printer then attached to the nickel-titanium tube using cyanocrylate glue. Fig. 3.6 shows the CAD model of the designed needle without the tip (refer to Fig.2.13 for the built needle without the tip) and Fig. 3.7-Left and Fig. 3.7-Right show the schematic of the fixed-angle nozzle and the angle at which the designed needle cuts the tissue, respectively.

Fig.3.8 shows the experimental setup in which a high pressure pump (PR-class Dual Piston, PR100PFT3D, Scientific Systems Inc., State College, PA, USA) provides a computer-controlled volumetric flow rate (up to  $100 \frac{mL}{min}$ ). When the water velocity exceeds the threshold necessary to fracture the tissue, a channel will be cut at an

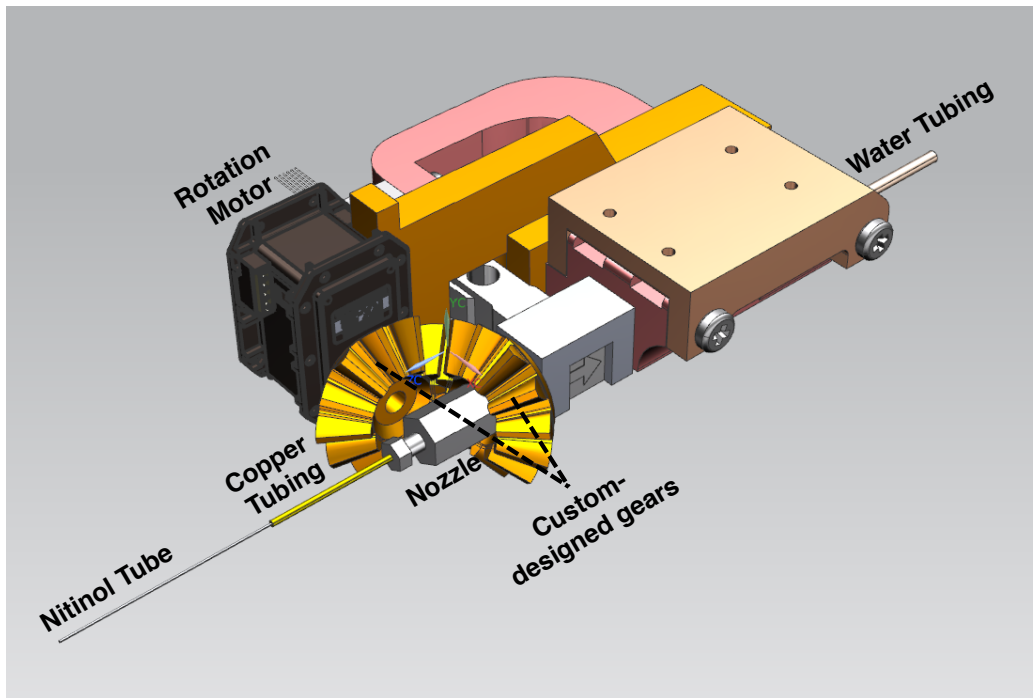


**Figure 3.6:** CAD model of the Waterjet Needle that consist of a Nitinol tube with sub-millimeter diameter soldered to a copper tubing which is connected to the waterjet nozzle and then PEEK tubing. Two custom-designed gears along with the motor provide the rotation at base of the needle to change the direction of the steering.

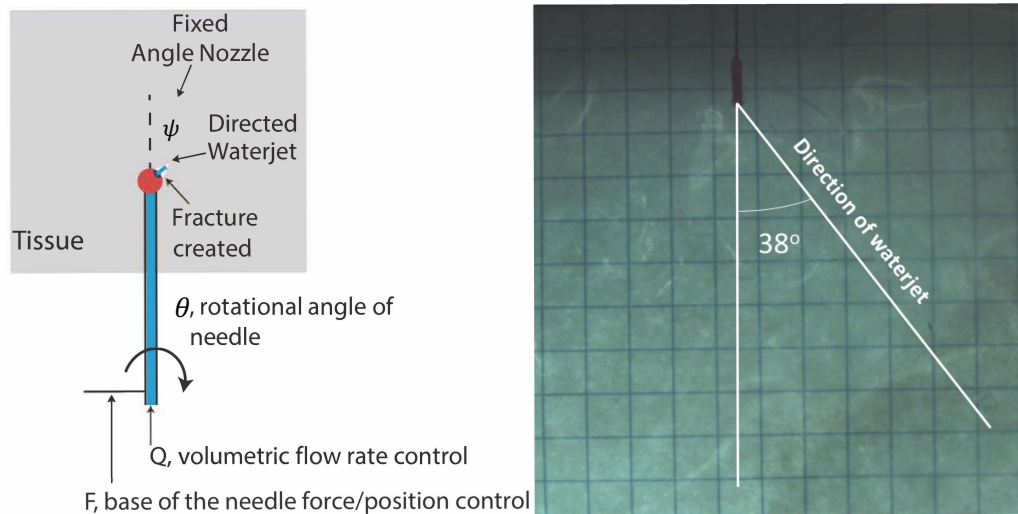


**Figure 3.7:** Waterjet fixed-angle tip used in the experiments in this section. (Left) Schematic of the fixed-angle nozzle principle and (Right) Waterjet needle tip with  $38^\circ$  angle.

angle (equal to the tip angle) relative to tangent to the needle tip, due to the nozzle design. For the experiments to study the effect of varying depth of cut on needle curvature, a  $30^\circ$  tip is used and for duty cycling experiments, the tip angle is  $38^\circ$ . Manufacturing of the nozzle at the exact intended angle is challenging and further research should be conducted to have repetitive manufacturing process at that small scale. Suction canister and a vacuum pump, are used to collect the water that sprays back out along the shaft of the needle during experiments. Telescopic sheath made of two concentric copper tubes is used to prevent buckling of the needle during insertions without waterjet (buckling is not an issue when inserting with waterjet). Rotation motor and gear are used to rotate the needle to change the direction of the steering.

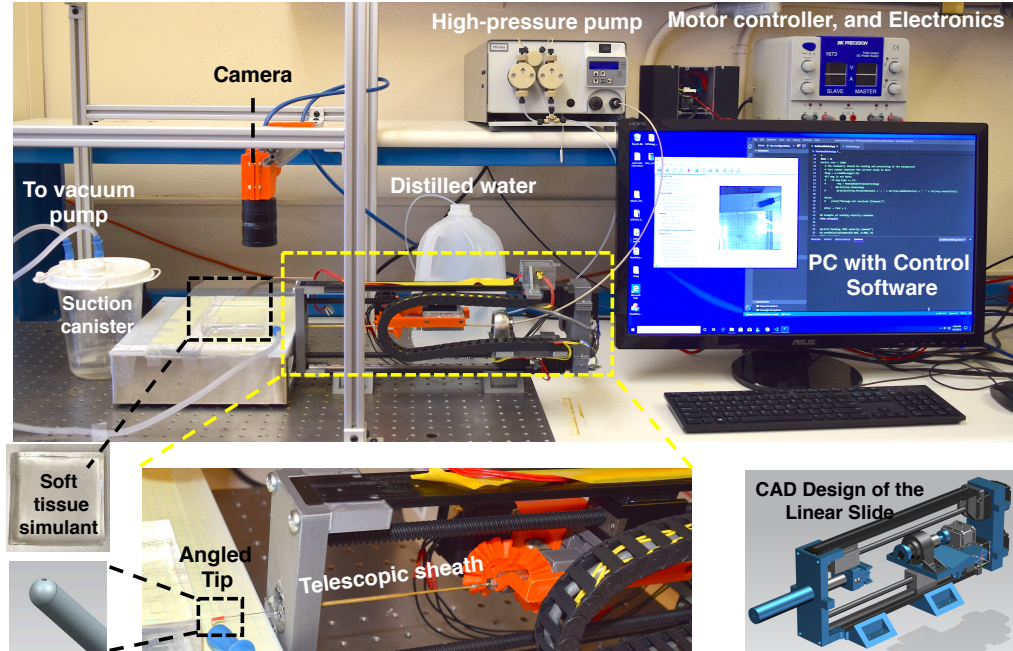


**Figure 3.8:** Setup for waterjet needle steering tests. For curvature control by varying cut-depth tests: First, high-pressure pump is set to the desired flow rate based on the desired depth-of-cut and then waterjet cuts a channel in tissue at  $30^\circ$ , the pump is turned off and the needle follows the channel with the velocity of insertion of  $1 \frac{mm}{s}$ . This process continues until the needle is steered in the tissue. For curvature control using waterjet duty cycling tests: First, high-pressure pump is set to the desired flow rate based on the stiffness of the tissue (for 10% SEBS, 15% SEBS and Knox Gelatin, the flow rates are set to 40, 70 and  $10 \frac{mL}{min}$ ) and then waterjet cuts a channel in tissue at  $38^\circ$  angle. The pump is turned off and then the needle follows the channel with the velocity of insertion of  $1 \frac{mm}{s}$ . For insertions without waterjet, the pump is turned off and the needle is inserted with velocity of insertion of  $0.5 \frac{mm}{s}$ . Telescopic sheath made of two copper tubes is used to prevent buckling of the needle during insertions without waterjet. The needle has inner diameter (ID) of 0.24 mm and outer diameter (OD) of 0.33 mm and the tip has ID = 0.24 mm.

For the experiments to study the effect of varying depth of cut on needle curvature, the desired depth of cut is controlled by the time and duration of the waterjet at a

specific water velocity. After a channel is cut by the waterjet, the pump is turned off and the needle is advanced to follow the cut channel with a velocity of insertion of  $1 \frac{mm}{s}$ . This insertion velocity is known to be relevant to insertions in real medical applications [4]. Through varying the waterjet velocity to control the cut-depth, subsequent insertion of the needle to follow the fractions and reorientation of the needle tip through whole-needle rotation, the waterjet needle can be steered in the soft tissue. Two velocities of the waterjet are tested for each soft tissue simulant in order to study the effect of the waterjet velocity and thus depth-of-cut, on the radius of curvature. Three tests are done for each velocity of the waterjet and the average radii for the tests are presented.

For duty cycling experiments, the curvature is controlled by changing the number of steps that waterjet is ON with highest curvature is for when all of the steps are traveled by the waterjet. Fig. 3.9 shows the concept of duty cycling of the waterjet to control the radius of curvature. 0% duty cycling means that waterjet is turned off for the entire length of insertion and 100% duty cycling means that waterjet is ON in the whole length of insertion. 3 tests are performed for each duty cycling rate and the average radius of curvature and standard deviation are calculated.

#### *Curvature measurement of the waterjet steerable needle*

The radius of curvature is measured by fitting a circle to the path of the needle using image processing software. The curvature ( $\kappa$ ) of the needle can simply be

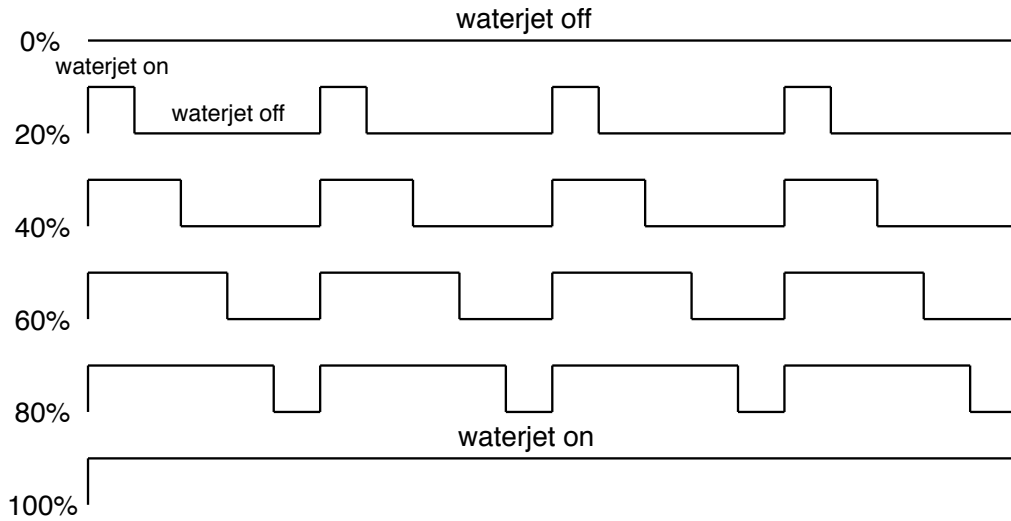


**Figure 3.9:** Schematic of the duty cycling of the waterjet in order to control the radius of curvature of the needle. For 0% duty cycling, the waterjet is off through the length of insertion and needle is inserted without waterjet and 100% duty cycling means that waterjet is ON for the entire length of insertion.

calculated by inverting the radius of curvature ( $r$ ):

$$\kappa = \frac{1}{r} \quad (3.2)$$

### *Kinematic Model of the Waterjet Steerable Needle*

In this part, the kinematic model of the needle motion is described that consist of a mechanics-based model for the prediction of the depth of cut of the waterjet in soft tissue (that is developed in Chapter 2) and a kinematics model to describe the needle path using this computed depth of cut.

## Depth-Of-Cut Model

We have developed a mechanics-based model for depth of cut of the waterjet in soft tissue that predicts the depth of cut based on tissue mechanical properties (constitutive response and fracture toughness), as well as waterjet properties (diameter and velocity) in Chapter 2. To summarize: the cut-depth of the waterjet in soft tissue can be expressed by the following ordinary differential equation, where  $A_{\text{surf}}$  and  $A_{\text{out}}$  are functions of  $h$  and their equations are given in Chapter 2. This equation can be readily integrated using standard methods such as Runge-Kutta integrators:

$$\frac{dh}{dt} = \frac{1}{P_w} \frac{\rho Q^3}{\pi^3 R^6} \frac{A_{\text{inj}} A_{\text{surf}}}{(A_{\text{surf}} + A_{\text{out}})^2} \quad (3.3)$$

Here,  $h$  is the depth of cut and  $P_w$ ,  $\rho$ ,  $Q$ ,  $R$ ,  $A_{\text{inj}}$ ,  $A_{\text{surf}}$  and  $A_{\text{out}}$  are penetration pressure of the waterjet ( $Pa$ ), density of the water ( $\frac{kg}{m^3}$ ), volumetric flow rate of the waterjet ( $\frac{m^3}{s}$ ), needle inner radius (in our case:  $2R = 0.24mm$ ) and injection, surface and backflow areas ( $m^2$ ), respectively. The penetration pressure of the waterjet in soft tissue can be expressed by the following equation:

$$P_w = \frac{4}{D(1 - (\frac{d}{D})^2)} \left\{ J_{IC}(\frac{d}{D}) + \frac{D}{4} \frac{2\mu}{\alpha^2} \left[ \int_1^\infty f(\frac{d}{D}, \gamma) d\gamma + 2(\frac{d}{D})^{2-\alpha} + (\frac{d}{D})^{2\alpha+2} - 3(\frac{d}{D})^2 \right] \right\}, \quad (3.4)$$

in which,  $D$ ,  $d$ ,  $J_{IC}$ ,  $\alpha$ ,  $\mu$ ,  $\rho$ ,  $v$  and  $T$  are waterjet diameter, steady-state diameter

after waterjet removal, mode I fracture toughness, strain hardening factor, shear modulus, water density, waterjet velocity and time, respectively. Function  $f(\frac{d}{D}, \gamma)$  can be expressed in the closed form as:

$$f(\frac{d}{D}, \gamma) = \left(\frac{\gamma + (\frac{d}{D})^2 - 1}{\gamma}\right)^{\frac{\alpha}{2}} + \left(\frac{\gamma}{\gamma + (\frac{d}{D})^2 - 1}\right)^{-\frac{\alpha}{2}} - 2 \quad (3.5)$$

Both the function  $f$  and the parameter  $\gamma$  are sub-computations that facilitate the derivation and computations of the integral and do not have any significant physical meaning (for detailed explanations please refer to Chapter 2).

#### Nonlinear Kinematic Model of the Waterjet Needle Steering

The kinematic model of the waterjet needle steering presented in this chapter is a discrete adaptation of the Bicycle model presented in [270]. Fig. 3.10 depicts the nonlinear kinematic model of needle steering. In this case,  $\delta\theta$ ,  $\delta\ell$  and  $r$  are the incremental needle rotation angle, incremental insertion distance and radius of curvature.  $\delta\ell$  is equal to the the depth of cut (h) of the waterjet in each step and if the number of steps is  $n$ , then the whole insertion length is  $\ell = \delta\ell \times n$ . In order to change the direction of the needle to re-orient the x-y plane in any given step  $\delta\theta$  should be applied to rotate the needle at its base and thus reorient the nozzle at the tip. In this model, the pose of the needle is described by the pose of the needle tip frame with respect to a reference frame. The needle has a position of  $\mathbf{p}_k$  and rotation  $\mathbf{R}_k$  at time  $k$ . Rotation of  $\delta\theta$  about the z-axis gives the rotated tip frame  $\mathbf{R}'_k = \mathbf{R}_k \mathbf{R}_z(\delta\theta)$ . The

position of the needle tip after insertion of  $\delta\ell$  can be calculated from the geometry of the circular path as:

$$\mathbf{p}_{k+1}^{k'} = \begin{bmatrix} 0 \\ r(1 - \cos(\Phi)) \\ r\sin(\Phi) \end{bmatrix}, \quad (3.6)$$

where  $\Phi = \frac{\delta\ell}{r}$ . The position of the needle tip at time  $k + 1$ , can be found by transforming this vector into the world frame:

$$\mathbf{p}_{k+1} = \mathbf{R}_k \mathbf{R}_z(\delta\theta) \mathbf{p}_{k+1}^{k'} + \mathbf{p}_k \quad (3.7)$$

Tip orientation at time  $k + 1$  can be calculated by:

$$\mathbf{R}_{k+1} = \mathbf{R}_k \mathbf{R}_z(\delta\theta) \mathbf{R}_x(-\Phi) \quad (3.8)$$

Note that:

$$\mathbf{R}_0 = \mathbf{R}_x(-\beta) = \begin{bmatrix} 1 & 0 & 0 \\ 0 & \cos(\beta) & \sin(\beta) \\ 0 & -\sin(\beta) & \cos(\beta) \end{bmatrix}, \quad (3.9)$$

Where  $\mathbf{R}_0$  is the rotation matrix around x-axis by a deflection angle of  $-\beta$ .  $\beta$  is defined as shown in Fig. 3.11:

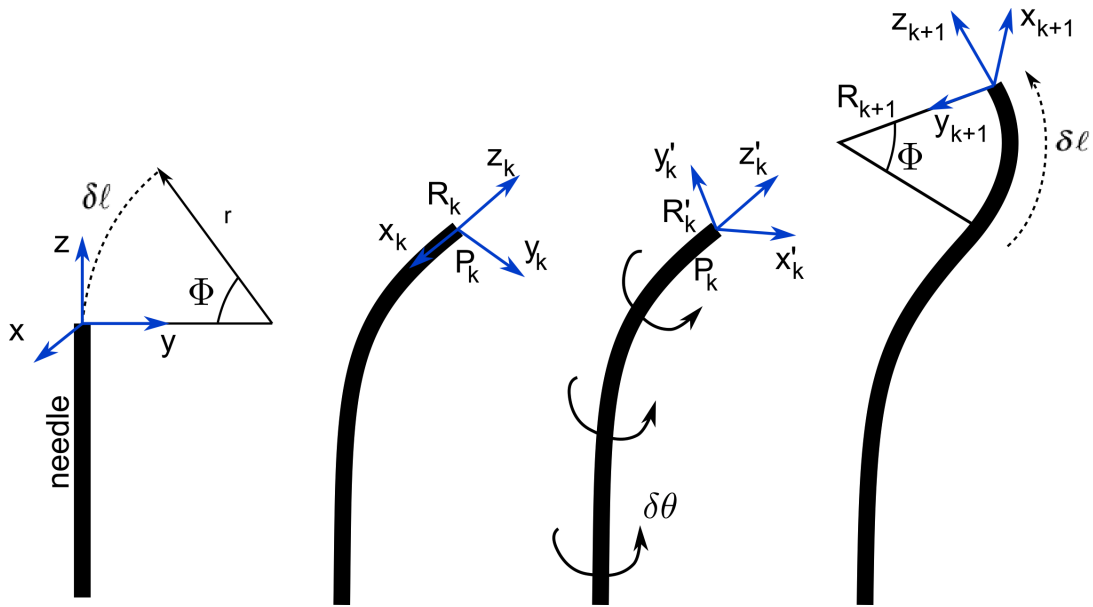


**Figure 3.10:** The kinematic model of the waterjet needle steering. The z-axis is assumed to be tangent to the needle at the tip and the y-axis is towards the center of the curvature. The needle follows a path in y-z plane with radius  $r$  and arc length  $\ell$ . The frame advances as the needle tip progresses during waterjet needle steering.  $\delta\theta$ ,  $\delta\ell$  and  $r$  are the incremental needle rotation angle, incremental insertion distance and radius of curvature, respectively. Note that,  $\delta\ell$  equals  $h$  (depth-of-cut).

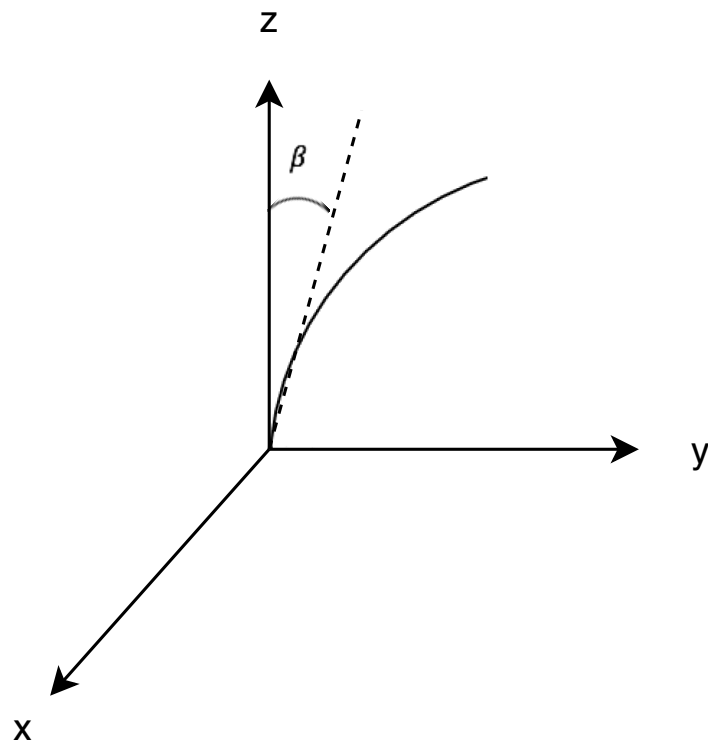


**Figure 3.11:** Definition of  $\beta$  in (3.9).  $\beta$  is defined as the deflection of the needle around x-axis.

### *Simple 2D Path Planning Using a Genetic Algorithm*

The optimal path planning is designed using a genetic algorithm (GA) in the environment map. The environment in the current study is a soft tissue. The tissue is discretized into parts divided into longitudinal and transverse directions. A value has been assigned to every point in this set of discrete parts, which is defined by a softness function. The softness function helps to penalize the desired distance from any obstacle. The softness value is minimal for normal points and is large for obstacles:

$$\text{softness}(y, z) = \begin{cases} 1 & \text{normal points} \\ 10^{10} & \text{obstacle points} \end{cases} \quad (3.10)$$

The genetic algorithm is used to make an optimized path. Every path can be constructed from some  $\delta\ell$ ,  $\delta\theta$  and  $r$ , which are the incremental path length (in our case depth of cut), incremental needle base rotation and radius of curvature, respectively.  $r$  is a function of  $\delta\ell$  and tissue type and in this chapter we measured  $r$  experimentally, so there are just two parameters that need to be optimized, that are  $\delta\ell$  and  $\delta\theta$ . Therefore, a path can be displayed in the following form:

$$\begin{array}{cc}
\delta\ell & \delta\theta \\
value_1 & value_1 \\
value_2 & value_2 \\
\cdot & \cdot \\
\cdot & \cdot \\
\cdot & \cdot
\end{array}
\left| \begin{array}{l} \\ \\ \downarrow \text{ steps} \end{array} \right. \quad (3.11)$$

For the first step of the genetic algorithm (initial population), some paths are randomly created with constant step size and evaluated by the cost function explained below.

The cost function consists of 3 terms. The first term includes the length of the path, the second term is related to the softness value of the environment and the third one is about the distance of the needle tip from the target point. As mentioned before, the tissue is discretized into some points in  $y$  and  $z$  coordinates. Every point of these coordinates of tissue has a value. This value is minimal for normal points and a big amount (here  $10^{10}$ ) for obstacle points. Therefore, when a path crosses an obstacle, the cost function would be so large and large amounts of the cost function cause the path to be excluded from optimization process in subsequent iterations. Also, because the distance of the target point is very important, this distance will be multiplied in a large number (here  $10^{10}$ ) to bring out the paths with large distances of

the target from the optimization process in subsequent iterations. The cost is defined as follows:

$$\text{cost} = c_1 + c_2 + c_3 \quad (3.12)$$

Where  $c_1$ ,  $c_2$  and  $c_3$  are the costs related to the path, the environment and the distance from the target:

$$c_1 = \sum_{i=1}^n \delta \ell_i \quad (3.13)$$

$$c_2 = \sum_{r=1}^m \text{softness}(y_r, z_r) \quad (3.14)$$

$$c_3 = 10^{10} \sqrt{(X - x_f)^2 + (Y - y_f)^2 + (Z - z_f)^2} \quad (3.15)$$

Where,  $n$  and  $m$  are the number of steps of the needle following the cut path by the waterjet and the number of points (cells) that the paths cross them in the environment, respectively.  $\begin{bmatrix} X & Y & Z \end{bmatrix}^T$  and  $\begin{bmatrix} x_f & y_f & z_f \end{bmatrix}^T$  are the coordinates of the ending point of the path (needle tip) and the desired target point, respectively. The needle tip position can be obtained using kinematic model of the needle in (3.7) and (3.8).  $(y_r, z_r)$  are the cells' coordinates that the needle crosses them. These cells

can be obtained using kinematic model of the needle.

The initial population is evaluated by cost function and the better ones are selected by the selection operator. The pair paths selected by the selection operator are combined by the single-point crossover operator. After applying the crossover operator on the population, the mutation occurs on some of the new paths. When mutation occurs, some bits of the paths are randomly selected and their contents are changed randomly. After the operators are applied on the paths, the new paths need to be evaluated and the cost of each one to be calculated. Then, the previous steps must be repeated until the stop condition is met. The explained algorithm is represented in Fig. 3.12.

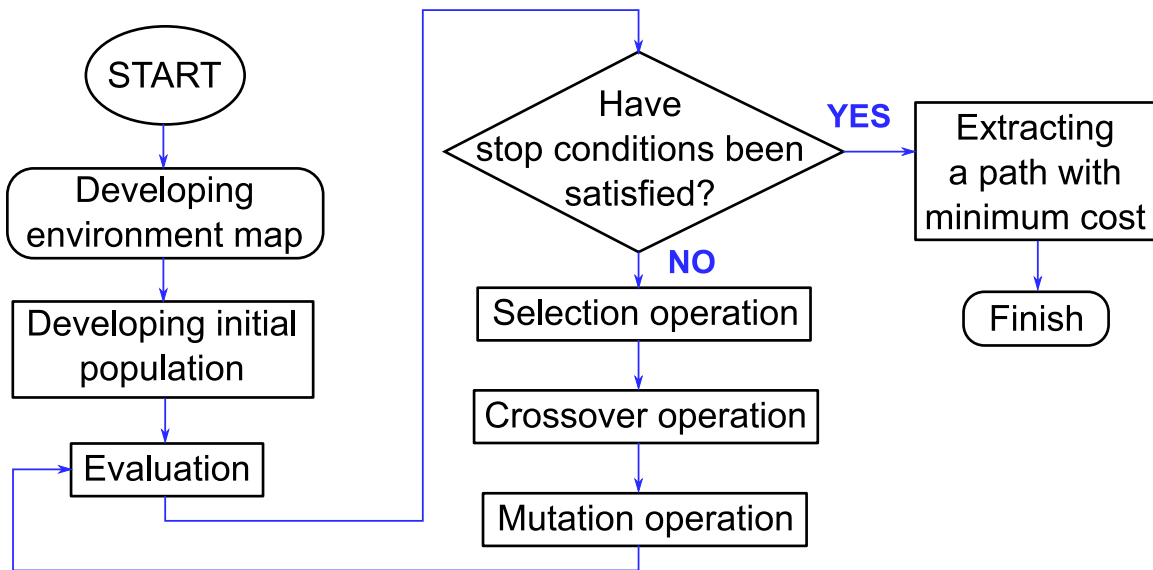


**Figure 3.12:** The flow chart of the algorithm used for path planning.

### 3.2.3 Results

In this section, the results of the curvature control of the waterjet with changing depth-of-cut, along with a comparison to the modeling, the results of the path planning and results of the duty cycling of the waterjet in order to control the curvature of the needle are presented in SEBS and Knox Gelatin soft tissue simulants. The smallest ROC in Knox Gelatin tissues is compared to the best ROC for conventional steerable needles in literature conducted in the same tissue medium.

#### *Curvature of the waterjet needle is a function of depth-of-cut of the waterjet*

In this part, it is shown that the waterjet curvature is a function of depth-of-cut of the waterjet in soft tissue which in turn is dependent on tissue and waterjet properties. Table 3.1 shows the soft tissue phantoms used, their properties from mechanical tests (at associated waterjet velocities), waterjet velocities and the associated depths-of-cut.  $\mu$  (MPa) and  $\alpha$  are shear modulus and strain hardening factor of soft tissue phantoms that are derived by fitting Ogden model [175] to experimental stress-strain data of the tissues. The duration of time used for the depth-of-cut measurements and predictions is 30 seconds. The depth of cut is experimentally measured and also predicted from the mechanics-based model shown in 3.3. Tissue properties are measured from Split-Hopkinson-Pressure-Bar tests (described in detail in Chapter 2) to be relevant to waterjet velocities (note that soft tissue goes through strain

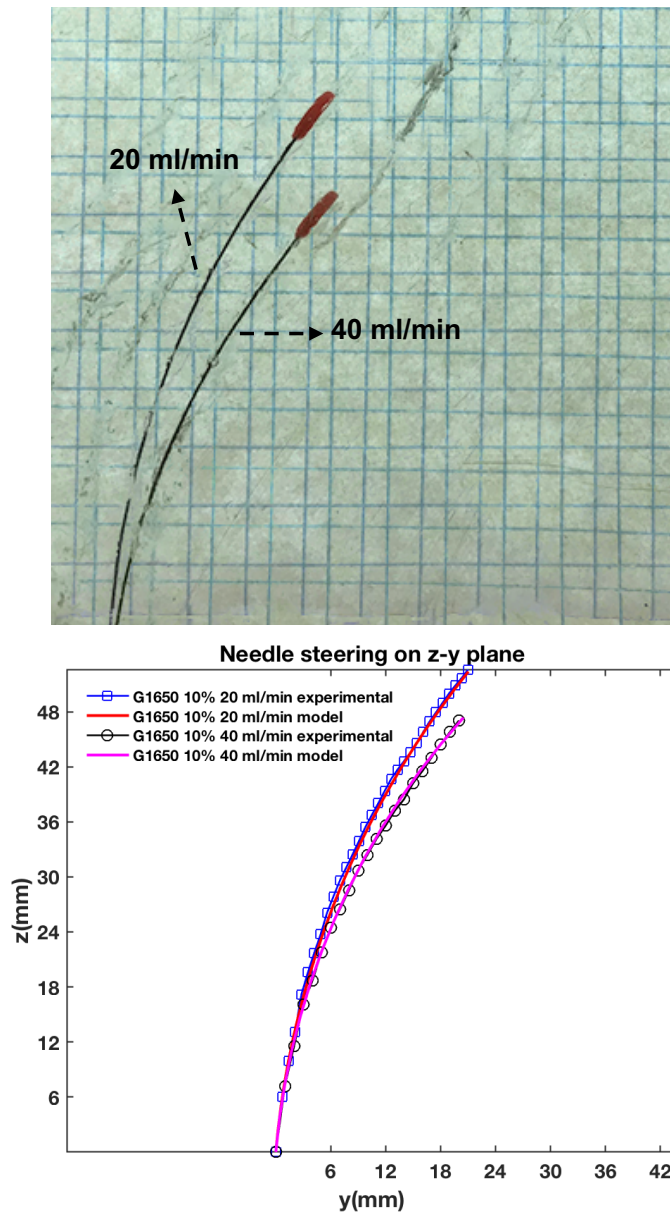
**Table 3.1:** Soft tissue phantoms, their properties and corresponding waterjet velocities and Depths-of-cut. These data are derived from tests described in Chapter 2.

Tissue 1 (G1650 10%)				
$\alpha = 1.2472$				
$Q(\frac{ml}{min})$	$v(\frac{m}{s})$	$\mu(MPa)$	h (mm)	
20	7.37	2.954	2.49	
40	14.74	6.27	3.75	
Tissue 2 (G1650 15%)				
$\alpha = 1.7008$				
$Q(\frac{ml}{min})$	$v(\frac{m}{s})$	$\mu(MPa)$	h (mm)	Fracture Toughness ( $\frac{kJ}{m^2}$ )
30	11.05	5.82	1.31	85.58
50	18.43	10.02	2.16	114.11

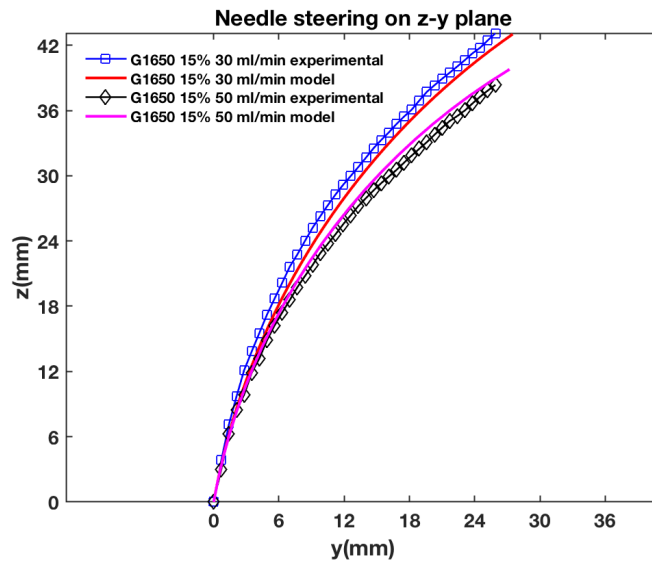
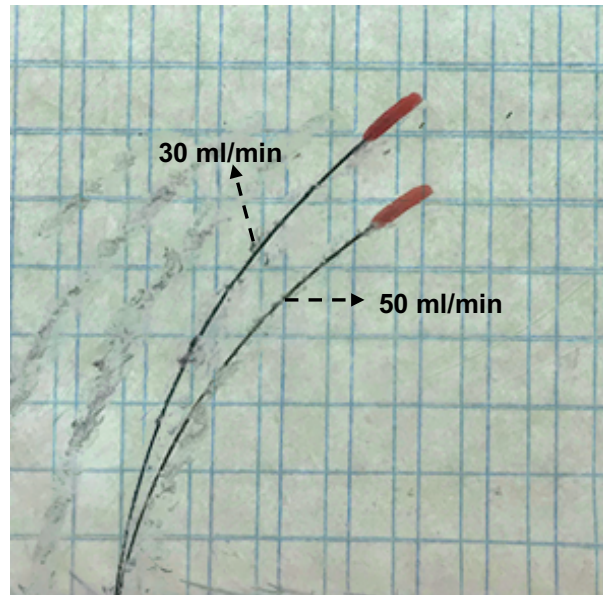
hardening at higher velocities).

Fig. 3.13 and Fig. 3.14 show the results of the waterjet needle steering in the z-y plane and the corresponding model of the steering in two soft tissue simulants. As can be seen from these figures, the needle curvature can be controlled by changing the velocity of the waterjet and thus depth-of-cut and that the radius of curvature is smaller in the harder soft tissue simulant. The needle base has no rotation in either of these figures.

Fig. 3.15 shows an example of the waterjet needle steering with a base rotation midway through the insertion. In this example,  $\delta\ell = 2.2$  mm with 10 steps for the first bend,  $\delta\theta = 0$   $180^\circ$  and then 20 steps for the second bend of the insertion.  $Q = 50 \frac{ml}{min}$  is selected for both bends (to give cut-depth of  $2.2mm$ ). An overlay of the model with the experimental results shows that the model can precisely predict the experiments.



**Figure 3.13:** An example of the waterjet needle steering in the z-y plane in SEBS G1650 10% tissue simulant. (up) Experimental results of the needle steering using two different waterjet velocities (two figures are overlaid on top of each other). (bottom) Experimental results (derived with image processing on successive photos of the needle path to determine the tip position) along with the kinematic model. Average radii of curvature for three experiments are: For  $20 \frac{ml}{min}$ :  $r_{ave} = 97.25mm$  (total insertion length  $\ell = 65$  mm) and for  $40 \frac{ml}{min}$ :  $r_{ave} = 81.79mm$  (total insertion length  $\ell = 57$  mm).



**Figure 3.14:** An example of the waterjet needle steering on z-y plane in SEBS G1650 15% tissue simulant. (up) Experimental results of the needle steering using two different waterjet velocities (the figures are overlaid on top of each other). (bottom) Experimental results along with the kinematic model. Average radii of curvature for three experiments are: For  $30 \frac{ml}{min}$ :  $r_{ave} = 66.49mm$  (total insertion length  $\ell = 56$  mm) and for  $50 \frac{ml}{min}$ :  $r_{ave} = 58.42mm$  (total insertion length  $\ell = 52$  mm).

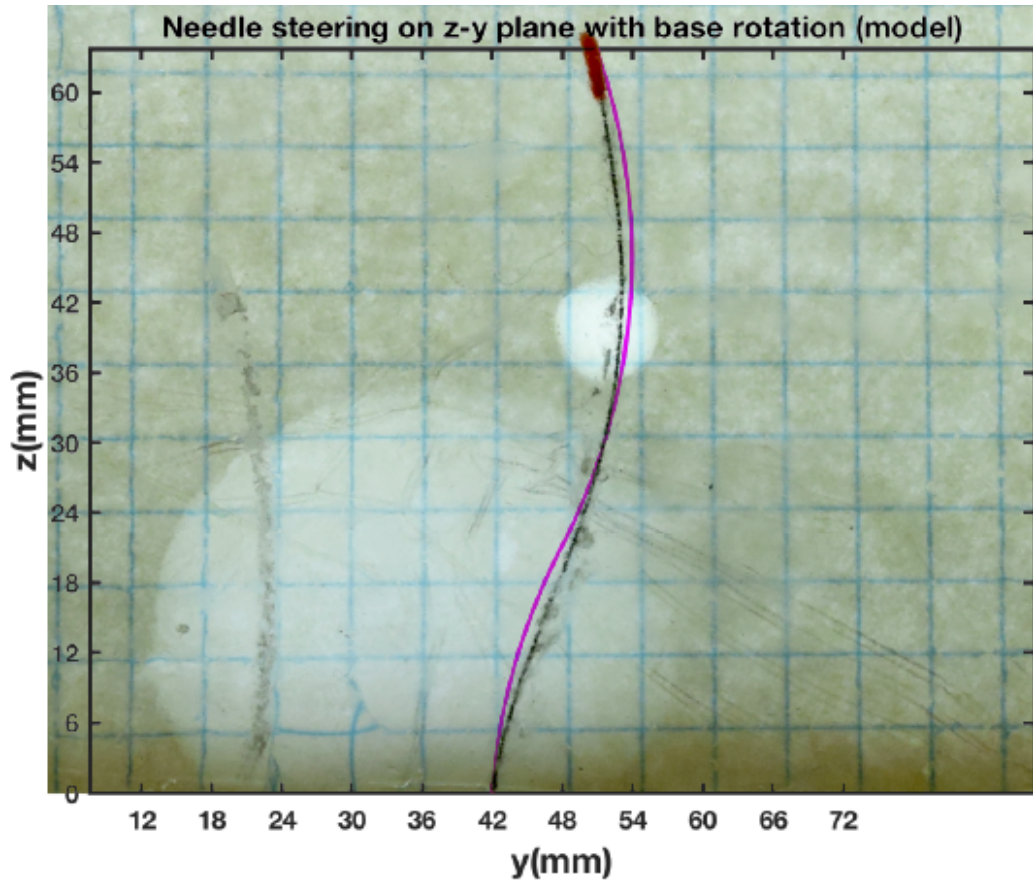


**Figure 3.15:** An example of the waterjet needle steering with a base rotation during the insertion. In this example,  $\delta\ell = 2.2$  mm with 10 steps for the first bend,  $\delta\theta = 0$  to  $180^\circ$  to flip the nozzle direction and 20 steps for the second bend.  $Q = 50 \frac{ml}{min}$  for both bends. The figure shows an overlap of the experimental result with the kinematic model.

### *Path planning results*

In this part, several 2D needle paths are made to show the effectiveness of the proposed path planning method. For the first path,  $\delta\theta$  is always zero (no rotation at the base).  $\begin{bmatrix} 0 & 5 & 0 \end{bmatrix}^T$  mm and  $\begin{bmatrix} 0 & 30 & 40 \end{bmatrix}^T$  mm are beginning and target points, respectively. The path has been constructed by 20 optimized steps. Fig. 3.16 shows this path with a high degree of the overlap between the simulated and experimental results.

In the second example path,  $\delta\theta$  is always zero except one  $180^\circ$  rotation. Beginning and target points are  $\begin{bmatrix} 0 & 20 & 0 \end{bmatrix}^T$  mm and  $\begin{bmatrix} 0 & 20 & 44 \end{bmatrix}^T$  mm, respectively. 20 optimized steps are used. Fig. 3.17 shows this path, again with agreement between the simulated trajectory and the experimental results.

In the third example, there is not any limitation on the rotation at the base of the needle,  $\theta$ . The initial point and the target point are chosen differently for three different needle paths. The paths have been constructed by 40 optimized steps. The initial points and the target points are:  $\begin{bmatrix} 0 & 20 & 0 \end{bmatrix}^T$  mm and  $\begin{bmatrix} 0 & 90 & 90 \end{bmatrix}^T$  mm,  $\begin{bmatrix} 0 & 20 & 0 \end{bmatrix}^T$  mm and  $\begin{bmatrix} 0 & 90 & 20 \end{bmatrix}^T$  mm and  $\begin{bmatrix} 0 & 90 & 0 \end{bmatrix}^T$  mm and  $\begin{bmatrix} 0 & 5 & 90 \end{bmatrix}^T$  mm, respectively.

Fig. 3.18 shows the optimized paths. As can be seen from the figure, the direction of the needle curvature can be controlled by varying waterjet velocity and controlling the depth-of-cut by changing the volumetric flow rate of the pump. It is also evident

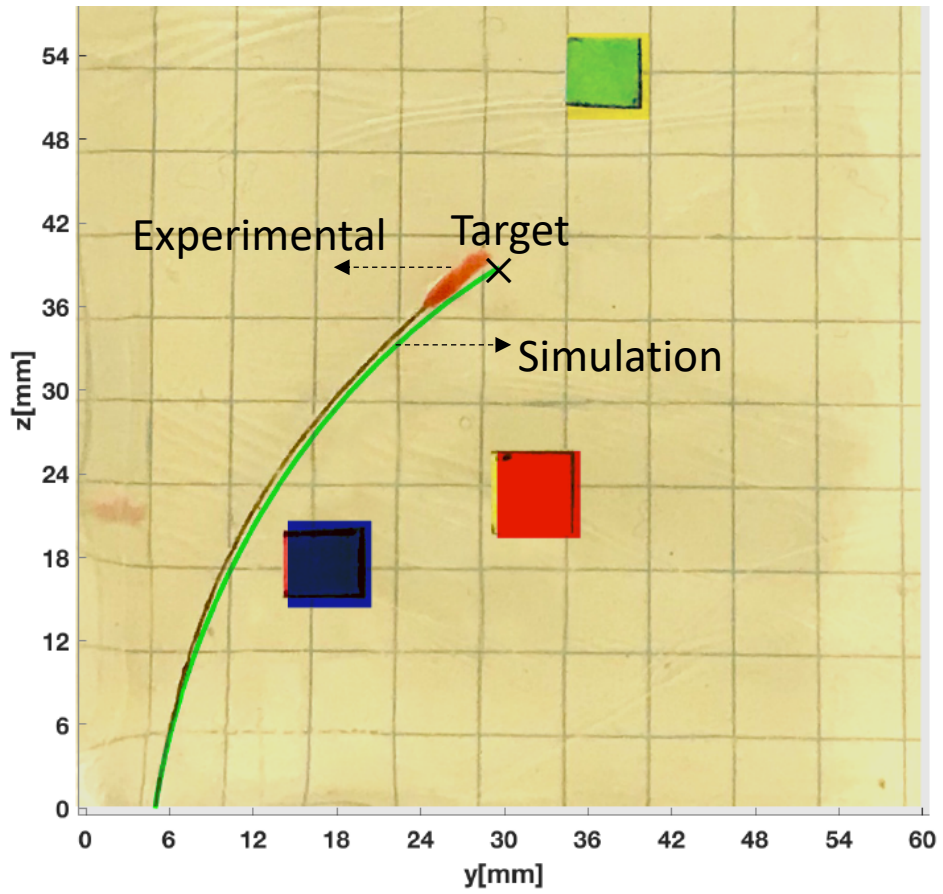


**Figure 3.16:** 2D path planning of the waterjet steerable needle with no base rotation. The Figure shows an overlap of the simulated path and experimental results.

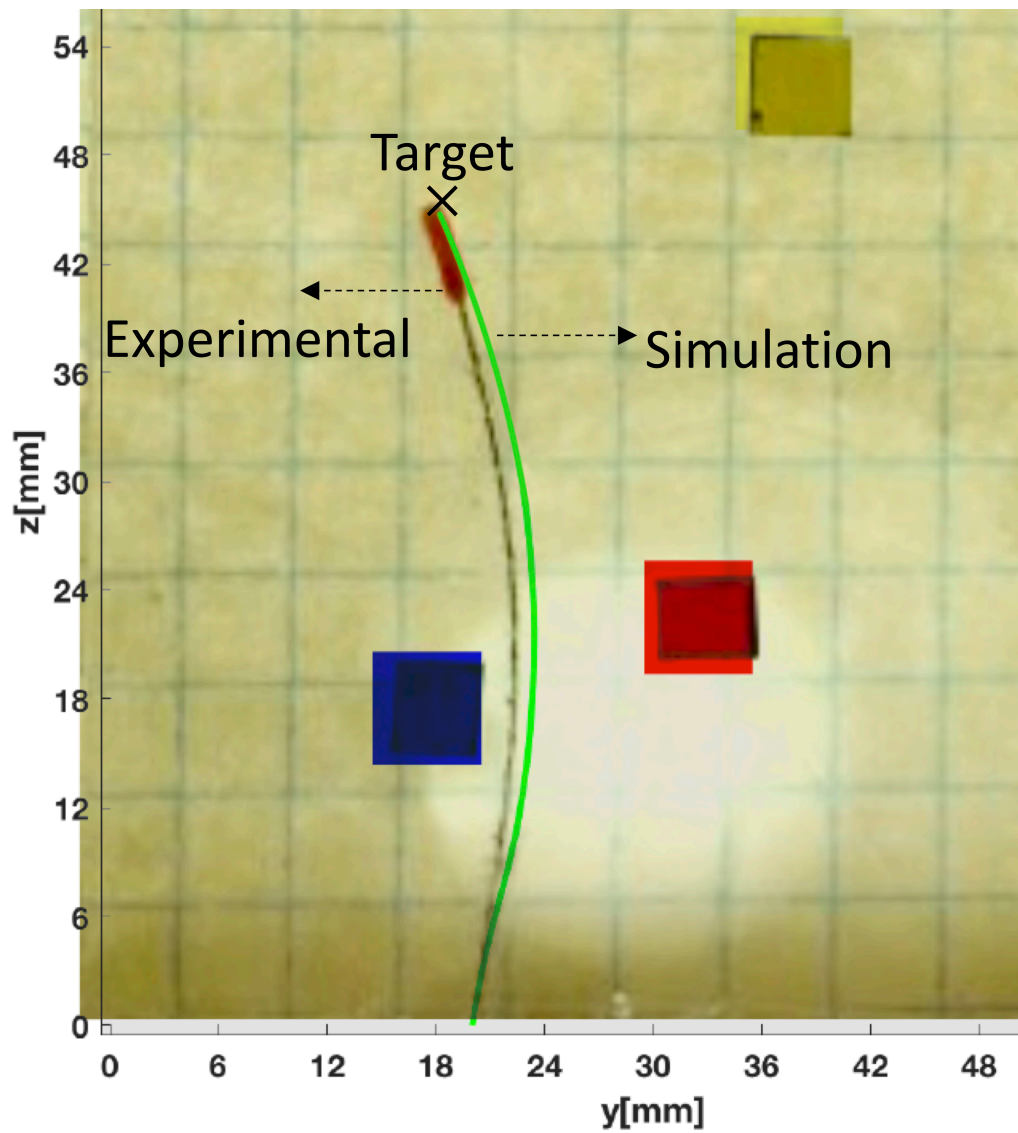


**Figure 3.17:** 2D path planning of the waterjet steerable needle with one 180° base rotation. The Figure shows an overlap of the simulated path and experimental result.

from this figure that the needle can reach multiple targets by one insertion into the tissue.

*Duty Cycling of the Waterjet for Waterjet Steerable Needles Can Improve Steerability and Radius-of-Curvature*

Another more better way to control the curvature of the waterjet steerable needles is by duty cycling of the waterjet. Fig. 3.19-Left and Middle show the results of the radius of curvature control using duty cycling of the waterjet in 10% (Tissue A) and 15% (Tissue B) SEBS in mineral oil soft tissue simulants. Fig. 3.19-Right shows the insertion of the needle with no tip while the waterjet cuts a straight channel in the tissue and then the needle follows the channel. Fig. 3.20-UP(Left) represents the results of radius of curvature control using duty cycling of the waterjet in 10% by Weight Knox Gelatin soft tissue simulants (Tissue C). As can be seen from these figures, duty cycling of the waterjet can be used to control the curvature of the needle from almost 0 (insertion without waterjet) to maximum curvature (insertion with waterjet ON for all steps). For Tissue A and Tissue B, volumetric flow rates of  $40 \frac{ml}{min}$  and  $70 \frac{ml}{min}$  are used, respectively (these flow rates give the same depths of cut in a given time in both tissues). For Tissue C, volumetric flow rate of  $10 \frac{ml}{min}$  is used to cause the same cut-depth in each step. Fig. 3.20-UP(Right) shows the Bicycle model [270, 8] of the needle motion and Fig. 3.20-Bottom depicts the overlay of the Bicycle model with needle path. As it is evident, there is a high agreement between

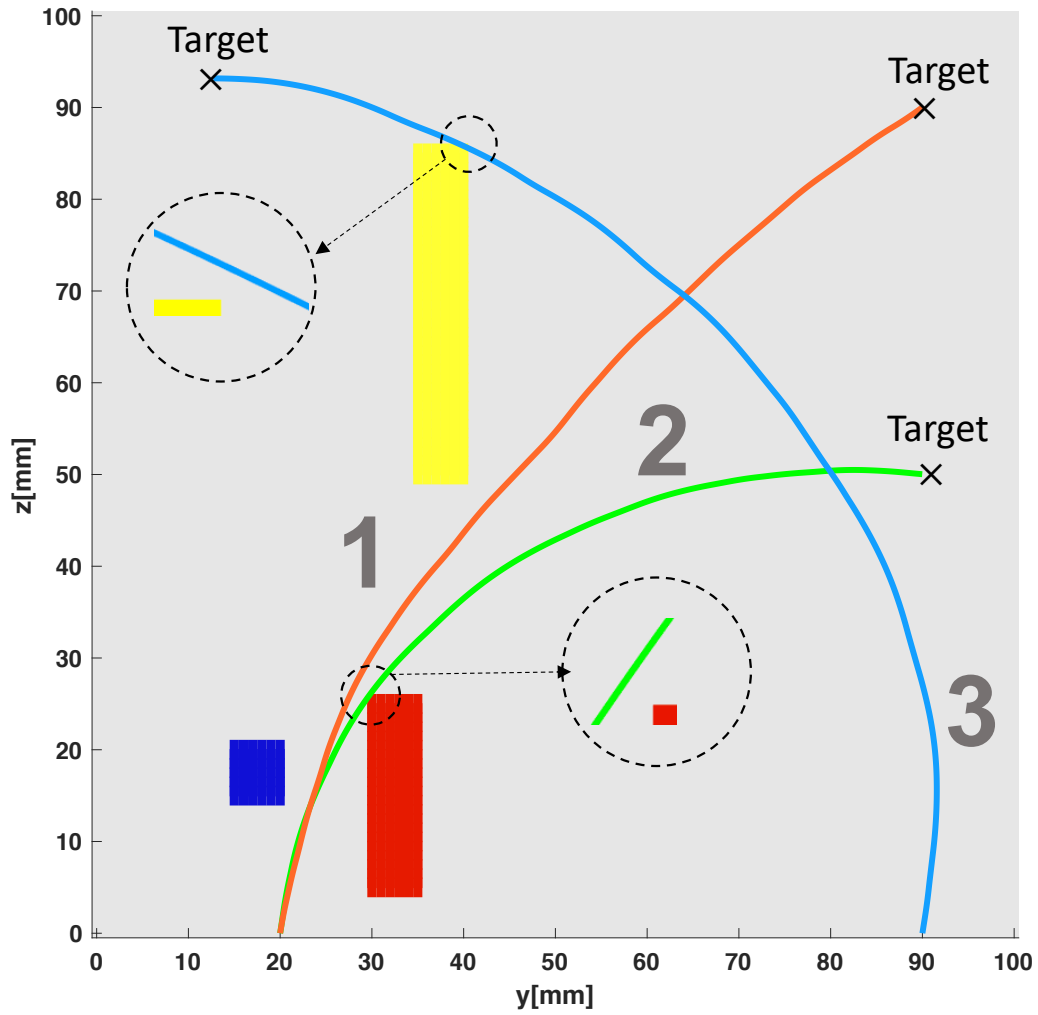


**Figure 3.18:** 2D path planning of the waterjet steerable needle with different base rotations. As can be seen from this figure, the curvature of the waterjet steerable needle can be controlled by changing the depths-of-cut of the waterjet that can be controlled by changing the velocity of the waterjet. It can also be seen from this figure that the waterjet steerable needle can reach different targets from one insertion in the soft tissue.

the experiments and the model.

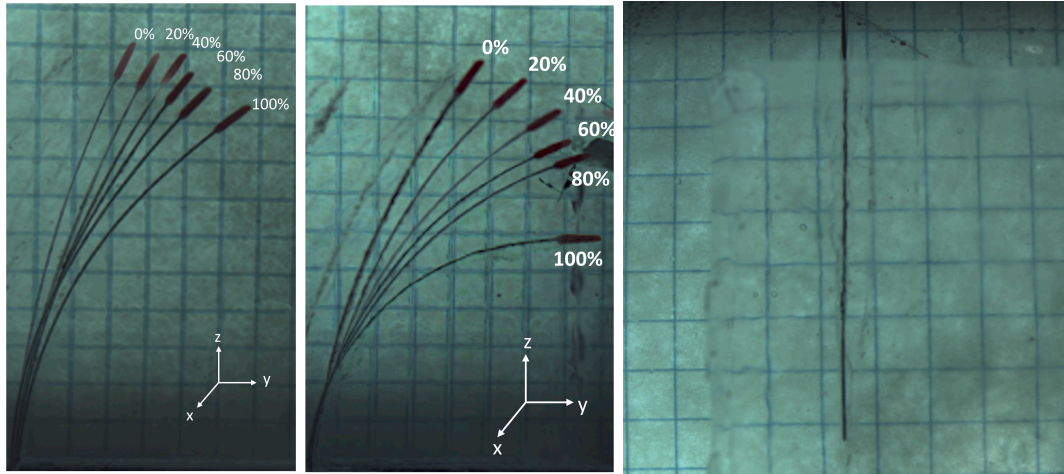


**Figure 3.19:** Waterjet duty cycling to control the radius of curvature of the waterjet steerable needle. (Left) 10% SEBS in mineral oil soft tissue simulants (Tissue A) and (Middle) 15% SEBS in mineral oil soft tissue simulants (Tissue B). The figures are obtained by overlaying 6 different experiments. The total insertion length is 70 mm. Flow rates of  $40 \frac{ml}{min}$  and  $70 \frac{ml}{min}$  are used to get the same cut-depths in the same amount of time for Tissue A and Tissue B, respectively. The best ROC for Tissue A and Tissue B are 75 and 49 mm. (Right) obtaining straight insertion using waterjet needle with no tip. The needle follows the cut path by the waterjet.

Table 3.2 presents a comparison of the Smallest Radius of Curvature obtained with Waterjet Steerable needle and some of the conventional steerable needles in literature in the same soft tissue medium. Flexture-based and bent-tip steerable needles are known to have the smallest radius of curvature in the literature [235]. Comparing our result to the results of the smallest radius of curvature in the literature we can see that the smallest radius of curvature of the waterjet steerable needle system is comparable to the bent-tip steerable needles without the tissue damage due to bent-

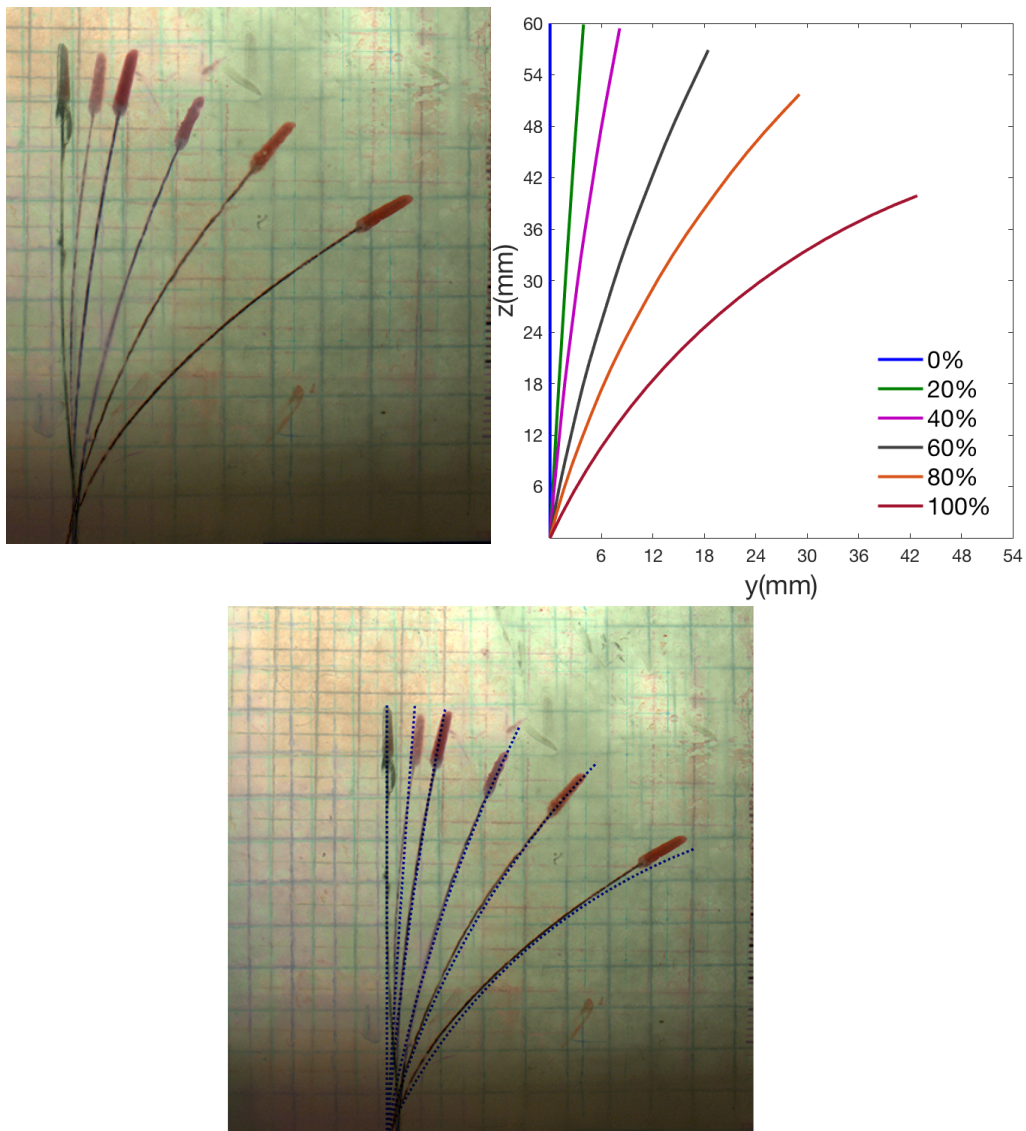


**Figure 3.20:** UP(Left) Controlling the curvature of the needle in 10% by weight Knox Gelatin soft tissue phantoms (Tissue C) by duty cycling of the waterjet. The total insertion length is 60 mm. Flow rate of  $10 \frac{ml}{min}$  is used to get the depth of cut of 3mm in each insertion step. UP(Right) Bicycle model of the needle motion and (Bottom) Overlay of the needle path with model.

tip and continuous rotation associated with these needles. Waterjet steerable needles can provide variable curvatures without resorting to rotational duty cycling.

*Curvature of the needle is a Linear Function of the Waterjet Duty Cycling in a Range of the Tissue Stiffnesses*

Fig. 3.21 and 3.22 depict the Curvature ( $cm^{-1}$ ) vs., duty cycling for Tissues A, B and C, respectively. Curvature is calculated by averaging the 3 trials and the error bars are one standard deviation above and one standard deviation below the data points. As can be seen from these figures, curvature of the waterjet steerable needle is a linear function of the duty cycling of the waterjet for the range of the tissue stiffnesses tested here. Curvature ( $\kappa$ ) can be easily calculated by inverting the radius of curvature.

### 3.2.4 Discussion

In this section, a new class of the steerable needles that we call fracture-directed waterjet steerable needles is presented in which the direction of the tissue fracture is controlled by sub-millimeter waterjet that is subsequently followed by the flexible Nitinol needle.

The effect of the cut-depth on needle curvature is studied using two different tissue stiffnesses and 4 different waterjet velocities. The results showed that by varying the velocity of the waterjet and thus cut-depth of the waterjet in soft tissue, the curvature

**Table 3.2:** Comparison of the Smallest Radius of Curvature (ROC) of the water-jet Steerable Needle with Conventional Steerable Needles in the Same Medium.

Reference	Needle Design/Material	Needle Diameter (mm)	Insertion Velocity (mm/s)	Soft Tissue	Best ROC (mm)
Our Proposed Method	Custom-designed/ Nitinol	ID = 0.24, OD = 0.33	1	Gelatin 10%	78
[235]	Bevel-tip ( $10^\circ$ ) Flexure max. angle ( $22^\circ$ )/ SS (body) Nitinol (flexure)	OD = 0.91 ID = 0.6	5	Gelatin 10 wt%	121
[273]	Flexure needle tip Bevel ( $10^\circ$ ) Notched wall/ Nitinol	0.91	-	Knox Gelatin 10 wt%	91.4
[113]	4-Segment Programmable bevel/ Rubber-like	12	1	Gelatin 6 wt% (E = 7 kPa)	178.6
[206]	Tendon-driven actuated tip (conical shape, $\ell = 5\text{mm}$ )/ Nitinol (needle) PEEK (cannula)	Needle (1) Cannula (2)	5	Gelatin 14.9 wt% (E = 35 kPa)	200
[247]	Cable Actuated (4 cables)/ SS Stylet PEEK Plastic Cannula	Stylet (0.5) Cannula (0.9) OD = 1	5	Gelatin 15 wt% (E = 10 kPa)	181
[67]	"Airfoil" Prebent ( $16^\circ$ , 6.3 mm) Bevel tip ( $20^\circ$ )/ Nitinol	0.15	-	Knox Gelatin 6 wt%	100
[36]	4 Actuated Shafts/ Special Flexible and Rigid materials	8	1	Gelatin 6 wt%	100
[34]	"Airfoil" Bevel-tip ( $12^\circ$ )/ Nitinol	0.46 (cannula) 0.24 (stylet)	3	Gelatin 6% Gelatin 10%	125 72
[155]	Prebent ( $15^\circ$ ) / Nitinol (body) SS (bevel-tip)	1.27 (tip) 0.28 (body)	-	Gelatin 6.5 wt% (Brain Phantom)	52
[114]	2-Segment Programmable bevel/ VeroWhite	4	0.5	Gelatin 6 wt% (E = 7 kPa)	70

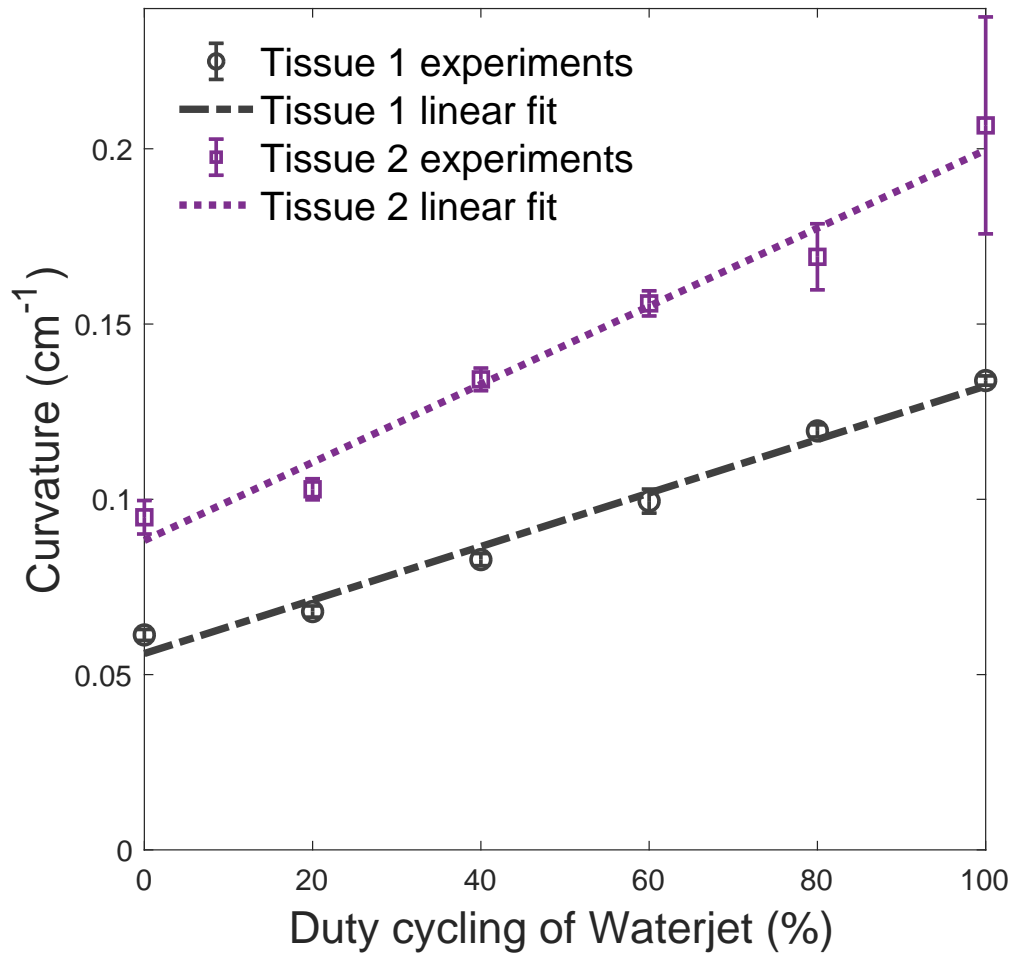


**Figure 3.21:** Curvature of the waterjet steerable needle vs. duty cycling of the waterjet for two different tissue stiffnesses. The values reported for Curvature are the average of the 3 trials. The error bars are one standard deviation above and one standard deviation below the data points. For Tissue A, the goodness of the fit is  $R^2 = 0.9839$  and for Tissue B,  $R^2 = 0.98$ .

can be controlled.

Then, duty cycling of the waterjet is used to control the curvature of the waterjet steerable needles. The results showed that duty cycling of the waterjet can lead to Radii of curvature as low as 75, 49 and 78 mm in soft tissue phantoms made

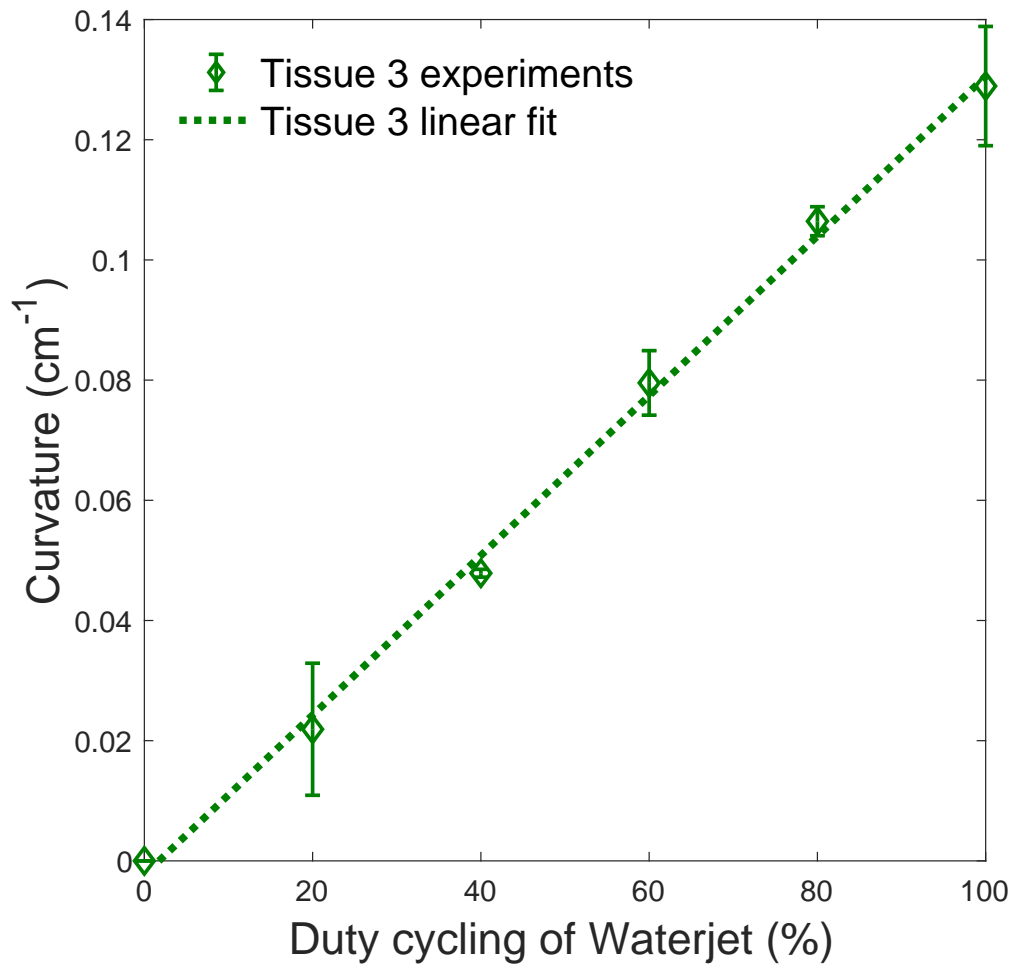


**Figure 3.22:** Curvature of the waterjet steerable needle vs. duty cycling of the waterjet in Tissue C. The values reported for Curvature are the average of the 3 trials. The error bars are one standard deviation above and one standard deviation below the data points. The goodness of the fit is  $R^2 = 0.9973$ .

of 10% SEBS in mineral oil (Tissue A), 15% SEBS in mineral oil (Tissue B) and 10% by weight Knox Gelatin (Tissue C), respectively. The results are compared to the traditional steerable needles and it is shown that waterjet steerable needle can reach to a ROC of 78 mm in Tissue C. The smallest radius of curvature obtained from

waterjet needle steering is comparable to bent-tip steerable needles [235, 75, 155, 148] where duty cycling is used to control the curvature without the considerable tissue damage of the bent tip and rotational duty cycling (continual spinning of the needle). This promises a better method for curvature control in comparison to the steerable needle literature. Duty-cycle methods must account for the inherent torsional windup associated with twisting a long, super-elastic needle about the insertion axis[203, 239]. Thus, waterjet steerable needles promise a better control over the tissue fracture and needle curvature that was unattainable with traditional steerable needles.

In Fig. 3.19, the needle curves in SEBS soft tissue simulants even when duty cycling is at 0%, whereas this is not the case in Fig. 3.20 for Tissue C. The reason for this is that the stiffnesses of Tissue A and Tissue B are higher than Tissue C and the tiny bevel angle of the tip of the waterjet steerable needle interacts with Tissues A and B causing it to bend. Fan et al. [284] showed that the curvature of the needle is a function of the bending stiffness of the tissue and the needle and in the case of Tissue C, the bending stiffness is lower in comparison to the Tissue A and B. On the other hand, the needle used in our study has a sub-millimeter tip (0.24 mm) which is much thinner and more flexible in comparison to the needles used in the literature therefore having a lower bending stiffness. The combined effect of the low bending stiffness of the needle and high bending stiffness of the Tissues A and B lead to bending of the needle even when the duty cycling is at 0%. This issue can be

solved by manufacturing better tips without this tiny bevel effect.

Insertion velocity of  $1 \frac{mm}{s}$  is chosen to insert the needle in the fractured path. This insertion velocity is known to be relevant to insertions in real medical applications [4]. Flow rates are set to 40, 70 and  $10 \frac{mL}{min}$  for Tissues A, B and C, respectively. Experimental results showed that these flow rates cause the same depth of fracture of 3 mm in these soft tissues in a given time thus keeping the step lengths the same throughout the experiments.

In this section, nozzles with fixed angles are used to cause angled fracture in tissue. Understanding the relationship between fixed angle nozzle and minimum achievable radius of curvature is important. It seems that minimum radius of curvature will be improved with increased nozzle angle. However, there might be some critical angle near 90 degrees after which the minimum radius of curvature does not improve anymore. Therefore, it is also necessary to study the effect of the nozzle angle on achievable radius of curvature of the waterjet steerable needle.

Young's moduli of Tissues A and B are 27 and 68, respectively, which are relevant to stiffnesses of the real biological tissues [274]. In particular, they are similar to uterus and cervix tissues, the Young's moduli of which are in the range of 30 – 90 kPa [112], prostate in the range of 62 – 69 kPa [123], thrombus in the range of 8 – 38 kPa [278], breast with modulus of 29 kPa [89] and muscle in the range of 7 – 57 kPa [185, 131]. Tissue C is also used because this tissue is widely used in literature as the

main soft tissue phantom [235, 113]. This made it possible to compare the results of the waterjet steerable needle to conventional steerable needles. It's Young's modulus is around 17 kPa which is well within the Young's modulus of the skeletal muscle tissue (10-32 kPa) [122], healthy liver (10-20 kPa) [190] and breast glandular tissue (7.5-66 kPa) [76].

Duty cycling of the waterjet is used to control the curvature of the waterjet steerable needle. The reason that increasing duty cycling of the waterjet improved the radius of curvature is that during the times that waterjet is ON, an angled path is cut in the tissue that causes the needle to curve in contrast to insertions with no waterjet that needle almost travels straight. Therefore, the radius of curvature is smaller for experiments where waterjet is ON during the steps and the more steps the waterjet is ON the smaller the radius. This is comparable to the effect of the bent-tip on needle steering.

Different insertion speeds are reported in literature for different medical procedures [252]. Insertions speeds of  $0.4 - 10 \frac{mm}{s}$  are reported for epidural procedures [275] and  $500 \frac{mm}{s}$  is reported for brachytherapy interventions [196]. Frictional force between the needle and tissue increases with the insertion speed. Kaboyashi et al. [116] reported that frictional force increased with speeds up to  $2 \frac{mm}{s}$  and reached a constant value for higher speeds when inserting a 17 G needle into porcine liver at different speeds. Insertion of the needle at high speed has the risk of imprecise movements.

Experimental results showed that the radius of curvature is smaller in stiffer tissues. Yang et al. [284] demonstrated that the curvature of the needle is a function of the bending stiffness of the needle as well as the bending stiffness of the tissue. For harder tissues, the bending stiffness of the tissue is larger thus making the needle to curve more while following the cut path by the waterjet. Future research involves tissue-agnostic waterjet needle steering by adding a sort of control on the tip of the waterjet steerable needle so that the needle follows exactly the cut path and not the path that is a function of the bending stiffness of the fractured path and the bending stiffness of the needle. With a control on the tip of the waterjet steerable needle, the needle can follow tightest curves with radii as low as 1 mm in softest tissues making this a promising method for tissue-agnostic needle steering in the future.

### 3.2.5 *Conclusions*

In this section, a new class of the steerable needles, namely waterjet steerable needles (in which the direction of the tissue fracture is controlled by the waterjet and then the flexible needle follows) is presented. Because of the needle tip design which has an angle from horizontal, a path can be cut at an angle in the tissue that helps the needle to steer by following the path. The effect of the cut-depth on radii of curvature of the needle for two tissue stiffnesses and 4 different waterjet velocities are investigated. The results showed that the curvature of the needle can be controlled by varying waterjet velocity and thus controlling the depth of cut. A mechanics-based

model for depth-of-cut as the main input to the system is presented and a bicycle model with the depth of cut as the main parameter defines a model of the kinematic motion of the needle. A genetic algorithm used to achieve path planning in 2D is also presented.

As another approach to control the curvature of the waterjet steerable needle, it is shown that curvature of the waterjet needle can be controlled by duty cycling of the waterjet (that means the duration of the whole insertion that the waterjet is ON) from 0% to 100% rates and the best radii of curvature can be obtained by 100% waterjet duty cycling which are 74 mm, 49 mm and 78 mm for Tissues A, B and C, respectively. It is found that the curvature is a linear function of the duty cycling for the range of tissue stiffnesses tested here and that the best radius of curvature obtained by the waterjet is improved in comparison to the conventional steerable needles.

Curvature of the needle is also dependent on the waterjet tip angle and in this section a constant angle nozzle is used. Future research involves developing controllable nozzles to further control the curvature as depicted in Fig. 3.5. The current limitation of the system is developing sub-millimeter waterjet tips with accurate angle with current machining techniques on the current materials. Future research also involves extending the current study to animal studies to see how the needle performs in real living tissues.

## CHAPTER FOUR

### CONCLUSION AND FUTURE WORK

This dissertation has presented the design, implementation and experimental validation of the fracture-directed waterjet steering for percutaneous and surgical applications including (1) a waterjet soft tissue interaction model, (2) a waterjet steerable needle design with slanted tip that achieves small radii of curvature in soft tissues, (3) waterjet steerable needle kinematic model which is a discrete adaptation of the "Bicycle" model and (4) two methods to control the curvature of the waterjet steerable needle system.

In the remainder of this chapter, we briefly summarize the results and contributions in each of these areas and describe ideas for future work. Finally, we conclude with possible extensions of the work to other areas of the medical robotics.

#### 4.1 Waterjet Soft-Tissue Interaction

In Chapter 2, waterjet - soft tissue interaction problem is studied. A Finite Element Analysis of the waterjet interacting with soft tissue is provided. This model could accurately predict the depth of cut of the waterjet in soft tissue and provided an insight in penetration pressure of the waterjet but it is computationally time-consuming. Thus, a mechanics-based model is provided to solve the physics of the waterjet - soft tissue interaction. This model provides a prediction for penetration

pressure and depth of cut of the waterjet in soft tissue based on the mechanical properties of the soft tissue (constitutive response and fracture toughness) as well as the waterjet needle properties (diameter and waterjet velocity). The mechanics based model is validated using penetration experiments in soft tissue simulants and soft tissue characterization tests using static compression tests and Split Hopkinson Pressure Bar tests and fitting the data with Ogden model.

There are several potential directions for this chapter. First off, we have validated the model using soft tissue mimicking simulants. Future research can involve validating this model in *ex vivo* animal tissues for correct characterization and design of the waterjet-assisted medical devices. Second, a high speed camera with a high frame per second rate to capture the behavior of the waterjet penetration and cutting over time is required. This will facilitate the design of the waterjet-assisted medical devices that speed is important.

## **4.2 Fracture-directed Waterjet Needle Steering**

In Chapter 3, we have shown that waterjet can get rid of the cutting force and thus decreases the forces applied to the base of the needle. This can drastically decrease buckling of the needle while inserting into the soft tissue since the needle will not do the cutting and it is the waterjet that does the actual cutting. Then, design, modeling and path planning for fracture directed waterjet steerable needles are discussed. A kinematic model that is a discrete adaptation of the famous "Bicycle"

model is proposed for waterjet in which the length of the steps is predicted with the mathematical description of the depth of cut of the waterjet. The feasibility of the waterjet steerable needle to reach different targets is shown and the effect of the step length (= depth of cut) on radius of curvature is studied. Then, it is shown that the curvature of the waterjet steerable needle can also be controlled by the duty cycling of the waterjet (alternate ON and OFF of the waterjet) and that the curvature is a linear function of the duty cycling rate. It is shown that the radii of curvature for tissues with Young's moduli of 112 and 25 kPa are 49mm and 78 mm, respectively.

In this dissertation, a fixed angle needle tip is used for waterjet steerable needle, where future research direction is to develop controllable nozzles that can shoot water in any direction and curvature control can be done by varying tip angle instead of the duty cycling of the waterjet. By choosing low bending stiffness materials for needle and tip and having some sort of control at the tip of the needle, tissue agnostic steering can be achieved in which the radius of curvature is not dependent on the stiffness of the tissue. Having controllable tip also makes the rotation-free direction change a possibility since rotating a long flexible needle around its access increase the torsional friction which in turn makes the base rotation angle and the tip angle to be out of sync.

Clinical environment remained to be a challenge in this dissertation. Future research can involve testing the waterjet steerable needle system in *ex vivo* and *in vivo*

tissues for realistic surgical applications.

### **4.3 Extensions**

Although this dissertation has focused narrowly on steerable needles, several of the described methods are relevant to other areas of the medical robotics. The FE and mechanics-based models developed in Chapter 2 can be used for designing other waterjet-assisted surgical procedures to predict the penetration pressure and cut depth of the waterjet in soft tissue.

Waterjet-assisted cutting can also be embedded in for example surgical tools along with a suction to perform different surgical operations such as liver dissection and tumor removal. The discrete kinematic model can also serve as a framework in a variety of the robotic interventions.

## BIBLIOGRAPHY

- [1] Momen Abayazid, Marco Kemp, and Sarthak Misra. 3d flexible needle steering in soft-tissue phantoms using fiber bragg grating sensors. In *2013 IEEE International Conference on Robotics and Automation*, pages 5843–5849. IEEE, 2013.
- [2] Momen Abayazid, Pedro Moreira, Navid Shahriari, Anastasios Zompas, and Sarthak Misra. Three-dimensional needle steering using automated breast volume scanner (abvs). *Journal of medical robotics research*, 1(01):1640005, 2016.
- [3] Momen Abayazid, Roy J Roesthuis, Rob Reilink, and Sarthak Misra. Integrating deflection models and image feedback for real-time flexible needle steering. *IEEE transactions on robotics*, 29(2):542–553, 2012.
- [4] Niki Abolhassani, Rajni Patel, and Mehrdad Moallem. Control of soft tissue deformation during robotic needle insertion. *Minimally invasive therapy & allied technologies*, 15(3):165–176, 2006.
- [5] Niki Abolhassani, Rajni Patel, and Mehrdad Moallem. Needle insertion into soft tissue: A survey. *Medical engineering & physics*, 29(4):413–431, 2007.
- [6] Troy K Adebar, Joseph D Greer, Paul F Laeseke, Gloria L Hwang, and Allison M Okamura. Methods for improving the curvature of steerable needles in

- biological tissue. *IEEE Transactions on Biomedical Engineering*, 63(6):1167–1177, 2015.
- [7] Troy K Adebar, Joseph D Greer, Paul F Laeseke, Gloria L Hwang, and Allison M Okamura. Methods for improving the curvature of steerable needles in biological tissue. *IEEE Transactions on Biomedical Engineering*, 63(6):1167–1177, 2016.
- [8] Troy K Adebar and Allison M Okamura. Recursive estimation of needle pose for control of 3d-ultrasound-guided robotic needle steering. In *2014 IEEE/RSJ International Conference on Intelligent Robots and Systems*, pages 4303–4308. IEEE, 2014.
- [9] Ron Alterovitz, Ken Goldberg, and Allison Okamura. Planning for steerable bevel-tip needle insertion through 2d soft tissue with obstacles. In *Proceedings of the 2005 IEEE international conference on robotics and automation*, pages 1640–1645. IEEE, 2005.
- [10] Ron Alterovitz, Kenneth Y Goldberg, Jean Pouliot, and I-Chow Hsu. Sensorless motion planning for medical needle insertion in deformable tissues. *IEEE Transactions on Information Technology in Biomedicine*, 13(2):217–225, 2008.
- [11] Ron Alterovitz, Andrew Lim, Ken Goldberg, Gregory S Chirikjian, and Allison M Okamura. Steering flexible needles under markov motion uncertainty. In

- 2005 IEEE/RSJ International Conference on Intelligent Robots and Systems*, pages 1570–1575. IEEE, 2005.
- [12] Ron Alterovitz, Thierry Siméon, and Ken Goldberg. The stochastic motion roadmap: A sampling framework for planning with markov motion uncertainty. 2007.
- [13] Ted L Anderson. *Fracture mechanics: fundamentals and applications*. CRC press, 2017.
- [14] GJ Appleby-Thomas, PJ Hazell, JM Wilgeroth, CJ Shepherd, DC Wood, and A Roberts. On the dynamic behavior of three readily available soft tissue simulants. *Journal of Applied Physics*, 109(8):084701, 2011.
- [15] Anubhav Arora, Itzhak Hakim, Joy Baxter, Ruben Rathnasingham, Ravi Srinivasan, Daniel A Fletcher, and Samir Mitragotri. Needle-free delivery of macromolecules across the skin by nanoliter-volume pulsed microjets. *Proceedings of the National Academy of Sciences*, 104(11):4255–4260, 2007.
- [16] Aziz Alami Aroussi, Ibrahim Mohamed Sami, Alain Leguerrier, and Jean Phillippe Verhoye. The blower: a useful tool to complete thrombectomy of the mechanical prosthetic valve. *The Annals of thoracic surgery*, 81(5):1911–1912, 2006.

- [17] Ali Asadian, Rajni V Patel, and Mehrdad R Kermani. Dynamics of translational friction in needle–tissue interaction during needle insertion. *Annals of biomedical engineering*, 42(1):73–85, 2014.
- [18] AG Atkins. Toughness and cutting: a new way of simultaneously determining ductile fracture toughness and strength. *Engineering fracture mechanics*, 72(6):849–860, 2005.
- [19] Elif Ayvali, Chia-Pin Liang, Mingyen Ho, Yu Chen, and Jaydev P Desai. Towards a discretely actuated steerable cannula for diagnostic and therapeutic procedures. *The International journal of robotics research*, 31(5):588–603, 2012.
- [20] Toufic Azar and Vincent Hayward. Estimation of the fracture toughness of soft tissue from needle insertion. In *International Symposium on Biomedical Simulation*, pages 166–175. Springer, 2008.
- [21] Mahdieh Babaiasl, Stefano Boccelli, Yao Chen, Fan Yang, Jow-Lian Ding, and John P Swensen. Predictive mechanics-based model for depth of cut (doc) of waterjet in soft tissue for waterjet-assisted medical applications. *Medical & Biological Engineering & Computing*, pages 1–28, 2020.
- [22] Mahdieh Babaiasl, Fan Yang, Yao Chen, Jow-Lian Ding, and John P Swensen. Predicting depth of cut of water-jet in soft tissue simulants based on finite element analysis with the application to fracture-directed water-jet steerable

- needles. In *2019 International Symposium on Medical Robotics (ISMR)*, pages 1–7. IEEE, 2019.
- [23] Mahdiah Babaiasl, Fan Yang, and John P Swensen. Towards water-jet steerable needles. In *2018 7th IEEE International Conference on Biomedical Robotics and Biomechatronics (Biorob)*, pages 601–608. IEEE, 2018.
- [24] HU Baer, GJ Maddern, and LH Blumgart. Hepatic surgery facilitated by a new jet dissector. *HPB Surgery*, 4(2):137–146, 1991.
- [25] HU Baer, GJ Maddern, and LH Blumgart. New water-jet dissector: initial experience in hepatic surgery. *The British journal of surgery*, 78(4):502, 1991.
- [26] Thomas Bahls, Florian A Fröhlich, Anja Hellings, Bastian Deutschmann, and Alin O Albu-Schäffer. Extending the capability of using a waterjet in surgical interventions by the use of robotics. *IEEE Transactions on Biomedical Engineering*, 64(2):284–294, 2016.
- [27] Andrew C Barnett, Yuan-Shin Lee, and Jason Z Moore. Fracture mechanics model of needle cutting tissue. *Journal of Manufacturing Science and Engineering*, 138(1):011005, 2016.
- [28] Joy Baxter and Samir Mitragotri. Jet-induced skin puncture and its impact on needle-free jet injections: experimental studies and a predictive model. *Journal of Controlled release*, 106(3):361–373, 2005.

- [29] Mariana C Bernardes, Bruno V Adorno, Geovany A Borges, and Philippe Poignet. 3d robust online motion planning for steerable needles in dynamic workspaces using duty-cycled rotation. *Journal of Control, Automation and Electrical Systems*, 25(2):216–227, 2014.
- [30] Mariana C Bernardes, Bruno V Adorno, Philippe Poignet, and Geovany A Borges. Semi-automatic needle steering system with robotic manipulator. In *2012 IEEE International Conference on Robotics and Automation*, pages 1595–1600. IEEE, 2012.
- [31] Mariana C Bernardes, Bruno V Adorno, Philippe Poignet, Nabil Zemiti, and Geovany A Borges. Adaptive path planning for steerable needles using duty-cycling. In *2011 IEEE/RSJ International Conference on Intelligent Robots and Systems*, pages 2545–2550. IEEE, 2011.
- [32] MC Bernardes, Bruno Vilhena Adorno, Philippe Poignet, and GA Borges. Robot-assisted automatic insertion of steerable needles with closed-loop imaging feedback and intraoperative trajectory replanning. *Mechatronics*, 23(6):630–645, 2013.
- [33] Richard J Black, Seokchang Ryu, Behzad Moslehi, and Joannes M Costa. Characterization of optically actuated mri-compatible active needles for medical interventions. In *Behavior and Mechanics of Multifunctional Materials and Com-*

- posites 2014*, volume 9058, page 90580J. International Society for Optics and Photonics, 2014.
- [34] Van Khuyen Bui, Sukho Park, Jong-Oh Park, and Seong Young Ko. A novel curvature-controllable steerable needle for percutaneous intervention. *Proceedings of the Institution of Mechanical Engineers, Part H: Journal of Engineering in Medicine*, 230(8):727–738, 2016.
- [35] Jessica Burgner, Philip J Swaney, Ray A Lathrop, Kyle D Weaver, and Robert J Webster. Debulking from within: a robotic steerable cannula for intracerebral hemorrhage evacuation. *IEEE Transactions on Biomedical Engineering*, 60(9):2567–2575, 2013.
- [36] Christopher Burrows, Riccardo Secoli, and Ferdinando Rodriguez y Baena. Experimental characterisation of a biologically inspired 3d steering needle. In *2013 13th International Conference on Control, Automation and Systems (ICCAS 2013)*, pages 1252–1257. IEEE, 2013.
- [37] Louise M Cannon, Andrew J Fagan, and Jacinta E Browne. Novel tissue mimicking materials for high frequency breast ultrasound phantoms. *Ultrasound in medicine & biology*, 37(1):122–135, 2011.
- [38] Wayne J Caputo, Donald J Beggs, Jessica L DeFede, Lisa Simm, and Hussein Dharma. A prospective randomised controlled clinical trial comparing hydro-

- surgery debridement with conventional surgical debridement in lower extremity ulcers. *International wound journal*, 5(2):288–294, 2008.
- [39] Dennis Ceh, Terry M Peters, and Elvis CS Chen. Acoustic characterization of polyvinyl chloride and self-healing silicone as phantom materials. In *Medical Imaging 2015: Physics of Medical Imaging*, volume 9412, page 94123G. International Society for Optics and Photonics, 2015.
- [40] Yu-Chung Chang, Yao Chen, Jialong Ning, Hao Cheng, Mitch Rock, Maher Amer, Shuo Feng, Mojtaba Falahati, Li-Ju Wang, Roland Kuen-Ren Chen, et al. No such thing as trash: A 3d printable polymer composite comprised of oil extracted spent coffee grounds and polylactic acid with enhanced impact toughness. *ACS Sustainable Chemistry & Engineering*, 2019.
- [41] Pierre Chatelain, Alexandre Krupa, and Nassir Navab. 3d ultrasound-guided robotic steering of a flexible needle via visual servoing. In *2015 IEEE International Conference on Robotics and Automation (ICRA)*, pages 2250–2255. IEEE, 2015.
- [42] Alvin I Chen, Max L Balter, Melanie I Chen, Daniel Gross, Sheikh K Alam, Timothy J Maguire, and Martin L Yarmush. Multilayered tissue mimicking skin and vessel phantoms with tunable mechanical, optical, and acoustic properties. *Medical physics*, 43(6Part1):3117–3131, 2016.

- [43] Nuttapong Chentanez, Ron Alterovitz, Daniel Ritchie, Lita Cho, Kris K Hauser, Ken Goldberg, Jonathan R Shewchuk, and James F O'Brien. Interactive simulation of surgical needle insertion and steering. In *ACM SIGGRAPH 2009 papers*, pages 1–10. 2009.
- [44] Beelee Chua, Shashi P Desai, Michael J Tierney, Janet A Tamada, and Arvind N Jina. Effect of microneedles shape on skin penetration and minimally invasive continuous glucose monitoring in vivo. *Sensors and Actuators A: Physical*, 203:373–381, 2013.
- [45] Kerstyn Comley and Norman Fleck. Deep penetration and liquid injection into adipose tissue. *Journal of Mechanics of Materials and Structures*, 6(1):127–140, 2011.
- [46] Noah J Cowan, Ken Goldberg, Gregory S Chirikjian, Gabor Fichtinger, Ron Alterovitz, Kyle B Reed, Vinutha Kallem, Wooram Park, Sarthak Misra, and Allison M Okamura. Robotic needle steering: Design, modeling, planning, and image guidance. In *Surgical robotics*, pages 557–582. Springer, 2011.
- [47] Jessica R Crouch, Chad M Schneider, Josh Wainer, and Allison M Okamura. A velocity-dependent model for needle insertion in soft tissue. In *International Conference on Medical Image Computing and Computer-Assisted Intervention*, pages 624–632. Springer, 2005.

- [48] Naresh V Datla and Parsaoran Hutapea. Flexure-based active needle for enhanced steering within soft tissue. *Journal of Medical Devices*, 9(4), 2015.
- [49] Shawn P Davis, Benjamin J Landis, Zachary H Adams, Mark G Allen, and Mark R Prausnitz. Insertion of microneedles into skin: measurement and prediction of insertion force and needle fracture force. *Journal of biomechanics*, 37(8):1155–1163, 2004.
- [50] Isabela Miller de Carvalho, Lucas Lobianco De Matheo, José Francisco Silva Costa Júnior, Cecília de Melo Borba, Marco Antonio von Krüger, Antonio Fernando Catelli Infantosi, and Wagner Coelho de Albuquerque Pereira. Polyvinyl chloride plastisol breast phantoms for ultrasound imaging. *Ultrasonics*, 70:98–106, 2016.
- [51] Iris De Falco, Costanza Culmone, Arianna Menciassi, Jenny Dankelman, and John J van den Dobbelen. A variable stiffness mechanism for steerable percutaneous instruments: integration in a needle. *Medical & biological engineering & computing*, 56(12):2185–2199, 2018.
- [52] Tonke L de Jong, Loes H Pluymen, Dennis J van Gerwen, Gert-Jan Kleinsink, Jenny Dankelman, and John J van den Dobbelen. Pva matches human liver in needle-tissue interaction. *Journal of the mechanical behavior of biomedical materials*, 69:223–228, 2017.

- [53] Tonke L De Jong, Nick J van de Berg, Lisette Tas, Adriaan Moelker, Jenny Dankelman, and John J van den Dobbelsteen. Needle placement errors: do we need steerable needles in interventional radiology? *Medical devices (Auckland, NZ)*, 11:259, 2018.
- [54] Ehsan Dehghan and Septimiu E Salcudean. Needle insertion parameter optimization for brachytherapy. *IEEE Transactions on Robotics*, 25(2):303–315, 2009.
- [55] Steven den Dunnen, Jenny Dankelman, Gino MMJ Kerkhoffs, and Gabrielle JM Tuijthof. How do jet time, pressure and bone volume fraction influence the drilling depth when waterjet drilling in porcine bone? *Journal of the mechanical behavior of biomedical materials*, 62:495–503, 2016.
- [56] Steven den Dunnen, Lars Mulder, Gino MMJ Kerkhoffs, Jenny Dankelman, and Gabrielle JM Tuijthof. Waterjet drilling in porcine bone: The effect of the nozzle diameter and bone architecture on the hole dimensions. *Journal of the mechanical behavior of biomedical materials*, 27:84–93, 2013.
- [57] Simon P DiMaio and SE Salcudean. Needle steering and model-based trajectory planning. In *International Conference on Medical Image Computing and Computer-Assisted Intervention*, pages 33–40. Springer, 2003.
- [58] Simon P DiMaio and Septimiu E Salcudean. Interactive simulation of needle

- insertion models. *IEEE transactions on biomedical engineering*, 52(7):1167–1179, 2005.
- [59] Simon P DiMaio and Septimiu E Salcudean. Needle steering and motion planning in soft tissues. *IEEE Transactions on Biomedical Engineering*, 52(6):965–974, 2005.
- [60] TW Duerig, A Pelton, and D Stöckel. An overview of nitinol medical applications. *Materials Science and Engineering: A*, 273:149–160, 1999.
- [61] Vincent Duintam, Ron Alterovitz, Shankar Sastry, and Ken Goldberg. Screw-based motion planning for bevel-tip flexible needles in 3d environments with obstacles. In *2008 IEEE international conference on robotics and automation*, pages 2483–2488. IEEE, 2008.
- [62] P Dupont, A Gosline, N Vasilyev, J Lock, E Butler, C Folk, A Cohen, R Chen, G Schmitz, H Ren, et al. Concentric tube robots for minimally invasive surgery. In *hamlyn symposium on medical robotics*, volume 7, page 8, 2012.
- [63] Pierre E Dupont, Jesse Lock, Brandon Itkowitz, and Evan Butler. Design and control of concentric-tube robots. *IEEE Transactions on Robotics*, 26(2):209–225, 2009.
- [64] Christian Duriez, Christophe Guébert, Maud Marchal, Stéphane Cotin, and Laurent Grisoni. Interactive simulation of flexible needle insertions based on

- constraint models. In *International Conference on Medical Image Computing and Computer-Assisted Intervention*, pages 291–299. Springer, 2009.
- [65] AA El-Domiaty and AA Abdel-Rahman. Fracture mechanics-based model of abrasive waterjet cutting for brittle materials. *The international journal of advanced manufacturing technology*, 13(3):172–181, 1997.
- [66] Johnathan A Engh, Davneet S Minhas, Douglas Kondziolka, and Cameron N Riviere. Percutaneous intracerebral navigation by duty-cycled spinning of flexible bevel-tipped needles. *Neurosurgery*, 67(4):1117–1123, 2010.
- [67] Johnathan A Engh, G Podnar, D Kondziolka, and Cameron N Riviere. Toward effective needle steering in brain tissue. In *2006 International Conference of the IEEE Engineering in Medicine and Biology Society*, pages 559–562. IEEE, 2006.
- [68] Mojtaba Falahati, Wenchen Zhou, Allen Yi, and Lei Li. Fabrication of polymeric lenses using magnetic liquid molds. *Applied Physics Letters*, 114(20):203701, 2019.
- [69] Mojtaba Falahati, Wenchen Zhou, Allen Yi, and Lei Li. Development of an adjustable-focus ferrogel mirror. *Optics & Laser Technology*, 125:106021, 2020.
- [70] Bitra Fallahi, Carlos Rossa, Ron S Sloboda, Nawaid Usmani, and Mahdi

- Tavakoli. Sliding-based switching control for image-guided needle steering in soft tissue. *IEEE Robotics and Automation Letters*, 1(2):860–867, 2016.
- [71] Alexis I Farrer, Henrik Odéen, Joshua de Bever, Brittany Coats, Dennis L Parker, Allison Payne, and Douglas A Christensen. Characterization and evaluation of tissue-mimicking gelatin phantoms for use with mrgfus. *Journal of therapeutic ultrasound*, 3(1):9, 2015.
- [72] M Fonseca, B Zeqiri, PC Beard, and BT Cox. Characterisation of a phantom for multiwavelength quantitative photoacoustic imaging. *Physics in Medicine & Biology*, 61(13):4950, 2016.
- [73] Antonio E Forte, Stefano Galvan, Francesco Manieri, Ferdinando Rodriguez y Baena, and Daniele Dini. A composite hydrogel for brain tissue phantoms. *Materials & Design*, 112:227–238, 2016.
- [74] L Frasson, SY Ko, A Turner, T Parittotokkaporn, Julian F Vincent, and F Rodriguez y Baena. Sting: a soft-tissue intervention and neurosurgical guide to access deep brain lesions through curved trajectories. *Proceedings of the Institution of Mechanical Engineers, Part H: Journal of Engineering in Medicine*, 224(6):775–788, 2010.
- [75] Mengyu Fu, Alan Kuntz, Robert J Webster, and Ron Alterovitz. Safe motion planning for steerable needles using cost maps automatically extracted from

- pulmonary images. In *2018 IEEE/RSJ International Conference on Intelligent Robots and Systems (IROS)*, pages 4942–4949. IEEE, 2018.
- [76] Amit Gefen and Benny Dilmoney. Mechanics of the normal woman’s breast. *Technology and Health Care*, 15(4):259–271, 2007.
- [77] Giada Gerboni, Joseph D Greer, Paul F Laeseke, Gloria L Hwang, and Allison M Okamura. Highly articulated robotic needle achieves distributed ablation of liver tissue. *IEEE Robotics and Automation Letters*, 2017.
- [78] Hunter B Gilbert, Joseph Neimat, and Robert J Webster. Concentric tube robots as steerable needles: Achieving follow-the-leader deployment. *IEEE Transactions on Robotics*, 31(2):246–258, 2015.
- [79] D. Glozman and M. Shoham. Image-guided robotic flexible needle steering. *IEEE Trans. Robot.*, 23(3):459–467, 2007.
- [80] Daniel Glozman and Moshe Shoham. Flexible needle steering and optimal trajectory planning for percutaneous therapies. In *International Conference on Medical Image Computing and Computer-Assisted Intervention*, pages 137–144. Springer, 2004.
- [81] Daniel Glozman and Moshe Shoham. Image-guided robotic flexible needle steering. *IEEE Transactions on Robotics*, 23(3):459–467, 2007.

- [82] Orcun Goksel, Ehsan Dehghan, and Septimiu E Salcudean. Modeling and simulation of flexible needles. *Medical engineering & physics*, 31(9):1069–1078, 2009.
- [83] Mark S Granick, John Posnett, Michael Jacoby, BS, Shyam Noruthun, Parham A Ganchi, and Ramazi O Datiashvili. Efficacy and cost-effectiveness of a high-powered parallel waterjet for wound debridement. *Wound repair and regeneration*, 14(4):394–397, 2006.
- [84] Peter D Grimm, John C Blasko, John E Sylvester, Robert M Meier, and William Cavanagh. 10-year biochemical (prostate-specific antigen) control of prostate cancer with 125i brachytherapy. *International Journal of Radiation Oncology\* Biology\* Physics*, 51(1):31–40, 2001.
- [85] Raffi Gurunluoglu. Experiences with waterjet hydrosurgery system in wound debridement. *World Journal of Emergency Surgery*, 2(1):10, 2007.
- [86] Junhyoung Ha, Georgios Fagogenis, and Pierre E Dupont. Modeling tube clearance and bounding the effect of friction in concentric tube robot kinematics. *IEEE Transactions on Robotics*, 35(2):353–370, 2018.
- [87] Amir Haddadi and Keyvan Hashtrudi-Zaad. Development of a dynamic model for bevel-tip flexible needle insertion into soft tissues. In *2011 Annual Inter-*

- national Conference of the IEEE Engineering in Medicine and Biology Society*, pages 7478–7482. IEEE, 2011.
- [88] Noura Hamz e, Igor Peterl ik, St ephane Cotin, and Caroline Essert. Preoperative trajectory planning for percutaneous procedures in deformable environments. *Computerized Medical Imaging and Graphics*, 47:16–28, 2016.
- [89] Lianghao Han, J Alison Noble, and Michael Burcher. A novel ultrasound indentation system for measuring biomechanical properties of in vivo soft tissue. *Ultrasound in medicine & biology*, 29(6):813–823, 2003.
- [90] Kris Hauser, Ron Alterovitz, Nuttapon Chentanez, Allison Okamura, and Ken Goldberg. Feedback control for steering needles through 3d deformable tissue using helical paths. *Robotics science and systems: online proceedings*, page 37, 2009.
- [91] Matt Heverly, Pierre Dupont, and John Triedman. Trajectory optimization for dynamic needle insertion. In *Robotics and Automation, 2005. ICRA 2005. Proceedings of the 2005 IEEE International Conference on*, pages 1646–1651. IEEE, 2005.
- [92] Sergej Hloch, Jan Valicek, and Dra zan Kozak. Preliminary results of experimental cutting of porcine bones by abrasive waterjet. *Tehnicki Vjesnik-Technical Gazette*, 18(3):467–470, 2011.

- [93] Xiaohua Hu, Ang Chen, Yigang Luo, Chris Zhang, and Edwin Zhang. Steerable catheters for minimally invasive surgery: a review and future directions. *Computer Assisted Surgery*, 23(1):21–41, 2018.
- [94] Y Hu, T Liu, JL Ding, and WH Zhong. Behavior of high density polyethylene and its nanocomposites under static and dynamic compression loadings. *Polymer Composites*, 34(3):417–425, 2013.
- [95] J Hubert, E Mourey, JM Sutry, A Coissard, J Floquet, and P Mangin. Water-jet dissection in renal surgery: experimental study of a new device in the pig. *Urological research*, 24(6):355–359, 1996.
- [96] Nikolai Hungr, Jean-Alexandre Long, Vincent Beix, and Jocelyne Troccaz. A realistic deformable prostate phantom for multimodal imaging and needle-insertion procedures. *Medical physics*, 39(4):2031–2041, 2012.
- [97] Mahdi Ilami, Reza James Ahmed, Alex Petras, Borhan Beigzadeh, and Hamid Marvi. Magnetic needle steering in soft phantom tissue. *Scientific Reports*, 10(1):1–11, 2020.
- [98] Shan Jiang, Nobuhiko Hata, and Ron Kikinis. Needle insertion simulation for image-guided brachytherapy of prostate cancer. In *2008 2nd International Conference on Bioinformatics and Biomedical Engineering*, pages 1682–1685. IEEE, 2008.

- [99] Shan Jiang, Pan Li, Yan Yu, Jun Liu, and Zhiyong Yang. Experimental study of needle–tissue interaction forces: effect of needle geometries, insertion methods and tissue characteristics. *Journal of biomechanics*, 47(13):3344–3353, 2014.
- [100] Shan Jiang, Sha Liu, and Wenhao Feng. Pva hydrogel properties for biomedical application. *Journal of the mechanical behavior of biomedical materials*, 4(7):1228–1233, 2011.
- [101] Shan Jiang, Zhiliang Su, Xingji Wang, Sha Liu, and Yan Yu. Development of a new tissue-equivalent material applied to optimizing surgical accuracy. *Materials Science and Engineering: C*, 33(7):3768–3774, 2013.
- [102] Mathieu Joinié-Maurin, Bernard Bayle, and Jacques Gangloff. Force feedback teleoperation with periodical disturbance compensation. In *2011 IEEE International Conference on Robotics and Automation*, pages 4828–4833. IEEE, 2011.
- [103] GFBA Kaehler, MG Sold, K Fischer, S Post, and M Enderle. Selective fluid cushion in the submucosal layer by water jet: advantage for endoscopic mucosal resection. *European Surgical Research*, 39(2):93–97, 2007.
- [104] Vinutha Kallem and Noah J Cowan. Image-guided control of flexible bevel-tip needles. In *Proceedings 2007 IEEE International Conference on Robotics and Automation*, pages 3015–3020. IEEE, 2007.

- [105] Takahisa Kato, Ichiro Okumura, Sang-Eun Song, Alexandra J Golby, and Nobuhiko Hata. Tendon-driven continuum robot for endoscopic surgery: Preclinical development and validation of a tension propagation model. *IEEE/ASME Transactions on Mechatronics*, 20(5):2252–2263, 2014.
- [106] Deborah R Kaye, Dan Stoianovici, and Misop Han. Robotic ultrasound and needle guidance for prostate cancer management: review of the contemporary literature. *Current opinion in urology*, 24(1):75, 2014.
- [107] Mohsen Khadem, Bitah Fallahi, Carlos Rossa, Ron S Sloboda, Nawaid Usmani, and Mahdi Tavakoli. A mechanics-based model for simulation and control of flexible needle insertion in soft tissue. In *2015 IEEE International Conference on Robotics and Automation (ICRA)*, pages 2264–2269. IEEE, 2015.
- [108] Mohsen Khadem, Carlos Rossa, Nawaid Usmani, Ron S Sloboda, and Mahdi Tavakoli. Introducing notched flexible needles with increased deflection curvature in soft tissue. In *Advanced Intelligent Mechatronics (AIM), 2016 IEEE International Conference on*, pages 1186–1191. IEEE, 2016.
- [109] Mohsen Khadem, Carlos Rossa, Nawaid Usmani, Ron S Sloboda, and Mahdi Tavakoli. A two-body rigid/flexible model of needle steering dynamics in soft tissue. *IEEE/ASME Transactions on Mechatronics*, 21(5):2352–2364, 2016.
- [110] Mohsen Khadem, Carlos Rossa, Nawaid Usmani, Ron S Sloboda, and Mahdi

- Tavakoli. Robotic-assisted needle steering around anatomical obstacles using notched steerable needles. *IEEE journal of biomedical and health informatics*, 22(6):1917–1928, 2017.
- [111] Yoonho Kim, German A Parada, Shengduo Liu, and Xuanhe Zhao. Ferromagnetic soft continuum robots. *Science Robotics*, 4(33):eaax7329, 2019.
- [112] Miklos Z Kiss, Maritza A Hobson, Tomy Varghese, Josephine Harter, Mark A Kliewer, Ellen M Hartenbach, and James A Zagzebski. Frequency-dependent complex modulus of the uterus: preliminary results. *Physics in Medicine & Biology*, 51(15):3683, 2006.
- [113] Seong Young Ko, Luca Frasson, and Ferdinando Rodriguez y Baena. Closed-loop planar motion control of a steerable probe with a “programmable bevel” inspired by nature. *IEEE Transactions on Robotics*, 27(5):970–983, 2011.
- [114] Seong Young Ko and Ferdinando Rodriguez y Baena. Toward a miniaturized needle steering system with path planning for obstacle avoidance. *IEEE Transactions on Biomedical Engineering*, 60(4):910–917, 2012.
- [115] Seong Young Ko and Ferdinando Rodriguez y Baena. Trajectory following for a flexible probe with state/input constraints: An approach based on model predictive control. *Robotics and Autonomous systems*, 60(4):509–521, 2012.

- [116] Yo Kobayashi, Takahiro Sato, and Masakatsu G Fujie. Modeling of friction force based on relative velocity between liver tissue and needle for needle insertion simulation. In *2009 Annual International Conference of the IEEE Engineering in Medicine and Biology Society*, pages 5274–5278. IEEE, 2009.
- [117] Aimee C Kok, Steven den Dunnen, Kaj TA Lambers, Gino MMJ Kerkhoffs, and Gabrielle JM Tuijthof. Feasibility study to determine if microfracture surgery using water jet drilling is potentially safe for talar chondral defects in a caprine model. *Cartilage*, page 1947603519880332, 2019.
- [118] Bardia Konh, Mohammad Honarvar, Kurosh Darvish, and Parsaoran Hutapea. Simulation and experimental studies in needle–tissue interactions. *Journal of clinical monitoring and computing*, 31(4):861–872, 2017.
- [119] Bardia Konh and Mahdi Motaleb. Evaluating the performance of an advanced smart needle prototype inside tissue. In *Active and Passive Smart Structures and Integrated Systems 2017*, volume 10164, page 101640G. International Society for Optics and Photonics, 2017.
- [120] Bardia Konh and Tarun K Podder. Design and fabrication of a robust active needle using sma wires. In *2017 Design of Medical Devices Conference*. American Society of Mechanical Engineers Digital Collection, 2017.
- [121] Bardia Konh, Dayne Sasaki, Tarun K Podder, and Hashem Ashrafiun. 3d

- manipulation of an active steerable needle via actuation of multiple sma wires. *Robotica*, 38(3):410–426, 2020.
- [122] Brian Chin Wing Kot, Zhi Jie Zhang, Arthur Wai Chun Lee, Vivian Yee Fong Leung, and Siu Ngor Fu. Elastic modulus of muscle and tendon with shear wave ultrasound elastography: variations with different technical settings. *PloS one*, 7(8), 2012.
- [123] Thomas A Krouskop, Thomas M Wheeler, Faouzi Kallel, Brian S Garra, and Timothy Hall. Elastic moduli of breast and prostate tissues under compression. *Ultrasonic imaging*, 20(4):260–274, 1998.
- [124] Alexandre Krupa. A new duty-cycling approach for 3d needle steering allowing the use of the classical visual servoing framework for targeting tasks. In *5th IEEE RAS/EMBS International Conference on Biomedical Robotics and Biomechatronics*, pages 301–307. IEEE, 2014.
- [125] Pijush K Kundu and Ira M Cohen. *Fluid mechanics 4th ed.* Academic Press San Diego, CA, 2008.
- [126] Jaeyeon Lee and Wooram Park. A probability-based path planning method using fuzzy logic. In *2014 IEEE/RSJ International Conference on Intelligent Robots and Systems*, pages 2978–2984. IEEE, 2014.

- [127] Jaeyeon Lee, Jing Wang, and Wooram Park. Efficient mechanism design and systematic operation planning for tube-wire flexible needles. *Journal of Mechanisms and Robotics*, 10(6), 2018.
- [128] Thomas Lehmann, Ronald Sloboda, Nawaid Usmani, and Mahdi Tavakoli. Model-based needle steering in soft tissue via lateral needle actuation. *IEEE Robotics and Automation Letters*, 3(4):3930–3936, 2018.
- [129] Alexander Leibinger, Antonio E Forte, Zhengchu Tan, Matthew J Oldfield, Frank Beyrau, Daniele Dini, and Ferdinando Rodriguez y Baena. Soft tissue phantoms for realistic needle insertion: a comparative study. *Annals of biomedical engineering*, 44(8):2442–2452, 2016.
- [130] Riccardo Lencioni, Laura Crocetti, Maria Clotilde Della Pina, and Dania Cioni. Percutaneous image-guided radiofrequency ablation of liver tumors. *Abdominal imaging*, 34(5):547–556, 2009.
- [131] Stephen F Levinson, Masahiko Shinagawa, and Takuso Sato. Sonoelastic determination of human skeletal muscle elasticity. *Journal of biomechanics*, 28(10):1145–1154, 1995.
- [132] Pan Li, Shan Jiang, Yan Yu, Jun Yang, and Zhiyong Yang. Biomaterial characteristics and application of silicone rubber and pva hydrogels mimicked in

- organ groups for prostate brachytherapy. *Journal of the mechanical behavior of biomedical materials*, 49:220–234, 2015.
- [133] Pan Li, Zhiyong Yang, and Shan Jiang. Needle-tissue interactive mechanism and steering control in image-guided robot-assisted minimally invasive surgery: a review. *Medical & biological engineering & computing*, 56(6):931–949, 2018.
- [134] Pan Li, Zhiyong Yang, and Shan Jiang. Tissue mimicking materials in image-guided needle-based interventions: A review. *Materials Science and Engineering: C*, 93:1116–1131, 2018.
- [135] Weisi Li, Barry Belmont, Joan M Greve, Adam B Manders, Brian C Downey, Xi Zhang, Zhen Xu, Dongming Guo, and Albert Shih. Polyvinyl chloride as a multimodal tissue-mimicking material with tuned mechanical and medical imaging properties. *Medical physics*, 43(10):5577–5592, 2016.
- [136] Weisi Li, Barry Belmont, and Albert Shih. Design and manufacture of polyvinyl chloride (pvc) tissue mimicking material for needle insertion. *Procedia Manufacturing*, 1:866–878, 2015.
- [137] Dun Liu, Hongtao Zhu, Chuanzhen Huang, Jun Wang, and Peng Yao. Prediction model of depth of penetration for alumina ceramics turned by abrasive waterjet—finite element method and experimental study. *The International Journal of Advanced Manufacturing Technology*, 87(9-12):2673–2682, 2016.

- [138] Jian Liu, Yuanli Bai, and Chengying Xu. Evaluation of ductile fracture models in finite element simulation of metal cutting processes. *Journal of Manufacturing Science and Engineering*, 136(1):011010, 2014.
- [139] Jing Liu, Jason H Ko, Erwin Secretov, Eric Huang, Christiana Chukwu, Julie West, Katherine Piserchia, and Robert D Galiano. Comparing the hydrosurgery system to conventional debridement techniques for the treatment of delayed healing wounds: a prospective, randomised clinical trial to investigate clinical efficacy and cost-effectiveness. *International wound journal*, 12(4):456–461, 2015.
- [140] Yuwang Liu, Zhuang Ge, Shangkui Yang, Ian D Walker, and Zhaojie Ju. Elephant’s trunk robot: An extremely versatile under-actuated continuum robot driven by a single motor. *Journal of Mechanisms and Robotics*, 11(5), 2019.
- [141] Julio R Lobo, Mehdi Moradi, Nick Chng, Ehsan Dehghan, William J Morris, Gabor Fichtinger, and Septimiu E Salcudean. Use of needle track detection to quantify the displacement of stranded seeds following prostate brachytherapy. *IEEE transactions on medical imaging*, 31(3):738–748, 2011.
- [142] Dylan P Losey, Peter A York, Philip J Swaney, Jessica Burgner, and Robert J Webster III. A flexure-based wrist for needle-sized surgical robots. In *Medical Imaging 2013: Image-Guided Procedures, Robotic Interventions, and Modeling*,

- volume 8671, page 86711G. International Society for Optics and Photonics, 2013.
- [143] Lisa A Lyons, Robert J Webster, and Ron Alterovitz. Planning active cannula configurations through tubular anatomy. In *2010 IEEE international conference on robotics and automation*, pages 2082–2087. IEEE, 2010.
- [144] A Maghsoudi and M Jahed. Needle dynamics modelling and control in prostate brachytherapy. *IET control theory & applications*, 6(11):1671–1681, 2012.
- [145] Mohsen Mahvash and Vincent Hayward. Haptic rendering of cutting: A fracture mechanics approach. 2001.
- [146] Ann Majewicz, Steven P Marra, Mark G Van Vledder, MingDe Lin, Michael A Choti, Danny Y Song, and Allison M Okamura. Behavior of tip-steerable needles in ex vivo and in vivo tissue. *IEEE Transactions on Biomedical Engineering*, 59(10):2705–2715, 2012.
- [147] Ann Majewicz and Allison M Okamura. Cartesian and joint space teleoperation for nonholonomic steerable needles. In *2013 World Haptics Conference (WHC)*, pages 395–400. IEEE, 2013.
- [148] Ann Majewicz, Joshua J Siegel, Andrew A Stanley, and Allison M Okamura. Design and evaluation of duty-cycling steering algorithms for robotically-driven

- steerable needles. In *2014 IEEE International Conference on Robotics and Automation (ICRA)*, pages 5883–5888. IEEE, 2014.
- [149] Ann Majewicz, Thomas R Wedlick, Kyle B Reed, and Allison M Okamura. Evaluation of robotic needle steering in ex vivo tissue. In *2010 IEEE International Conference on Robotics and Automation*, pages 2068–2073. IEEE, 2010.
- [150] Vishnu G Mallapragada, Nilanjan Sarkar, and Tarun K Podder. Robot-assisted real-time tumor manipulation for breast biopsy. *IEEE Transactions on Robotics*, 25(2):316–324, 2009.
- [151] Eloise Matheson, Riccardo Secoli, Christopher Burrows, Alexander Leibinger, and Ferdinando Rodriguez y Baena. Cyclic motion control for programmable bevel-tip needles to reduce tissue deformation. *Journal of Medical Robotics Research*, 4(01):1842001, 2019.
- [152] MA Meltsner, NJ Ferrier, and BR Thomadsen. Observations on rotating needle insertions using a brachytherapy robot. *Physics in Medicine & Biology*, 52(19):6027, 2007.
- [153] Paul Mignon, Philippe Poinet, and Jocelyne Troccaz. Beveled-tip needle-steering using 3d ultrasound, mechanical-based kalman filter and curvilinear roi prediction. In *2016 14th International Conference on Control, Automation, Robotics and Vision (ICARCV)*, pages 1–6. IEEE, 2016.

- [154] Paul Mignon, Philippe Poignet, and Jocelyne Troccaz. Automatic robotic steering of flexible needles from 3d ultrasound images in phantoms and ex vivo biological tissue. *Annals of biomedical engineering*, 46(9):1385–1396, 2018.
- [155] Davneet S Minhas, Johnathan A Engh, Michele M Fenske, and Cameron N Riviere. Modeling of needle steering via duty-cycled spinning. In *2007 29th Annual International Conference of the IEEE Engineering in Medicine and Biology Society*, pages 2756–2759. IEEE, 2007.
- [156] Joshua A Minton, Amin Iravani, and Azizeh-Mitra Yousefi. Improving the homogeneity of tissue-mimicking cryogel phantoms for medical imaging. *Medical physics*, 39(11):6796–6807, 2012.
- [157] Sarthak Misra, Kyle B Reed, Andrew S Douglas, KT Ramesh, and Allison M Okamura. Needle-tissue interaction forces for bevel-tip steerable needles. In *Biomedical Robotics and Biomechatronics, 2008. BioRob 2008. 2nd IEEE RAS & EMBS International Conference on*, pages 224–231. IEEE, 2008.
- [158] Sarthak Misra, Kyle B Reed, Benjamin W Schafer, KT Ramesh, and Allison M Okamura. Observations and models for needle-tissue interactions. In *2009 IEEE International Conference on Robotics and Automation*, pages 2687–2692. IEEE, 2009.
- [159] Sarthak Misra, Kyle B Reed, Benjamin W Schafer, KT Ramesh, and Allison M

- Okamura. Mechanics of flexible needles robotically steered through soft tissue. *The International journal of robotics research*, 29(13):1640–1660, 2010.
- [160] Samir Mitragotri. Current status and future prospects of needle-free liquid jet injectors. *Nature reviews Drug discovery*, 5(7):543, 2006.
- [161] Oscar Caravaca Mora, Philippe Zanne, Lucile Zorn, Florent Nageotte, Natalia Zulina, Sara Gravelyn, Paul Montgomery, Michel de Mathelin, Bernard Dallemagne, and Michalina J Gora. Steerable oct catheter for real-time assistance during teleoperated endoscopic treatment of colorectal cancer. *Biomedical optics express*, 11(3):1231–1243, 2020.
- [162] Samir Morad, Christian Ulbricht, Paul Harkin, Justin Chan, Kim Parker, and Ravi Vaidyanathan. Flexible robotic device for spinal surgery. In *2014 IEEE International Conference on Robotics and Biomimetics (ROBIO 2014)*, pages 235–240. IEEE, 2014.
- [163] Samir Morad, Christian Ulbricht, Paul Harkin, Justin Chan, Kim Parker, and Ravi Vaidyanathan. Modelling and control of a water jet cutting probe for flexible surgical robot. In *2015 IEEE International Conference on Automation Science and Engineering (CASE)*, pages 1159–1164. IEEE, 2015.
- [164] M Moradiafrapoli and JO Marston. High-speed video investigation of jet dy-

- namics from narrow orifices for needle-free injection. *Chemical Engineering Research and Design*, 117:110–121, 2017.
- [165] Pedro Moreira and Sarthak Misra. Biomechanics-based curvature estimation for ultrasound-guided flexible needle steering in biological tissues. *Annals of biomedical engineering*, 43(8):1716–1726, 2015.
- [166] Pedro Moreira, Sachin Patil, Ron Alterovitz, and Sarthak Misra. Needle steering in biological tissue using ultrasound-based online curvature estimation. In *2014 IEEE International Conference on Robotics and Automation (ICRA)*, pages 4368–4373. IEEE, 2014.
- [167] Pedro Moreira, Gert van de Steeg, Thijs Krabben, Jonathan Zandman, Edsko EG Hekman, Ferdinand van der Heijden, Ronald Borra, and Sarthak Misra. The miriam robot: A novel robotic system for mr-guided needle insertion in the prostate. *Journal of medical robotics research*, 2(04):1750006, 2017.
- [168] Randy A Mrozek, Brad Leighliter, Christopher S Gold, Ian R Beringer, H Yu Jian, Mark R VanLandingham, Paul Moy, Mark H Foster, and Joseph L Lenhart. The relationship between mechanical properties and ballistic penetration depth in a viscoelastic gel. *Journal of the mechanical behavior of biomedical materials*, 44:109–120, 2015.
- [169] Meenakshi Narayan, Michael A Choti, and Ann Majewicz Fey. Data-driven

- detection of needle buckling events in robotic needle steering. *Journal of Medical Robotics Research*, 4(02):1850005, 2019.
- [170] Zipi Neubach and Moshe Shoham. Ultrasound-guided robot for flexible needle steering. *IEEE Transactions on Biomedical Engineering*, 57(4):799–805, 2009.
- [171] Joachim Oertel, Michael Robert Gaab, Andreas Knapp, Harald Essig, Rolf Warzok, and Juergen Piek. Water jet dissection in neurosurgery: experimental results in the porcine cadaveric brain. *Neurosurgery*, 52(1):153–159, 2003.
- [172] Joachim Oertel, Michael Robert Gaab, Rolf Warzok, and Jürgen Piek. Waterjet dissection in the brain: review of the experimental and clinical data with special reference to meningioma surgery. *Neurosurgical review*, 26(26-4):168–174, 2003.
- [173] Joachim Oertel, Michail Gen, Joachim K Krauss, Matthias Zumkeller, and Michael R Gaab. The use of waterjet dissection in endoscopic neurosurgery. *Journal of neurosurgery*, 105(6):928–931, 2006.
- [174] Raymond William Ogden. Large deformation isotropic elasticity—on the correlation of theory and experiment for incompressible rubberlike solids. *Proceedings of the Royal Society of London. A. Mathematical and Physical Sciences*, 326(1567):565–584, 1972.
- [175] RW Ogden, Giuseppe Saccomandi, and Ivonne Sgura. Fitting hyperelastic models to experimental data. *Computational Mechanics*, 34(6):484–502, 2004.

- [176] Tae-Min Oh and Gye-Chun Cho. Rock cutting depth model based on kinetic energy of abrasive waterjet. *Rock Mechanics and Rock Engineering*, 49(3):1059–1072, 2016.
- [177] Allison M Okamura, Christina Simone, and Mark D O’leary. Force modeling for needle insertion into soft tissue. *IEEE transactions on biomedical engineering*, 51(10):1707–1716, 2004.
- [178] Stephen Okazawa, Richelle Ebrahimi, Jason Chuang, Septimiu E Salcudean, and Robert Rohling. Hand-held steerable needle device. *IEEE/ASME Transactions on Mechatronics*, 10(3):285–296, 2005.
- [179] Kazimierz A Orłowski, Tomasz Ochrymiuk, Anthony Atkins, and Daniel Chuchala. Application of fracture mechanics for energetic effects predictions while wood sawing. *Wood Science and Technology*, 47(5):949–963, 2013.
- [180] Kevin O’Brien, Zachary R Boyer, Benjamin G Mart, Cory T Broliar, Thomas L Carroll, and Loris Fichera. Towards flexible steerable instruments for office-based laryngeal surgery. In *2019 Design of Medical Devices Conference*. American Society of Mechanical Engineers Digital Collection, 2019.
- [181] Dimitrios N Papachristou and Richard Barthers. Resection of the liver with a water jet. *British journal of Surgery*, 69(2):93–94, 1982.

- [182] Wooram Park, Jin Seob Kim, Yu Zhou, Noah J Cowan, Allison M Okamura, and Gregory S Chirikjian. Diffusion-based motion planning for a nonholonomic flexible needle model. In *Proceedings of the 2005 IEEE International Conference on Robotics and Automation*, pages 4600–4605. IEEE, 2005.
- [183] Wooram Park, Kyle B Reed, Allison M Okamura, and Gregory S Chirikjian. Estimation of model parameters for steerable needles. In *2010 IEEE International Conference on Robotics and Automation*, pages 3703–3708. IEEE, 2010.
- [184] Yong-Lae Park, Santhi Elayaperumal, Bruce Daniel, Seok Chang Ryu, Mihye Shin, Joan Savall, Richard J Black, Behzad Moslehi, and Mark R Cutkosky. Real-time estimation of 3-d needle shape and deflection for mri-guided interventions. *IEEE/ASME Transactions On Mechatronics*, 15(6):906–915, 2010.
- [185] KJ Parker, SR Huang, RA Musulin, and RM Lerner. Tissue response to mechanical vibrations for “sonoelasticity imaging”. *Ultrasound in medicine & biology*, 16(3):241–246, 1990.
- [186] Niravkumar A Patel, Tim van Katwijk, Gang Li, Pedro Moreira, Weijian Shang, Sarthak Misra, and Gregory S Fischer. Closed-loop asymmetric-tip needle steering under continuous intraoperative mri guidance. In *2015 37th Annual International Conference of the IEEE Engineering in Medicine and Biology Society (EMBC)*, pages 4869–4874. IEEE, 2015.

- [187] Sachin Patil and Ron Alterovitz. Interactive motion planning for steerable needles in 3d environments with obstacles. In *2010 3rd IEEE RAS & EMBS International Conference on Biomedical Robotics and Biomechatronics*, pages 893–899. IEEE, 2010.
- [188] Sachin Patil, Jessica Burgner, Robert J Webster, and Ron Alterovitz. Needle steering in 3-d via rapid replanning. *IEEE Transactions on Robotics*, 30(4):853–864, 2014.
- [189] Sachin Patil et al. Motion planning under uncertainty in highly deformable environments. *Robotics science and systems: online proceedings*, 2011.
- [190] Yohan Payan. *Soft tissue biomechanical modeling for computer assisted surgery*, volume 11. Springer, 2012.
- [191] Roumen D Penchev, Julian E Losanoff, and Kirien T Kjossev. Reconstructive renal surgery using a water jet. *The Journal of urology*, 162(3):772–774, 1999.
- [192] BG Persson, B Jeppsson, KG Tranberg, K Roslund, and S Bengmark. Transection of the liver with a water jet. *Surg Gynecol Obstet*, 168(3):267–268, 1989.
- [193] Olivier Piccin, Laurent Barbe, Bernard Bayle, Michel De Mathelin, and Afshin Gangi. A force feedback teleoperated needle insertion device for percutaneous procedures. *The International Journal of Robotics Research*, 28(9):1154–1168, 2009.

- [194] Juergen Piek, Joachim Oertel, and Michael Robert Gaab. Waterjet dissection in neurosurgical procedures: clinical results in 35 patients. *Journal of neurosurgery*, 96(4):690–696, 2002.
- [195] T Podder, D Clark, J Sherman, D Fuller, E Messing, D Rubens, J Strang, Y Zhang, W O’Dell, W Ng, et al. Effects of tip geometry of surgical needles: an assessment of force and deflection. In *IFMBE Proc*, volume 11, pages 1727–1983, 2005.
- [196] Tarun Podder, Douglas Clark, Jason Sherman, Dave Fuller, Edward Messing, Deborah Rubens, John Strang, Ralph Brasacchio, Lydia Liao, Wan-Sing Ng, et al. In vivo motion and force measurement of surgical needle intervention during prostate brachytherapy. *Medical physics*, 33(8):2915–2922, 2006.
- [197] HG Rau, AP Duessel, and S Wurzbacher. The use of water-jet dissection in open and laparoscopic liver resection. *HPB*, 10(4):275–280, 2008.
- [198] HG Rau, G Meyer, KW Jauch, TU Cohnert, E Buttler, and FW Schildberg. Liver resection with the water jet: conventional and laparoscopic surgery. *Der Chirurg; Zeitschrift fur alle Gebiete der operativen Medizen*, 67(5):546–551, 1996.
- [199] Kyle B Reed, Vinutha Kallem, Ron Alterovitz, Ken Goldbergx, Allison M Okamura, and Noah J Cowan. Integrated planning and image-guided control

- for planar needle steering. In *2008 2nd IEEE RAS & EMBS International Conference on Biomedical Robotics and Biomechatronics*, pages 819–824. IEEE, 2008.
- [200] Kyle B Reed, Ann Majewicz, Vinutha Kallem, Ron Alterovitz, Ken Goldberg, Noah J Cowan, and Allison M Okamura. Robot-assisted needle steering. *IEEE robotics & automation magazine*, 18(4):35–46, 2011.
- [201] Kyle B Reed, Allison M Okamura, and Noah J Cowan. Controlling a robotically steered needle in the presence of torsional friction. In *2009 IEEE International Conference on Robotics and Automation*, pages 3476–3481. IEEE, 2009.
- [202] Kyle B Reed, Allison M Okamura, and Noah J Cowan. Modeling and control of needles with torsional friction. *IEEE transactions on biomedical engineering*, 56(12):2905–2916, 2009.
- [203] Kyle B. Reed, Allison M. Okamura, and Noah J. Cowan. Modeling and control of needles with torsional friction. *IEEE Trans. Biomed. Eng.*, 56(12):2905–2916, December 2009. NIHMS192959.
- [204] Rogers C Ritter, Elizabeth G Quate, George T Gillies, M Sean Grady, MA Howard, and William C Broaddus. Measurement of friction on straight catheters in in vitro brain and phantom material. *IEEE transactions on biomedical engineering*, 45(4):476–485, 1998.

- [205] Roy J Roesthuis, Momen Abayazid, and Sarthak Misra. Mechanics-based model for predicting in-plane needle deflection with multiple bends. In *2012 4th IEEE RAS & EMBS International Conference on Biomedical Robotics and Biomechanics (BioRob)*, pages 69–74. IEEE, 2012.
- [206] Roy J Roesthuis, Nick J van de Berg, John J van den Dobbelen, and Sarthak Misra. Modeling and steering of a novel actuated-tip needle through a soft-tissue simulant using fiber bragg grating sensors. In *Robotics and Automation (ICRA), 2015 IEEE International Conference on*, pages 2283–2289. IEEE, 2015.
- [207] Roy J Roesthuis, Youri RJ Van Veen, Alex Jahya, and Sarthak Misra. Mechanics of needle-tissue interaction. In *Intelligent Robots and Systems (IROS), 2011 IEEE/RSJ International Conference on*, pages 2557–2563. IEEE, 2011.
- [208] Joseph M Romano, Robert J Webster, and Allison M Okamura. Teleoperation of steerable needles. In *Proceedings 2007 IEEE International Conference on Robotics and Automation*, pages 934–939. IEEE, 2007.
- [209] Anne M Römgens, Debbie Rem-Bronneberg, Roel Kassies, Markus Hijlkema, Dan L Bader, Cees WJ Oomens, and Michel PB van Bruggen. Penetration and delivery characteristics of repetitive microjet injection into the skin. *Journal of controlled release*, 234:98–103, 2016.
- [210] Laura Ros-Freixedes, Anzhu Gao, Ning Liu, Mali Shen, and Guang-Zhong Yang.

- Design optimization of a contact-aided continuum robot for endobronchial interventions based on anatomical constraints. *International journal of computer assisted radiology and surgery*, 14(7):1137–1146, 2019.
- [211] D Caleb Rucker, Jadav Das, Hunter B Gilbert, Philip J Swaney, Michael I Miga, Nilanjan Sarkar, and Robert J Webster. Sliding mode control of steerable needles. *IEEE Transactions on Robotics*, 29(5):1289–1299, 2013.
- [212] D Caleb Rucker and Robert J Webster. Mechanics-based modeling of bending and torsion in active cannulas. In *2008 2nd IEEE RAS & EMBS International Conference on Biomedical Robotics and Biomechatronics*, pages 704–709. IEEE, 2008.
- [213] Marvin Ryou, Petros C Benias, and Vivek Kumbhari. Initial clinical experience of a steerable access device for eus-guided biliary drainage. *Gastrointestinal endoscopy*, 91(1):178–184, 2020.
- [214] Chiaki Sato, Toru Nakano, Atsuhiko Nakagawa, Masato Yamada, Hiroaki Yamamoto, Takashi Kamei, Go Miyata, Akira Sato, Fumiyoshi Fujishima, Masaaki Nakai, et al. Experimental application of pulsed laser-induced water jet for endoscopic submucosal dissection: Mechanical investigation and preliminary experiment in swine. *Digestive Endoscopy*, 25(3):255–263, 2013.
- [215] M Scali, Davey Kreeft, P Breedveld, and Dimitra Dodou. Design and evalua-

- tion of a wasp-inspired steerable needle. In *Bioinspiration, Biomimetics, and Bioreplication 2017*, volume 10162, page 1016207. International Society for Optics and Photonics, 2017.
- [216] Marta Scali, Paulien AH Veldhoven, Paul WJ Henselmans, Dimitra Dodou, and Paul Breedveld. Design of an ultra-thin steerable probe for percutaneous interventions and preliminary evaluation in a gelatine phantom. *PloS one*, 14(9), 2019.
- [217] Joy Schramm-Baxter, Jeffrey Katrencik, and Samir Mitragotri. Jet injection into polyacrylamide gels: investigation of jet injection mechanics. *Journal of biomechanics*, 37(8):1181–1188, 2004.
- [218] Joy Schramm-Baxter and Samir Mitragotri. Needle-free jet injections: dependence of jet penetration and dispersion in the skin on jet power. *Journal of Controlled Release*, 97(3):527–535, 2004.
- [219] Karsten Schwieger, Volker Carrero, Reemt Rentzsch, Axel Becker, Nick Bishop, Ekkehard Hille, Hartmut Louis, Michael Morlock, and Matthias Honl. Abrasive water jet cutting as a new procedure for cutting cancellous bone—in vitro testing in comparison with the oscillating saw. *Journal of Biomedical Materials Research Part B: Applied Biomaterials*, 71(2):223–228, 2004.
- [220] Patrick Sears and Pierre Dupont. A steerable needle technology using curved

- concentric tubes. In *2006 IEEE/RSJ international conference on intelligent robots and systems*, pages 2850–2856. IEEE, 2006.
- [221] Riccardo Secoli and Ferdinando Rodriguez y Baena. Closed-loop 3d motion modeling and control of a steerable needle for soft tissue surgery. In *2013 IEEE International Conference on Robotics and Automation*, pages 5831–5836. IEEE, 2013.
- [222] Reza Seifabadi, Fereshteh Aalamifar, Iulian Iordachita, and Gabor Fichtinger. Toward teleoperated needle steering under continuous mri guidance for prostate percutaneous interventions. *The International Journal of Medical Robotics and Computer Assisted Surgery*, 12(3):355–369, 2016.
- [223] Reza Seifabadi, Sang-Eun Song, Axel Krieger, Nathan Bongjoon Cho, Junichi Tokuda, Gabor Fichtinger, and Iulian Iordachita. Robotic system for mri-guided prostate biopsy: feasibility of teleoperated needle insertion and ex vivo phantom study. *International journal of computer assisted radiology and surgery*, 7(2):181–190, 2012.
- [224] Joon Seok, Chang Taek Oh, Hyun Jung Kwon, Tae Rin Kwon, Eun Ja Choi, Sun Young Choi, Seog Kyun Mun, Seung-Ho Han, Beom Joon Kim, and Myeung Nam Kim. Investigating skin penetration depth and shape following needle-

- free injection at different pressures: A cadaveric study. *Lasers in surgery and medicine*, 48(6):624–628, 2016.
- [225] Takeshi Seto, Hiroaki Yamamoto, Kazuyoshi Takayama, Atsuhiro Nakagawa, and Teiji Tominaga. Characteristics of an actuator-driven pulsed water jet generator to dissecting soft tissue. *Review of Scientific Instruments*, 82(5):055105, 2011.
- [226] Navid Shahriari, Wout Heerink, Tim Van Katwijk, Edsko Hekman, Matthijs Oudkerk, and Sarthak Misra. Computed tomography (ct)-compatible remote center of motion needle steering robot: fusing ct images and electromagnetic sensor data. *Medical engineering & physics*, 45:71–77, 2017.
- [227] Jun Sheng, Nancy J Deaton, and Jaydev P Desai. A large-deflection fbg bending sensor for sma bending modules for steerable surgical robots. In *2019 International Conference on Robotics and Automation (ICRA)*, pages 900–906. IEEE, 2019.
- [228] Oliver A Shergold and Norman A Fleck. Mechanisms of deep penetration of soft solids, with application to the injection and wounding of skin. *Proceedings of the Royal Society of London. Series A: Mathematical, Physical and Engineering Sciences*, 460(2050):3037–3058, 2004.
- [229] Oliver A Shergold, Norman A Fleck, and Toby S King. The penetration of a

- soft solid by a liquid jet, with application to the administration of a needle-free injection. *Journal of biomechanics*, 39(14):2593–2602, 2006.
- [230] Oliver A Shergold, Norman A Fleck, and Darren Radford. The uniaxial stress versus strain response of pig skin and silicone rubber at low and high strain rates. *International Journal of Impact Engineering*, 32(9):1384–1402, 2006.
- [231] Hong Shi, Sheng-Jun Jiang, Bin Li, Deng-Ke Fu, Pei Xin, and Yong-Guang Wang. Natural orifice transluminal endoscopic wedge hepatic resection with a water-jet hybrid knife in a non-survival porcine model. *World Journal of Gastroenterology: WJG*, 17(7):926, 2011.
- [232] B Todd Sitzman and David R Uncles. The effects of needle type, gauge, and tip bend on spinal needle deflection. *Anesthesia & Analgesia*, 82(2):297–301, 1996.
- [233] David A Summers. *Waterjetting technology*. CRC Press, 2003.
- [234] Wen Sun and Ron Alterovitz. Motion planning under uncertainty for medical needle steering using optimization in belief space. In *2014 IEEE/RSJ International Conference on Intelligent Robots and Systems*, pages 1775–1781. IEEE, 2014.
- [235] Philip J Swaney, Jessica Burgner, Hunter B Gilbert, and Robert J Webster.

- A flexure-based steerable needle: high curvature with reduced tissue damage. *IEEE Transactions on Biomedical Engineering*, 60(4):906–909, 2012.
- [236] Philip J Swaney, Jessica Burgner, Thomas S Pfeiffer, D Caleb Rucker, Hunter B Gilbert, Janet E Ondrake, Amber L Simpson, E Clif Burdette, Michael I Miga, and Robert J Webster III. Tracked 3d ultrasound targeting with an active cannula. In *Medical Imaging 2012: Image-Guided Procedures, Robotic Interventions, and Modeling*, volume 8316, page 83160R. International Society for Optics and Photonics, 2012.
- [237] Philip J Swaney, Hunter B Gilbert, Richard J Hendrick, Oliver Commichau, Ron Alterovitz, and Robert J Webster III. Transoral steerable needles in the lung: How non-annular concentric tube robots can improve targeting. In *Hamlyn Symp. Medical Robotics*, 2015.
- [238] Philip J Swaney, Arthur W Mahoney, Bryan I Hartley, Andria A Ramirez, Erik Lamers, Richard H Feins, Ron Alterovitz, and Robert J Webster III. Toward transoral peripheral lung access: Combining continuum robots and steerable needles. *Journal of medical robotics research*, 2(01):1750001, 2017.
- [239] John P Swensen and Noah J Cowan. Torsional dynamics compensation enhances robotic control of tip-steerable needles. In *Robotics and Automation (ICRA), 2012 IEEE International Conference on*, pages 1601–1606. IEEE, 2012.

- [240] John P Swensen, MingDe Lin, Allison M Okamura, and Noah J Cowan. Torsional dynamics of steerable needles: modeling and fluoroscopic guidance. *IEEE Transactions on Biomedical Engineering*, 61(11):2707–2717, 2014.
- [241] Yoshiyuki Tagawa, Nikolai Oudalov, A El Ghalbzouri, Chao Sun, and Detlef Lohse. Needle-free injection into skin and soft matter with highly focused microjets. *Lab on a Chip*, 13(7):1357–1363, 2013.
- [242] Wen Tang and Tao Ruan Wan. Constraint-based soft tissue simulation for virtual surgical training. *IEEE Transactions on Biomedical Engineering*, 61(11):2698–2706, 2014.
- [243] Meysam Torabi, Kris Hauser, Ron Alterovitz, Vincent Duindam, and Ken Goldberg. Guiding medical needles using single-point tissue manipulation. In *2009 IEEE International Conference on Robotics and Automation*, pages 2705–2710. IEEE, 2009.
- [244] Lindsey A Torre, Freddie Bray, Rebecca L Siegel, Jacques Ferlay, Joannie Lortet-Tieulent, and Ahmedin Jemal. Global cancer statistics, 2012. *CA: a cancer journal for clinicians*, 65(2):87–108, 2015.
- [245] CA Tschan, K Tschan, JK Krauss, and J Oertel. First experimental results with a new waterjet dissector: Erbejet 2. *Acta neurochirurgica*, 151(11):1473–1482, 2009.

- [246] Yoshie Une, Junichi Uchino, Takashi Horie, Yuji Sato, Kazuhiro Ogasawara, Akira Kakita, and Fumio Sano. Liver resection using a water jet. *Cancer chemotherapy and pharmacology*, 23:S74–S77, 1989.
- [247] Nick J van de Berg, Jenny Dankelman, and John J van den Dobbelsteen. Design of an actively controlled steerable needle with tendon actuation and fbg-based shape sensing. *Medical engineering & physics*, 37(6):617–622, 2015.
- [248] Nick J van de Berg, Jenny Dankelman, and John J van den Dobbelsteen. End-point accuracy in manual control of a steerable needle. *Journal of Vascular and Interventional Radiology*, 28(2):276–283, 2017.
- [249] Nick J van de Berg, Tonke L de Jong, Dennis J van Gerwen, Jenny Dankelman, and John J van den Dobbelsteen. The influence of tip shape on bending force during needle insertion. *Scientific Reports*, 7:40477, 2017.
- [250] Nick J van de Berg, Dennis J van Gerwen, Jenny Dankelman, and John J van den Dobbelsteen. Design choices in needle steering—a review. *IEEE/ASME Transactions on Mechatronics*, 20(5):2172–2183, 2014.
- [251] Jur Van Den Berg, Sachin Patil, Ron Alterovitz, Pieter Abbeel, and Ken Goldberg. Lqg-based planning, sensing, and control of steerable needles. In *Algorithmic Foundations of Robotics IX*, pages 373–389. Springer, 2010.

- [252] Dennis J van Gerwen, Jenny Dankelman, and John J van den Dobbela. Needle–tissue interaction forces—a survey of experimental data. *Medical engineering & physics*, 34(6):665–680, 2012.
- [253] Youri RJ van Veen, Alex Jahya, and Sarthak Misra. Macroscopic and microscopic observations of needle insertion into gels. *Proceedings of the Institution of Mechanical Engineers, Part H: Journal of Engineering in Medicine*, 226(6):441–449, 2012.
- [254] Alessandro Vandini, Christos Bergeles, Fang-Yu Lin, and Guang-Zhong Yang. Vision-based intraoperative shape sensing of concentric tube robots. In *2015 IEEE/RSJ International Conference on Intelligent Robots and Systems (IROS)*, pages 2603–2610. IEEE, 2015.
- [255] William C Vogt, Congxian Jia, Keith A Wear, Brian S Garra, and T Joshua Pfeffer. Biologically relevant photoacoustic imaging phantoms with tunable optical and acoustic properties. *Journal of biomedical optics*, 21(10):101405, 2016.
- [256] Charles M Vollmer, Elijah Dixon, Ajay Sahajpal, Mark S Cattral, David R Grant, Steven Gallinger, Bryce R Taylor, and Paul D Greig. Water-jet dissection for parenchymal division during hepatectomy. *HPB*, 8(5):377–385, 2006.
- [257] Gang Wan, Zhouping Wei, Lori Gardi, Donal B Downey, and Aaron Fenster.

- Brachytherapy needle deflection evaluation and correction. *Medical physics*, 32(4):902–909, 2005.
- [258] J Wang. Predictive depth of jet penetration models for abrasive waterjet cutting of alumina ceramics. *International Journal of Mechanical Sciences*, 49(3):306–316, 2007.
- [259] J Wang. A new model for predicting the depth of cut in abrasive waterjet contouring of alumina ceramics. *Journal of materials processing technology*, 209(5):2314–2320, 2009.
- [260] J Wang and DM Guo. A predictive depth of penetration model for abrasive waterjet cutting of polymer matrix composites. *Journal of materials processing technology*, 121(2-3):390–394, 2002.
- [261] Jianjun Wang, Xiangpeng Li, Jinjin Zheng, and Dong Sun. Mechanics-based modeling of needle insertion into soft tissue. In *2013 IEEE/ASME International Conference on Advanced Intelligent Mechatronics*, pages 38–43. IEEE, 2013.
- [262] Jiaole Wang, Junhyoung Ha, and Pierre E Dupont. Steering a multi-armed robotic sheath using eccentric precurved tubes. In *2019 International Conference on Robotics and Automation (ICRA)*, pages 9834–9840. IEEE, 2019.
- [263] Tzu-Wei Wang and Myron Spector. Development of hyaluronic acid-based scaffolds for brain tissue engineering. *Acta biomaterialia*, 5(7):2371–2384, 2009.

- [264] Yancheng Wang, Bruce L Tai, Roland K Chen, and Albert J Shih. The needle with lancet point: geometry for needle tip grinding and tissue insertion force. *Journal of Manufacturing Science and Engineering*, 135(4):041010, 2013.
- [265] Yancheng Wang, Bruce L Tai, Hongwei Yu, and Albert J Shih. Silicone-based tissue-mimicking phantom for needle insertion simulation. *Journal of Medical Devices*, 8(2), 2014.
- [266] Thomas Watts, Riccardo Secoli, and Ferdinando Rodriguez y Baena. A mechanics-based model for 3-d steering of programmable bevel-tip needles. *IEEE Transactions on Robotics*, 35(2):371–386, 2018.
- [267] Robert J Webster, Jasenka Memisevic, and Allison M Okamura. Design considerations for robotic needle steering. In *Proceedings of the 2005 IEEE International Conference on Robotics and Automation*, pages 3588–3594. IEEE, 2005.
- [268] Robert J Webster, Allison M Okamura, and Nah J Cowan. Toward active cannulas: Miniature snake-like surgical robots. In *2006 IEEE/RSJ international conference on intelligent robots and systems*, pages 2857–2863. IEEE, 2006.
- [269] Robert J Webster, Joseph M Romano, and Noah J Cowan. Kinematics and calibration of active cannulas. In *2008 IEEE International Conference on Robotics and Automation*, pages 3888–3895. IEEE, 2008.

- [270] Robert J Webster III, Jin Seob Kim, Noah J Cowan, Gregory S Chirikjian, and Allison M Okamura. Nonholonomic modeling of needle steering. *The International Journal of Robotics Research*, 25(5-6):509–525, 2006.
- [271] Robert J Webster III, Joseph M Romano, and Noah J Cowan. Mechanics of precurved-tube continuum robots. *IEEE Transactions on Robotics*, 25(1):67–78, 2008.
- [272] Thomas R Wedlick and Allison M Okamura. Characterization of pre-curved needles for steering in tissue. In *Engineering in Medicine and Biology Society, 2009. EMBC 2009. Annual International Conference of the IEEE*, pages 1200–1203. IEEE, 2009.
- [273] Patrick S Wellborn, Philip J Swaney, and Robert J Webster. Curving clinical biopsy needles: can we steer needles and still obtain core biopsy samples? *Journal of Medical Devices*, 10(3), 2016.
- [274] Peter NT Wells and Hai-Dong Liang. Medical ultrasound: imaging of soft tissue strain and elasticity. *Journal of the Royal Society Interface*, 8(64):1521–1549, 2011.
- [275] James D Westwood et al. In vivo force during arterial interventional radiology needle puncture procedures. In *Medicine Meets Virtual Reality: The Magical Next Becomes the Medical Now*, volume 111, pages 178–184. IOS Press, 2005.

- [276] RJ Wilkins and EE Graham. An erosion model for waterjet cutting. *Journal of engineering for industry*, 115(1):57–61, 1993.
- [277] Nathan A Wood, Craig A Lehocky, and Cameron N Riviere. Algorithm for three-dimensional control of needle steering via duty-cycled rotation. In *2013 IEEE International Conference on Mechatronics (ICM)*, pages 237–241. IEEE, 2013.
- [278] Hua Xie, Kang Kim, Salavat R Aglyamov, Stanislav Y Emelianov, Matthew O’Donnell, William F Weitzel, Shirley K Wroblewski, Daniel D Myers, Thomas W Wakefield, and Jonathan M Rubin. Correspondence of ultrasound elasticity imaging to direct mechanical measurement in aging dvt in rats. *Ultrasound in medicine & biology*, 31(10):1351–1359, 2005.
- [279] Jijie Xu, Vincent Duindam, Ron Alterovitz, and Ken Goldberg. Motion planning for steerable needles in 3d environments with obstacles using rapidly-exploring random trees and backchaining. In *2008 IEEE international conference on automation science and engineering*, pages 41–46. IEEE, 2008.
- [280] Naohisa Yahagi, H Neuhaus, B Schumacher, A Neugebauer, GF Kaehler, M Schenk, K Fischer, M Fujishiro, and MD Enderle. Comparison of standard endoscopic submucosal dissection (esd) versus an optimized esd technique for the colon: an animal study. *Endoscopy*, 41(04):340–345, 2009.

- [281] Masato Yamada, Toru Nakano, Chiaki Sato, Atsuhiko Nakagawa, Fumiyoshi Fujishima, Naoki Kawagishi, Chikashi Nakanishi, Tadashi Sakurai, Go Miyata, Teiji Tominaga, et al. The dissection profile and mechanism of tissue-selective dissection of the piezo actuator-driven pulsed water jet as a surgical instrument: Laboratory investigation using swine liver. *European Surgical Research*, 53(1-4):61–72, 2014.
- [282] Satoshi Yamaguchi, Kihei Tsutsui, Koji Satake, Shigehiro Morikawa, Yoshiaki Shirai, and Hiromi T Tanaka. Dynamic analysis of a needle insertion for soft materials: Arbitrary lagrangian–eulerian-based three-dimensional finite element analysis. *Computers in Biology and Medicine*, 53:42–47, 2014.
- [283] Kai Guo Yan, Tarun Podder, Yan Yu, Tien-I Liu, Christopher WS Cheng, and Wan Sing Ng. Flexible needle–tissue interaction modeling with depth-varying mean parameter: preliminary study. *IEEE Transactions on Biomedical Engineering*, 56(2):255–262, 2008.
- [284] Fan Yang, Mahdieh Babaiasl, and John P Swensen. Fracture-directed steerable needles. *Journal of Medical Robotics Research*, 4(01):1842002, 2019.
- [285] Yang-Ho Na Takayuki Kurokawa Jian Ping Gong Yoshimi Tanaka, Rikimaru Kuwabara and Yoshihito Osada. Determination of fracture energy of

- high strength double network hydrogels. *The Journal of Physical Chemistry B*, 109:11559–11562, 2005.
- [286] Karin Zell, Jonathan I Sperl, Mika W Vogel, Reinhard Niessner, and Christoph Haisch. Acoustical properties of selected tissue phantom materials for ultrasound imaging. *Physics in Medicine & Biology*, 52(20):N475, 2007.
- [287] Yu Zhou, Kaarvannan Thiruvalluvan, Lukasz Krzeminski, William H Moore, Zhigang Xu, and Zhengrong Liang. Ct-guided robotic needle biopsy of lung nodules with respiratory motion–experimental system and preliminary test. *The International Journal of Medical Robotics and Computer Assisted Surgery*, 9(3):317–330, 2013.